Michael Landl, BSc

# Turbulence and Transition Modeling for Thermal Turbomachinery

## Master's Thesis

to achieve the university degree of

Diplom-Ingenieur

Master's degree programme: Mechanical Engineering

submitted to

## Graz University of Technology

Supervisor

Ao.Univ.-Prof. Dipl-Ing. Dr.techn. Wolfgang Sanz

Institute of Thermal Turbomachinery and Machine Dynamics
Head: Univ.-Prof. Dr.-Ing. Franz Heitmeir

Graz, June 2019

# Affidavit

I declare that I have authored this thesis independently, that I have not used other than the declared sources/resources, and that I have explicitly indicated all material which has been quoted either literally or by content from the sources used. The text document uploaded to TUGRAZonline is identical to the present master's thesis.

_____          _____
Date                                      Signature

# Acknowledgments

*In loving memory of **Cedrik***
*† 15.10.2018*

# Kurzfassung

Die vorliegende Arbeit beschäftigte sich mit Turbulenzmodellierung und der Vorhersage des Umschlages von laminarer auf turbulente Strömung in wandnahen Grenzschichten mit dem Fokus auf die Anwendung in thermischen Turbomaschinen. Die untersuchten Modelle sind vom Typ der Wirbelviskositätsmodelle und lösen das Schließungsproblem der Reynolds-gemittelten Navier-Stokes Gleichungen mit Hilfe der Boussinesq-Annahme. Obwohl in der Forschung vermehrt direkte numerische Simulation (DNS) und Grobstruktursimulation (LES) eingesetzt wird, sind Wirbelviskositätsmodelle weiterhin von zentraler Bedeutung für die Industrie und kommen zum Einsatz bei der Optimierung unzähliger technisch relevanter Strömungen. Durch die Wahl geeigneter Modelle können gravierende und kostspielige Fehler in der Entwicklung von Bauteilen und der Optimierung von Prozessen vermieden werden.

Im Zuge dieser Arbeit wurde das auf lokalen Korrelationen basierende $\gamma$ Transitionsmodell, welches eine Vereinfachung des bekannten $\gamma$-$Re_{\theta t}$ Modells darstellt, und das $k$-$\overline{v^2}$-$\omega$ Modell, welches eine Modifikation des $k$-$k_L$-$\omega$ Modells ist, in den institutseigenen numerischen Strömungslöser LINARS implementiert. Das $k$-$k_L$-$\omega$ Modell, welches bereits implementiert war, wurde in die Formulierung für kompressible Fluide umgeschrieben mit der Erwartung sowohl die Vorhersagen zu verbessern als auch die Stabilität der Simulationen zu erhöhen. Diese Implementierungen wurden für zwei Testfälle mit kommerzieller Software verglichen und für weitere Testfälle hinsichtlich ihrer Qualität untersucht. Dabei kamen neben einer ebenen Plattenströmung ohne Druckgradienten zwei lineare Kaskaden, welche quasi-dreidimensional untersucht wurden, sowie ein voll dreidimensionaler Testfall mit gegenläufig drehenden Hochdruck- und Niederdruck-Turbinen zur Anwendung. Soweit verfügbar wurden die Ergebnisse mit hochwertigen Messergebnissen verglichen.

Die neuen Implementierungen konnten erfolgreich validiert werden. Es zeigte sich aber, dass die Modelle auf unterschiedliche numerische Methoden, welche zur Lösung der Transportgleichungen zum Einsatz kommen, sensibel sind. Die erhaltenen Vorhersagen waren größtenteils plausibel. Ohne die verfügbaren Messungen hätte aber nur sehr schwer eine Aussage über die quantitative Korrektheit getroffen werden können. Daher wird dringlich geraten die Ergebnisse von Simulationen, sofern keine umfassenden Erfahrungswerte vorliegen, mit Versuchen abzusichern.

# Abstract

Topic of the present work was turbulence modeling and the prediction of laminar to turbulent flow transition of wall boundary layers with a focus on the application in thermal turbomachinery. The investigated models solve the closure problem of the Reynolds-averaged Navier-Stokes equations by employing the Boussinesq assumption. Although Direct Numerical Simulation (DNS) and Large Eddy Simulation (LES) are currently heavily researched, Eddy Viscosity Models are still of high importance for the industry and are used to optimize countless technical flows. By applying suitable models, severe and costly errors in the development of components and the optimization of processes can be avoided.

In this thesis, the $\gamma$ transition model, which is based on local correlations and represents a simplification of the well-known $\gamma$-$Re_{\theta t}$ model, and the $k$-$\overline{v^2}$-$\omega$ model, which is a modification of the $k$-$k_L$-$\omega$ model, were implemented in LINARS, the in-house numerical flow solver. The $k$-$k_L$-$\omega$ model, which was already implemented, was rewritten into the formulation for compressible fluid flow with the expectation of both improving prediction accuracy and increasing stability of the simulation. The implementations were compared for two test cases with commercial software, and in additional test cases their quality was investigated. In addition to the flow along a flat plate without pressure gradient, two linear cascade flows, which were investigated quasi three-dimensionally, and a fully three-dimensional test case with counter-rotating high-pressure and low-pressure turbines were used. Where available, the results were compared to high-quality measurements.

The new implementations were successfully validated. However, it turned out that the models are sensitive to the numerical methods used to solve the transport equations. The obtained predictions for transition onset were plausible in most cases. Without the available measurements, however, it would have been very difficult to assess the predictions quantitatively. Therefore, it is highly recommended that experiments are carried out to validate the predictions, for the case that no comprehensive experience for a specific configuration is available.

# Contents

# Acronyms

AIAA        American Institute of Aeronautics and Astronautics

BC          boundary condition
BP          bypass
BSL         base line

CFD         Computational Fluid Dynamics
CFL         Courant–Friedrichs–Lewy

DDES        Delayed Detached Eddy Simulation
DES         Detached Eddy Simulation
DNS         Direct Numerical Simulation

ERCOFTAC    European Research Community on Flow, Turbulence and Combustion
EVM         Eddy Viscosity Model

FVM         Finite Volume Method

GPLv3       GNU General Public License v3

HPR         high pressure rotor
HPS         high pressure stator

IDDES       Improved Delayed Detached Eddy Simulation
ITTM        Institute of Thermal Turbomachinery and Machine Dynamics

LCTM        Local Correlation-Based Transition Model
LES         Large Eddy Simulation

| | |
|---|---|
| LHS | left hand side |
| LPR | low pressure rotor |
| | |
| MPI | Message Passing Interface |
| MUSCL | Monotone Upstream-Centered Schemes for Conservation Laws |
| | |
| NAT | natural |
| | |
| ODE | ordinary differential equation |
| openMP | Open Multi-Processing |
| | |
| PDE | partial differential equation |
| | |
| RANS | Reynolds-averaged Navier-Stokes |
| RHS | right hand side |
| RMS | root mean square |
| RSM | Reynolds Stress Model |
| | |
| SGS | sub-grid-scale |
| SST | Shear Stress Transport |
| | |
| TMBWG | Turbulence Model Benchmarking Working Group |
| TMTF | turning mid turbine frame |
| TS | Tollmien-Schlichting |
| TTTF | Transonic Test Turbine Facility |
| TVD | total variation diminishing |
| | |
| URANS | Unsteady Reynolds-averaged Navier-Stokes |
| | |
| VKI | Von Karman Institute for Fluid Dynamics |
| | |
| WENO | Weighted Essentially Non-Oscillatory |
| WM-LES | Wall Modeled Large Eddy Simulation |

# List of Symbols

## Roman Symbols

| Symbol | Description | Unit |
|--------|-------------|------|
| $A$ | face area | $\mathrm{m^2}$ |
| $a$ | speed of sound | $\mathrm{m/s}$ |
| $a_1$ | Bradshaw constant | — |
| $a_t$ | turbulent heat diffusivity | $\mathrm{m^2/s}$ |
| $B$ | constant for law of the wall | — |
| $C$ | axial chord length | m |
| $C_k$ | model constant for $P_{k,lim}$ | — |
| $C_{l1,l2}$ | model constants | — |
| $C_S$ | Sutherland constant | K |
| $C_{\mathrm{sep}}$ | model constant for $P_{k,lim}$ | — |
| $C_{PG1}$ | adjustment parameter for favorable pressure gradients | — |
| $C_{PG2}$ | adjustment parameter for adverse pressure gradients | — |
| $C_{PG3}$ | adjustment parameter for regions with separation | — |
| $C_{PG1}^{\mathrm{lim}}$ | limit in case of adverse pressure gradients | — |
| $C_{PG2}^{\mathrm{lim}}$ | limit in case of favorable pressure gradients | — |
| $C_{TU1}$ | minimal value of the critical Reynolds Theta number | — |
| $C_{TU2}$ | offset from minimal value for maximal value of $Re_{\theta,c}$ | — |
| $C_{TU3}$ | shrinkage parameter | — |
| $C_{SS}$ | model constant for shear-sheltering | — |
| $C_\mu = \beta^*$ | dimensionless eddy viscosity coefficient | — |
| $C_{\omega R}$ | constant for $k$-$k_L$-$\omega$ model | — |
| $CD_{k\omega}$ | $k$-$\omega$ cross-diffusion term | $\mathrm{kg/m\,s^2}$ |

| Symbol | Description | Unit |
|---|---|---|
| $c$ | arbitrary constant | |
| $ca_{1,2}$ | modeling constants in $\gamma$ destruction term | — |
| $ce_{1,2}$ | modeling constants in $\gamma$ production term | — |
| $c_f$ | local skin friction coefficient | — |
| $c_p$ | heat capacity at constant pressure | $\mathrm{J/kg\,K}$ |
| $c_v$ | heat capacity at constant volume | $\mathrm{J/kg\,K}$ |
| $c_{\theta t}$ | modeling constant in $Re_{\theta t}$ production term | — |
| $c_{\omega 1,2,3}$ | constant for $k$-$k_L$-$\omega$ model | — |
| $d_w$ | minimal distance to closest wall | m |
| $d_{\mathrm{eff}}$ | effective (limited) distance to closest wall | m |
| $dV$ | infinitesimal volume element | $\mathrm{m^3}$ |
| $D_k$ | destruction term of turbulence kinetic energy | $\mathrm{kg/m\,s^3}$ |
| $\hat{D}_k$ | limited destruction term of turbulence kinetic energy | $\mathrm{kg/m\,s^3}$ |
| $D_T$ | anisotropic diffusion term of turbulence kinetic energy | $\mathrm{m^2/s^3}$ |
| $D_L$ | anisotropic diffusion term of laminar kinetic energy | $\mathrm{m^2/s^3}$ |
| $D_{\overline{v^2}}$ | anisotropic diffusion term of wall-normal velocity fluctuations | $\mathrm{m^2/s^3}$ |
| $e$ | total specific internal energy | $\mathrm{J/kg}$ |
| $E_\gamma$ | destruction term for intermittency | $\mathrm{kg/m^3\,s}$ |
| $F$ | fluctuation frequencies | Hz |
| $F_{1,2,3}$ | SST model blending functions | — |
| $F_{PG}$ | pressure gradient function | — |
| $F_{\theta t}$ | $\gamma$-$Re_{\theta t}$ model blending function | — |
| $F_{\mathrm{length}}$ | corrected transition length (constant for $\gamma$ model) | — |
| $\hat{F}_{\mathrm{length}}$ | empirical correlation for the transition length | — |
| $F_{\mathrm{onset}}$ | final value for the onset sensor | — |
| $F_{\mathrm{onset1,2,3}}$ | intermittent values for the onset sensor | — |
| $F_{\mathrm{onlim}}$ | limited onset function | — |
| $F_{\mathrm{reattach}}$ | reattachment damping function | — |
| $F_{\mathrm{sublayer}}$ | sublayer damping function | — |

| Symbol | Description | Unit |
|---|---|---|
| $F_{\text{turb}}$ | damping function for fully turbulent regions | — |
| $F_{\text{wake}}$ | wake region activation term | — |
| $f_i^b$ | body force vector | $\text{m/s}^2$ |
| $f_{\text{INT}}$ | empirical damping function of the intermittency | — |
| $f_W$ | near wall non-viscous damping function | — |
| $f_\omega$ | $\omega$ damping function | — |
| $f_{SS}$ | shear-sheltering factor (transition sensor) | — |
| $f_\nu$ | viscous damping function (viscous wall effect) | — |
| $F_{\lambda\theta}$ | empirical pressure-gradient function (correlation) | — |
| $f_{\tau,l}$ | turbulent time scale damping function | — |
| $g$ | spacing of blades, pitch | m |
| $h$ | specific enthalpy | $\text{J/kg}$ |
| $H$ | shape factor | — |
| $K$ | Launder acceleration parameter | — |
| $k$ | (specific) turbulence kinetic energy | $\text{m}^2/\text{s}^2$ |
| $k_L$ | laminar kinetic energy | $\text{m}^2/\text{s}^2$ |
| $k_{t,s}$ | small scale turbulence kinetic energy | $\text{m}^2/\text{s}^2$ |
| $k_{t,l}$ | large scale turbulence kinetic energy | $\text{m}^2/\text{s}^2$ |
| $L$ | characteristic length | m |
| $L_c$ | chord length | m |
| $L_p$ | length of flat plate (T3A test case) | m |
| $l_{\text{turb}}$ | turbulence length scale | m |
| $m$ | mass | kg |
| $\dot{m}$ | mass flow | $\text{kg/s}$ |
| $M$ | molar mass | $\text{kg/mol}$ |
| $Ma$ | Mach Number $Ma = U/a$ | — |
| $Ma_{\text{is}}$ | istentropic Mach number | — |
| $n$ | wall-normal coordinate | m |

| Symbol | Description | Unit |
|---|---|---|
| $n$ | wall-normal vector | m |
| $n_r$ | rotational speed | $1/\text{min}$ |
| $n_R$ | counter for flow realizations | — |
| $N$ | total number of flow realizations | — |
| | | |
| $p$ | static pressure | Pa |
| $p_{\text{tot}}$ | total pressure | Pa |
| $P_{...}$ | production terms ($k, k_L, \omega, \gamma, \theta t$), | |
| $P_k^{lim}$ | additional turbulence kinetic energy production term | $\text{kg}/\text{m}^3\,\text{s}^2$ |
| $\widetilde{P}_{...}$ | limited production terms | |
| $\hat{P}_{...}$ | limited modified production terms | |
| $Pr$ | Prandtl number $Pr = \frac{\mu c_p}{\lambda}$ | — |
| $Pr_t$ | turbulence Prandtl number | — |
| | | |
| $Q$ | second invariant of Jacobian | $1/\text{s}$ |
| $q_i$ | heat flux vector | $\text{W}/\text{m}^2$ |
| $q_{ti}$ | turbulent heat flux vector $q_{ti} = c_p \overline{\rho u_j'' T''}$ | $\text{W}/\text{m}^2$ |
| $q_w$ | local heat flux at wall | $\text{W}/\text{m}^2$ |
| | | |
| $r$ | radial coordinate | m |
| $Re$ | Reynolds number | — |
| $Re_S$ | strain-rate Reynolds number | — |
| $Re_v$ | vorticity Reynolds number | — |
| $Re_\Omega$ | vorticity Reynolds number | — |
| $Re_{d_w}$ | wall-distance Reynolds number | — |
| $Re_x$ | local Reynolds number | — |
| $Re_\theta$ | momentum thickness Reynolds number | — |
| $Re_{\theta c}$ | critical momentum thickness Reynolds number | — |
| $Re_{\theta c}^{\text{lim}}$ | critical momentum thickness Reynolds number in $F_{\text{onlim}}$ | — |
| $Re_{\theta t}$ | momentum thickness transitional Reynolds number | — |
| $\hat{Re}_{\theta t}$ | transported momentum thickness transitional Reynolds number | — |

| Symbol | Description | Unit |
|---|---|---|
| $R_T$ | ratio of eddy to shear viscosity | — |
| $R_m$ | molar (universal) gas constant $R_m = 8.3144598$ | $\mathrm{J/mol\,K}$ |
| $R$ | specific gas constant $R = R_m/M$ | $\mathrm{J/kg\,K}$ |
| $R_{\mathrm{NAT}}$ | kinetic energy redistribution term for natural transition | $\mathrm{m^2/s^3}$ |
| $R_{\mathrm{BP}}$ | kinetic energy redistribution term for bypass transition | $\mathrm{m^2/s^3}$ |
| $R_\omega$ | dimensionless scaling for the sublayer modification | — |
| | | |
| $s$ | blade coordinate | m |
| $s/C$ | relative blade coordinate | — |
| $S$ | mean value of the strain rate tensor | $\mathrm{1/s}$ |
| $S_{ij}$ | strain rate tensor $S_{ij} = \frac{1}{2}\left(\frac{\partial u_i}{\partial x_j} + \frac{\partial u_j}{\partial x_i}\right)$ | $\mathrm{1/s}$ |
| $\hat{S}_{ij}$ | traceless strain rate tensor | $\mathrm{1/s}$ |
| $\hat{S}$ | mean value of the traceless strain rate tensor | $\mathrm{1/s}$ |
| $S_T$ | Sutherland temperature exponent | — |
| | | |
| $t$ | time | s |
| $t_{\theta t}$ | time-scale for production term | s |
| $T_{1,2}$ | time scales | s |
| $T$ | temperature | K |
| $T_{\mathrm{tot}}$ | total temperature | K |
| $T_S$ | reference temperature for Sutherland's law of viscosity | K |
| $Ti$ | time interval | s |
| $Ti_1$ | time-scale of turbulence fluctuations | s |
| $Ti_2$ | time-scale of the mean flow variation | s |
| $Tu$ | free-stream turbulence intensity | — |
| $Tu_L$ | local turbulence intensity | — |
| | | |
| $U$ | velocity magnitude $U = \sqrt{u^2 + v^2 + w^2}$ | $\mathrm{m/s}$ |
| $\overline{U}$ | magnitude of mean flow | $\mathrm{m/s}$ |
| $u$ | velocity component into x-coordinate-direction | $\mathrm{m/s}$ |
| $u^+$ | dimensionless velocity (parallel to wall) | — |
| $u_\tau$ | friction velocity | $\mathrm{m/s}$ |

| Symbol | Description | Unit |
|---|---|---|
| $u_i$ | Cartesian velocity vector | m/s |
| $\overline{u_i'^2}$ | variance of velocity fluctuation | m²/s² |
| $u_{\text{int}}$ | internal specific energy | J/kg |
| $v$ | velocity component into y-coordinate-direction | m/s |
| $\overline{v^2}$ | kinetic energy of the wall-normal turbulent velocity fluctuations | m²/s² |
| $\overline{v_l^2}$ | large scale kinetic energy of the wall-normal turbulent velocity fluctuations | m²/s² |
| $w$ | velocity component into z-coordinate-direction | m/s |
| $x_i$ | Cartesian position vector | m |
| $x$ | axial coordinate | m |
| $x$ | arbitrary ordinate | |
| $x/C$ | relative axial coordinate | — |
| $y$ | arbitrary abscissa | |
| $y^+$ | dimensionless wall distance | — |

## Greek Symbols

| Symbol | Description | Unit |
|---|---|---|
| $\alpha$ | turbulence modeling constant ($k$-$\omega$, $k$-$\varepsilon$ model) | — |
| $\alpha$ | local heat transfer coefficient | $\mathrm{W/m^2\,K}$ |
| $\alpha_{1,2}$ | turbulence modeling constants | — |
| $\alpha_t$ | turbulent diffusion | $\mathrm{m^2/s}$ |
| $\beta$ | turbulence modeling constant ($k$-$\omega$, $k$-$\varepsilon$ model) | — |
| $\beta_{1,2}$ | turbulence modeling constants | — |
| $\beta_{\mathrm{in}}$ | inlet flow angle | — |
| $\beta_{\mathrm{TS}}$ | Tollmien-Schlichting threshold function | — |
| $\beta^* = C_\mu$ | dimensionless eddy viscosity constant | — |
| $\gamma$ | intermittency | — |
| $\gamma^*$ | intermittency like transition indicator variable | — |
| $\gamma_c$ | heat capacity ratio $\gamma_c = c_p/c_v$ | — |
| $\gamma_{\mathrm{eff}}$ | effective intermittency | — |
| $\gamma_{\mathrm{sep}}$ | separation intermittency | — |
| $\delta$ | boundary layer thickness | m |
| $\delta^*$ | boundary layer thickness, approximation SST | m |
| $\delta_1$ | displacement thickness | m |
| $\delta_2 = \theta$ | momentum thickness | m |
| $\Delta t$ | discrete time increment | s |
| $\varepsilon$ | (specific) turbulence dissipation | $\mathrm{m^2/s^2}$ |
| $\zeta$ | volume viscosity | $\mathrm{Pa\,s}$ |
| $\theta = \delta_2$ | momentum thickness | m |
| $\kappa$ | von Kármán constant | — |
| $\lambda$ | thermal conductivity | $\mathrm{W/m\,K}$ |
| $\lambda_{\theta,L}$ | local pressure gradient parameter | — |

| Symbol | Description | Unit |
|---|---|---|
| $\lambda_\theta$ | pressure gradient parameter | — |
| $\lambda_{\text{eff}}$ | effective length-scale | m |
| $\mu$ | dynamic (shear) viscosity | Pa s |
| $\mu_t$ | dynamic eddy viscosity | Pa s |
| $\mu_S$ | reference dynamic viscosity for Sutherland's formula | Pa s |
| $\nu$ | kinematic (shear) viscosity | $\text{m}^2/\text{s}$ |
| $\nu_t$ | kinematic eddy viscosity | $\text{m}^2/\text{s}$ |
| $\nu_{t,s}$ | kinematic small-scale eddy viscosity | $\text{m}^2/\text{s}$ |
| $\nu_{t,l}$ | kinematic large-scale eddy viscosity | $\text{m}^2/\text{s}$ |
| $\rho$ | density | $\text{kg}/\text{m}^3$ |
| $\sigma_{...}$ | Prandtl-Schmidt numbers $(k, \omega, \varepsilon, \omega1, \omega2, \gamma, \theta t)$ | — |
| $\sigma_{ij}$ | (total) stress tensor | $\text{N}/\text{m}^2$ |
| $\tau_{ij}$ | viscous stress tensor | $\text{N}/\text{m}^2$ |
| $\tau_{tij}$ | Reynolds stress tensor $\tau_{tij} = -\overline{\rho u_i'' u_j''}$ | $\text{N}/\text{m}^2$ |
| $\tau_w$ | wall shear-stress magnitude | $\text{N}/\text{m}^2$ |
| $\phi$ | arbitrary flow quantity | |
| $\psi$ | arbitrary flow quantity | |
| $\omega$ | (specific) turbulence dissipation rate | $1/\text{s}$ |
| $\Omega_{ij}$ | vorticity tensor $\Omega_{ij} = \frac{1}{2}\left(\frac{\partial u_i}{\partial x_j} - \frac{\partial u_j}{\partial x_i}\right)$ | $1/\text{s}$ |
| $\Omega$ | magnitude of the vorticity tensor | $1/\text{s}$ |

# Subscripts

| Symbol | Description |
| --- | --- |
| c | critical |
| in | inlet |
| is | isentropic |
| L | local |
| lam | laminar |
| out | outlet |
| tot | total |
| turb | turbulent |
| $\infty$ | free-stream |

# Operators

| Symbol | Description |
| --- | --- |
| $D$ | Lagrange (substantial) derivative |
| $\langle \phi \rangle$ | Ensemble Reynolds average |
| $\overline{\phi}$ | Reynolds time average |
| $\widetilde{\phi}$ | Favre average |
| $\phi'$ | Reynolds fluctuation |
| $\phi''$ | Favre fluctuation |
| $\overline{\phi'^2}$ | Variance of fluctuating quantity |
| $\delta_{ij}$ | Kronecker delta |
| $\Delta$ | discrete increment |
| $\exp[\dots]$ | Euler's number to the power of the expression $i.e., e^{(\dots)}$ |
| $\underline{\underline{A}}$ | Tensor in vector notation |
| $\lVert \underline{A} \rVert$ | Tensor norm |
| $\vec{\phi}$ | Vector notations |

# Miscellaneous

| Symbol | Description |
| --- | --- |
| $ds$ | stream-wise differential operator |
| $dU/ds$ | stream-wise velocity gradient |
| $dV/dy$ | wall-normal velocity gradient |
| $i, j, k$ | index notation |
| $1, 2, 3$ | index notation |

# List of Figures

# List of Tables

# 1. Introduction

Before diving deep into the mathematical modeling of turbulent flow, a brief introduction to turbulence (sec. 1.1) and boundary layer theory (sec. 1.2), as well as an overview of strategies to simulate turbulent flow (sec. 1.3) are given. For a more comprehensive introduction to turbulence, the books of Davidson [1], Pope [2], and Wilcox [3] are highly recommended, on which the following synopsis is based. Finally, at the end of the chapter, the motivation and goal (sec. 1.4) of this thesis are formulated.

## 1.1. Turbulence

Many great scientists devoted their research to turbulent flow. The attraction and fascination for this topic are easily explained. Turbulent flow is not only the most complex form of fluid flow, but it is also the most common [4]. It can be observed throughout nature and in almost all technical processes. While the engineering target often is to reduce the influence of negative effects of turbulent flow such as increased wall friction and associated losses, it is highly beneficial to other processes due to the greatly improved mixing of fluids and the enhanced heat transfer, caused by the increased diffusivity.

The dimensionless characteristic Reynolds number $Re$ allows to assess if a given fluid flow could be turbulent and is usually the first characteristic number of interest. It is named after Osborne Reynolds who famously studied the onset of turbulent flow inside a pipe in 1883 [5]. It relates the inertial forces to the viscous forces and is given by

$$Re = \frac{UL}{\nu},$$
(1.1)

where $U$ is the velocity magnitude, $L$ is a characteristic length and $\nu$ is the kinematic viscosity of the fluid. Below a certain value, known as the critical Reynolds number $Re_{\mathrm{crit}}$, the fluid flow is controlled by viscous forces and is observed to be well behaved and stays predominantly within distinct layers. This form of flow is called laminar. The critical Reynolds number is different for every geometry and usually only the lower critical Reynolds number is given, below which the flow is ensured

to be laminar because the viscous forces dampen the turbulent fluctuations. For very smooth upstream conditions, the transition onset can be delayed substantially beyond the lower critical Reynolds number. However, for high Reynolds numbers, the laminar flow becomes unstable and fast, seemingly random, fluctuations of various flow variables, such as the velocity and the pressure can be observed. Especially in wall-near regions, the fluctuations are substantial compared to the mean flow velocity magnitude.
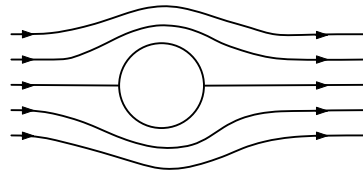
(a) $Re < 4$ Laminar attached - Steady
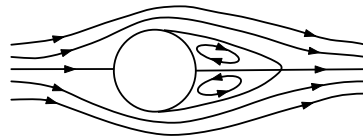
(b) $Re < 40$ Laminar separated - Steady
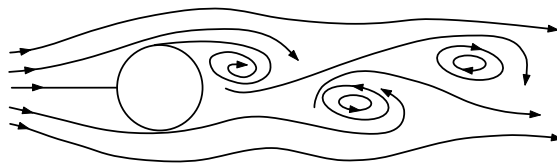
(c) $Re < 200$ Laminar separated - Periodic unsteady
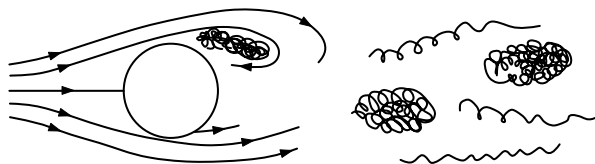
(d) $Re \approx 10^4$ Laminar separation with turbulent wake flow - Periodic unsteady
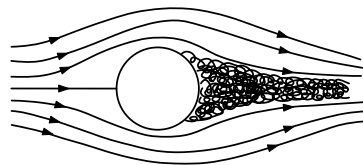
(e) $Re \approx 10^6$ Turbulent separation with chaotic wake flow

Figure 1.1.: Influence of the Reynolds Number $Re$ on the flow around a cylinder as observed by experiments. Adapted from Davidson [1].

Exemplary Figure 1.1 shows the schematics of the increasingly unstable fluid flow

around a cylinder for increasing Reynolds numbers. For very low Reynolds numbers ($Re < 4$) the flow is laminar, steady and attached to the cylinder. With increasing Reynolds numbers the fluid flow separates in the wake of the cylinder and two counterrotating vortices form. With further increasing Reynolds number ($Re < 200$) the vortices detach periodically and the so-called Kármán vortex street forms. At $Re \approx 10^4$ the detached vortices and the flow further downstream become turbulent. Finally, at $Re \approx 10^6$ the separation process is fully turbulent and the wake shows chaotic flow behavior.

Until now it only has been established that turbulent flow can be observed for sufficient high Reynolds numbers. Because no precise definition of turbulence exists, the effort to describe it qualitatively is made:

(i) **Turbulent Eddies**
   The flow consists of distinct patches of fluid, so-called eddies, where the vorticity is very high. These eddies exist on a very large span of scales, where the largest scales are in comparable size to the geometric flow dimensions, for example the diameter of a pipe or the height of a boundary layer. The largest eddies interact with the mean flow by a process called vortex stretching and transport the energy further down to the smaller scales until they are small enough to directly interact on a molecular level and dissipate. This handing down of energy is called the energy cascade. The large eddies travel for long distances before they decompose, which is the main reason why turbulence can not be described solely on local flow properties and the upstream history has to be taken into account. Note that there exist flows with high vorticity which are not turbulent.

(ii) **Chaotic flow behavior**
   The various flow variables fluctuate seemingly random around their mean values, but in fact, the motion is deterministic. Due to the chaotic nature, the flow is very sensitive to small changes in the initial values. This is the reason, why it is impossible to realize exactly the same flow in two concurrent experiments.

(iii) **Increased diffusivity and mixing of fluid**
   Caused by the chaotic flow behavior and the migration of large eddies, the diffusivity and mixing of fluid are increased substantially compared to laminar flow. From an engineering standpoint this effects are the most interesting and can be beneficial or disadvantageous, based on the application.

(iv) **Continuum phenomenon**
   Although the eddies exist on a very large span of scales, it can be shown that the smallest eddies are still distinctly larger than the mean free path in a fluid. Therefore turbulence is assumed to be a continuum phenomenon and it is

agreed upon that the Navier-Stokes equations contain the turbulent solutions.

(v) **Non-linearity**
The dominating inertial forces for flows with high Reynolds numbers are non-linear (second term on the left hand side of equation 2.8). Although this is not a unique problem, since most technical interesting systems are non-linear, it is the main reason why the Navier-Stokes equations are that challenging to solve.

(vi) **Three-dimensionality and unsteadiness**
Additional complexity for finding proper solutions is added by the fact that turbulence is always a three-dimensional and unsteady flow phenomenon.

As mentioned, it is agreed upon that the Navier-Stokes equations contain the turbulent solutions. Unfortunately, they can only be solved analytically for special cases, where specific terms are neglected. In fact, the equations are that challenging to solve, that there is currently a one million dollar reward by the Clay Mathematics Institute [6] for the first proof, that given a smooth initial state, a smooth and physically plausible solution to the Navier-Stokes equations **always** exists. Note that it is not necessary to provide the actual solution.

Finally, the poem of Richardson is a surprisingly descriptive, yet beautiful, narration of the energy cascading process:

*"Big whirls have little whirls that feed on their velocity,*
*and little whirls have lesser whirls and so on to viscosity."*
Lewis F. Richardson 1881 - 1953

## 1.2. Boundary layer theory

For fluid flow with sufficiently large Reynolds numbers ($Re \gg 1$), inertial forces dominate the viscous forces and it is reasonable to neglect friction. On the other hand, due to the no-slip condition on a solid wall, the velocity changes within a very thin layer from zero to the free-stream velocity. These steep velocity gradients inflict high viscous forces even for low viscosity fluids. The flow regime can, therefore, be partitioned into two regions. The inviscid free-stream and a very thin, compared to the characteristic length $L$, boundary layer where viscous forces dominate. The boundary layer thickness $\delta$ is typically defined by the wall normal distance, where 99% of the free-stream velocity is recovered. Figure 1.2 shows the asymptotic growth of a boundary layer along a flat plate, starting from the leading edge. It can be seen
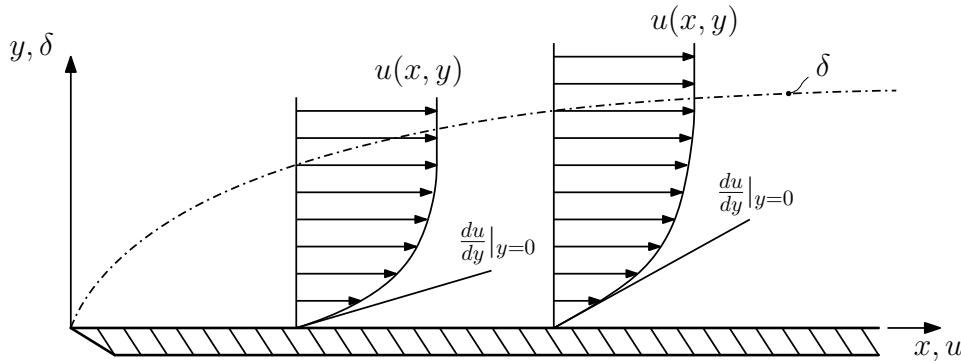
Figure 1.2.: Asymptotic growth of a boundary layer along a flat plate together with the associated velocity profiles.

that the velocity profile gets stretched further downstream resulting in a reduced velocity gradient which leads to a lower local wall shear stress, which is given by

$$\tau_w = \mu \frac{\partial u}{\partial y}\bigg|_{y=0}. \tag{1.2}$$

Prandtl [7] famously provided a set of equations to calculate boundary layers in 1904.

Two important measures to quantify the form of a boundary layer are the displacement thickness $\delta_1$ and the momentum thickness ($\theta$, or $\delta_2$). For continuity reasons, the stream-lines are pushed away from the body due to the formation of a boundary layer. The distance between the imaginary stream-line for inviscid flow and the real stream-line is quantified as the displacement thickness $\delta_1$ and can be calculated for a compressible fluid by

$$\delta_1(x) = \theta = \int_0^\infty \left(1 - \frac{\rho u}{\rho_\infty U_\infty}\right) dy, \tag{1.3}$$

where the subscript $\infty$ indicates reference quantities of the free-stream. Inside the boundary layer the velocity is reduced from the free-stream velocity $U_\infty$ to zero, which causes a loss of momentum. This loss of momentum can by quantified by the momentum thickness, given by

$$\delta_2(x) = \int_0^\infty \frac{\rho u}{\rho_\infty u_\infty} \left(1 - \frac{u}{U_\infty}\right) dy. \tag{1.4}$$

In other words, (a) $\delta_1$ or (b) $\delta_2$ can be seen as distances by which an imaginary plate would have to be moved normal to the wall to give (a) the same mass-flow or (b) the same total momentum for inviscid flow, compared to the viscous flow.

### 1.2.1. Flow separation
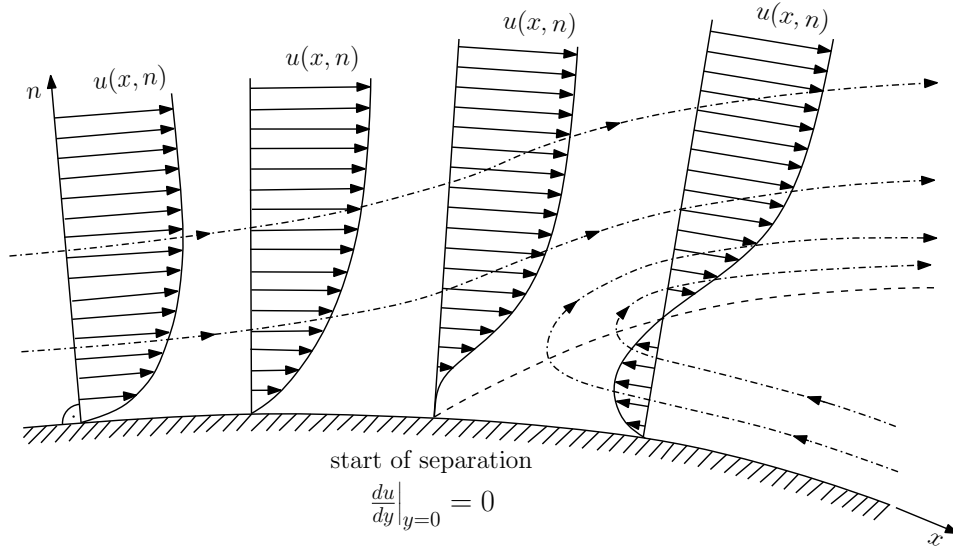


Figure 1.3.: Schematics of boundary-layer separation caused by a positive pressure gradient as it could be encountered inside a diffuser. Dash-dotted lines represent stream-lines and the dashed line indicates zero wall-parallel velocity. Reproduced from Żurański [8]

In regions where a pressure gradient acts against the flow direction, separation of the fluid flow from a smooth and steady surface can occur. Fluid particles near the wall, slowed by the viscous forces acting on them, contain substantially lower kinetic energy than particles outside of the boundary layer. Since the pressure is imposed from the free-stream and approximately constant inside a boundary layer, it inflicts equal forces on all particles. When the wall-near particles can no longer penetrate into the higher pressure regions, they separate from the wall and flow reversal along the wall occurs. Turbulent boundary layers, due to a transfer of momentum from the energy-bearing to the low-energy layers, can withstand much higher pressure gradients before separating than laminar boundary layers.

Figure 1.3 shows the schematics of boundary layer separation as it could be encountered inside a diffuser. The start of separation can be identified at the position, where the velocity-gradient at the wall is zero.

### 1.2.2. Laminar to turbulent transition

Virtually all boundary layers start laminar and transition to turbulent flow over a finite area. Mayle [9] named in his paper several distinct transition modes relevant

to thermal turbomachinery. For low free-stream turbulence, the transition follows the orderly route and the mode is called **natural** transition. Typically, the free-stream turbulence intensity of flow inside of thermal turbomachinery is very high. In that case, the transition process is said to bypass some stages of the natural transition process and thus is known as **bypass** transition. Another possibility for transition is **separation** induced transition, where the laminar flow separates and later reattaches turbulent, forming a separation bubble. Additionally, the flow can transition from laminar to turbulent flow due to **periodically unsteady** effects, for example the periodic passage of wakes or shocks from blade rows of upstream stages. Highly accelerated boundary layers can return to their laminar form. This is called **relaminarization** or sometimes also known as **reverse transition**.

Transition models, which are coupled to statistical turbulence models, usually account for the different transition modes by separate functions or correlations, using a so-called building block approach. They usually only perform well for flows they were designed for and calibrated against.
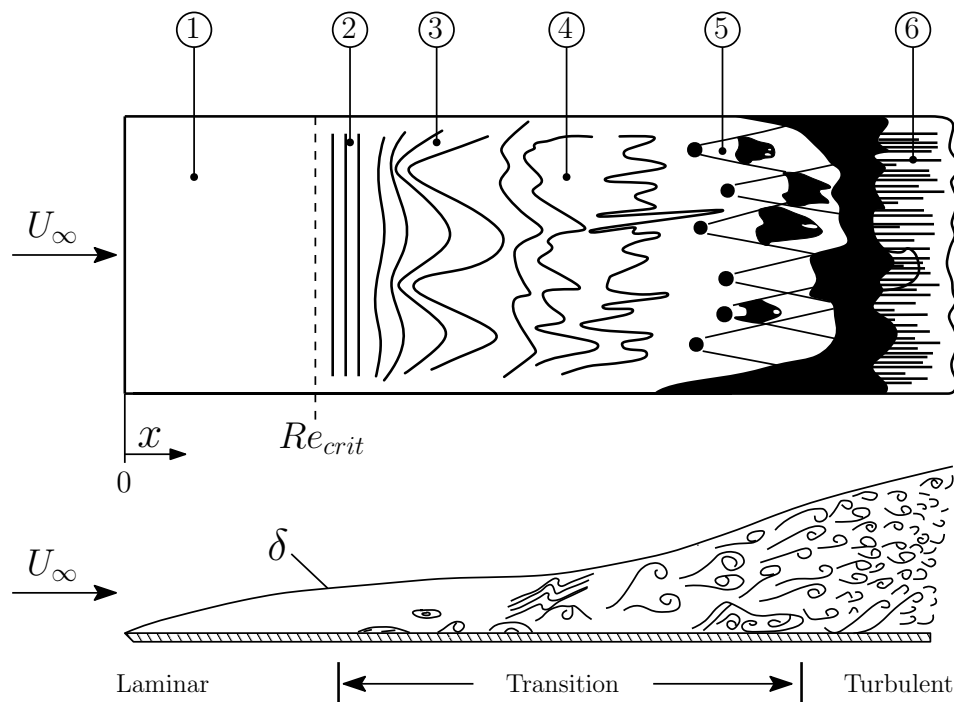


Figure 1.4.: Stages of natural transition for the flow along a smooth and flat plate. Reproduced from Schlichting [10].

Figure 1.4 shows the natural transition process for the boundary layer along a smooth and flat plate, where the transition process according to Schlichting [10] and White [11] can be described as follows:

(1) Stable laminar flow downstream the leading edge
(2) Formation of unstable two-dimensional Tollmien-Schlichting waves
(3) Development of three-dimensional unstable waves and vortex formation
(4) Vortex breakdown into fully three-dimensional (turbulent) fluctuations
(5) Formation of turbulent spots at locally intense velocity fluctuations
(6) Merging of spots into fully turbulent flow

In region (5), due to the finite dimensions of the plate, large patches of turbulent flow form near the edges. In bypass transition stages (2), (3), and (4) are *skipped* and turbulent spots form directly, which further downstream merge together into fully turbulent flow. According to Durbin [12] streaks, in the form of elongated perturbations, instead of unstable Tollmien-Schlichting (TS) waves are the precursors to bypass transition.
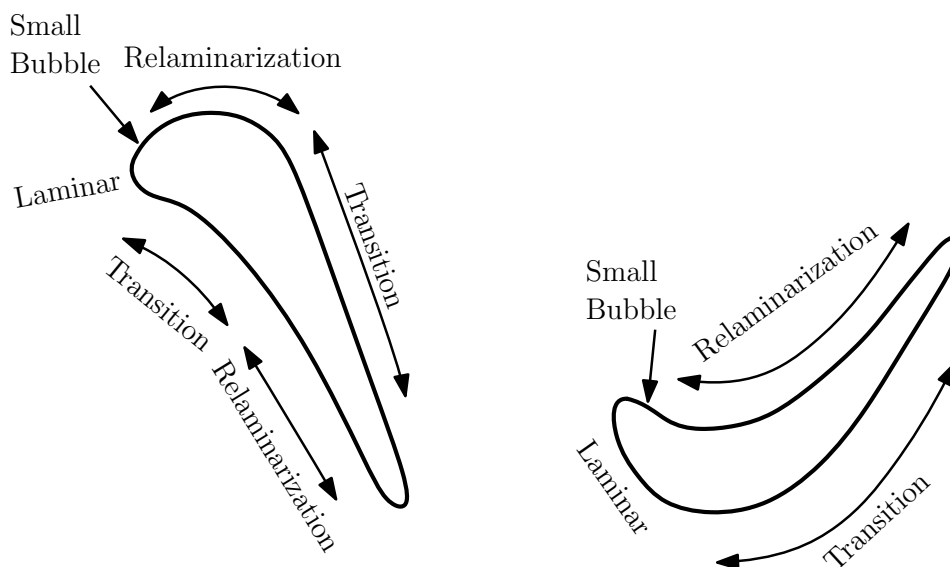


Figure 1.5.: Typical regions of transition and relaminarization along the stator and rotor of a high pressure turbine. Adapted from Mayle [13].

Figure 1.5 shows typical regions of transition, relaminarization, and separation induced transition for the stator and rotor of a high-pressure turbine. Due to the typically high free-stream turbulence inside thermal turbomachinery, the transition process is most likely bypass transition.

### 1.2.3. Turbulent boundary layer

After the transition process is finished, the boundary layer continues to grow asymptotic in its turbulent state. Figure 1.6 shows the laminar and turbulent boundary
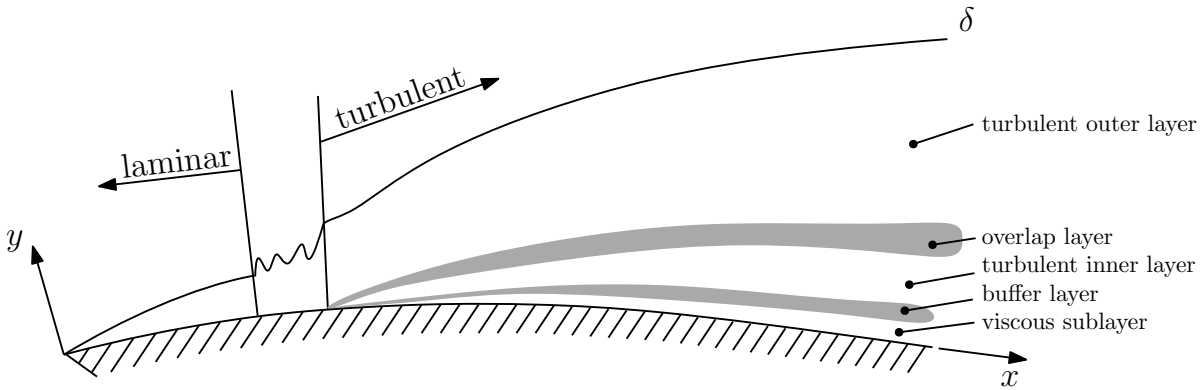
Figure 1.6.: Sublayers of the turbulent boundary layer. Adapted from Steiner [14] (with modifications).

layer together, where several turbulent sublayers can be identified. Closest to the wall is the viscous sublayer, where the flow is laminar. The turbulent inner layer and the viscous sublayer are separated by the buffer layer and the turbulent outer layer is separated from the turbulent inner layer by the overlap layer. The approximate location of the sublayers and the shape of the velocity profile can be described using the dimensionless wall quantities $y^+$ and $u^+$. The dimensionless wall distance $y^+$ is defined by

$$y^+ = \frac{u_\tau}{\nu} y, \tag{1.5}$$

where $y$ is the wall normal distance and $u_\tau$ is the friction velocity given by

$$u_\tau = \sqrt{\frac{\tau_w}{\rho}}. \tag{1.6}$$

Finally, the dimensionless velocity $u^+$ is defined as

$$u^+ = \frac{\bar{u}}{u_\tau}, \tag{1.7}$$

where $\bar{u}$ is the mean velocity of the flow parallel to the wall.

Figure 1.7 shows the characteristic dimensionless averaged turbulent velocity profile, where two regions with universal velocity laws can be discerned. Within the viscous sublayer ($y^+ < 5$) it can be shown that the dimensionless velocity is equal to the dimensionless wall distance, that is $u^+ = y^+$. In the turbulent inner layer ($y^+ < 50$, $y/\delta < 0.2$) the logarithmic law of the wall is valid, given by

$$u^+ = \frac{1}{\kappa} \ln \left( y^+ \right) + B, \tag{1.8}$$
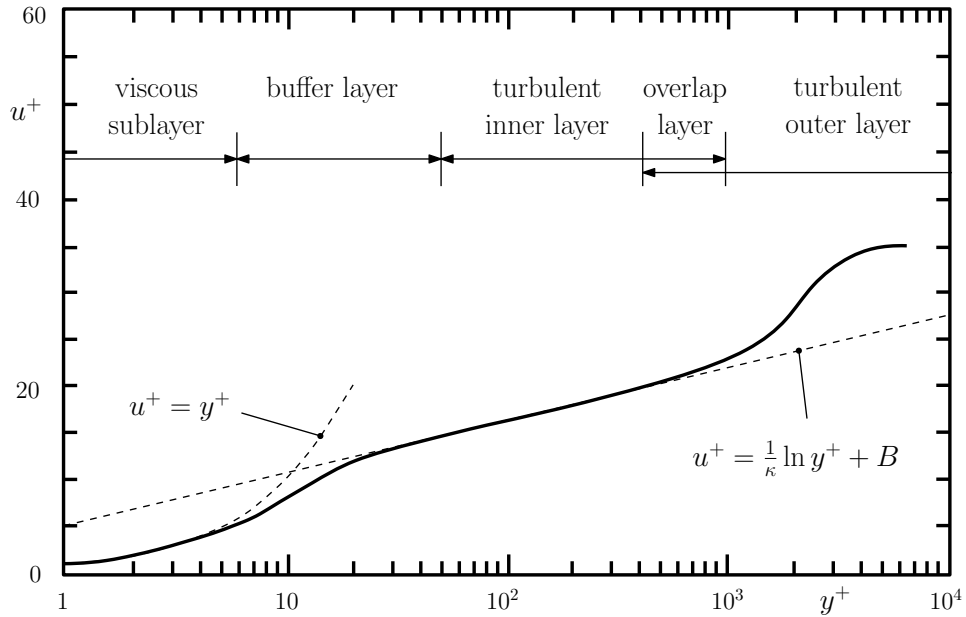
Figure 1.7.: Typical dimensionless velocity profile inside a turbulent boundary layer. Dimensionless velocity $u^+$ versus dimensionless wall-distance $y^+$, where the abscissa is plotted logarithmic. Adopted, from Wilcox [3] with the classifications of Steiner [14].

where $\kappa$ and $B$ are empirical constants. For a flat plate, they usually are chosen to be $\kappa = 0.45$ and $B = 5$. The viscous sublayer and the turbulent inner layer are separated by the buffer layer ($5 < y^+ < 50$) where neither of the laws is applicable. The velocity profile in the outer turbulent layer ($y/\delta > 0.2$) is influenced by the pressure gradient imposed from the free-stream and no universal law exists. Depending on the pressure gradient, the S-shaped bend can be approximated. Note that different classifications and naming for the sublayers of the turbulent boundary layer exist. For example, the turbulent outer layer is also known as wake-region.

Figure 1.8 shows a schematic comparison of typical laminar versus turbulent velocity profile inside the boundary layer. Based on the previously introduced displacement thickness $\delta_1$ (Eq. (1.3)) and the momentum thickness $\delta_2$ (Eq. (1.4)) the shape factor $H$, defined by

$$H = \frac{\delta_1}{\delta_2} \tag{1.9}$$

can be used to discern boundary layer states. For an attached laminar boundary layer the shape factor is $H \approx 2.6$, at separation $H \approx 3$, for an attached turbulent boundary layer $H \approx 1.4$ and in the range of $1.8 < H < 2.2$ at separation [15].

Compared to the laminar boundary layer the following three main differences for turbulent boundary layers can be observed:

(a) laminar          (b) turbulent
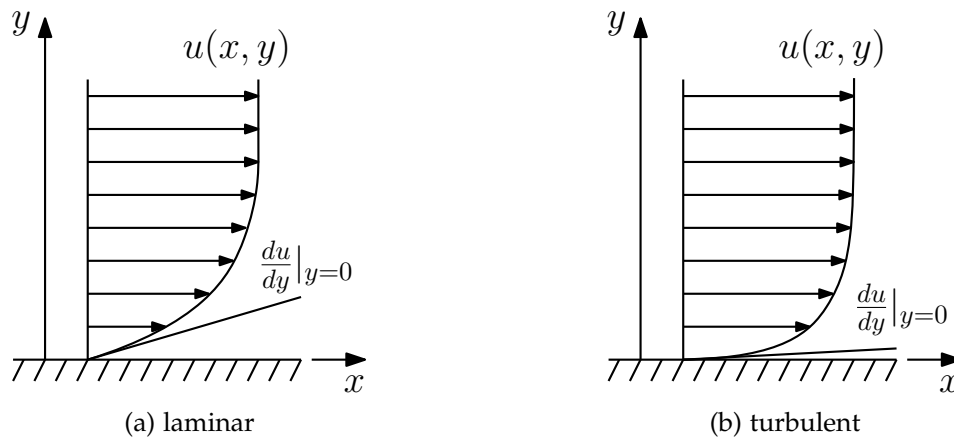
Figure 1.8.: Schematic comparison of the velocity profiles inside (a) a laminar boundary layer and (b) a turbulent boundary layer.

- steeper velocity gradients and therefore higher wall-shear stress
- increased temperature gradients, which results in improved heat transport
- decreased risk of flow separation due to momentum transfer from layers with higher kinetic energy to the wall-near layers

## 1.3. Turbulent flow simulation
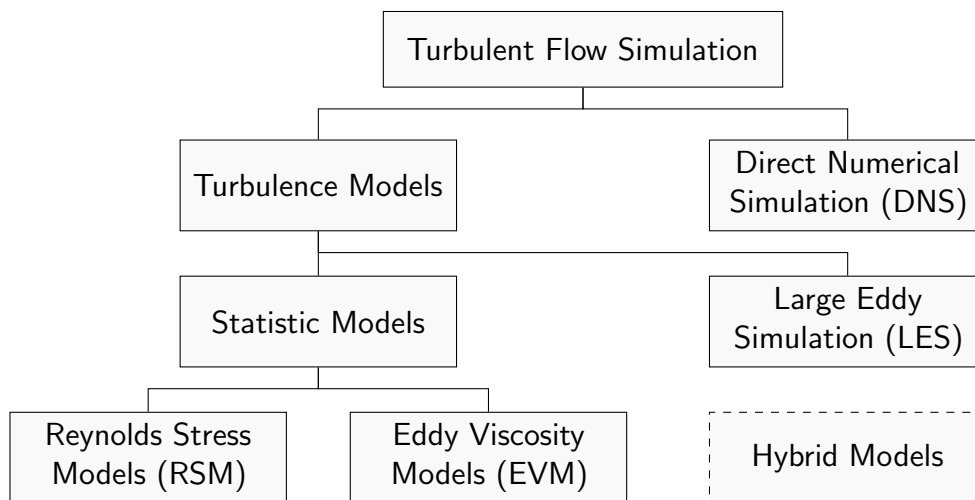


Figure 1.9.: Classification of turbulent flow simulations, adapted from Lücke [16].

For the prediction of turbulent flow several strategies exist. A basic classification on turbulent flow simulation can be seen in Figure 1.9, where from top to bottom

increasingly more modeling is applied and the computational cost is decreased. Following a brief description is given.

**Direct Numerical Simulation (DNS)** applies no modeling and solves the discretized Navier-Stokes-Equations directly. In order to resolve all length scales, a very fine mesh is necessary and advanced numerical schemes have to be employed in order to introduce very little (acceptable) numerical dissipation. Due to the computational requirements, it is still only viable for simple geometries and relatively low Reynolds numbers. The results are predominantly used for validating turbulence models and further understanding the nature and physics of turbulence and the transition process. Advantages compared to measurements are the reliable repeatability, which is impossible in experiments due to the chaotic nature of turbulent flow, and that the simulations yield predictions of the higher order fluctuating terms, which are currently impossible to measure.

**Large Eddy Simulation (LES)** resolves large energy-bearing eddies directly and models smaller eddies by a sub-grid-scale (SGS) model, where it is assumed that only little information is lost. Lots of research effort is currently put into this type of simulation since computational hardware has advanced enough to make it viable for relatively complex geometries and technically relevant Reynolds numbers on a research level. For industrial day-to-day use it is still too computationally expensive. It is believed that LES will be used in the future in favor of Reynolds Stress Models (RSMs) for flows where Eddy Viscosity Models (EVMs) fail due to their limitations.

From an engineering standpoint most of the time only the average effect of turbulence on the flow is from interest. Therefore, averaging the governing equations itself before the simulation comes to mind. Reynolds and Favre averaging is introduced and by applying these averaging processes to the governing equations of fluid flow the Reynolds-averaged Navier-Stokes (RANS) equations are obtained, where the **closure problem** is encountered (see section 2.2). To close the resulting system of equations, the Reynolds stress tensor has to be computed. The following strategies exist:

**Reynolds Stress Models (RSMs)** compute the Reynolds stress tensor directly. Exploiting the symmetry of the Reynolds stress tensor, six individual components remain for which six transport equations are introduced. Usually, one additional transport equation is used to determine the turbulence length scale. In cases where the anisotropy of the turbulent stresses is important these models potentially yield better predictions then EVMs. The main problem, besides high computational cost, is their complexity and the large amount of modeling, which is necessary to close all equations. For these reasons they are not widely used and are not as validated as the classic EVMs.

**Eddy Viscosity Models (EVMs)** usually approximate the Reynolds stress tensor by employing Bousinesq's assumption (Eq. (2.47)), which relates the turbulent stresses to

the gradients of the mean velocity linearly by introducing the eddy viscosity. Besides algebraic models, one- and two-equation models are very popular, but more-equation models exist, where typically one or two additional equations are used to predict transitional behavior or model the anisotropy of turbulence. All turbulence and transition models investigated in the present work are from this type. Note that due to the Reynolds and Favre averaging process lots of information is lost and the only information the mean flow gets from the turbulence model is the eddy-viscosity. Therefore, it is clear that it is impossible to formulate a simple turbulence model which fits all kinds of turbulent flow. However, it is assumed that the currently used correlations and closing parameters can be further improved by using results from DNS and LES, but since eddy-viscosity is only a concept and not a physical property of turbulent flow it is not a straight forward process. As Menter [17] stated: *"It is not clear why fitting the DNS data for k and ε should lead to an improved eddy-viscosity distribution."*

**Hybrid Models** have been developed in order to bridge the gap between Reynolds-averaged Navier-Stokes (RANS) based models and LES. The most popular models are Detached Eddy Simulation (DES) and Wall Modeled Large Eddy Simulation (WM-LES), which share the basic idea to use a RANS based formulation in an attached boundary layer and switch to a LES formulation away from the wall [18]. The initial formulation of the DES has undergone drastic changes as researchers applied the model to different types of flow and fixed issues along the way. Problems with the DES model, for example, are a grid-induced flow separation and the log-layer mismatch of the RANS and LES regions in channel-flows [18]. A model which sets out to fix these issues, for example, is the Improved Delayed Detached Eddy Simulation (IDDES) model by Gritskevich et. al. [19]. The main problem with hybrid models is that they are very complicated and special care has to go into grid generation.

## 1.4. Motivation and Goal

Due to the widespread use of thermal turbomachinery, for example as aero-engines, industrial compressors, or gas- and steam-turbines in energy conversion, further optimization of the fluid flow has a tremendous environmental impact. While lots of research effort is currently invested in LES and DNS, they are still not viable for the design level of engineering applications. Therefore, turbulence and transition modeling is from high interest for the industry. The research effort on LES and DNS poses also a great opportunity by providing high-quality data for validating turbulence and transition models and improving the used correlations and model constants. Furthermore, theoretical concepts for physics-based models can be refined or even new theories can be sparked by gaining further insight into the physics

behind turbulence and the transition process. This makes it a rewarding task to best possibly utilize the research output by further improving the tools for tackling practical engineering challenges.

Most commercial software solutions nowadays implement an extensive number of models. But using the turbulence and transition models outside of their calibrated and documented design space may introduce extensive errors. Together with unsuitable boundary conditions and poorly designed meshes, mostly generated by unthoughtful use of automatic meshing capabilities in commercial software, they contribute to the observed extreme deviations from measurements. Therefore, it is vital to understand the capabilities and limitations of readily available models. Hybrid models, which are progressively used in industrial applications, need an even deeper understanding of turbulence and the underlying assumptions of the models in order to yield satisfactory flow predictions.

The current industry standard for simulating wall-bounded fluid flow, such as the flow inside thermal turbomachinery, is the Shear Stress Transport (SST) turbulence model in combination with the $\gamma$-$Re_{\theta t}$ transition model. Together with the five basic equations governing fluid flow (continuum, momentum in three dimensions, and energy), they constitute a closed system of nine partial differential equations (PDEs).

In order to gain further insight into the status of transition modeling, the present work sets out to implement, validate and test alternative transition models with the in-house Computational Fluid Dynamics (CFD) solver LINARS. The considered additional models are the $\gamma$ model, which besides using one less transport equation, employs simplified correlations, making it a prime candidate for the development of in-house correlations. The goal, therefore, is to evaluate if the model yields predictions from comparable quality to the $\gamma$-$Re_{\theta t}$ model, justifying the effort to develop in-house correlations for a specific purpose. The $k$-$\overline{v^2}$-$\omega$ model is a modification of the transition sensitive $k$-$k_L$-$\omega$ turbulence model which showed very promising results in the open literature, indicating more versatile applicability than the $k$-$k_L$-$\omega$ model. Therefore, it is from interest if the predictions of the transitional flow in thermal turbomachinery improve compared to the $k$-$k_L$-$\omega$ model and how they compare to the current industry standard, the $\gamma$-$Re_{\theta t}$ model. Additionally, by reimplementing the $k$-$k_L$-$\omega$ model in the compressible formulation it is expected to improve the stability of the simulations and the quality of the predictions for high Mach number flow.

# 2. Mathematical modeling

In this chapter first the basic equations, which govern fluid flow, are presented. Reynolds and Favre averaging is introduced in order to derive the Reynolds-averaged Navier-Stokes (RANS) equations, where the turbulent closure problem caused by the averaging process is encountered. Finally, the turbulence and transition models which were investigated in this thesis are presented, where the main focus lies on the Local Correlation-Based Transition Models (LCTMs). For the present work Eddy Viscosity Models (EVMs), which all are based on the Boussinesq assumption (Eq. (2.47)) were used.

Consistent with most literature and publications on turbulence and transition modeling all equations are given in index notation. Please note that there is no distinction between tangent and cotangent spaces and summation over indexes which appear twice in a single term is implied. Therefore the scalar product between two arbitrary vectors $\vec{x}$ and $\vec{y}$ is written as

$$\vec{x} \cdot \vec{y} = x_1 y_1 + x_2 y_2 + x_3 y_3 = x_i y_i. \tag{2.1}$$

Furthermore, the Kronecker delta $\delta_{ij}$ is defined as

$$\delta_{ij} = \begin{cases} 1 & \text{if } i = j, \\ 0 & \text{otherwise.} \end{cases} \tag{2.2}$$

## 2.1. Governing equations

Based on the textbooks of Versteeg and Malalasekera [20] and Wilcox [21], a quick synopsis of the basic equations governing fluid flow is given. The equations are formulated in their differential form with the basic flow quantities density $\rho$, Cartesian velocity vector $u_i$, pressure $p$, temperature $T$ and the Cartesian position vector $x_i$. The equations can be derived by balancing the change of mass, momentum and energy for an infinitesimal volume element $dV$, where it is assumed that for every point in space a sufficient amount of particles is present, such that the density, and the body- and surface-forces are well defined. This assumption is known as the continuum hypothesis. Simply said, there is no empty space inside the fluid.

### 2.1.1. Continuity equation
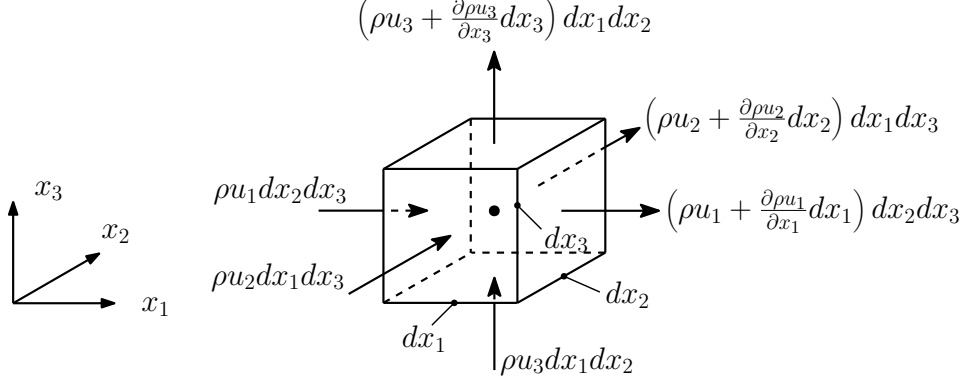


Figure 2.1.: Schematics of the mass-flow over the volume boundaries, using a Taylor series expansion.

Exemplary, the derivation of the continuity equation is shown, and it works in a similar way for the momentum and energy equation. Figure 2.1 shows the infinitesimal volume element $dV$ with the edge lengths $dx_1$, $dx_2$, and $dx_3$. The mass flows are calculated from $\dot{m} = \rho u A$, where $u$ is the face-normal velocity magnitude and $A$ is the associated face area. The mass flow on the outlet faces is defined in terms of a Taylor series expansion. The change inside the volume has to be equal to the sum of the flow over the volume boundaries which can be written as

$$
\begin{aligned}
\frac{\partial \rho}{\partial t} dV = {} & \rho u_1 \, dx_2 dx_3 - \left( \rho u_1 + \frac{\partial \rho u_1}{\partial x_1} dx_1 \right) dx_2 dx_3 \\
& + \rho u_2 \, dx_1 dx_3 - \left( \rho u_2 + \frac{\partial \rho u_2}{\partial x_2} dx_2 \right) dx_1 dx_3 \\
& + \rho u_3 \, dx_1 dx_2 - \left( \rho u_3 + \frac{\partial \rho u_3}{\partial x_3} dx_3 \right) dx_1 dx_2 .
\end{aligned}
\tag{2.3}
$$

Simplifying equation (2.3) and dividing by the volume $dV = dx_1 dx_2 dx_3$ yields the continuity equation in the well-known form of

$$
\frac{\partial \rho}{\partial t} + \left( \frac{\partial \rho u_1}{\partial x_1} + \frac{\partial \rho u_2}{\partial x_2} + \frac{\partial \rho u_3}{\partial x_3} \right) = 0,
\tag{2.4}
$$

which can be rewritten in index notation as

$$
\frac{\partial \rho}{\partial t} + \frac{\partial \rho u_j}{\partial x_j} = 0,
\tag{2.5}
$$

where the first term on the left hand side (LHS) represents the local change of the density $\rho$ and the second term accounts for convective transport through the volume boundaries.

## 2.1.2. Momentum equation

The momentum equation represents the balance of the change of momentum and the forces acting on the volume element $dV$ and is given by

$$\frac{\partial \rho u_i}{\partial t} + \frac{\partial \rho u_i u_j}{\partial x_j} = \frac{\partial \sigma_{ij}}{\partial x_j} + \rho f_i^b. \tag{2.6}$$

The first term on the LHS represents the local change of momentum and the second term accounts for the flux of momentum over the surface of the volume element. The first term on the right hand side (RHS) represents surface forces and the second term body forces, respectively. In an inertial reference frame, gravitational forces are the most significant forces. Typically the body forces due to the external field can be neglected in comparison to inertial forces.

The (total) stress tensor $\sigma_{ij}$ can be rewritten as

$$\sigma_{ij} = -p \delta_{ij} + \tau_{ij}, \tag{2.7}$$

where the contribution of the pressure $p$ is separated and $\tau_{ij}$ represents viscous stress, which is only present in a moving fluid. Thus the momentum equation finally reads:

$$\frac{\partial \rho u_i}{\partial t} + \frac{\partial \rho u_i u_j}{\partial x_j} = -\frac{\partial p}{\partial x_i} + \frac{\partial \tau_{ij}}{\partial x_j} \tag{2.8}$$

**Newtonian Fluid**

For an isotropic compressible Newtonian fluid with the dynamic viscosity $\mu$ and the volume viscosity $\zeta$ the viscous stress tensor $\tau_{ij}$ is given by

$$\tau_{ij} = 2\mu S_{ij} + \zeta S_{kk} \delta_{ij}, \tag{2.9}$$

where $S_{ij}$ is the strain-rate tensor, defined as

$$S_{ij} = \frac{1}{2} \left( \frac{\partial u_i}{\partial x_j} + \frac{\partial u_j}{\partial x_i} \right). \tag{2.10}$$

The first term on the RHS of equation (2.9) is due to linear deformation ($i = j$) and angular distortion ($i \neq j$), while the second term is caused by dilatation and thus is only present in a compressible fluid.

Ensuring that the viscous stress does not contribute to the pressure, the volume viscosity $\zeta$ is generally assumed to be

$$\zeta = -\frac{2}{3}\mu. \tag{2.11}$$

Inserting the volume viscosity $\zeta$ (Eq. (2.11)) into equation (2.9) and utilizing the definition of the strain-rate tensor (Eq. (2.10)), the stress-tensor $\tau_{ij}$ is usually written in one of two forms:

$$\tau_{ij} = 2\mu \left( S_{ij} - \frac{1}{3}S_{kk}\delta_{ij} \right) = \mu \left[ \left( \frac{\partial u_i}{\partial x_j} + \frac{\partial u_j}{\partial x_i} \right) - \frac{2}{3}\frac{\partial u_k}{\partial x_k}\delta_{ij} \right] \tag{2.12}$$

The temperature dependency of the dynamic viscosity for an ideal gas is often accounted for by Sutherland's formula for viscosity which is based upon the kinetic theory of gases and given by

$$\mu = \mu_S \left( \frac{T}{T_S} \right)^{S_T} \frac{T_S + C_S}{T + C_S}, \tag{2.13}$$

with the reference viscosity $\mu_S$, reference temperature $T_S$, the temperature exponent $S_T$, Sutherland's constant $C_S$ and the fluid temperature $T$. Table 2.1 presents the constants used for air as an ideal gas in the present work.

| | | |
|---|---|---|
| $\mu_S$ | 17.16E-6 | Pa s |
| $T_S$ | 273.11 | K |
| $C_S$ | 110.56 | K |
| $S_T$ | 1.5 | – |

Table 2.1.: Constants for Sutherland's formula for viscosity, used for air as an ideal gas in the present work.

### 2.1.3. Energy equation

For application in CFD the energy equation often is formulated in terms of the total specific internal energy $e$, defined as

$$e = u_{\text{int}} + \frac{u_i u_i}{2}, \tag{2.14}$$

where the contribution of potential energy is neglected. This allows for a conservative formulation of the energy equation (2.15) as

$$\frac{\partial \rho e}{\partial t} + \frac{\partial \rho u_j e}{\partial x_j} + \frac{\partial u_j p}{\partial x_j} = \frac{\partial u_j \tau_{ij}}{\partial x_j} - \frac{\partial q_j}{\partial x_j} + \rho u_j f_j^b + \frac{\partial Q}{\partial t}, \tag{2.15}$$

where the first two terms on the LHS represent the local change of total internal energy and the energy flux through the volume boundaries, respectively. The third term on the LHS represents the power of the pressure forces. On the RHS, the first term is the power required for the deformation of the fluid particle due to the viscous forces. The second term corresponds to energy exchange by heat conduction, the third term accounts for the power of the body forces and the last term describes the energy change due to internal heat sources or heat sinks. In analogy to the momentum equation (2.8) the contribution of the body forces is neglected. Additionally, the absence of internal heat sources is assumed.

The heat flux vector $q_j$ is usually computed by Fourier's law given by

$$q_j = -\lambda \frac{\partial T}{\partial x_j}. \tag{2.16}$$

The thermal conductivity $\lambda$ for an ideal gas is calculated by rearranging the definition of the Prandtl number $Pr$, which is a fluid property, as

$$\lambda = \frac{\mu c_p}{Pr}, \tag{2.17}$$

with the heat capacity at constant pressure $c_p$.

**Equation of state**

To close the system of equations (2.5, 2.8, and 2.15) an equation of state has to be specified. Considering the ideal gas equation, where $R$ is the specific gas constant,

$$\frac{p}{\rho} = RT \tag{2.18}$$

and assuming a perfect gas (ideal gas with constant heat capacities $c_v$ and $c_p$), with the enthalpy $h$ and the specific internal energy $u_{\text{int}}$ defined as $h = c_p T$, and $u_{\text{int}} = c_v T$ an equation for the total internal energy $e$ can be given as

$$e = \frac{p}{\rho(\gamma_c - 1)} + \frac{u_i u_i}{2}, \tag{2.19}$$

where $\gamma_c = c_p / c_v$ is the ratio of the heat capacities. Formulated in terms of the fluid temperature $T$ the equation of state reads

$$T = \frac{(\gamma_c - 1)}{R} \left( e - \frac{u_i u_i}{2} \right). \tag{2.20}$$

19

## 2.2. Reynolds-averaged Navier-Stokes (RANS) equations

As mentioned in the introduction, from an engineering standpoint often only the average influence of turbulence on fluid flow is from interest. Even though the turbulent fluctuations are not completely random, statistical methods can be used due to the chaotic nature of turbulence. Reynolds averaging, introduced by Reynolds in 1895 [22], is the method of choice. In order to avoid additional unknown correlations, arising for compressible fluids, Favre averaging [23] is introduced. The following derivation follows roughly the textbook of Wilcox [3].

### 2.2.1. Reynolds and Favre averaging
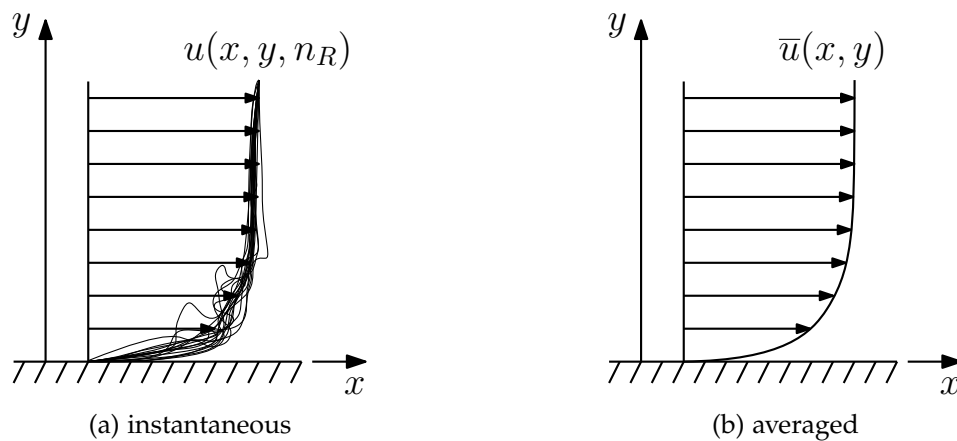


Figure 2.2.: Schematics of the velocity profile inside a turbulent boundary layer, where subfigure (a) depicts several instantaneous realizations of the same fluid flow and (b) the averaged velocity profile. Based on Cebeci and Smith [24].

Figure 2.2a shows the schematics of the velocity profile inside a turbulent boundary layer for several instantaneous realizations $n_R$ of the same fluid flow, which will differ due to the chaotic nature of turbulence minimally. In Figure 2.2b, the associated averaged velocity profile is shown.

**Reynolds averaging**

For the derivation of the Reynolds-averaged Navier-Stokes (RANS) equations a universal instantaneous flow quantity $\phi$ is decomposed into a mean value $\overline{\phi}$ and its
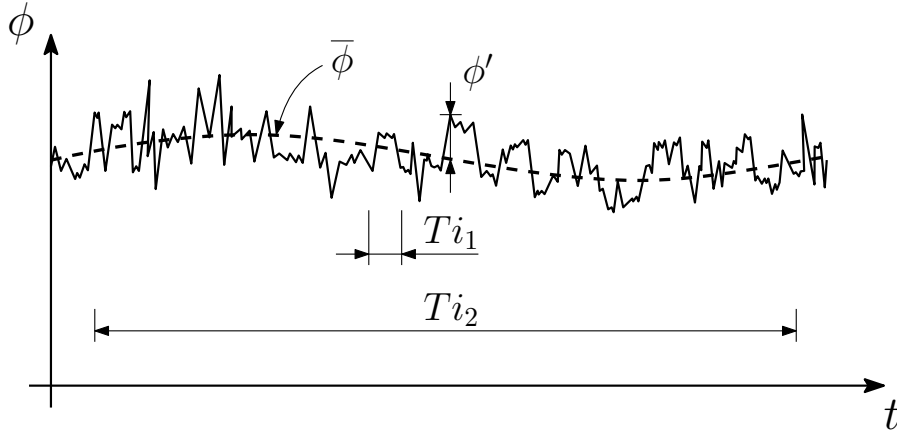
Figure 2.3.: Relation between instantaneous value $\phi$, fluctuation $\phi'$ and mean value $\overline{\phi}$. Showing the different timescales for the variation of the mean flow and the fluctuations. Reproduced with changes from Wilcox [21].

fluctuations $\phi'$, where the relationship is given by

$$\phi = \overline{\phi} + \phi'. \tag{2.21}$$

The original formulation of Reynolds averaging calculates a mean value by taking the ensemble-average as

$$\langle \phi \rangle = \lim_{N \to \infty} \frac{1}{N} \sum_{n_R=1}^{N} \phi_{(n_R)}, \tag{2.22}$$

where $N$ is the total number of realizations. Alternatively, the Reynolds-average can be formulated as a time-average, denoted by an overline, as

$$\overline{\phi} = \lim_{Ti \to \infty} \frac{1}{Ti} \int_{t}^{t+Ti} \phi \, dt, \tag{2.23}$$

which for an infinite time interval ($Ti \to \infty$) yields the same result as equation (2.22). For a practical application, the time-span $Ti$ has to take a finite value and therefore it is common to define the Reynolds-average, for the general case of non-stationary turbulent flow, as

$$\overline{\phi} = \frac{1}{\Delta t} \int_{t}^{t+\Delta t} \phi \, dt, \tag{2.24}$$

where $\Delta t$ is a constant, finite time interval. Note that it is implicitly assumed that the mean value varies on a significantly lager time scale ($Ti_2$) than the turbulent fluctuations ($Ti_1$), i.e. $Ti_1 \ll \Delta t \ll Ti_2$. This assumption is specifically needed for the

so called Unsteady Reynolds-averaged Navier-Stokes (URANS) equations. It shall be noted that this assumption might not always hold. Figure 2.3 shows the different timescales $Ti_1$ and $Ti_2$ for the turbulent fluctuations and the variation of the mean value, respectively. Additionally the relationship between the instantaneous value, the mean value $\bar{\phi}$ and the fluctuations $\phi'$, as given by equation (2.21), can be seen.

The following general rules apply to Reynolds averaging, implying that it is a linear operation. $\phi$ and $\psi$ are arbitrary flow quantities and $c$ is a constant value:

$$\overline{\phi + \psi} = \bar{\phi} + \bar{\psi} \qquad\qquad \overline{c\phi} = c\bar{\phi}$$
$$\overline{\bar{\phi}\psi} = \bar{\phi}\,\bar{\psi} \neq \overline{\phi\psi} \qquad\qquad \bar{c} = c$$
$$\overline{\phi'} \equiv 0 \qquad\qquad \overline{\bar{\phi}\psi'} \equiv 0$$
$$\overline{\left(\frac{\partial \phi}{\partial x_i}\right)} = \frac{\partial \bar{\phi}}{\partial x_i} \qquad\qquad \overline{\left(\frac{\partial \phi}{\partial t}\right)} = \frac{\partial \bar{\phi}}{\partial t} \qquad (2.25)$$

It is important to note that double correlations, i.e. time-averaged products of flow quantities, are generally not equal to the product of the individually averaged quantities, i.e. $\overline{\phi\psi} \neq \bar{\phi}\,\bar{\psi}$. This can be shown by simply decomposing the flow quantities $\phi$ and $\psi$ according to equation (2.21) and consistently using the rules, given in equation (2.25), in order to derive

$$\overline{\phi\psi} = \overline{\left(\bar{\phi} + \phi'\right)\left(\bar{\psi} + \psi'\right)}$$
$$\overline{\phi\psi} = \overline{\bar{\phi}\,\bar{\psi} + \bar{\phi}\psi' + \phi'\bar{\psi} + \phi'\psi'}$$
$$\overline{\phi\psi} = \bar{\phi}\,\bar{\psi} + \overline{\phi'\psi'}, \qquad (2.26)$$

where the second term on the RHS of the last line does generally not vanish. Similar relations can be shown for triple and higher correlations.

For incompressible flow, Reynolds averaging would be sufficient to obtain the RANS equations, but for compressible flow the following issue emerges. Inserting the decomposed density $\rho = \bar{\rho} + \rho'$ and velocity components $u_j = \bar{u}_j + u'_j$ into the continuum equation (2.5) leads after expanding to

$$\frac{\partial \bar{\rho} + \rho'}{\partial t} + \frac{\partial}{\partial x_j}\left(\bar{\rho}\,\bar{u}_j + \bar{\rho}u'_j + \rho'\bar{u}_j + \rho'u'_j\right) = 0, \qquad (2.27)$$

and subsequent time averaging yields

$$\frac{\partial \bar{\rho}}{\partial t} + \frac{\partial}{\partial x_j}\left(\bar{\rho}\,\bar{u}_j + \overline{\rho'u'_j}\right) = 0, \qquad (2.28)$$

where $\overline{\rho'u'_j}$ is an unknown double correlation which can be avoided by introducing Favre averaging. Additionally, it can be seen that this term vanishes for incompressible fluids since there are no density fluctuations, i.e. $\rho' = 0$.

**Favre averaging**

In analogy to Reynolds averaging an instantaneous quantity $\phi$ is again decomposed into a mean $\widetilde{\phi}$ and a fluctuating part $\phi''$ as

$$\phi = \widetilde{\phi} + \phi''. \tag{2.29}$$

The Favre averaging process is a mass-weighted time averaging and it is defined by

$$\widetilde{\phi} = \frac{1}{\overline{\rho}\,\Delta t} \int\limits_{t}^{t+\Delta t} \rho\phi\, dt, \tag{2.30}$$

from which the following relationship can readily be derived

$$\widetilde{\phi} = \frac{\overline{\rho\phi}}{\overline{\rho}} \quad \rightarrow \quad \overline{\rho\phi} = \overline{\rho}\,\widetilde{\phi}. \tag{2.31}$$

Expanding equation (2.29) with the density $\rho$ and time averaging the result leads to

$$\overline{\rho\phi} = \overline{\rho}\widetilde{\phi} + \overline{\rho\phi''}. \tag{2.32}$$

From a comparison with equation (2.31) follows that the second term on the RHS must be zero, i.e. $\overline{\rho\phi''} \equiv 0$. It is important to notice that, in contrast to the Reynolds decomposition, the time average of the Favre fluctuations does not vanish, i.e. $\overline{\phi''} \neq 0$. This can be shown by rearranging equation (2.29) and inserting the relation obtained by equation (2.31) for $\widetilde{\phi}$

$$\phi'' = \phi - \frac{\overline{\rho\,\phi}}{\overline{\rho}}, \tag{2.33}$$

furthermore replacing the double correlation on the RHS (compare Eq. 2.26) yields

$$\phi'' = \phi - \frac{\overline{\rho}\,\overline{\phi} + \overline{\rho'\phi'}}{\overline{\rho}}$$
$$\phi'' = \phi - \overline{\phi} - \frac{\overline{\rho'\phi'}}{\overline{\rho}}. \tag{2.34}$$

Finally, taking the time average of equation (2.34) leads to

$$\overline{\phi''} = -\frac{\overline{\rho'\phi'}}{\overline{\rho}} \neq 0. \tag{2.35}$$

Finally it can be shown that with Favre averaging the unknown correlation in the averaged continuum equation can be avoided. Decomposing the density as $\rho = \overline{\rho} + \rho'$

and the velocity components as $u_j = \widetilde{u}_j + u_j''$, inserting into the continuum equation (2.5) and time averaging the result leads to

$$\frac{\partial \overline{\rho} + \rho'}{\partial t} + \frac{\partial}{\partial x_j} \left( \rho(\widetilde{u}_j + u_j'') \right) = 0$$

$$\frac{\partial \overline{\rho}}{\partial t} + \frac{\partial}{\partial x_j} \left( \overline{\rho}\widetilde{u}_j + \overline{\rho u_j''} \right) = 0. \tag{2.36}$$

As shown previously (Eq. (2.31) and Eq. (2.32)), the second term inside the brackets on the LHS is zero per definition ($\overline{\rho u_j''} = 0$), leading to the Favre-averaged continuum equation

$$\frac{\partial \overline{\rho}}{\partial t} + \frac{\partial \overline{\rho}\widetilde{u}_j}{\partial x_j} = 0. \tag{2.37}$$

## 2.2.2. System of equations

Reynolds and Favre averaging can be employed on the instantaneous momentum equations (2.8) and energy equation (2.15) in a similar manner, as presented for the instantaneous continuum equation (2.5) in section (2.2.1). Since most literature does not distinguish between Reynolds-averaged Navier-Stokes equations and Favre-averaged Navier-Stokes equations, it will be referred to the following system of equations as RANS equations.

Decomposing density, pressure and heatflux according to Reynolds (Eq. (2.21))

$$\rho = \overline{\rho} + \rho', \qquad p = \overline{p} + p', \qquad q_j = \overline{q}_j + q_j' \tag{2.38}$$

and using Favre decomposition (Eq. (2.29)) for the velocity components, specific total energy and temperature as

$$u_i = \widetilde{u}_i + u_i'', \qquad e = \widetilde{e} + e'', \qquad T = \widetilde{T} + T'' \tag{2.39}$$

leads after inserting them into continuum (Eq. (2.5)), momentum (Eq. (2.8)) and energy equation (Eq. (2.15)) and subsequent time averaging to following system of equations:

$$\frac{\partial \overline{\rho}}{\partial t} + \frac{\partial \overline{\rho}\widetilde{u}_j}{\partial x_j} = 0 \tag{2.40}$$

$$\frac{\partial \overline{\rho}\widetilde{u}_i}{\partial t} + \frac{\partial \overline{\rho}\widetilde{u}_i\widetilde{u}_j}{\partial x_j} = -\frac{\partial \overline{p}}{\partial x_i} + \frac{\partial}{\partial x_j} \left( \overline{\tau}_{ij} - \overline{\rho u_i'' u_j''} \right) \tag{2.41}$$

$$\frac{\partial \overline{\rho}\widetilde{e}}{\partial t} + \frac{\partial \overline{\rho}\widetilde{u}_i\widetilde{e}}{\partial x_i} + \frac{\partial \widetilde{u}_i\overline{p}}{\partial x_i} = \frac{\partial}{\partial x_j} \left( \widetilde{u}_i\overline{\tau}_{ij} - \widetilde{u}_i\overline{\rho u_i'' u_j''} - c_p\frac{\mu}{Pr}\frac{\partial \widetilde{T}}{\partial x_j} + c_p\overline{\rho u_j'' T''} \right) \tag{2.42}$$

For the time-average of the Favre decomposed viscous stress tensor $\overline{\tau_{ij}} = \widetilde{\tau}_{ij} + \overline{\tau''_{ij}}$ the contributions of the time-averaged Favre fluctuations are assumed to be negligible, that is

$$\overline{\tau''_{ij}} = \mu \left[ \left( \frac{\partial \overline{u''_i}}{\partial x_j} + \frac{\partial \overline{u''_j}}{\partial x_i} \right) - \frac{2}{3} \delta_{ij} \frac{\partial \overline{u''_k}}{\partial x_k} \right] \approx 0. \tag{2.43}$$

Therefore the averaged viscous stress tensor is given by

$$\overline{\tau}_{ij} = \mu \left[ \left( \frac{\partial \widetilde{u}_i}{\partial x_j} + \frac{\partial \widetilde{u}_j}{\partial x_i} \right) - \frac{2}{3} \delta_{ij} \frac{\partial \widetilde{u}_k}{\partial x_k} \right]. \tag{2.44}$$

Due to the averaging process two unknown correlations appear in the momentum equations (2.41) and in the energy equation (2.42), known as the Reynolds stress tensor $\tau_{tij} = -\overline{\rho u''_i u''_j}$ and the turbulent heat-flux vector $q_{ti} = c_p \overline{\rho u''_j T''}$, respectively. These unknown correlation are famously known as the **closure problem** of RANS and determining them is the object of statistical turbulence modeling.

### 2.2.3. Turbulence kinetic energy $k$ and turbulence intensity $Tu$

An important measure for turbulent flow is the turbulence (specific, per unit mass) kinetic energy $k$ which is defined by taking half of the sum of the variance of the turbulence velocity fluctuations $u'_i$ [20] as

$$k = \frac{1}{2} \left( \overline{u'_i u'_i} \right) = \frac{1}{2} \left( \overline{u'^2} + \overline{v'^2} + \overline{w'^2} \right). \tag{2.45}$$

Taking the root mean square (RMS) of the velocity fluctuations and normalizing with the magnitude of the mean velocity $\overline{U}$ leads to the turbulence intensity $Tu$, which is often given in percent and can be related to the turbulence kinetic energy $k$ by

$$Tu = \frac{\sqrt{\frac{1}{3} \left( \overline{u'^2} + \overline{v'^2} + \overline{w'^2} \right)}}{\overline{U}} 100 = \frac{\sqrt{\frac{2}{3} k}}{\overline{U}} 100 \quad \text{(in \%)}. \tag{2.46}$$

Note that it is possible to obtain an exact transport equation for the turbulence kinetic energy from the RANS equations, whose derivation is omitted since it would go beyond the scope of this thesis. For further information see for example the textbooks of Versteeg and Malalasekera [20] or Wilcox [3].

## 2.2.4. Reynolds-Stress tensor

Recalling the classification of turbulent flow simulation established in Figure 1.9, two general types of models for determining the Reynolds-Stress tensor $\tau_{tij}$ exist. For a quick synopsis on RSMs see section (1.3) and for a more complete overview see for example the textbook of Wilcox [3]. The present work used EVMs for closing the RANS equations for which an overview follows.

**Eddy Viscosity Models (EVM)**

For calculating the Reynolds stress tensor most EVMs employ Boussinesq's assumption, which linearly relates the turbulent stresses to the gradient of the mean velocity field written as

$$\tau_{tij} = -\overline{\rho u_i'' u_j''} = \mu_t \left( \frac{\partial \widetilde{u}_i}{\partial x_j} + \frac{\partial \widetilde{u}_j}{\partial x_i} - \frac{2}{3} \frac{\partial \widetilde{u}_k}{\partial x_k} \delta_{ij} \right) - \frac{2}{3} \overline{\rho} k \delta_{ij}, \qquad (2.47)$$

where $k$ is the turbulence kinetic energy. Hence, the closure problem reduces to determining the eddy viscosity $\nu_t = \mu_t / \rho$. The assumption of isotropic turbulent properties is an inherent shortcoming of all models based upon this approach.

*On a historical side-note, pointed out by Schmitt [25], it is fascinating that Boussinesq introduced a local averaging of the Navier-Stokes equations, although in a way that prevented him from discovering the Reynolds-Stress tensor, and proposed a closure for the resulting equations in his publication from 1877 [26], which substantially predates the averaging process published by Reynolds in 1895 [22].*

EVMs are typically grouped by the number of transport equations that are additionally introduced in order to determine the eddy viscosity $\nu_t$.

**Zero-equation models:**
Turbulence models, which only use algebraic equations to determine the eddy viscosity, are termed zero-equation models. They are based on Prandtl's mixing-length theory and perform, according to Wilcox [3], surprisingly well for simple flows with relatively-slowly-varying properties. They are very simple to implement and typically no numerical difficulties are encountered. However, they are known to fail for separated flows. The most popular models are the Cebeci-Smith [27] and the Baldwin-Lomax [28] model.

**One-equation models:**
Usually, one-equation models either use the turbulence kinetic energy $k$ or the kinematic turbulent viscosity $\nu_t$ as their conserved quantity for the additional transport equation. In case the turbulence kinetic energy $k$ is not readily available, the last term

in Boussinesq's assumption (Eq. (2.47)) is often neglected. The Spalart-Allmaras [29] model is very popular and yields good results for many engineering applications. It is readily available in many commercial CFD software packages and also implemented in the in-house solver LINARS, where it is often used to compute an initial solution on a coarse mesh for subsequent computations with more complex turbulence models.

**Two-equation models:**
In addition to the turbulence kinetic energy $k$ two-equation models implement another transport equation to determine the turbulence length scale. In contrast to zero- and one-equation models they are sometimes called *complete* models. The most popular choices for the second variable is either the turbulence dissipation $\varepsilon$ or the specific dissipation rate $\omega$. According to Kolmogorov [30, 31], based on dimensional considerations the eddy viscosity, the turbulence length scale and the turbulence dissipation are related in the following way:

$$\nu_t \sim k/\omega, \quad l_t \sim \sqrt{k}/\omega, \quad \varepsilon \sim \omega k \tag{2.48}$$

Their advantage is that they solve a wide field of technically relevant flows very well, where no prior knowledge about the turbulent flow is needed, except for boundary conditions. The two most popular models are the Standard $k$-$\varepsilon$ model [32] and the Wilcox $k$-$\omega$ model [33]. Another very popular model is Menter's SST model [34], which besides redefining the formula for computing the eddy viscosity is a blend between the Standard $k$-$\varepsilon$ [32] and the 1988 formulation of the Wilcox $k$-$\omega$ [35] model.

**More-equation models:**
Most more-equation models are based on two-equation models and account for additional physical phenomena, which are not captured by classic two-equation models, by introducing further equations. For example, one group of models sets out to include the anisotropy of the turbulence near walls and another group of models adds further transport equations in order to include the transitional behavior of the boundary layer, which is either done in a phenomenological, physics-based way or by using empirical local correlations.

Throughout this work, Menter's SST model is used as a base-line for fully turbulent predictions and is directly linked to the $\gamma$-$Re_{\theta t}$ transition model and $\gamma$ transition model, where the $\gamma$-$Re_{\theta t}$ model is used as a base-line for transitional results, due to its wide application in industry and research. The $k$-$k_L$-$\omega$ and the $k$-$\overline{v^2}$-$\omega$ model are transitional turbulence models and the underlying $k$-$\omega$ based transport equations are part of their formulation. Table 2.2 provides an overview of the number of transport equations used by the models, where for the $k$-$k_L$-$\omega$ model no sharp distinction between turbulence and transition related equations can be drawn. It can be seen that the turbulence and transition models contribute substantially to the overall computational cost.

| Model | RANS | Turbulence | Transition | Total |
|-------|------|------------|------------|-------|
| SST | 5 | 2 | 0 | 7 |
| SST + $\gamma$-$Re_{\theta t}$ | 5 | 2 | 2 | 9 |
| SST + $\gamma$ | 5 | 2 | 1 | 8 |
| $k$-$k_L$-$\omega$ | 5 | 3 | | 8 |
| $k$-$\overline{v^2}$-$\omega$ | 5 | 2 | 1 | 8 |

Table 2.2.: Comparison of the number of transports equations which have to be solved in order to compute predictions for the turbulent flow for the investigated turbulence and transition models.

### 2.2.5. Turbulent heat-flux vector

A common closure for the turbulent heat-flux vector is

$$q_{ti} = c_p \overline{\rho u_j'' T''} = -\frac{\mu_t c_p}{Pr_t} \frac{\partial \widetilde{T}}{\partial x_i}, \qquad (2.49)$$

where the definition of the turbulent Prandtl number $Pr_t = \nu_t / a_t$ is used and $a_t$ is the turbulent heat diffusivity. In contrast to the Prandtl number $Pr$, $Pr_t$ is not a fluid property but rather a relation between the transport of momentum and the transport of heat due to the turbulent mixing [14]. The turbulent Prandtl number is empirically determined and in the present work assumed to be $Pr_t \approx 0.9$.

Some turbulence models, for example, the $k$-$k_l$-$\omega$ and the $k$-$\overline{v^2}$-$\omega$ model, offer their own calibrated closures for the turbulent heat-flux vector. The present work employed the approximation as given in equation (2.49) rather than more sophisticated formulations.

## 2.3. Turbulence modeling

This section presents the Standard $k$-$\varepsilon$, the Wilcox $k$-$\omega$ and Menter's SST turbulence model, which is based on the two former models. It is not intended to give a complete list or overview of available EVMs. For further information regarding two-equation EVMs the textbook of Wilcox [3] is highly recommended.

For consistency reasons all model equations are given for a compressible fluid and written in their conservative form. If applicable the model parameters were termed in a consistent way. For the sake of readability the averaging operators $\overline{\phi}$ and $\widetilde{\phi}$ are dropped from the mean variables $\left( \overline{\rho}, \overline{p}, \overline{q_i}, \widetilde{u_i}, \widetilde{e}, \widetilde{T} \right)$.

The substantial derivative for an arbitrary variable $\varphi$ is denoted as

$$\frac{D\phi}{Dt} = \frac{\partial \phi}{\partial t} + \frac{\partial \phi}{\partial x_j}. \tag{2.50}$$

All of the following models are Eddy Viscosity Models (EVMs) and employ Boussinesq's assumption (Eq. (2.47)) for calculating the Reynolds Stress Tensor $\tau_{tij}$.

Important measures in turbulence modeling are the strain-rate tensor

$$S_{ij} = \frac{1}{2} \left( \frac{\partial u_i}{\partial x_j} + \frac{\partial u_j}{\partial x_i} \right), \tag{2.51}$$

its trace-less variation

$$\hat{S}_{ij} = S_{ij} - \frac{1}{3} \frac{\partial u_k}{\partial x_k} \delta_{ij} \tag{2.52}$$

and the vorticity tensor

$$\Omega_{ij} = \frac{1}{2} \left( \frac{\partial u_i}{\partial x_j} - \frac{\partial u_j}{\partial x_i} \right). \tag{2.53}$$

The mean values of $S$ and $\hat{S}$, and the vorticity magnitude are calculated from

$$S = \sqrt{2S_{ij}S_{ij}} \qquad \hat{S} = \sqrt{2\hat{S}_{ij}\hat{S}_{ij}} \qquad \Omega = \sqrt{2\Omega_{ij}\Omega_{ij}}, \tag{2.54}$$

respectively.

### 2.3.1. Standard $k$-$\varepsilon$ model

The $k$-$\varepsilon$ model was initially developed by Jones and Launder [36] and later revised by Launder and Spalding [32] which is often termed the Standard $k$-$\varepsilon$ model. Further insight into the model was gained from the book of Versteeg and Malalasekera [20].

The model introduces transport equations for the turbulence kinetic energy $k$ and the turbulence specific dissipation $\varepsilon$, respectively. For high Reynolds numbers, the model is given by

$$\frac{D\rho k}{Dt} = P_k - \rho\varepsilon + \frac{\partial}{\partial x_j} \left[ \left( \mu + \frac{\mu_t}{\sigma_k} \right) \frac{\partial k}{\partial x_j} \right] \tag{2.55}$$

and

$$\frac{D\rho\varepsilon}{Dt} = \alpha \frac{\varepsilon}{k} P_k - \beta \frac{\rho\varepsilon^2}{k} + \frac{\partial}{\partial x_j} \left[ \left( \mu + \frac{\mu_t}{\sigma_\varepsilon} \right) \frac{\partial \varepsilon}{\partial x_j} \right]. \tag{2.56}$$

The production term $P_k$ follows directly from the exact transport equation of the turbulence kinetic energy (see for example [20]) and is given by

$$P_k = \tau_{tij} \frac{\partial u_i}{\partial x_j}, \tag{2.57}$$

where the Reynolds stress tensor is calculated by Boussinesq's assumption (Eq. (2.47)). Thus the production term can be written as

$$P_k = \mu_t \hat{S}\hat{S} - \frac{2}{3}\rho k \delta_{ij} \frac{\partial u_i}{\partial x_j}, \tag{2.58}$$

where $\hat{S}$ is the mean value of the traceless strain-rate tensor, defined in equation (2.54). Note that the second term in equation (2.58) is neglected in many publications and in fact is zero for incompressible flows.

The destruction term (second term on the RHS of Eq. (2.55)) is closely related to the production term of the turbulence kinetic energy. Which is reasonable, because in regions with high turbulence kinetic energy the turbulence dissipation will also be high [20]. Production as well as destruction of the dissipation rate $\varepsilon$ is assumed to be linearly dependent on those terms of the turbulence kinetic energy $k$, where $\alpha$ and $\beta$ are proportionality constants. The factor $\varepsilon/k$ ensures correct dimensions [20].

The last term on the RHS of the transport equations (2.55) and (2.56) model the transport by diffusion, where the eddy viscosity is related to the diffusivity of $k$ and $\varepsilon$ by the Prandtl-Schmidt numbers $\sigma_k$ and $\sigma_\varepsilon$, respectively.

From dimensional considerations, the eddy viscosity is calculated by

$$\mu_t = \rho C_\mu \frac{k^2}{\varepsilon}, \tag{2.59}$$

where $C_\mu$ is a dimensionless constant.

Close to a wall, the turbulent Reynolds number inevitable becomes small and viscous forces dominate. The presented high-Reynolds formulation of the $k$-$\varepsilon$ equations loses its applicability. To circumvent this problem it is popular to use either wall-functions, based on the law of the wall (Eq. (1.8)) or additional damping functions for the production and destruction terms of the transport equation of $\varepsilon$ [32]. Since the present work did not employ any of these formulations, an in-depth explanation is omitted. Further insight can be gained from the textbook of Wilcox [3].

The model is very popular for free-shear flows but is known to yield unsatisfactory results for adverse pressure gradients and is hence unreliable in the prediction of boundary-layer separation. Therefore it is not viable for predicting the flow in thermal turbomachinery.

**Model parameters**

The parameters for the Standard $k$-$\varepsilon$ model [32] are given as:

$$C_\mu = 0.09 \qquad \alpha = 1.44 \qquad \beta = 1.92 \qquad \sigma_k = 1.0 \qquad \sigma_\varepsilon = 1.3 \qquad (2.60)$$

## 2.3.2. Wilcox $k$-$\omega$ model

Besides the turbulence dissipation $\varepsilon$, another very popular choice for the length determining variable is the specific (turbulence) dissipation rate $\omega$. The model of Wilcox is the most popular model and was first published in 1988 [35]. Although it was refined by Wilcox in 1998 [21], 2006 [3] and last published in 2008 [33], the present work describes the initial formulation from 1988, because it was the basis for Menter's base line (BSL) and SST model. For the Wilcox $k$-$\omega$ model, the specific (turbulence) dissipation rate is defined as

$$\omega = \frac{\varepsilon}{\beta^* k}, \qquad (2.61)$$

where $\beta^*$ is a modeling constant and equal to $\beta^* = C_\mu$.

The transport equation for the turbulence kinetic energy reads

$$\frac{D\rho k}{Dt} = P_k - \beta^* \rho k \omega + \frac{\partial}{\partial x_j}\left[(\mu + \sigma_k \mu_t)\frac{\partial k}{\partial x_j}\right], \qquad (2.62)$$

where the production term $P_k$ is defined identical as in the Standard $k$-$\varepsilon$ model (Eq. (2.58)), and the destruction term is reformulated in terms of $\omega$ ($\varepsilon = \beta^* k \omega$). The $\omega$ transport equation is given by

$$\frac{D\rho\omega}{Dt} = \alpha\frac{\omega}{k}P_k - \beta\rho\omega^2 + \frac{\partial}{\partial x_j}\left[(\mu + \sigma_\omega \mu_t)\frac{\partial \omega}{\partial x_j}\right], \qquad (2.63)$$

where $\alpha$ and $\beta$ are modeling constants which relate the production and destruction terms of the $\omega$ equation to the respective terms of the $k$ equation, the term $\omega/k$ is present in the production term and implicitly included in the destruction term ensuring correct dimensions.

The transport by diffusion is modeled similarly to the $k$-$\varepsilon$ model, except that the Prandtl-Schmidt numbers $\sigma_k$ and $\sigma_\omega$ were formally moved from the denominator to the numerator.

The eddy viscosity then is calculated from

$$\mu_t = \rho \frac{k}{\omega},$$

(2.64)

which follows from the same dimensional reasoning as equation (2.59) of the $k$-$\varepsilon$ model.

While the 1988 formulation of the $k$-$\omega$ model of Wilcox is known to perform substantially better for wall-bounded flows and predicts flow separation quite reliably, it is known for a problematic strong dependency of the eddy viscosity on the values of $\omega$ outside the boundary layer, which are largely influenced by their initial and boundary conditions. Please note that this shortcoming was resolved for the better part in the latest 2006 version of the model.

**Model parameters**

The parameters for the 1988 formulation of the Wilcox $k$-$\omega$ model [35] are given by

$$\beta^* = C_\mu = 0.09 \quad \alpha = 5/9 \approx 0.5556 \quad \beta = 3/40 = 0.075 \quad \sigma_k = 0.5 \quad \sigma_\omega = 0.5 \quad (2.65)$$

## 2.3.3. Menter Shear Stress Transport (SST) model

At the time Menter developed his two-equation eddy viscosity turbulence model, the two most commonly used turbulence models were the $k$-$\varepsilon$ model (sec. 2.3.1) and the 1988 version of the $k$-$\omega$ model of Wilcox [35] (sec. 2.3.2). For the usage in aerodynamics and thermal turbomachinery, the $k$-$\varepsilon$ model yields unsatisfactory results due to its lack of sensitivity for adverse pressure gradients and therefore it is unreliable in the prediction of separation. While the $k$-$\omega$ model is superior to the $k$-$\varepsilon$ model in that sense it shows a problematic strong dependency of the eddy viscosity on the values of $\omega$ outside the boundary layer.

Driven by his dissatisfaction with the advancement of turbulence models for engineering applications in terms of accuracy, which he believed was caused by the denial of the underlying empirical aspect of turbulence models by the scientific community [17], Menter suggested to blend between the two models in order to exploit the benefits while not inheriting their shortcomings. The model was first presented on a conference in 1993 [37] and later published in his paper in 1994 [17], where the resulting model was termed the new BSL model and its performance is very similar to the $k$-$\omega$ model, but without its free-stream dependency.

For the Shear Stress Transport (SST) model, Menter additionally modified the definition of the eddy viscosity in order to account for the transport of the turbulent shear

stress. This is done by enforcing Bradshaw's observation, that the turbulent shear stress is proportional to the turbulence kinetic energy in the wake region (turbulent outer layer) of the boundary layer. Menter et. al. revisited the model in 2003 [34] and all following equations and model constants are given with respect to the 2003 publication, except for a typographical mistake in the original publication, which was pointed out by the Turbulence Model Benchmarking Working Group (TMBWG) of the Fluid Dynamics Technical Committee of the American Institute of Aeronautics and Astronautics (AIAA) [38].

The model is also formulated in terms of two transport equations, one for the turbulence kinetic energy $k$ (Eq. (2.66)) and one for the specific turbulence dissipation $\omega$ (Eq. (2.67)). For the derivation, first the original equation for the turbulence dissipation $\varepsilon$ from the Standard $k$-$\varepsilon$ model (Eq. (2.56)) is reformulated in terms of omega. Next, the reformulated equation and the transport equation for $k$ (Eq. (2.55)) are multiplied by the term $(1 - F_1)$ and summed up with the corresponding equations of the Wilcox $k$-$\omega$ model which are first multiplied by the blending Function $F_1$.

The resulting two transport equations read

$$\frac{D\rho k}{Dt} = \widetilde{P}_k - \beta^* \rho k \omega + \frac{\partial}{\partial x_i}\left[ (\mu + \sigma_k \mu_t)\frac{\partial k}{\partial x_i} \right], \quad (2.66)$$

and

$$\frac{D\rho \omega}{Dt} = \hat{P}_\omega - \beta \rho \omega^2 + \frac{\partial}{\partial x_i}\left[ (\mu + \sigma_\omega \mu_t)\frac{\partial \omega}{\partial x_i} \right] + (1 - F1)\, CD_{k\omega}, \quad (2.67)$$

where in the $\omega$ equation an additional $k$-$\omega$ cross-diffusion term is present, which is caused by the reformulation of the $\varepsilon$ transport equation and has no direct counterpart in the $k$-$\omega$ model. The $k$-$\omega$ cross-diffusion term $CD_{k\omega}$ is given by

$$CD_{k\omega} = \max\left( 2\rho\sigma_{\omega 2}\frac{1}{\omega}\frac{\partial k}{\partial x_i}\frac{\partial \omega}{\partial x_i}, 10^{-10} \right) \quad (2.68)$$

and for numerical stability bounded by $10^{-10}$. The blending function F1 is defined as

$$F_1 = \tanh\left\{ \min\left[ \max\left( \frac{\sqrt{k}}{\beta^* \omega d}, \frac{500\nu}{d^2\omega} \right), \frac{4\rho\sigma_{\omega 2}k}{CD_{k\omega}\, d^2} \right]^4 \right\} \quad (2.69)$$

and designed to be unity inside the laminar sublayer and the logarithmic region and continuously switches to zero inside the outer region of the boundary layer. This function serves two purposes. As described later, it is used to calculate a specific blend between two sets of model parameters, but it also activates the cross-diffusion term in the outer region of the boundary layer and for the free-shear flow region. Wilcox [21] originally argued that because the $\varepsilon$ equation is not more fundamental than the

$\omega$ equation, it is unjustified to assess that the cross-diffusion term, arising from the transformation of the $\varepsilon$ equation, is formally missing from the original $\omega$ equation. Nevertheless, he included a cross-diffusion term, although in a different form, in his later formulations of the model [3, 33] because the SST model had proven that the term reduces the dependency of the eddy viscosity on the free stream values.

The production term for the turbulence kinetic energy is given by

$$P_k = \tau_{tij}\frac{\partial u_i}{\partial x_j} = \mu_t \hat{S}\hat{S} - \frac{2}{3}\rho k \delta_{ij}\frac{\partial u_i}{\partial x_j}, \tag{2.70}$$

where the Reynolds stress tensor $\tau_{tij}$ is computed from Boussinesq's assumption (Eq. 2.47). Due to the unphysical production of turbulence kinetic energy in stagnation regions, which is caused by excessively large values of the mean value of the trace-less strain-rate tensor $\hat{S}$, the production term is usually limited by one of two methods. One possibility is to use a clip-limiter in the form of

$$\widetilde{P_k} = \min\left(P_k, 10\beta^* \rho k \omega\right), \tag{2.71}$$

where the production term is limited to ten times the value of the destruction term. Alternatively, the Kato and Launder formulation for the production term [39] can be used, which is given by

$$\widetilde{P_k} = \mu_t \hat{S}\Omega - \frac{2}{3}\rho k \delta_{ij}\frac{\partial u_i}{\partial x_j}, \tag{2.72}$$

and exploits the fact that the deformation near a stagnation point is almost irrotational, thus the vorticity is approximately zero, i.e. $\Omega \approx 0$. On the other hand, the vorticity is equal to the strain rate for free shear flows, therefore recovering the original formulation. Usually selecting one of these limiters suffices and the software CFX, for instance, does not allow selection of both limiters at the same time.

According to the TMBWG [38], the production term for $\omega$ should use the limited production term and is defined as

$$\widetilde{P_\omega} = \frac{\alpha}{\nu_t}\widetilde{P_k}. \tag{2.73}$$

Finally, the eponymous modification for the SST model, compared to the BSL model, enforces Bradshaw's assumption, that the eddy viscosity $\nu_t$ is proportional to the turbulence kinetic energy $k$ inside the boundary layer by modifying the definition of the determining equation to

$$\nu_t = \frac{a_1 k}{\max\left(a_1\omega, SF_2\right)}. \tag{2.74}$$

The second blending function $F_2$ is given by

$$F_2 = \tanh \left\{ \max \left[ \frac{2\sqrt{k}}{\beta^* \omega d}, \frac{500\nu}{d^2 \omega} \right]^2 \right\}$$

(2.75)

and is designed to be unity for boundary layer flows and zero for free shear layers, ensuring that Bradshaw's assumption is only used inside the boundary layer and the original formulation of the eddy viscosity is recovered for free shear flows.

**Model parameters**

The model constants are defined in two sets (Eq. (2.77)) [34], corresponding to the $k$-$\omega$ model (subscript 1) and the $k$-$\varepsilon$ model (subscript 2), respectively. The actual model constants are computed as a local blend by

$$\phi = F_1 \phi_1 + (1 - F_1)\phi_2,$$

(2.76)

where $\phi$ stands for an arbitrary model constant ($\sigma_k, \sigma_\omega, \alpha, \beta$).

$$\begin{array}{llll} \alpha_1 = 5/9 & \beta_1 = 0.0750 & \sigma_{k1} = 0.85 & \sigma_{\omega 1} = 0.5 \\ \alpha_2 = 0.44 & \beta_2 = 0.0828 & \sigma_{k2} = 1.0 & \sigma_{\omega 2} = 0.856 \\ \beta^* = C_\mu = 0.09 & \kappa = 0.41 & a_1 = 0.31 & \end{array}$$

(2.77)

# 2.4. Transition modeling

Transition models are often split into two groups or families. First LCTMs, and second phenomenological, also known as physics-based, models. The present work investigated two models from each group. The $\gamma$-$Re_{\theta t}$ and the $\gamma$ model use local correlations for determining the transition onset and growth, while the $k$-$k_L$-$\omega$ and the $k$-$\overline{v^2}$-$\omega$ models use a physics-based approach. The LCTMs have to be linked to an underlying $k$-$\omega$ based model and were developed with the SST model in mind. The physics-based models are transition sensitive turbulence models and provide their own $k$-$\omega$ transport equations within their formulation.

Within the families, the investigated models are closely related. The $\gamma$ model is basically a simplified version of the $\gamma$-$Re_{\theta t}$ model and the $k$-$\overline{v^2}$-$\omega$ model is a modification of the $k$-$k_L$-$\omega$ model, but introduces a more fundamental change by giving up the idea of pre-transitional laminar fluctuations in favor of wall-normal velocity fluctuations as a transition sensor. Since turbulence is significantly influenced by the upstream

flow history, all models employ transport equations in the form of partial differential equations with convection, diffusion and source terms.

For the LCTMs a fundamental quantity is the intermittency $\gamma$, which is defined as the fraction of time a flow is turbulent at a given location. $\gamma$ is zero for laminar flow, unity for fully turbulent flow and takes a value in-between ($0 \leq \gamma \leq 1$) for transitional flow. However, $\gamma \leq 1$ is usually not enforced and the $\gamma$-$Re_{\theta t}$ model for example allows the intermittency to raise beyond unity in order to speed up the transition process under some special conditions. The $\gamma$ model instead introduces for the same reasons a second production term into the turbulence kinetic energy transport equation.

**Transition onset sensors**

All investigated transition models use transition sensors to either activate turbulence production starting from transition onset or inhibit turbulence production in the pre-transitional laminar boundary layer. According to Dick and Kubacki [40], most of these sensors are ratios of time-, velocity- and length-scales in the form of Reynolds numbers. Knowledge about the specific transition process is exploited in order to define meaningful sensors and make suitable substitutions or local approximations of otherwise unknown quantities, where needed.

For example, it is known from observation that transition occurs when a critical value of the momentum thickness Reynolds number $Re_\theta$ is exceeded. Inside a laminar attached boundary layer, the momentum thickness Reynolds number $Re_\theta$ can be approximated by

$$Re_\theta = \frac{\theta U}{\nu} \approx \frac{\max\left(Re_v\right)}{2.193},\tag{2.78}$$

where the vorticity Reynolds number is defined, using the wall-normal distance $d_w$ and the magnitude of the vorticity tensor $\Omega$, as

$$Re_v = \frac{d_w^2 \Omega}{\nu}.\tag{2.79}$$

From this, a transition onset sensor for the $\gamma$-$Re_{\theta t}$ model is constructed as

$$F_{\text{onset1}} = \frac{Re_S}{2.193 Re_{\theta_C}},\tag{2.80}$$

where instead of the vorticity Reynolds number $Re_v$ the strain-rate Reynolds number $Re_S$ given by

$$Re_S = \frac{d_w^2 S}{\nu}\tag{2.81}$$

is used together with empirical correlations for the critical value of the momentum thickness Reynolds number $Re_{\theta c}$. These empirical correlations depend mainly on the pressure-gradient imposed from free-stream and the local turbulence intensity $Tu$. The $\gamma$ model uses a slightly modified sensor, where the constant value was changed from 2.193 to 2.2.

On side of the physics-based models, shear-sheltering, which was confirmed by DNS and is the damping of small-scale fluctuations in the pre-transitional boundary layer, is used [40]. For the $k$-$k_L$-$\omega$ model a transition onset sensor is then based on the wall-distance Reynolds number

$$Re_{d_w} = \frac{\sqrt{k}d_w}{\nu},$$ (2.82)

and expressed in the form of

$$f_{SS} = \exp\left[-\left(\frac{C_{SS}\nu}{\sqrt{k}d_w}\right)^2\right],$$ (2.83)

where $C_{SS}$ is a model parameter.

The following sections present each transition model in more detail, where the focus was laid on LCTMs. The review paper of Dick and Kubacki [40] is an excellent resource for a more complete overview on available transition models and the corresponding original publications are given for reference.

## 2.4.1. Local correlation-based $\gamma$-$Re_{\theta t}$ transition model

This transition model introduces two additional transport equations and was first presented in a two-part paper by Menter et. al. [41, 42], where the empirical correlations were initially deemed proprietary and omitted. In the present work, the latest published correlations by Menter and Langtry [43] were used. Collins (Kelterer) et. al. [44] provided a correlation fine-tuned to the in-house solver LINARS.

The transport equation for the intermittency $\gamma$ reads

$$\frac{D\rho\gamma}{Dt} = P_\gamma - E_\gamma + \frac{\partial}{\partial x_j}\left[\left(\mu + \frac{\mu_t}{\sigma_\gamma}\right)\frac{\partial\gamma}{\partial x_j}\right],$$ (2.84)

where the LHS accounts for the local change and the convective transport, and on the RHS a production term, a destruction term and transport due to diffusion are present. The Prandtl-Schmidt number $\sigma_\gamma$ relates the eddy viscosity to the turbulent diffusion and the total diffusion is given as the sum of laminar and turbulent diffusion.

The production term is given by

$$P_\gamma = c_{a1} F_{\text{length}} \, \rho S \, (1 - c_{e1}\gamma) \, (\gamma \, F_{\text{onset}})^{c_\alpha} \, , \tag{2.85}$$

where $F_{\text{length}}$ is an empirical correlation that controls the transition length by setting the magnitude of the production term. The function $F_{\text{onset}}$ suppresses the production upstream to the transition onset and the term $(1 - c_{e1}\gamma)$ ensures that production is deactivated, when $\gamma$ reaches unity. The density and the mean of the shear-rate tensor are present for dimensional reasons.

The empirical correlation for the transition length is given by

$$\hat{F}_{\text{length}} = \begin{cases} 0.3188 & \hat{R}e_{\theta t} \geq 1200 \\ 0.5 - 3.0\text{E-}4 \left( \hat{R}e_{\theta t} - 596.0 \right) & 596 \leq \hat{R}e_{\theta t} < 1200 \\ 263.404 - \left( \begin{array}{l} 1.23939 \, \hat{R}e_{\theta t} - 194.548\text{E-}5 \, \hat{R}e_{\theta t}^2 \\ + \, 101.695\text{E-}8 \, \hat{R}e_{\theta t}^3 \end{array} \right) & 400 \leq \hat{R}e_{\theta t} < 596 \\ 39.8189 - 119.270\text{E-}4 \, \hat{R}e_{\theta t} - 132.567\text{E-}6 \, \hat{R}e_{\theta t}^2 & \hat{R}e_{\theta t} < 400, \end{cases} \tag{2.86}$$

where $\hat{R}e_{\theta t}$ is the transported transitional momentum thickness Reynolds number from the second transport equation (Eq. (2.97)).

To prevent unphysical behavior in the sublayer Menter and Langtry [43] proposed to limit the transition length to $F_{\text{length}} = 40$ inside the sublayer with the following functions:

$$F_{\text{sublayer}} = \exp \left[ -\left( \frac{R_\omega}{0.4} \right)^2 \right], \qquad R_\omega = \frac{\rho d_w^2 \omega}{500 \mu} \tag{2.87}$$

$$F_{\text{length}} = \hat{F}_{\text{length}} \left( 1 - F_{\text{sublayer}} \right) + 40 F_{\text{sublayer}} \tag{2.88}$$

The transition onset is controlled by the following functions:

$$F_{\text{onset1}} = \frac{Re_S}{2.193 Re_{\theta_C}} \tag{2.89}$$

$$F_{\text{onset2}} = \min \left( \max \left( F_{\text{onset1}}, F_{\text{onset1}}^4 \right), 2 \right) \tag{2.90}$$

$$F_{\text{onset3}} = \max \left( 1 - \left( \frac{R_T}{2.5} \right)^3, 0 \right) \tag{2.91}$$

$$F_{\text{onset}} = \max \left( F_{\text{onset2}} - F_{\text{onset3}}, 0 \right) \tag{2.92}$$

$F_{\text{onset3}}$ was introduced to prevent stalling of the transition progress due to the changing velocity profile inside the transitional boundary layer, and $R_T$ can be interpreted as the ratio of the turbulent viscosity to the molecular viscosity given by

$$R_T = \frac{\rho k}{\mu \omega}. \tag{2.93}$$

The strain-rate Reynolds number is defined by equation (2.81).

The critical Reynolds number, at which production of intermittency first is encountered, is given by the empirical correlation

$$Re_{\theta c} = \begin{cases} \hat{Re}_{\theta t} - \left( \begin{array}{l} 396.035\text{E-2} - 120.656\text{E-4}\,\hat{Re}_{\theta t} + 868.230\text{E-6}\,\hat{Re}_{\theta t}^2 \\ - 696.506\text{E-9}\,\hat{Re}_{\theta t}^3 + 174.105\text{E-12}\,\hat{Re}_{\theta t}^4 \end{array} \right) & \hat{Re}_{\theta t} \leq 1870 \\ \hat{Re}_{\theta t} - \left( 593.11 + 0.482\,(\hat{Re}_{\theta t} - 1870.0) \right) & \hat{Re}_{\theta t} > 1870. \end{cases} \tag{2.94}$$

The destruction term reads

$$E_\gamma = c_{a2} F_{\text{turb}}\, \rho \Omega\, (c_{e2}\gamma - 1)\, \gamma \tag{2.95}$$

and ensures that the intermittency is zero inside the laminar boundary layer. This term also controls the relaminarization, when the onset criteria is no longer satisfied. Instead of the mean strain-rate $S$, the vorticity magnitude $\Omega$ is used here to ensure that the intermittency $\gamma$ is not reduced in the free shear-stream due to high strain-rate values. It is deactivated by the expression

$$F_{\text{turb}} = \exp\left[ -\left(\frac{R_T}{4}\right)^4 \right] \tag{2.96}$$

for fully turbulent regions.

The second transport equation is for the transitional momentum thickness Reynolds number, $\hat{Re}_{\theta t}$,

$$\frac{D\rho\hat{Re}_{\theta t}}{Dt} = P_{\theta t} + \frac{\partial}{\partial x_j}\left[ \sigma_{\theta t}\,(\mu + \mu_t)\,\frac{\partial \hat{Re}_{\theta t}}{\partial x_j} \right], \tag{2.97}$$

where the caret (^) distinguishes the transported from the empirical transitional momentum thickness Reynolds number $Re_{\theta t}$.

The source term forces $\hat{Re}_{\theta t}$ to match an empirical local correlation of the transition momentum thickness Reynolds number $Re_{\theta t}$ outside of the boundary layer and is given by

$$P_{\theta t} = c_{\theta t}\frac{\rho}{t_{\theta t}}\,(Re_{\theta t} - \hat{Re}_{\theta t})\,(1.0 - F_{\theta t}), \tag{2.98}$$

where $F_{\theta t}$ is a blending function which deactivates the production term inside the boundary layer in order to allow $\hat{Re}_{\theta t}$ to diffuse into the boundary layer from the free stream. To ensure proper dimensions of the production term the time scale

$$t_{\theta t} = \frac{500\mu}{\rho U^2} \qquad (2.99)$$

is introduced, where $U$ is the velocity magnitude.

The blending function is given by

$$F_{\theta t} = \min\left[\max\left(F_{\text{wake}}\,\exp\left[-\left(\frac{d_w}{\delta^*}\right)^4\right], 1.0 - \left(\frac{c_{e2}\gamma - 1}{c_{e2} - 1}\right)^2\right), 1.0\right], \qquad (2.100)$$

with

$$\delta^* = \frac{375\,\Omega\mu d_w}{\rho U^2}\hat{Re}_{\theta t} \qquad \text{and} \qquad F_{\text{wake}} = \exp\left[-\left(Re_\omega/1.0\text{E}5\right)^2\right], \qquad (2.101)$$

where $F_{\text{wake}}$ ensures that the production term $P_{\theta t}$ is active in the wake region, for example downstream of a blade, and $\delta^*$ is an approximation for the boundary layer thickness.

The free-stream value of $Re_{\theta t}$ is given by the empirical correlation

$$Re_{\theta t} = \begin{cases} \left(1173.51 - 589.428\,Tu + 0.2196\,Tu^{-2}\right)F_{\lambda_\theta} & Tu \leq 1.3 \\ 331.50\left(Tu - 0.5658\right)^{-0.671}F_{\lambda_\theta} & Tu > 1.3 \end{cases} \qquad (2.102)$$

and an additional correlation for the pressure-gradient function $F_{\lambda_\theta}$ as

$$F_{\lambda_\theta} = \begin{cases} 1 - \left(-12.986\lambda_\theta - 123.66\lambda_\theta^2 - 405.689\lambda_\theta^3\right)\exp\left[-\left(\frac{Tu}{1.5}\right)^{1.5}\right] & \lambda_\theta \leq 0 \\ 1 + 0.275\left(1 - \exp\left[-35\lambda_\theta\right]\right)\exp\left[-2\,Tu\right] & \lambda_\theta > 0. \end{cases} \qquad (2.103)$$

The local turbulence intensity is calculated from

$$Tu = 100\frac{\sqrt{2/3k}}{U}, \qquad (2.104)$$

and the pressure gradient parameter is defined as

$$\lambda_\theta = \frac{\rho\theta^2}{\mu}\frac{dU}{ds}, \qquad (2.105)$$

where the derivative $dU/ds$ on the RHS is the acceleration into the stream-wise direction and the momentum thickness $\theta$ is calculated by rearranging the definition of the momentum thickness Reynolds number as

$$\theta = \frac{Re_{\theta t}\mu}{\rho U}. \tag{2.106}$$

Equations (2.102) to (2.106) have to be solved iteratively because $\theta$ is implicitly present on both sides of the correlation for pressure-gradient function (Eq. (2.103)).

The acceleration along the stream-wise direction can be calculated by summing up the contributions of the derivatives of the velocity magnitude $U$ with respect to the individual components of the Cartesian position vector $x_i$ as

$$\frac{\partial U}{\partial x} = \frac{1}{U}\left( u\frac{\partial u}{\partial x} + v\frac{\partial v}{\partial x} + w\frac{\partial w}{\partial x} \right),$$

$$\frac{\partial U}{\partial y} = \frac{1}{U}\left( u\frac{\partial u}{\partial y} + v\frac{\partial v}{\partial y} + w\frac{\partial w}{\partial y} \right),$$

$$\frac{\partial U}{\partial z} = \frac{1}{U}\left( u\frac{\partial u}{\partial z} + v\frac{\partial v}{\partial z} + w\frac{\partial w}{\partial z} \right),$$

$$\frac{dU}{ds} = \frac{u}{U}\frac{\partial U}{\partial x} + \frac{v}{U}\frac{\partial U}{\partial y} + \frac{w}{U}\frac{\partial U}{\partial z}. \tag{2.107}$$

Note that the Prandl-Schmidt number in the diffusion term of the transport equation for $\hat{Re}_{\theta t}$ (Eq. (2.97)) affects both the molecular diffusion and the turbulent diffusion.

**Interaction with the turbulence model**

The model was designed to interact with Menter's SST (sec. 2.3.3) turbulence model, but according to the authors, it should work well with every $k$-$\omega$ based turbulence model. First, the production and destructions terms of the turbulence kinetic energy equation are modified in such a way that the transition model can suppress the production of turbulence kinetic energy inside the boundary layer upstream of transition onset.

The modified transport equation for the turbulence kinetic energy $k$ reads,

$$\frac{D\rho k}{Dt} = \hat{P}_k - \hat{D}_k + \frac{\partial}{\partial x_i}\left[ (\mu + \sigma_k \mu_t)\frac{\partial k}{\partial x_i} \right], \tag{2.108}$$

where the production and destruction terms are modified as follows:

$$\hat{P}_k = \gamma_{\text{eff}}\widetilde{P}_k \tag{2.109}$$

$$\hat{D}_k = \min\left(\max\left(\gamma_{\text{eff}}, 0.1\right), 1.0\right)\widetilde{D}_k \tag{2.110}$$

An additional variable, $\gamma_{\text{sep}}$, is introduced in order to improve the prediction of separation bubbles, which is calculated by

$$\gamma_{\text{sep}} = \min\left[2.0\max\left(\frac{Re_v}{3.235\,Re_{\theta c}} - 1.0, 0\right)F_{\text{reattach}}, 2.0\right]F_{\theta t}, \tag{2.111}$$

where the fraction inside the brackets accounts for the change in the approximation of $Re_\theta t$ due to the change of the velocity profile during flow separation. $F_{\text{reattach}}$ given by

$$F_{\text{reattach}} = \exp\left[-\left(\frac{R_T}{20}\right)^4\right] \tag{2.112}$$

deactivates the function for fully turbulent flow and $F_{\theta t}$ is given by equation (2.100). Finally, the larger value of $\gamma$ and $\gamma_{\text{sep}}$ is used for the effective value:

$$\gamma_{\text{eff}} = \max\left(\gamma, \gamma_{\text{sep}}\right) \tag{2.113}$$

This allows, together with limiting the effective intermittency in the destruction term (Eq. (2.110)), the intermittency to increase beyond unity in order to speed up the transition process.

Since Menter's SST model was designed for fully turbulent flow, the blending function $F_1$ (Eq. (2.69)) was modified in order to ensure that the underlying $k$-$\omega$ model stays active inside the transitional boundary layer as

$$F_1 = \max\left(F_{1\text{orig}}, F_3\right), \tag{2.114}$$

where $F_{1\text{orig}}$ is the original blending function from the SST model and an additional blending function $F_3$ is defined, using the wall-distance Reynolds number $Re_{d_w}$ (Eq. (2.82)), as

$$F_3 = \exp\left[-\left(\frac{Re_{d_w}}{120}\right)^8\right]. \tag{2.115}$$

**Model parameters**

For the $\gamma$-$Re_{\theta t}$ model, the set of model parameters [43] is given by:

$$
\begin{array}{llll}
ce_1 = 1.0 & ca_1 = 2.0 & c_\alpha = 0.5 & \sigma_\gamma = 1.0 \\
ce_2 = 50 & ca_2 = 0.06 & c_{\theta t} = 0.03 & \sigma_{\theta t} = 2.0
\end{array} \tag{2.116}
$$

## 2.4.2. Local correlation-based $\gamma$ transition model

In an effort to significantly reduce the complexity of the correlations of the $\gamma$-$Re_{\theta t}$ model and in order to avoid the necessity of the second additional transport equation, besides the one for the intermittency $\gamma$, Menter et. al. [45] developed the one-equation $\gamma$ LCTM. Additionally, Galilean invariance was achieved by avoiding the need for computing the acceleration into stream-wise direction. Besides these major differences, some more subtle changes were made to the model which are pointed out directly in the following description.

The single additional transport equation is formally identical to the $\gamma$ transport equation of the $\gamma$-$Re_{\theta t}$ model (compare Eq. (2.84)) and is given by

$$\frac{D\rho\gamma}{Dt} = P_\gamma - E_\gamma + \frac{\partial}{\partial x_j}\left[\left(\mu + \frac{\mu_t}{\sigma_\gamma}\right)\frac{\partial\gamma}{\partial x_j}\right]. \tag{2.117}$$

The production term reads very similar to the equation of the $\gamma$-$Re_{\theta t}$ model (Eq. (2.85)), when setting the constants $c_{a1}$ and $c_\alpha$ to unity:

$$P_\gamma = F_{\text{length}}\,\rho S(1-\gamma)\gamma\,F_{\text{onset}} \tag{2.118}$$

$F_{\text{length}}$ is a correlation in the $\gamma$-$Re_{\theta t}$ model, and a constant for the $\gamma$ model. The density $\rho$ and the mean value of the strain-rate tensor $S$ are present for dimensional reasons and the term $(1-\gamma)$ deactivates the production term, once $\gamma$ reaches unity.

The transition onset is calculated similarly to the $\gamma$-$Re_{\theta t}$ model using

$$F_{\text{onset1}} = \frac{Re_S}{2.2Re_{\theta_C}}, \tag{2.119}$$

$$F_{\text{onset2}} = \min\left(F_{\text{onset1}}, 2\right), \tag{2.120}$$

$$F_{\text{onset3}} = \max\left(1 - \left(\frac{R_T}{3.5}\right)^3, 0\right), \tag{2.121}$$

and

$$F_{\text{onset}} = \max\left(F_{\text{onset2}} - F_{\text{onset3}}, 0\right) \tag{2.122}$$

with three modifications:

- the constant in the nominator of equation (2.119) was changed from 2.193 to 2.2
- $F_{\text{onset2}}$ (Eq. (2.120)) was simplified
- nominator in $F_{\text{onset3}}$ (Eq. (2.121)) was changed from 2.5 to 3.5

$R_T$ is again the ratio of turbulent to molecular viscosity (Eq. (2.93)) and the strain-rate Reynolds number is given by equation (2.81).

A major difference between $\gamma$-$Re_{\theta t}$ and $\gamma$ model is how the critical momentum thickness Reynolds number $Re_{\theta_C}$ is estimated. In the $\gamma$-$Re_{\theta t}$ model extensive correlations are used, but for the $\gamma$ model it is calculated from local approximations for the turbulence intensity $Tu_L$ and the local pressure gradient parameter $\lambda_{\theta_L}$, that is

$$Re_{\theta c} = f\left(Tu_L, \lambda_{\theta L}\right). \tag{2.123}$$

The local turbulence intensity is calculated from

$$Tu_L = \min\left(100\frac{\sqrt{2/3k}}{\omega d_w}, 100\right), \tag{2.124}$$

where the term $\omega d_w$ substitutes the velocity magnitude $U$ compared to the definition of the turbulence intensity $Tu$ given by equation (2.46). A parameter to account for the influence of the pressure gradient, imposed from the free-stream, is calculated from

$$\lambda_{\theta L} = -7.57\text{E-}3\frac{dV}{dy}\frac{d_w^2}{\nu} + 0.0128, \tag{2.125}$$

where $dV/dy$ (see Eq. (2.127)) is the wall-normal velocity gradient. By avoiding the stream-wise acceleration $dU/ds$, as used in the $\gamma$-$Re_{\theta t}$ model (compare Eq. (2.105)), the $\gamma$ model maintains Galilean invariance.

For numerical stability $\lambda_{\theta L}$ is bounded by

$$\lambda_{\theta L} = \min\left(\max\left(\lambda_{\theta L}, -1.0\right), 1.0\right). \tag{2.126}$$

The wall-normal velocity gradient $dV/dy$ can be calculated by

$$\begin{aligned}
\frac{dV}{dy} = & \left(\frac{\partial n_x u}{\partial x} + \frac{\partial n_y v}{\partial x} + \frac{\partial n_z w}{\partial x}\right) n_x \\
& + \left(\frac{\partial n_x u}{\partial y} + \frac{\partial n_y v}{\partial y} + \frac{\partial n_z w}{\partial y}\right) n_y \\
& + \left(\frac{\partial n_x u}{\partial z} + \frac{\partial n_y v}{\partial z} + \frac{\partial n_z w}{\partial z}\right) n_z,
\end{aligned} \tag{2.127}$$

where $n_x, n_y, n_z$ are the components of the wall-normal vector $n_i$.

From this local parameter, a value for the pressure gradient function $F_{PG}$ is calculated from the correlation

$$F_{PG} = \begin{cases} \min\left(1 + C_{PG1}\lambda_{\theta L}, C_{PG1}^{\lim}\right), & \lambda_{\theta L} \geq 0 \\ \min\left(1 + C_{PG2}\lambda_{\theta L} + C_{PG3}\min\left(\lambda_{\theta L} + 0.0681, 0\right), C_{PG2}^{\lim}\right) & \lambda_{\theta L} < 0. \end{cases} \tag{2.128}$$

Even though not necessary for the standard set of parameters, a limiter is applied as

$$F_{PG} = \max\left(F_{PG}, 0\right), \tag{2.129}$$

in order to avoid negative values. Finally, the value for the critical momentum thickness Reynolds number is calculated from the correlation

$$Re_{\theta c} = C_{TU1} + C_{TU2} \exp\left[-C_{TU3} Tu_L F_{PG}\right], \tag{2.130}$$

where $C_{TU1}$, $C_{TU2}$, and $C_{TU3}$ are modeling constants. $C_{TU1}$ and $C_{TU2}$ set the minimal and maximal value of $Re_{\theta c}$ and $C_{TU3}$ controls how fast $Re_{\theta c}$ decreases with increasing turbulence intensities.

Finally, the destruction term is identical to the one of the $\gamma$-$Re_{\theta t}$ model (Eq. (2.95)) and given by

$$E_\gamma = c_{a2} F_{\text{turb}} \rho \Omega \left(c_{e2}\gamma - 1\right)\gamma, \tag{2.131}$$

where the denominator in $F_{\text{turb}}$ was changed from 4 to 2. $F_{\text{turb}}$ ensures that the destruction term is deactivated in the fully turbulent region and is given by

$$F_{\text{turb}} = \exp\left[-\left(\frac{R_T}{2}\right)^4\right]. \tag{2.132}$$

The destruction term again also ensures that the intermittency is zero in a pre-transitional boundary layer and also controls relaminarization.

**Interaction with the turbulence model**

The model was also designed to work with the SST model, but should, according to the authors, work well with every $k$-$\omega$ based turbulence model. The modified transport equation for the turbulence kinetic energy reads

$$\frac{D\rho k}{Dt} = \hat{P}_k + P_k^{\text{lim}} - \hat{D}_k + \frac{\partial}{\partial x_j}\left[\left(\mu + \sigma_k \mu_t\right)\frac{\partial k}{\partial x_j}\right], \tag{2.133}$$

where the production and destruction terms were modified as follows:

$$\hat{P}_k = \gamma \widetilde{P}_k \tag{2.134}$$

$$\hat{D}_k = \max\left(\gamma, 0.1\right)\widetilde{D}_k \tag{2.135}$$

The modification is very similar to the $\gamma$-$Re_{\theta t}$ models with the key difference, that instead of introducing the variable $\gamma_{\text{eff}}$ and allowing $\gamma$ to increase beyond unity to speed up the transition process in regions of separation, an additional source term $P_k^{\text{lim}}$

is introduced. Therefore $\gamma$ has not to be limited to unity in the modified destruction term $\hat{D}_k$. This additional source term was designed to increase the reliability of the transition model for low turbulence intensities and when the transition onset is inside a laminar separation bubble and is given by

$$P_k^{\text{lim}} = 5C_k \max\left(\gamma - 0.2, 0\right)\left(1 - \gamma\right) F_{\text{on}}^{\text{lim}} \max\left(3C_{\text{SEP}}\mu - \mu_t, 0\right) S\Omega. \tag{2.136}$$

The term $\max\left(\gamma - 0.2, 0\right)$ ensures that the additional production term is only active once the transition model triggered, $\left(1 - \gamma\right)$ deactivates the production term once $\gamma$ reached unity, $\max\left(3C_{\text{SEP}}\mu - \mu_t, 0\right)$ ensures deactivation in the fully turbulent regions, where $C_{\text{SEP}}$ is a constant, and allows to control the length of the separation bubble. Finally, $F_{\text{on}}^{\text{lim}}$ triggers the production of turbulence and is given by

$$F_{\text{on}}^{\text{lim}} = \min\left(\max\left(\frac{Re_S}{2.2Re_{\theta C}^{\text{lim}}} - 1, 0\right), 3\right), \tag{2.137}$$

where $Re_{\theta C}^{\text{lim}}$ is a model constant instead of a correlation.

Additionally Menter et. al. [45] suggested that instead of a clip-limiter (Eq. (2.71)) for the production term $P_k$, the Kato-Launder formulation [39] (Eq. (2.72)) should be used.

The blending function $F_1$ of the original SST model has to be modified identically to the $\gamma$-$Re_{\theta t}$ model, in order to ensure that the $k$-$\omega$ model stays active inside the transitional boundary layer (see equations 2.114 and 2.115).

**Model parameters**

For the $\gamma$ model, the complete set of parameters [45] is given by:

$$
\begin{array}{lll}
F_{\text{length}} = 100 & ce_2 = 50 & ca_2 = 0.06 \\
C_{TU1} = 100.0 & C_{TU2} = 1000.0 & C_{TU3} = 1.0 \\
C_{PG1} = 14.68 & C_{PG2} = -7.34 & C_{PG3} = 0.0 \\
C_{PG1}^{\text{lim}} = 1.5 & C_{PG2}^{\text{lim}} = 3.0 & \sigma_\gamma = 1.0 \\
Re_{\theta C}^{\text{lim}} = 1100 & C_k = 1.0 & C_{\text{SEP}} = 1.0
\end{array}
\tag{2.138}
$$

Note that ANSYS Fluent offers a modified set of parameters and equations, which yield identical values for the pressure gradient function $F_{PG}$. Further information can be seen in appendix A.

### 2.4.3. Physics-based transition sensitive $k$-$k_L$-$\omega$ turbulence model

The model was initially developed by Walters and Leylek [46, 47] and later modified by Walters and Cokljat [48]. Unfortunately, the last publication [48] contained typographical errors. Fürst et. al. [49] provided corrections and Lopez and Walters [50] officially corrected the errors later. Bechter [51] implemented the model into the in-house solver LINARS and in the present work it was rewritten in its formulation for a compressible fluid with the expectation of both improving predictions and increasing stability for the usage in high Mach number flows inside thermal turbomachinery. The following equations are given in reference to Fürst et. al. [49].

The model is a $k$-$\omega$ based turbulence model with the addition of a third transport equation for the laminar kinetic energy $k_L$, which is the kinetic energy of the pre-transitional fluctuations. Under low free-stream conditions these low-frequency and low-amplitude pre-transitional fluctuations are essentially the Tollmien-Schlichting (TS) waves. During vortex breakdown or under high free-stream turbulence intensities, streaks in the form of elongated perturbations can be observed and are known as Klebanoff modes. Transition onset is initiated by transferring laminar kinetic energy to turbulent kinetic energy. The model uses, similar to the LCTMs, only local variables to estimate production, destruction and transport of $k$, $k_L$, and $\omega$.

In the case the boundary conditions for $\omega$ are derived from the turbulence length scale $l_{\text{turb}}$, it is important to know that $\omega$ is implicitly defined as $\omega = \varepsilon/k$ for this model and the values for $\omega$ have to be adapted in comparison to the previously presented turbulence models. See appendix B for further informations.

The transport equations for the turbulence kinetic energy and the laminar kinetic energy read

$$\frac{D\rho k}{Dt} = \rho \left[ P_k + R_{\text{NAT}} + R_{\text{BP}} - \omega k - D_T \right] + \frac{\partial}{\partial x_j} \left[ \left( \mu + \rho \frac{\alpha_T}{\sigma_k} \right) \frac{\partial k}{\partial x_j} \right], \qquad (2.139)$$

$$\frac{D\rho k_L}{Dt} = \rho \left[ P_{k_L} - R_{\text{NAT}} - R_{\text{BP}} - D_L \right] + \frac{\partial}{\partial x_j} \left[ \mu \frac{\partial k_L}{\partial x_j} \right], \qquad (2.140)$$

where the production terms for the kinetic energies are defined as

$$P_k = v_{t,s} S S \quad \text{and} \quad P_{k_L} = v_{t,l} S S, \qquad (2.141)$$

where $S$ is the mean value of the strain-rate tensor. $v_{t,s}$ represents the small-scale and $v_{t,l}$ the large-scale eddy viscosity. Usually no additional production limiter is used for this type of model.

The small-scale eddy viscosity is calculated from

$$\nu_{t,s} = f_\nu f_{\text{INT}} C_\mu \sqrt{k_{t,s}} \lambda_{\text{eff}}. \tag{2.142}$$

Recalling Kolmogorov's relations (Eq. (2.48)), equation (2.142) can be understood from a dimensional analysis. From

$$\nu_t \sim \frac{k}{\omega} = \frac{\sqrt{k}\sqrt{k}}{\omega}, \tag{2.143}$$

and

$$l_{\text{turb}} \sim \frac{\sqrt{k}}{\omega} \rightarrow \omega \sim \frac{\sqrt{k}}{l_{\text{turb}}} \tag{2.144}$$

follows that the eddy viscosity scales with the square root of the turbulence kinetic energy and the turbulence length scale as

$$\nu_t \sim \sqrt{k}\, l_{\text{turb}}. \tag{2.145}$$

The model then uses an effective small-scale turbulence kinetic energy $k_{t,s}$ for $k$ and an effective (wall-limited) turbulence length scale $\lambda_{\text{eff}}$ for $l_{\text{turb}}$. $f_\nu$ and $f_{\text{INT}}$ are damping functions which include the viscous wall effect and the influence of intermittency, respectively. The turbulent viscosity coefficient $C_\mu$ for this model is not a constant but rather a function in order to satisfy the realizability constraint [48].

The large-scale eddy viscosity $\nu_{t,l}$ is the sum of contributions from Klebanoff modes and self-exited modes from TS waves and calculated by

$$\nu_{t,l} = \min\left( \beta_{\text{TS}} C_{l2} Re_\nu d_w^2 \Omega + f_{\tau,l} C_{l1} \left( \frac{\Omega \lambda_{\text{eff}}^2}{\nu} \right) \sqrt{k_{t,l}} \lambda_{\text{eff}}, \frac{k_L + k_{t,l}}{2S} \right), \tag{2.146}$$

where $\beta_{\text{TS}}$ is the Tolmien-Schlichting threshold function, $Re_\nu$ is the vorticity Reynolds number (Eq. (2.79)) and $C_{l2}$ is an empirical model constant. The Klebanoff contribution in Eq. (2.146) again uses the relation from Eq. (2.142), where for the turbulence kinetic energy an effective large-scale turbulence kinetic energy $k_{t,l}$ is used and $l_{\text{turb}}$ is substituted with $\lambda_{\text{eff}}$. The term inside the brackets reads similar to the vorticity Reynolds number, where instead of the wall distance the wall-limited turbulence length scale is used. $f_{\tau,l}$ is a damping function for the turbulent time scale and $C_{l1}$ is a model constant. Finally, the large-scale eddy viscosity is limited in order to satisfy the realizability constraint for the total Reynolds stress contribution [48].

The eddy viscosity in Boussinesq's assumption (Eq. 2.47) for closing the RANS equations is defined as the sum of the small-scale and large-scale eddy viscosities

$$\nu_t = \nu_{t,s} + \nu_{t,l}. \tag{2.147}$$

The terms $R_{\text{NAT}}$ and $R_{BP}$ account for a redistribution of kinetic energy from laminar to turbulence kinetic energy, where transition onset is controlled by threshold functions, for the natural transition process (NAT) and for bypass transition (BP), respectively. $D_T$ and $D_L$ are anisotropic (near-wall) dissipation terms. The destruction term for $k$ is similar to other $k$-$\omega$ models. Transport by diffusion is accounted for with a gradient-diffusion term, but instead of the eddy viscosity an effective turbulence diffusivity $\alpha_t$ is introduced, which is related to the molecular diffusion by the Prandtl-Schmidt numbers $\sigma_k$ and $\sigma_\omega$. Note that for the diffusion of the laminar kinetic energy, naturally no turbulent contribution is added.

Finally, the transport equation of $\omega$ is given by

$$\frac{D\rho\omega}{Dt} = \rho \left[ P_\omega + \left( \frac{C_{\omega R}}{f_W} - 1 \right) \frac{\omega}{k} \left( R_{\text{NAT}} + R_{\text{BP}} \right) - C_{\omega 2}\omega^2 f_W^2 \right.$$
$$\left. + C_{\omega 3} f_\omega \alpha_t f_W^2 \frac{\sqrt{k}}{d_w^3} \right] + \frac{\partial}{\partial x_j} \left[ \left( \mu + \rho \frac{\alpha_t}{\sigma_\omega} \right) \frac{\partial \omega}{\partial x_j} \right], \quad (2.148)$$

where several additional source terms are present and the transport due to diffusion is similarly calculated as in the transport equation for the turbulence kinetic energy (Eq. (2.139)). $P_\omega$ is defined similar to other $k$-$\omega$ models as

$$P_\omega = C_{\omega 1} \frac{\omega}{k} P_k, \quad (2.149)$$

where the constant $C_{\omega 1}$ relates the production of $\omega$ to the production of $k$ and $\omega/k$ is present for dimensionality reasons. The second term on the RHS is present to reduce the turbulence length scale during transition [48]. The third term is the typical $\omega$ destruction term, but accompanied by a wall-near damping function $f_W$. Finally, the fourth source term is intended to improve the behavior in the boundary layer wake region.

### 2.4.4. Physics-based transition sensitive $k$-$\overline{v^2}$-$\omega$ turbulence model

The model is a modification of the $k$-$k_L$-$\omega$ model made by the same working group and was published by Lopez and Walters [52]. Instead of decomposing the kinetic energy of the fluctuations into a turbulence and a laminar contribution, wall normal velocity fluctuations, represented by the transported variable $\overline{v^2}$, are used to predict transition onset. The laminar kinetic energy $k_L$ is related to the new variable by

$$k_L \approx k - \overline{v^2}. \quad (2.150)$$

According to Lopez and Walters [52], the growth of $k_L$ has been shown to correlate with low-frequency normal fluctuations of the free-stream turbulence. Therefore, most of the equations read similar to the $k$-$k_L$-$\omega$ model, where the model constants were recalibrated using a zero-pressure-gradient flat plate test case. The model is a transition sensitive $k$-$\omega$ based turbulence model and consists of three transport equations, which reduces to a two-equation $k$-$\omega$ turbulence model in fully turbulent regions. Note that for this model the specific dissipation rate $\omega$ is also implicitly defined as $\omega = \varepsilon / k$, which has to be accounted for when calculating $\omega$ boundary conditions from the turbulence length scale (see appendix B).

The transport equation for the turbulence kinetic energy is given by

$$\frac{D\rho k}{Dt} = \rho \left[ P_k - \min(\omega k, \omega \overline{v^2}) - D_k \right] + \frac{\partial}{\partial x_j} \left[ \left( \mu + \rho \frac{\alpha_t}{\sigma_k} \right) \frac{\partial k}{\partial x_j} \right]. \tag{2.151}$$

Instead of redistributing energy via the terms $R_{\mathrm{BP}}$ and $R_{\mathrm{NAT}}$, production of turbulence kinetic energy is solely governed by the wall-normal velocity fluctuations $\overline{v^2}$ via the production term for the turbulence kinetic energy

$$P_k = \nu_t SS, \tag{2.152}$$

where $\nu_t$ is the sum of the large-scale and the small-scale eddy viscosities

$$\nu_t = \nu_{t,s} + \nu_{t,l}. \tag{2.153}$$

The small-scale eddy viscosity $\nu_{t,s}$ is calculated similarly to the $k$-$k_L$-$\omega$ model from the dimensional deliberation, that the eddy viscosity scales with the square root of the turbulence kinetic energy and the turbulence length scale (see Eq. (2.145)) as

$$\nu_{t,s} = f_\nu f_{\mathrm{INT}} C_\mu \sqrt{\overline{v^2}} \lambda_{\mathrm{eff}}, \tag{2.154}$$

where instead of the turbulence kinetic energy the effective small-scale turbulence $\overline{v_s^2}$ given by

$$\overline{v_s^2} = f_{SS} f_W \overline{v^2} \tag{2.155}$$

is used. And the turbulence length scale $l_{\mathrm{turb}}$ is substituted by an effective (wall-limited) turbulence length scale $\lambda_{\mathrm{eff}}$. $f_{SS}$ is the shear-sheltering factor, suppressing the fluctuations $\overline{v^2}$ in the pre-transitional region and $f_W$ the near-wall non-viscous damping function. $f_\nu$ and $f_{\mathrm{INT}}$ are damping functions which include the viscous wall effect and the influence of intermittency, respectively.

The large-scale eddy viscosity $\nu_{t,l}$ is the sum of contributions from Klebanoff modes and self-exited modes from TS waves and calculated by

$$\nu_{t,l} = \min \left( \beta_{\mathrm{TS}} C_{l2} \left( \frac{\Omega d_{\mathrm{eff}}^2}{\nu} \right) d_{\mathrm{eff}}^2 \Omega, + f_{\tau,l} C_{l1} \left( \frac{\Omega \lambda_{\mathrm{eff}}^2}{\nu} \right) \sqrt{\overline{v_l^2}} \lambda_{\mathrm{eff}}, \frac{k - \overline{v_s^2}}{2S} \right), \tag{2.156}$$

which again reads very similar to the $k$-$k_L$-$\omega$ model (compare Eq. (2.146)). The main difference is the usage of an effective (limited) wall distance $d_{\text{eff}}$ instead of the wall distance $d_w$ which inhibits the unphysical production of natural pretransitional modes far away from the wall in fully turbulent regions. $\overline{v_l^2}$ represents the energy contained in the large-scale turbulent motions. All other constants remain the same. Finally, the large-scale eddy viscosity is again limited in order to satisfy the realizability constraint for the total Reynolds stress contribution [48].

The transport equation for the wall normal velocity fluctuations is given by

$$\frac{D\rho\overline{v^2}}{Dt} = \rho\left[P_{\overline{v^2}} + R_{\text{NAT}} + R_{\text{BP}} - \omega\overline{v^2} - D_{\overline{v^2}}\right] + \frac{\partial}{\partial x_j}\left[\left(\mu + \rho\frac{\alpha_t}{\sigma_k}\right)\frac{\partial\overline{v^2}}{\partial x_j}\right], \qquad (2.157)$$

with the production term

$$P_{\overline{v^2}} = \nu_{t,s}SS, \qquad (2.158)$$

where the small-scale eddy-viscosity $\nu_{T,s}$ is defined in equation (2.154). Production is initiated, when either $R_{\text{NAT}}$ or $R_{\text{BP}}$ exceeds a non-negligible value, which represent threshold functions for natural (NAT) and bypass (BP) transition. In the fully turbulent regions, these terms are zero again. $D_k$ and $D_{\overline{v^2}}$ are anisotropic (near-wall) dissipation terms and the destruction terms for both $k$ and $\overline{v^2}$ are similar to other $k$-$\omega$ based turbulence models.

Finally, the transport equation for $\omega$ reads

$$\frac{D\rho\omega}{Dt} = \rho\left[P_\omega + \left(\frac{C_{\omega R}}{f_W} - 1\right)\frac{\omega}{\overline{v^2}}\left(R_{\text{NAT}} + R_{\text{BP}}\right) - C_{\omega 2}\omega^2 f_W^2\right.$$

$$\left. + (1 - F_1^*)\,CD_{k\omega} + \frac{\partial}{\partial x_j}\left[\left(\mu + \rho\frac{\alpha_T}{\sigma_\omega}\right)\frac{\partial\omega}{\partial x_j}\right]\right], \quad (2.159)$$

which is very similar to the $k$-$k_L$-$\omega$ model. The main difference is that the term responsible for improving the predictions inside the wake-region of the boundary layer (fourth term on the RHS of Eq. (2.148)) was replaced with a $k$-$\omega$ cross-diffusion term, similar to the SST model as

$$CD_{k\omega} = \max\left(2\rho\sigma_{\omega 2}\frac{1}{\omega}\frac{\partial k}{\partial x_i}\frac{\partial\omega}{\partial x_i}, 10^{-10}\right). \qquad (2.160)$$

The modified blending function $F_1^*$ is given by

$$F_1^* = 1 - \left[(1 - F_1)\,f_{SS}\right], \qquad (2.161)$$

where the shear sheltering factor $f_{SS}$ deactivates the cross-diffusion term in the pre-transitional regions and the blending function $F_1$ is adopted from the SST turbulence model (compare Eq. (2.69)) as

$$F_1 = \tanh\left\{\min\left[\max\left(\frac{\sqrt{\overline{v^2}}}{\omega d_w}, \frac{500\nu\beta^*}{d_w^2\omega}\right), \frac{4\sigma_{\omega 2}k}{CD_{k\omega}\,d_w^2}\right]^4\right\},\qquad(2.162)$$

which is designed to be unity inside the laminar sublayer and the logarithmic region of the boundary layer and continuously switches to zero inside the wake region, ensuring that the cross-diffusion term $CD_{k\omega}$ is only active in the free-shear stream and the wake region of the boundary layer.

The difference of the definition of $\omega$ between the SST model and the $k$-$\overline{v^2}$-$\omega$ model was accounted for by substituting $\omega$ with $\omega/\beta^*$ in the first and second term inside the brackets of Eq. (2.162). Inserting the first term of Eq. (2.160) into the third term of the blending function $F_1$ yields

$$\frac{2k\omega}{\rho d_w^2}\left[\frac{\partial k}{\partial x_i}\frac{\partial \omega}{\partial x_i}\right]^{-1},\qquad(2.163)$$

therefore it is not quite clear why the modification of $\omega$ was skipped for this term and why the density was dropped from the numerator of third term of the blending function $F_1$, compared to the formulation of the SST model (Eq. (2.69)). Therefore the density does not cancel in Eq. (2.163). Note that the value of the modeling constant $\sigma_{\omega 2}$ differs from the SST model (SST: $\sigma_{\omega 2} = 0.856$, $k$-$k_L$-$\omega$: $\sigma_{\omega 2} = 1.856$) and might implicitly account for the difference in $\omega$. However, the missing density in the numerator of the third term of Eq. (2.162) is most likely a typographical error.

The production term for $\omega$ is defined similar to other $k$-$\omega$ models as

$$P_\omega = C_{\omega 1}\frac{\omega}{\overline{v^2}}P_k,\qquad(2.164)$$

where the constant $C_{\omega 1}$ relates the production of $\omega$ to the production of $k$ and $\omega/\overline{v^2}$ is present for dimensionality reasons. The second term on the RHS of the $\omega$ transport equation is present in order to reduce the turbulence length scale during transition [48] and finally, the third term is the typical $\omega$ destruction term, but accompanied by a wall-near damping function $f_W$.

Transport by diffusion is modeled in all transport equations of the $k$-$\overline{v^2}$-$\omega$ model by gradient-diffusion terms, where the effective turbulent diffusivity $\alpha_T$ is related to the molecular diffusion by the Prandtl-Schmidt numbers $\sigma_k$ and $\sigma_\omega$.

In fully turbulent regions the model yields $k = \overline{v^2}$ and the threshold functions $R_{\mathrm{BP}}$ and $R_{\mathrm{NAT}}$ are zero again. Therefore, the transport equations for $k$ and $\overline{v^2}$ are formally identical for fully turbulent regions, thus reducing the turbulence model to a two-equation $k$-$\omega$ turbulence model given by:

$$\frac{D\rho k}{Dt} = \rho\left[P_k - \omega k - D_k\right] + \frac{\partial}{\partial x_j}\left[\left(\mu + \rho\frac{\alpha_t}{\sigma_k}\right)\frac{\partial k}{\partial x_j}\right] \tag{2.165}$$

$$\frac{D\rho\omega}{Dt} = \rho\left[C_{\omega1}\frac{\omega}{k}P_k - C_{\omega2}\omega^2 f_W^2\right] + (1 - F_1^*)\,CD_{k\omega} + \frac{\partial}{\partial x_j}\left[\left(\mu + \rho\frac{\alpha_T}{\sigma_\omega}\right)\frac{\partial\omega}{\partial x_j}\right] \tag{2.166}$$

Finally, note that the shear sheltering factor $f_{SS}$ given by

$$f_{SS} = \exp\left[-\left(\frac{C_{SS}\nu\Omega}{\overline{v^2}}\right)^2\right] \tag{2.167}$$

uses a different scaling compared to the $k$-$k_L$-$\omega$ model (Eq. (2.83)).

## 2.4.5. Boundary conditions

Finally, this section summarizes the boundary conditions used for the turbulence and transition models in the present work. According to the original publications of the used models [34, 43, 45, 48, 52], the boundary conditions at the inlet and for walls have to be specified.

At the inlet usually, constant values for $k$ and $\omega$ are set, where the value for $k$ is typically calculated from the turbulence intensity at the inlet $Tu_{\mathrm{in}}$ and $\omega$ is either chosen to fit available free-stream informations or has to be estimated otherwise. See appendix B for further information. For the laminar kinetic energy zero is chosen for the inlet and from the relation $\overline{v^2} \approx k - k_L$ follows $\overline{v^2} = k$ at the inlet. The value of $Re_{\theta t}$ at the inlet is calculated from the correlation given by Eq. (2.102) and the intermittency $\gamma$ is set to unity, implying fully turbulent flow at the inlet.

At solid boundaries, the no-slip condition readily yields that $k$, $k_L$ and $\overline{v^2}$ are zero. For $\omega$, $\gamma$ and $Re_{\theta t}$ the zero normal gradient condition is used at a solid boundary, which is given by

$$\frac{\partial\omega}{\partial n} = 0, \qquad \frac{\partial\gamma}{\partial n} = 0, \qquad \frac{\partial Re_{\theta t}}{\partial n} = 0, \tag{2.168}$$

where $n$ is the wall-normal coordinate.

# 3. Numerical solutions

Computational Fluid Dynamics (CFD) can be divided into three primary fields. First, physical models, which describe fluid flow and its phenomena, need to be formulated in a mathematical form. Next, the computational domain has to be discretized into cells, where the values of the conserved quantities are calculated. Finally, algorithms are required for solving the governing equations on the discretized domain. Figure 3.1 depicts these fundamental fields of CFD. Furthermore, the obtained solutions are usually post–processed and presented in a comprehensible form, for example, tables of characteristic values, diagrams or contour plots.
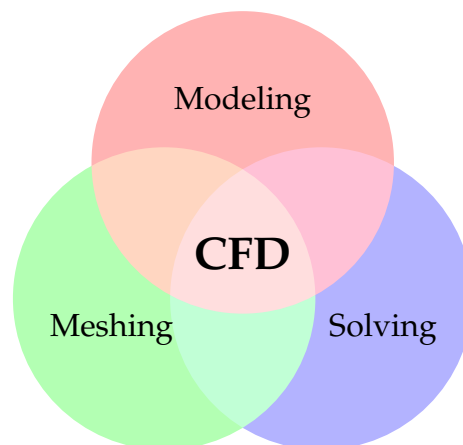


Figure 3.1.: Primary fields of Computational Fluid Dynamics (CFD).

## 3.1. Models

Chapter 2 presented the used models and their corresponding equations for the present work. These were the compressible Reynolds- and Favre-averaged Navier-Stokes equations in conservative formulation, together with equations of state for the considered fluid, turbulence and transition models. Many more models exist for various physical phenomena. For example, heat transport by radiation, chemical kinetics, or multi-phase models are highly relevant for many industrial processes.

From a practical standpoint, it is beneficial if a model can be expressed either in algebraic form or in the form of transport equations, which ideally only depend on local variables. This allows to implement them into already established solvers, where validated accurate numerical schemes are readily available. Furthermore, parallelization of the solving can be implemented efficiently and straightforward.

## 3.2. Meshing

In the present work, all computational meshes were generated by the meshing software AiGrid3D [53]. The meshes are curvilinear and structured. For the cells quads are used, which are known for their superior numerical qualities. The mesh is generated by first defining the blade contour and the domain boundaries. Within these boundaries, blocks are specified. For the region around complex geometries, e.g. blades, usually O-type meshes are used. For regions near the inlet and outlet, H-type meshes are common. Figure 3.2a shows exemplary a Quasi-3D computational mesh for a transonic guide vane, where the inlet blocks (green) are H-type, the region around the blade (gray) is O-type and the outlet region (blue) is again an H-type mesh. Figure 3.2b shows a close-up of the region near the trailing edge of the blade.



(a) complete computational domain          (b) close-up of the trailing edge of the blade
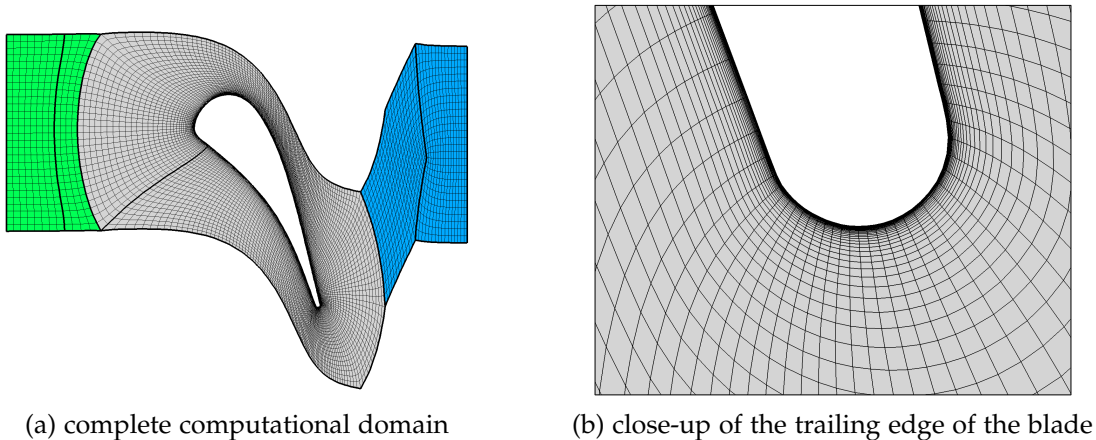
Figure 3.2.: Example for a Quasi-3D computational mesh for a transonic guide vane, where (a) shows the different block-types for inlet (green), outlet (blue) and wall-near regions (gray) and (b) shows a close-up of the region near the trailing edge of the blade.

For the domain boundaries and contours Bézier curves are used (see for example Yagdi [54]). Turbulence and transition models demand special care for the wall-near regions. An important measure is the dimensionless wall distance $y^+$ (eq. 1.5), which is required to be $y^+ \leq 1$ for most models, but also the growth factor of the

neighboring cells can have a big influence on the quality on the predictions. AiGrid3D controls the distribution of the mesh nodes by hyperbolic tangent functions, which can optionally be extended by linear regions at the start, middle and end. The middle section is defined as the location with the highest gradient. Figure 3.3 presents the steps for constructing a hyperbolic tangent density function. First, parametrically defined parts, of a hyperbolic tangent (tanh) function are extracted. For this example the interval $-1.6 \leq x \leq 2.0$ was considered. Next, the abscissa is normalized (Fig. 3.3b) and optional linear sections (red) are inserted at the beginning, middle, and end. Figure 3.3c shows the final hyperbolic density function, where in a final step both axes were normalized. The corresponding derivative $dy/dx$ is plotted in Figure 3.3d, where the optional linear sections are depicted in red. AiGrid3D allows to specify the length of each of these optional linear sections parametrically.

(a) $-1.6 \leq x \leq 2$

(b) normalizing of abscissa

(c) inserting linear sections, normalizing both axes

(d) derivative $dy/dx$
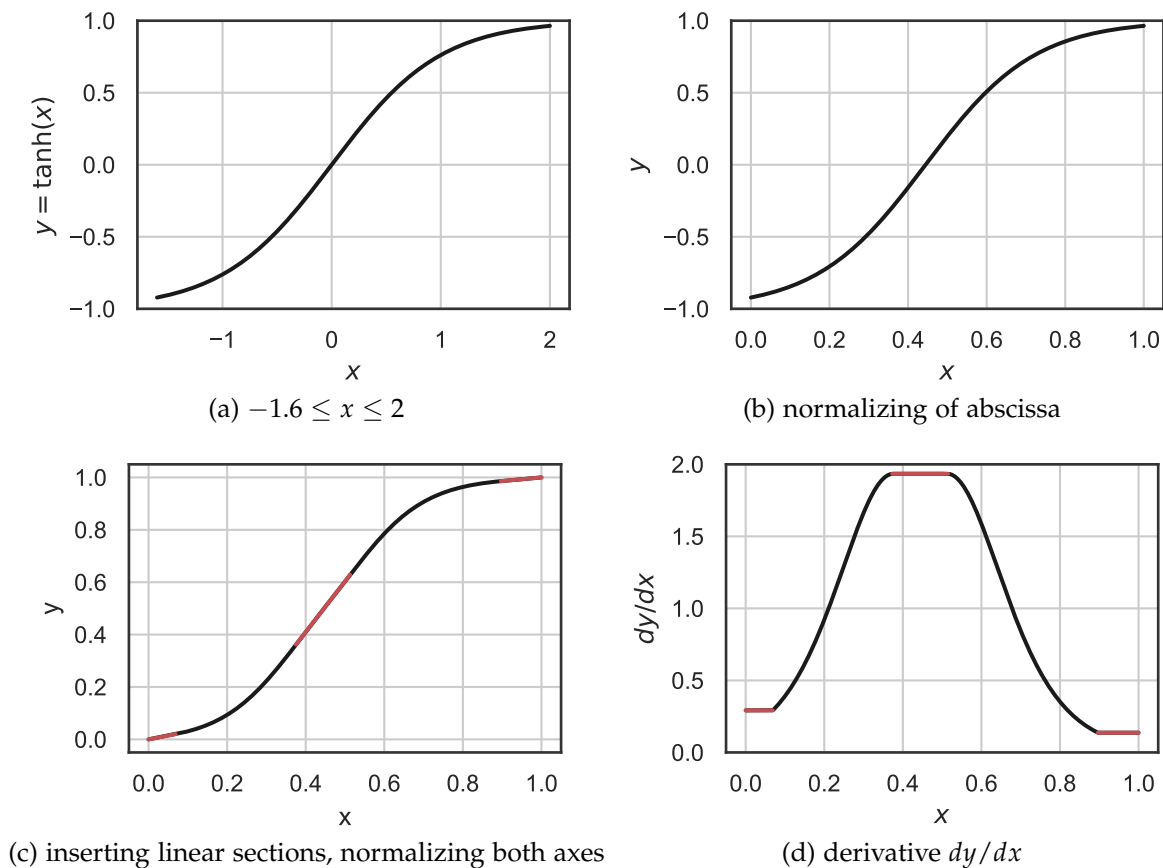
Figure 3.3.: Step by step construction of a hyperbolic tangent density function with optional linear elements (red) in the start, end and middle section as used by AiGrid3D. Reproduced from [53].

Figure 3.4 shows the hyperbolic tangent density function applied to a quadratic Bézier curve, with the control points $A = (0,0)$, $B = (0,1)$, and $C = (0.5, 0.4)$.
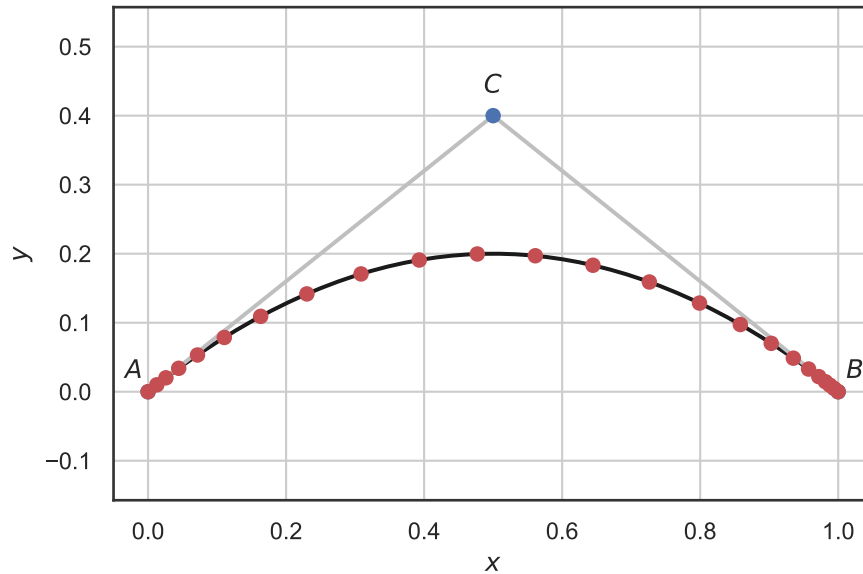
Figure 3.4.: Quadratic Bézier curve (black), defined by three control points (*A*, *B*, *C*), where the red points are positioned by using the hyperbolic tangent density function from Figure 3.3. Reproduced from [53].

Quasi-3D meshes consist of a single layer of cells, which can optionally vary in height. In order to create a fully three-dimensional mesh, several of these layers are defined in a similar way and subsequently connected linearly. Within the software, the mesh is defined by a series of instructions with a syntax similar to the programming language C++. The computational meshes are carefully designed in such a way that the individual blocks fit well together without discontinuities. Special care has to go into the periodicity of the mesh, since usually only one passage is simulated in order to reduce the computational cost, and the flow is assumed to be perfectly periodic. For parallelization of the simulations several blocks are defined, which are solved separately for each time-step. Finally, the mesh is smoothened by a relaxation method based on Laplace equations. Further information and validation of AiGrid3D can be seen in the Master's thesis of Yagdi [54].

## 3.3. Solvers

In this thesis, simulations for all test cases were carried out with the in-house solver LINARS [55], which has been developed at the Institute of Thermal Turbomachinery and Machine Dynamics (ITTM) since 2005 (Pecnik et. al. [56]) and continuously

improved and extended ever since. It is written in C++ and follows an object-oriented programming paradigm, which allows straightforward implementation of new turbulence and transition models. The computation is parallelized by using a block-mesh approach and allows to utilize either local resources (Open Multi-Processing (openMP)) or high-performance computing clusters (Message Passing Interface (MPI)), where it is possible to use a large number of processors spanning several computational nodes.

LINARS features fully implicit time-iterative solution of the conservative form of the compressible Reynolds- and Favre-averaged Navier–Stokes (RANS) equations by using the Finite Volume Method (FVM). The inviscid flux is discretized with the upwind flux-difference splitting method of Roe, where second-order accuracy is achieved by using a total variation diminishing (TVD) based reconstruction. The viscid flux vector is described by a second-order accurate central-differencing scheme. For interpolating the values of the cells onto the cell faces, a third-order Monotone Upstream-Centered Schemes for Conservation Laws (MUSCL) interpolation is used. The implicit solutions are obtained with a line Gauss-Seidel method, where the main flow equations and the turbulence- and transition equations are solved sequentially. The current version also supports LES, together with Weighted Essentially Non-Oscillatory (WENO) methods for the computation of the cell-fluxes (see for example Bertolini et. al. [57]).

Cross-validation of the $\gamma$ and $k$-$k_L$-$\omega$ model was carried out with the commercial software ANSYS-Fluent [58, 59] and ANSYS-CFX [60, 61], where the solvers were configured as similar to LINARS as possible.

An in-depth explanation of the discretization and solving methods would go beyond the scope of the present work. For further information, the lecture-notes of Sanz [62] and the textbook of Versteeg and Malalasekera [20] are highly recommended.

## 3.4. Post-Processing

The predictions for the flow field are exported into several binary- and text-files. Post-processing was mainly done with the open source software Python [63] and the aid of the core packages Numpy, Matplotlib, Pandas from the SciPy ecosystem [64] with the addition of the Seaborn package [65]. The Anaconda Software Distribution [66] provides Python together with many useful packages in order to offer a comparable capability to other popular engineering scripting environments. For the generation of curvilinear contour plots in proximity to the wall (e.g. Fig. 4.28) a Python script was developed. Other contour plots of the flow field, representations of the computational meshes and three dimensional figures were created with the software Tecplot [67].

# 4. Computational results and discussion

For the evaluation of models a broad range of test cases was selected. They consist of three different Quasi-3D test cases, namely the common flat plate test case without pressure gradient (T3A, section 4.1), a turbine blade cascade (VKI, section 4.2) and a transonic guide vane cascade (MUR, section 4.3). Quasi-3D means that the computational mesh only extends for one cell into the $z-$direction. Additionally a fully three-dimensional test case of a two-stage two-spool counter-rotating turbine configuration was selected, where the present work focused on the flow around the high pressure stator (HPS) (section 4.4). For all test cases the stationary solutions of the flow field were computed.

All test cases were simulated with the in-house CFD solver LINARS. For the T3A and the VKI test cases, additionally the commercially available codes CFX [60, 61] and Fluent [58, 59] in their respective versions 19.1 were used for cross-validation.

All employed computational meshes were used in previous numerical investigations and provided by the working-group Turbomachinery Optimization and CFD Methods at the ITTM, Graz University of Technology. The meshes were generated by the meshing software AiGrid3D [53]. Because the T3A mesh was not available for the latest version of the meshing software it was re-built in such a way that it is identical to the previously used mesh, but with the additional option of refinement (see sections 4.1.1 and 4.1.3).

Because the compressible implementation of the $k$-$k_L$-$\omega$ model yields very similar results to the incompressible formulation, implemented into LINARS by Bechter [51], the results of the incompressible formulation are omitted in the present work.

## 4.1. T3A – Flat plate without pressure gradient

In order to validate the implementations of the $\gamma$, the $k$-$k_L$-$\omega$ and the $k$-$\overline{v^2}$-$\omega$ model in the in-house solver LINARS and to investigate basic properties of the models, the simple test case of a flat plate without pressure gradient was selected. Experimental data, using hot-wire anemometry, obtained by Coupland [68] was made available by the European Research Community on Flow, Turbulence and Combustion (ERCOFTAC) special interests group on transition [69].

### 4.1.1. Computational domain
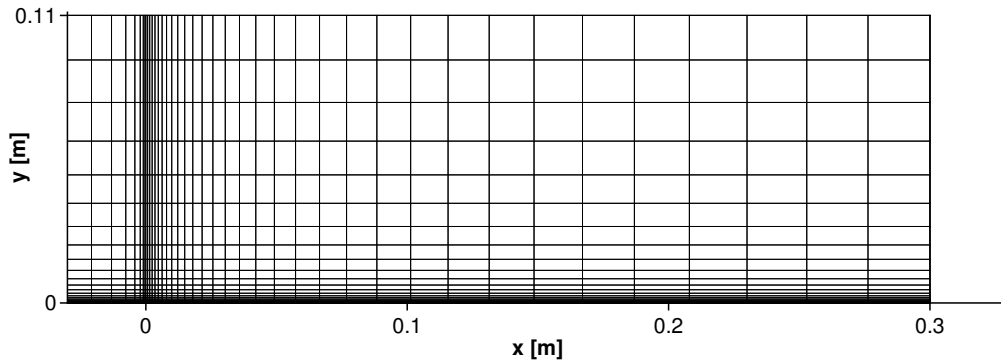


Figure 4.1.: Computational mesh for the T3A test case, showing every other grid point for the coarsest mesh (index factor 2).

Preliminary tests revealed a sensitivity of the newly implemented models regarding the mesh-resolution. Therefore four gradually refined meshes were created (see table 4.1), where the overall dimensions and characteristics of the mesh were preserved. Figure 4.1 shows the computational mesh, where every other grid line is drawn for the coarsest mesh variant. The inlet is positioned at $x = -0.03$m and the plate extends for additional 0.3m. The upper boundary into the wall-normal direction is positioned at $y = 0.11$m. In proximity to the wall, which is located at $y = 0$m, the mesh resolution was increased in order to properly resolve the boundary layer. The mesh is also denser at the beginning of the wall ($x = 0$m). The mesh is Quasi-3D, with one cell into the $z$-direction, where the thickness is kept constant at 0.012m.

### 4.1.2. Boundary conditions and fluid properties

Compared to the experimental configuration, the plate was shortened to a length of $L = 0.3$m and the free-stream velocity was increased to a Mach Number of $Ma \approx 0.3$.

| index factor | i-max | j-max | k-max | cells |
|---|---|---|---|---|
| 2 | 80 | 64 | 1 | 5120 |
| 4 | 160 | 128 | 1 | 20480 |
| 6 | 240 | 192 | 1 | 46080 |
| 8 | 320 | 256 | 1 | 81920 |

Table 4.1.: Total number of cells for the gradually refined meshes of the T3A test case, where i-max, j-max and k-max are the number of grid cells into the $x$-, $y$- and $z$-direction.

| | | |
|---|---|---|
| $p_{\text{tot,in}}$ | 1.01634E5 | Pa |
| $T_{\text{tot,in}}$ | 293.15 | K |
| $\beta_{\text{in}}$ | 0 | ° |
| $Tu_{\text{in}}$ | 5.4 | % |
| $l_{\text{turb,in}}$ | 0.205 | mm |
| $p_{\text{stat,out}}$ | 0.953E5 | Pa |

Table 4.2.: T3A Boundary Conditions

| | | |
|---|---|---|
| $R$ | 287 | J/kg K |
| $\gamma_c$ | 1.4 | – |
| $Pr$ | 0.72 | – |
| $\mu$ | 6.74299E-5 | Pa s |
| $c_p$ | 1004.5 | J/kg K |
| $\lambda$ | 0.0940741 | W/m K |
| $M_R$ | 28.97 | kg/kmol |

Table 4.3.: T3A Fluid Properties

This was done in order to improve the convergence speed and therefore reduce the computational cost. To allow comparisons to the measurements [68], the viscosity of the fluid was determined by enforcing Reynolds similarity. For the fluid air as an ideal gas with constant fluid properties was selected. The total pressure and the total temperature at the inlet and the static pressure at the outlet were calculated accordingly. The inlet velocity vector is normal to the inlet boundary, resulting in an inlet flow angle of $\beta_{\text{in}} = 0$. The wall boundary conditions were chosen for a smooth and adiabatic wall. At the lower domain boundary, in front of the plate, and at the upper domain boundary, symmetric flow is enforced. The free-stream turbulence intensity $Tu$ at the inlet was chosen in such a way, that it matches the measurements at the beginning of the plate. The turbulence length scale was selected such that the decay of $Tu$ along the flat plate matches the measurement. Figure 4.2 shows a variation of the turbulence length scale $l_{\text{turb}}$ and its influence on the decay of the free stream turbulence intensity. $l_{\text{turb}}$ was arbitrarily varied by approximately ±67%. The decay of $Tu$ was verified for every solver and every transition model. Figure 4.3 exemplary shows the decay of $Tu$ along the upper domain boundary, compared to the measurement [68] for the SST turbulence model as obtained by the solvers LINARS, CFX and Fluent. Due to the different definition of the turbulence length scale $l_{\text{turb}}$ between LINARS, CFX and FLUENT, a factor has to be applied to the turbulence length scale $l_{\text{turb}}$ in order to achieve similar results as obtained by the solver LINARS (see Appendix B). Table 4.2 and Table 4.3 summarize the used boundary conditions

and the fluid properties for the T3A test case, respectively.

### 4.1.3. Mesh dependency

Preliminary tests revealed that predictions obtained with different solvers yield considerably large differences between the solvers for the $\gamma$ and the $k$-$k_L$-$\omega$ model, compared to the $\gamma$-$Re_{\theta t}$ model (see also sec. 4.1.4). In private communications with the ANSYS Support Firm CADFEM, the primary model developer Menter confirmed that the $\gamma$ model is overall more sensitive to numerical disparities. In other words, the mesh-quality and the used discretization methods for the governing equations, probably cause the observed differences between the solvers in the predictions using the $\gamma$ transition model.

Regarding the mesh sensitivity, simulations for gradually refined meshes were carried out with the in-house solver LINARS. Figure 4.4 shows predictions for the local skin friction coefficient $c_f$ along the flat plate for these meshes together with an analytical solution for the fully laminar flow given by Blasius as

$$c_{f,\text{lam}} = 0.664 \, Re_x^{-1/2} \tag{4.1}$$

and an empirical solution for the fully turbulent flow, according to Schlichting [10], as

$$c_{f,\text{turb}} = 0.0592 \, Re_x^{-1/5}, \tag{4.2}$$

respectively. The local Reynolds number $Re_x$ is given by

$$Re_x = \frac{x U_\infty}{\nu}, \tag{4.3}$$

where $x$ is the coordinate along the wall, starting from the beginning of the plate and $U_\infty$ is the local free-stream velocity magnitude. The local skin friction coefficient is computed from

$$c_f = \frac{\tau_w}{0.5 \rho U_\infty^2}, \tag{4.4}$$

where $\tau_w$ is the wall shear stress magnitude. In Figure 4.4 it can be seen that the $\gamma$-$Re_{\theta t}$ model shows the best behavior among the investigated models, where almost no difference between the different meshes can be discerned. The $\gamma$ model shows not only a further upstream transition onset, but also the distribution of the local $c_f$ value in the transitional area is different for the coarsest mesh. It lacks the characteristic steep gradient, followed by a brief bend at the transition onset. Both, the $k$-$k_L$-$\omega$ and $k$-$\overline{v^2}$-$\omega$ model show a more upstream transition onset for the coarsest mesh but retain the overall shape inside the transitional region and predict a consistent transition length.
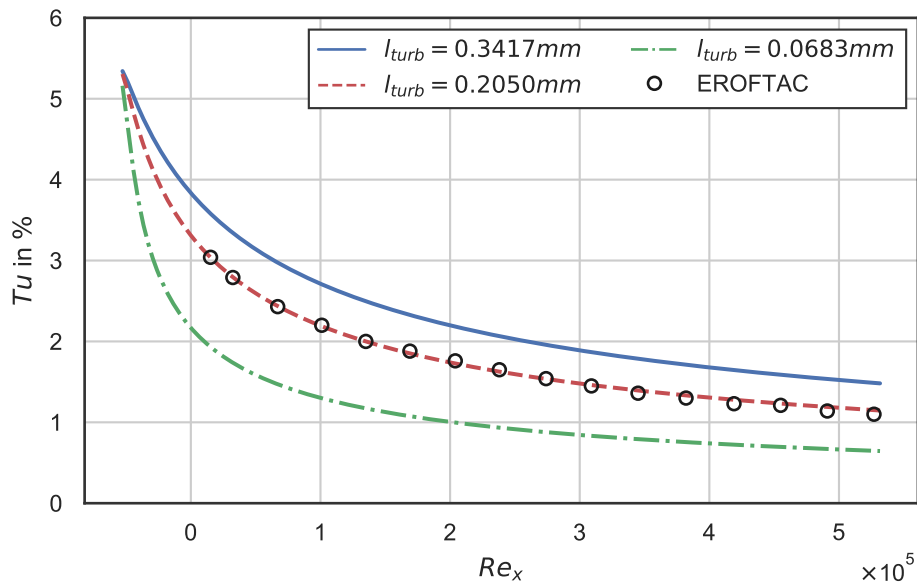
Figure 4.2.: Predictions for the free-stream turbulence intensity $Tu$ along the flat plate obtained from the solver LINARS for a variation of the turbulence length scale $l_{\text{turb}}$ versus the ERCOFTAC experiment for the SST turbulence model.
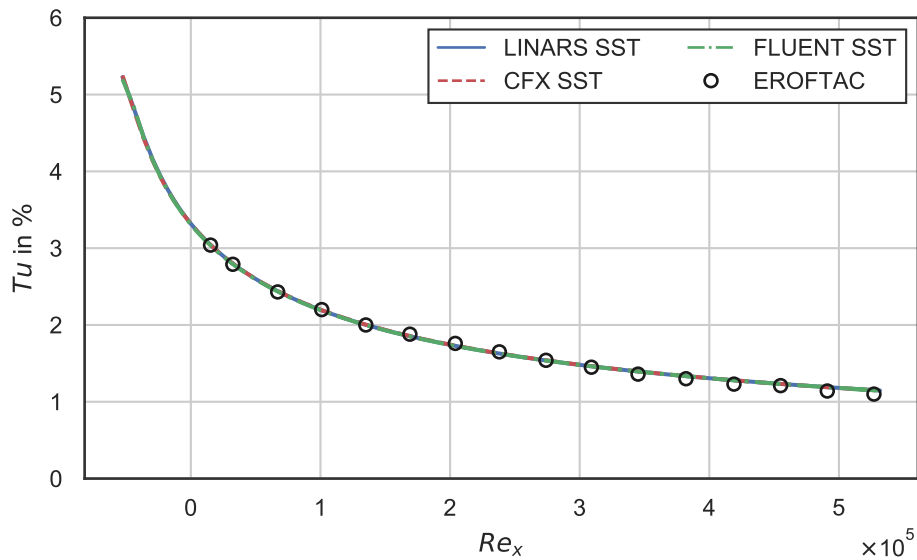


Figure 4.3.: Predictions for the free-stream turbulence intensity $Tu$ along the flat plate obtained from the solvers LINARS, CFX and Fluent versus the ERCOFTAC experiment for the SST turbulence model.

Figure 4.4.: Predictions for the local skin friction coefficient $c_f$ along the flat plate obtained from the solver LINARS for gradually refined meshes, showing the dependency on the grid-size of all investigated transition models.
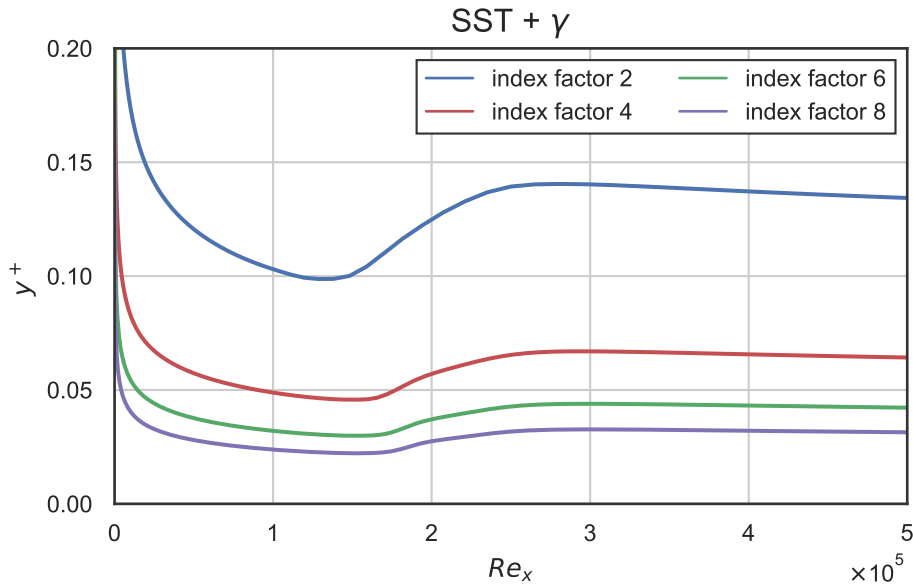
Figure 4.5.: Dimensionless wall distance $y^+$ for the first grid cell, along the flat plate obtained from the in-house solver LINARS with the $\gamma$ model for gradually refined meshes.

From this investigation follows that for the T3A test case at least the first mesh-refinement stage should be used (index factor 4). This result is surprising since the dimensionless wall-distance $y^+$ for the first cell next to the wall is already below $y^+ < 0.2$, where a value of $y^+ \leq 1$ is typically suitable for a mesh used with transition models. Figure 4.5 shows the dimensionless wall distance $y^+$ for the first cell along the flat plate for the various meshes for the $\gamma$ model, as obtained by the solver LINARS. The original publication of the model [45] showed a strong dependency on the mesh expansion factor into wall-normal direction, which could also be further investigated. Because the mesh with index-factor 2 produces a satisfying prediction it was omitted.

## 4.1.4. Implementation validation

As a first step for validating the new implementations and changes in the in-house solver LINARS the predictions for the local skin friction coefficient $c_f$ along the flat plate for the test case T3A are compared to predictions obtained with different solvers. Additional comparisons for the underlying SST turbulence model and for the already implemented $\gamma$-$Re_{\theta t}$ transition model were made in order to establish a basis on how well the predictions obtained with the same model but from different solvers should agree. Since the $k$-$\overline{v^2}$-$\omega$ model currently is not implemented into CFX nor Fluent it

Figure 4.6.: Predictions for the local skin friction coefficient $c_f$ along the flat plate obtained from the solvers LINARS, CFX and Fluent for the SST turbulence model together with analytical solutions for fully turbulent and fully laminar flow.

was compared to the original developers published solutions [52] for the T3A test case. Figures 4.6 - 4.10 show these predictions together with analytical solutions for fully laminar flow given by Blasius (Eq. (4.1)), and empirical solutions for fully turbulent flow according to Schlichting (Eq. (4.2)).

Figure 4.6 shows predictions for the local skin friction coefficient $c_f$ along the plate for the SST turbulence model, obtained by the solvers LINARS, CFX and Fluent. It can be seen that the predictions are almost identical. Figure 4.7 depicts the same comparison for the $\gamma$-$Re_{\theta t}$ model. The solutions obtained from LINARS and Fluent are almost the same, while the transition onset is predicted slightly further downstream by the solver CFX. The transition length is predicted almost identical by all three solvers. From these first two comparisons it is within reason to expect very similar solutions for the newly implemented models as well.

A comparison of the predictions for $c_f$ for the $\gamma$ model can be seen in Figure 4.8. The prediction obtained by Fluent correlates very well with the solution of the in-house solver LINARS, while CFX shows a noticeable difference by predicting earlier transition onset. Transition length as well as the overall shape of the transition is predicted very similar by all three solvers. Since these simulations were already carried out with the finest mesh variant (index factor 8), the difference is probably caused by the sensitivity to the numerical schemes used by the solvers, as earlier mentioned and suggested by Menter.

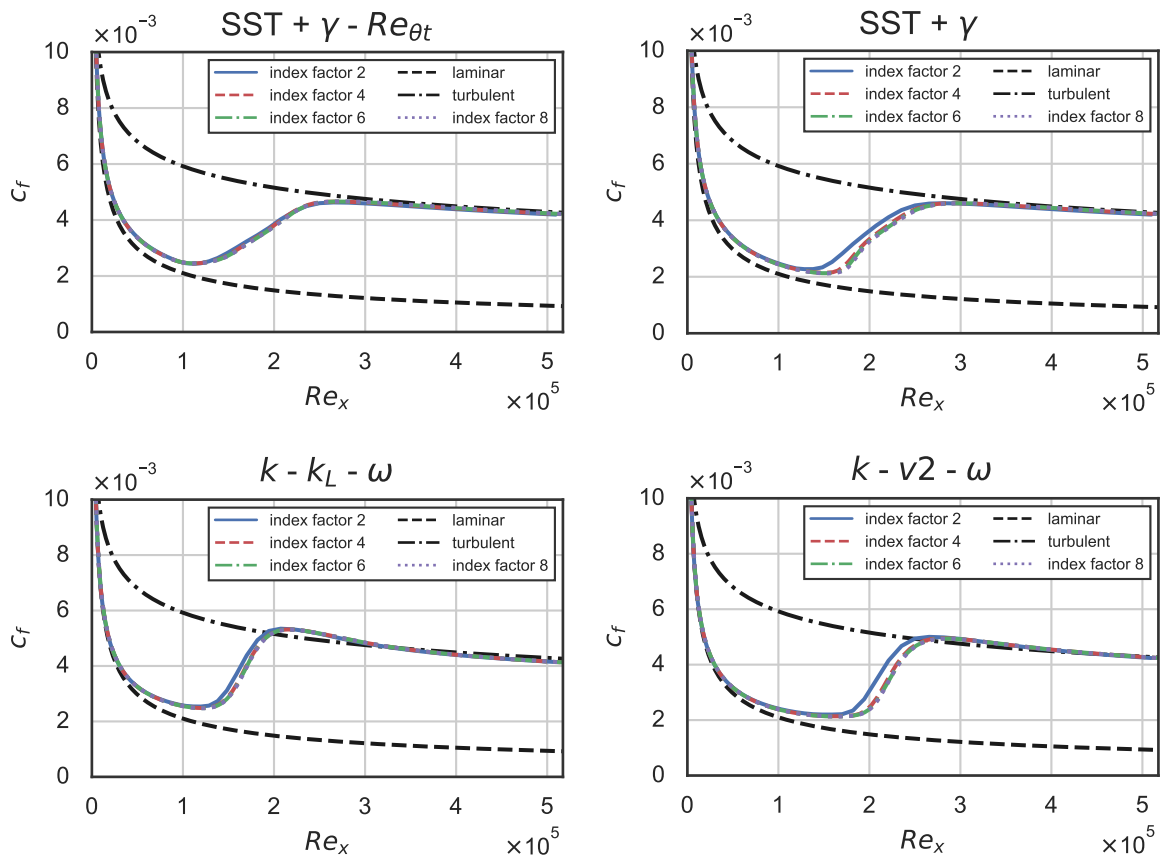Figure 4.7.: Predictions for the local skin friction coefficient $c_f$ along the flat plate obtained from the solvers LINARS, CFX and Fluent for the $\gamma$-$Re_{\theta t}$ transition model linked to the SST turbulence model together with analytical solutions for fully turbulent and fully laminar flow.
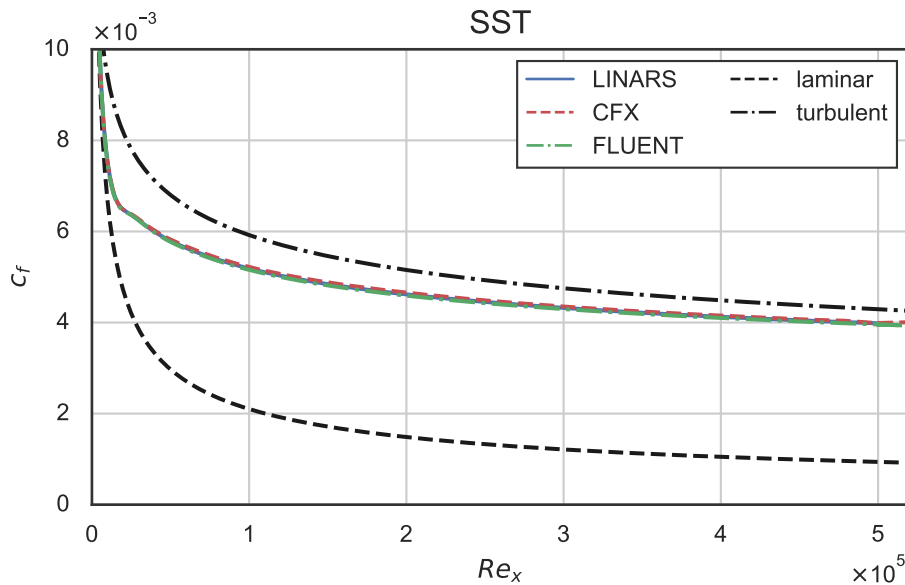


Figure 4.8.: Predictions for the local skin friction coefficient $c_f$ along the flat plate obtained from the solvers LINARS, CFX and Fluent for the $\gamma$ transition model linked to the SST turbulence model together with analytical solutions for fully turbulent and fully laminar flow.

Figure 4.9.: Predictions for the skin friction coefficient $c_f$ along the flat plate obtained from the solvers LINARS and Fluent for the $k$-$k_L$-$\omega$ transition sensitive turbulence model together with analytical solutions for fully turbulent and fully laminar flow.

Figure 4.9 shows a comparison of the predictions obtained by LINARS and Fluent with the $k$-$k_L$-$\omega$ model. The model is currently not implemented in CFX. LINARS predicts a slightly earlier transition onset, but transition length as well as the overall shape of the transitional area are predicted nearly identical.

The $k$-$\overline{v^2}$-$\omega$ model is currently neither implemented in CFX nor Fluent. Therefore Figure 4.10 compares the predictions obtained from LINARS with the predictions obtained by Lopez and Walters [52], which were extracted directly from the publication. As a baseline the solutions for the $k$-$k_L$-$\omega$ model obtained by LINARS and Lopez are compared as well. The solutions for the $k$-$k_L$-$\omega$ model correlate remarkably well, while the $k$-$\overline{v^2}$-$\omega$ solution obtained by LINARS predicts a slightly further downstream transition onset than Lopez and Walters. Considering that these predictions were computed using different meshes and solvers, it is a delightful surprise how well the solutions correlate.

In summary, except for the $\gamma$ prediction obtained by CFX, all solutions correlate reasonably well and some confidence in the implementation of the models into the in-house solver LINARS was gained. Before coming to a final verdict regarding the implementation, solutions for the turbine blade cascade VKI - LS59 were also compared to the results of commercial solvers (see section 4.2).
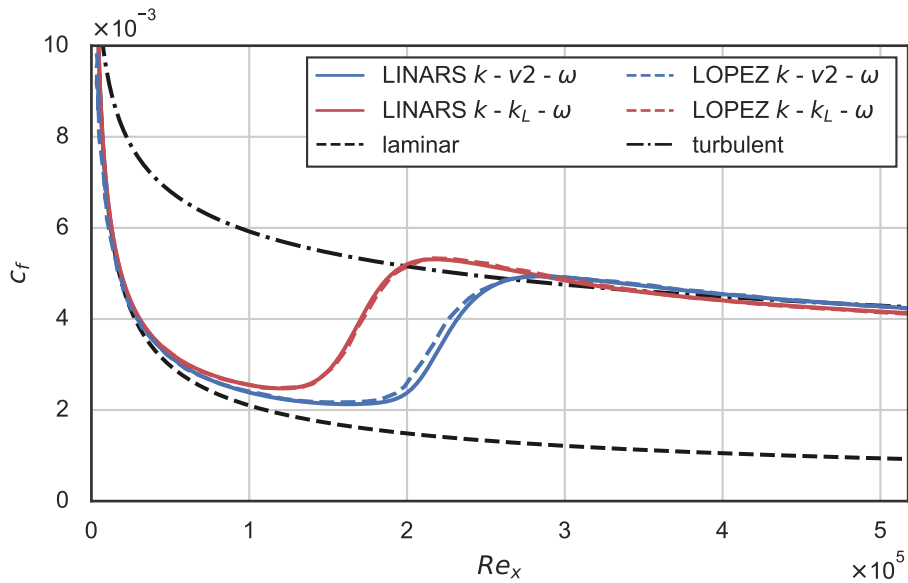
Figure 4.10.: Predictions for the local skin friction coefficient $c_f$ along the flat plate obtained from the solver LINARS for the $k$-$\overline{v^2}$-$\omega$ transition sensitive turbulence model versus predictions obtained by Lopez [52] together with analytical solutions for fully turbulent and fully laminar flow.

## 4.1.5. Variation of the turbulence intensity at the inlet

The influence of the turbulence intensity at the inlet on the transition onset was briefly investigated by increasing and decreasing $Tu$ at the inlet by 1% starting from the base value of $Tu = 5.4\%$. The results are depicted in Figure 4.11. All investigated models show physical plausible behavior, where an increased value of $Tu$ at the inlet leads to a further upstream transition onset, while decreasing $Tu$ retards the transition onset compared to the base-line. It is interesting that with further downstream transition onset the $\gamma$ model predicts shorter transition lengths resulting in steeper gradients in the prediction of $c_f$ at transition onset. All other models show the same general shape within the transitional area, shifted into the stream-wise coordinate of the plate. Noteworthy is that compared to the other models the $k$-$\overline{v^2}$-$\omega$ model is influenced the most by a variation of $Tu$ at the inlet. Regarding the accuracy of the $\pm1\% Tu$ predictions no assertion can be made since no measurements are readily available.
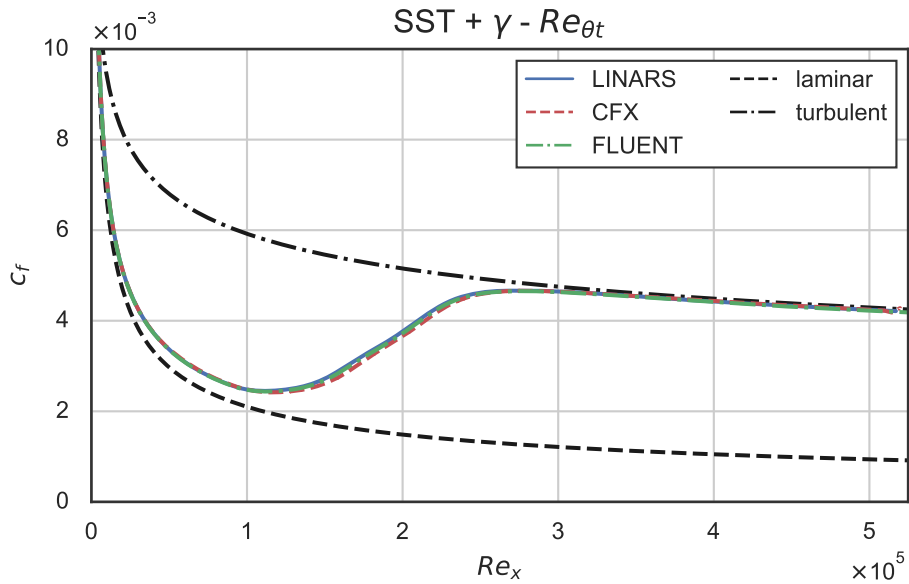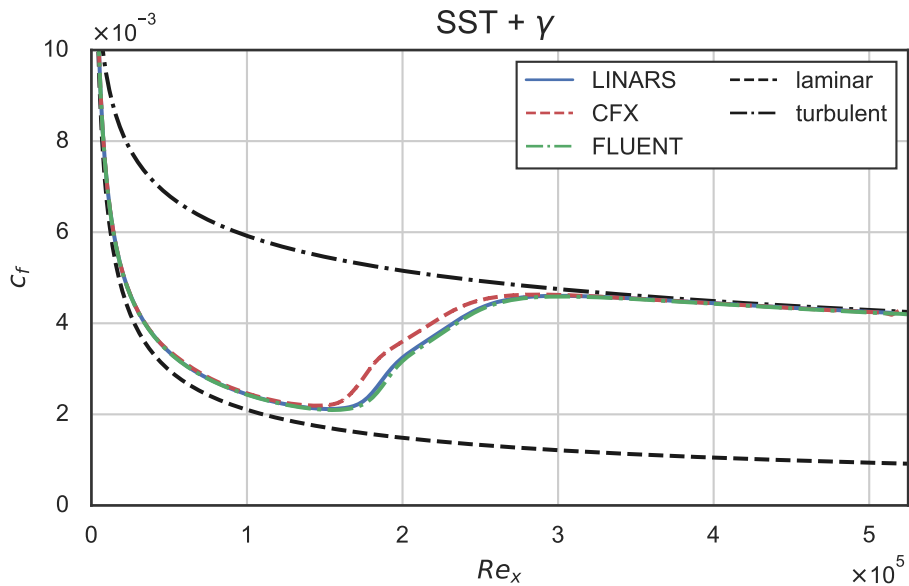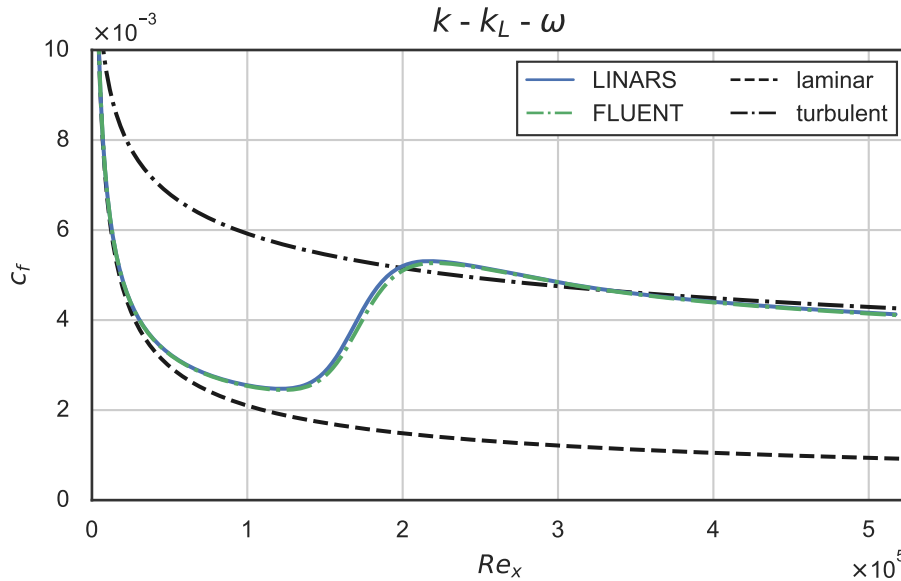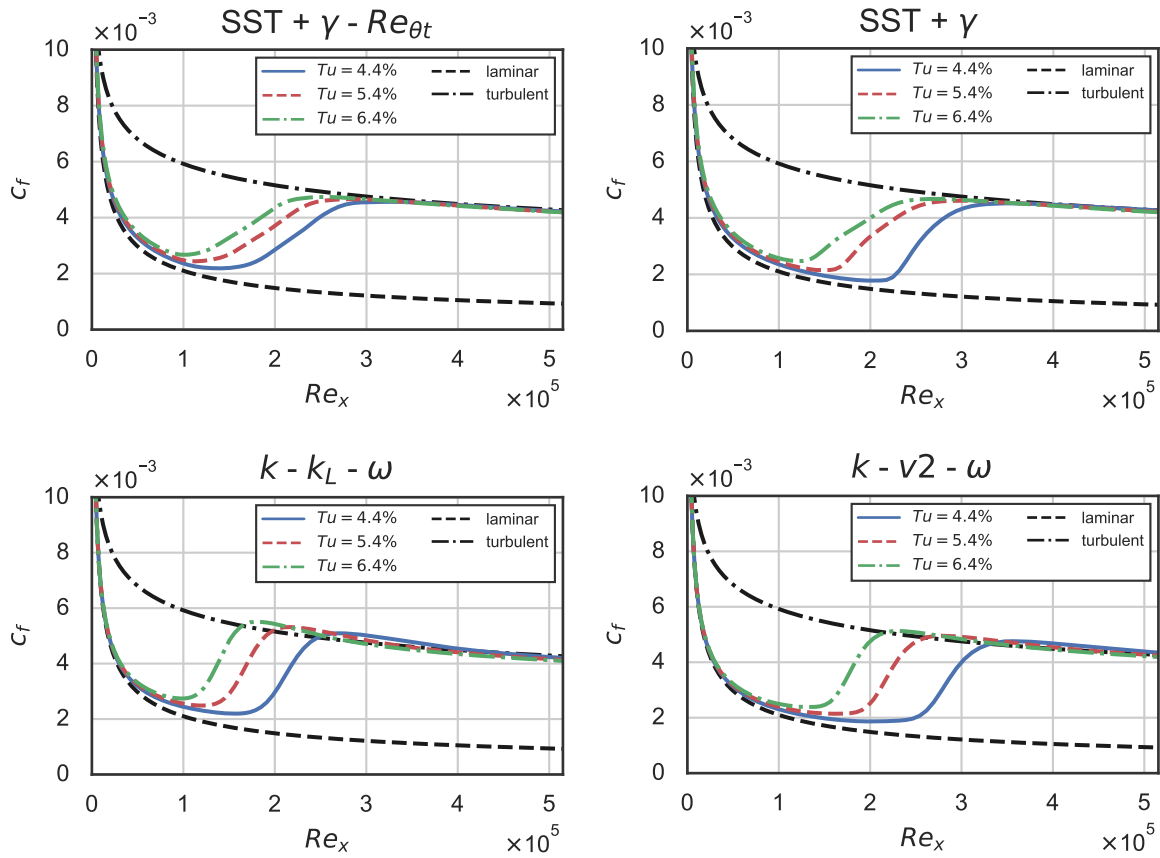
Figure 4.11.: Predictions for the skin friction coefficient $c_f$ along the flat plate obtained from the solver LINARS for a variation of the free-stream turbulence intensity at the inlet. (all investigated transition models)

## 4.1.6. Comparison to experimental data

Finally, the predictions obtained by the in-house solver LINARS were compared to the ERCOFTAC experiment [69]. Typically transition models perform very well for the T3A test case because it is a popular test case for calibrating transition models. However, sometimes a trade-off is necessary in order to yield better results for more complex flow. Figure 4.12 shows a comparison of all investigated transition models versus the measurement data obtained by Coupland [68] and made available by ERCOFTAC [69]. It is evident that in fact a comparison between two different families of transition models was made. Both the $k$-$k_L$-$\omega$ and the $k$-$\overline{v^2}$-$\omega$ model share the short transition length, where the $k$-$k_L$-$\omega$ model predicts a transition onset far more upstream, compared to the $k$-$\overline{v^2}$-$\omega$ model. Interestingly, it coincides with the predicted transition onset of the $\gamma$-$Re_{\theta t}$ model, but which due to its longer transition length
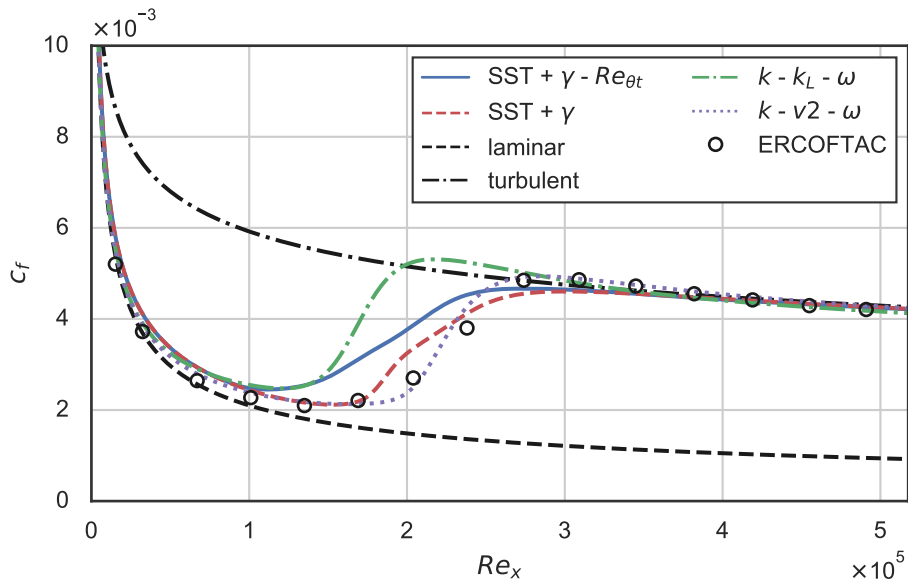
Figure 4.12.: Predictions for the skin friction coefficient $c_f$ along the flat plate for all investigated transition models versus the ERCOFTAC experiment and analytical solutions for fully turbulent and fully laminar flow. All numerical solutions were obtained by the in-house solver LINARS.

finishes the transition in good correlation with the measurement. The $\gamma$ model most accurately predicts the transition onset, but on the other hand over-predicts the transition length. The $k$-$\overline{v^2}$-$\omega$ model shows the overall most promising transitional prediction, but was, according to the original developer, specifically calibrated for this test case. The transition onset is predicted a bit too far downstream but due to its short transition length it is able to reproduce the measurement best. Interestingly, another distinction between the two families of transition models can be made. Both phenomenological transition models reproduce the measured slight overshoot of the local skin friction coefficient of the empirical solution for fully turbulent flow. This behavior is not predicted by the two empirical local correlation models $\gamma$ and $\gamma$-$Re_{\theta t}$. Overall all models perform reasonably well, where the $k$-$k_L$-$\omega$, due to its early transition onset together with a short transition length, deviates the most from the measurement.

## 4.1.7. Conclusion

This simple test case already gave valuable insight into the behavior of the models. It was discovered the the newly implemented models ($k$-$k_L$-$\omega$, $k$-$\overline{v^2}$-$\omega$ and $\gamma$) show

an increased sensitivity to the numerical methods used to solve the transport equations as well as an increased sensitivity regarding the mesh resolution. Therefore, even more care has to go into the generation of high quality meshes. All models performed reasonable well, where the $k\text{-}\overline{v^2}\text{-}\omega$ model showed the best agreement with the measurement data. However, the actual agreement with the measurement data for this simple test case allows no conclusion for more complex flow because the results depend highly on the calibration of the model. For example, the $k\text{-}\overline{v^2}\text{-}\omega$ model was according to the developer specifically calibrated for this test case [52]. Sometimes a trade-off is necessary in order to yield better results for more complex flow. The robustness of the $\gamma\text{-}Re_{\theta t}$ model in regard to the mesh resolution and different solvers is a highly desirable characteristic for a transition model and sets the model apart from the other implemented models.

## 4.2. VKI LS59 – Turbine blade cascade

In this test case, the sub-sonic flow inside a linear cascade of VKI LS59 high turning turbine blades was investigated. It was selected due to the availability of laser interferometric vibrometer measurements carried out by Mayrhofer [70], and Mayrhofer and Woisetschläger [71], a readily available computational mesh and the recent LES results obtained by Bertolini et. al. [57].

### 4.2.1. Computational domain
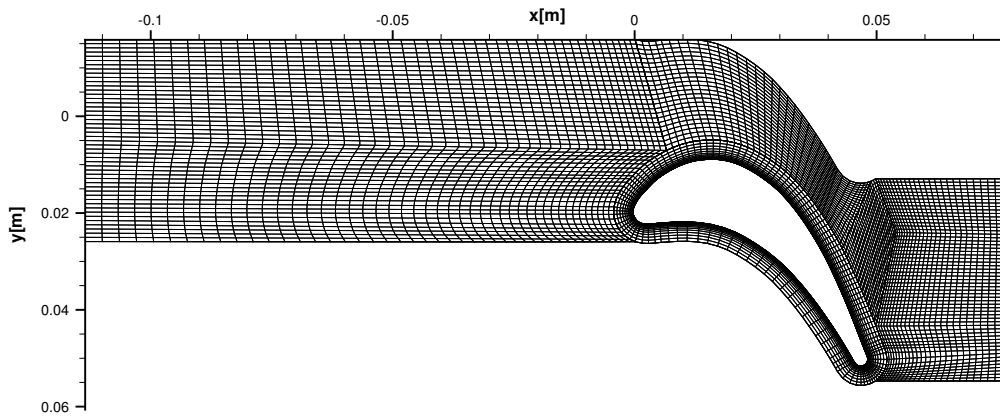


Figure 4.13.: Computational mesh for the VKI test case, showing every fourth grid point.

Figure 4.13 shows the computational mesh for the VKI test case, where every fourth grid point is shown. The inlet position was chosen atypically far upstream at $x = -0.1136$m due to the availability of inlet conditions from the measurements. The outlet is located at $x = 0.07748$m. The increased number of cells, caused by the inlet position was acceptable, since only steady-state Quasi-3D RANS simulations were carried out in the present study. A preliminary mesh-independence study showed that for this test case a rather fine mesh is needed. In total, the mesh consists of 120512 cells, which in the proximity of the blade are aligned in an O-shape and otherwise in an H-shape. The mesh was generated with the mesh-generator AI-Grid3D [53]. The chord length of the VKI LS59 profile is $L_c = 58$mm, the axial chord length is $C = 48.46$mm and the spacing of the blades was reported as $g = 41.18$mm. For the simulations, however, the allegedly measured value of $g = 41.77$mm from the actual test rig was used.

### 4.2.2. Boundary conditions and fluid properties

As defined in Table 4.4 at the inlet total pressure $p_{\text{tot}}$, total temperature $T_{\text{tot}}$, flow-angle $\beta_{\text{in}}$, free-stream turbulence intensity $Tu$ and turbulence length scale $l_{turb}$ were prescribed. The static pressure $p_{\text{stat}}$ was set at the outlet. At the domain boundaries into $y$-direction periodic boundary conditions were selected. The boundary conditions at the wall were set for a smooth and adiabatic wall. Because there was no data for the turbulence dissipation available, the turbulence length scale had to be estimated. Values in the range of 0.5% to 5% of the chord length are typical. Based on the chord length of $L_c = 58\,\text{mm}$ simulations for $l_{\text{turb}} = 0.6\,\text{mm}$, and $l_{\text{turb}} = 3\,\text{mm}$ were carried out. For the fluid air as an ideal gas with the fluid properties given by Table 4.5 was selected. The dynamic viscosity $\mu$ was calculated by the law of Sutherland (Eq. (2.13)) and the thermal conductivity $\lambda$ was calculated by rearranging the definition of the Prandtl Number $Pr$ (Eq. (2.17)).

| | | |
|---|---|---|
| $p_{\text{tot,in}}$ | 1.49091E5 | Pa |
| $T_{\text{tot,in}}$ | 307 | K |
| $\beta_{\text{in}}$ | $-30$ | ° |
| $Tu_{\text{in}}$ | 5 | % |
| $l_{\text{turb,in}}$ | 0.6 and 3 | mm |
| $p_{\text{stat,out}}$ | 1.01651E5 | Pa |

Table 4.4.: VKI Boundary Conditions

| | | |
|---|---|---|
| $R$ | 287 | J/kg K |
| $\gamma_c$ | 1.4 | – |
| $Pr$ | 0.72 | – |
| $c_p$ | 1004.5 | J/kg K |
| $M_R$ | 28.97 | kg/kmol |

Table 4.5.: VKI Fluid Properties



(a) probe position



(b) static pressure $p_{\text{stat}}$
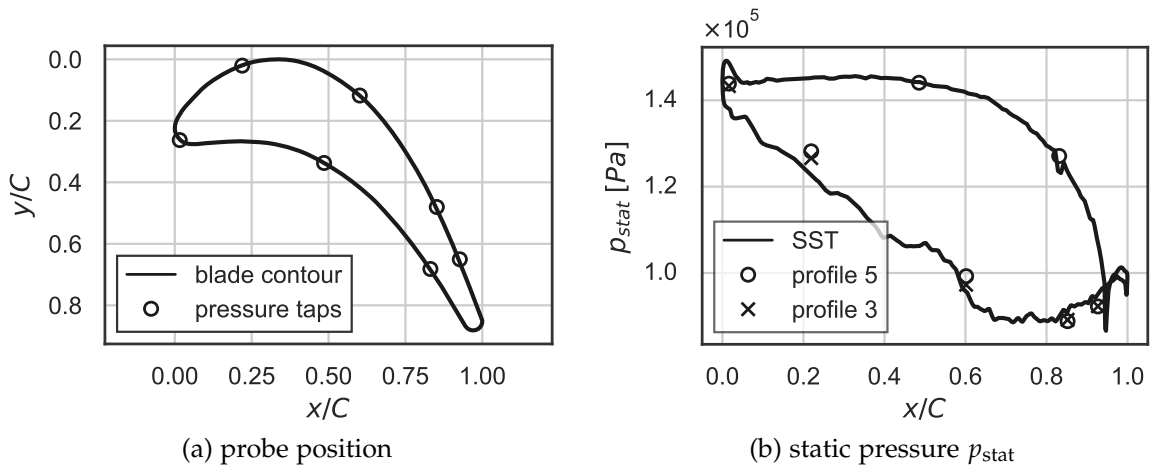
Figure 4.14.: Subfigure (a) shows the location of the probes on the blade contour and (b) plots the static pressure along the blade obtained by LINARS with the SST turbulence model versus the measured values on profile 3 and 5.

In the experiments [70, 71] seven VKI LS59 profiles were positioned in a linear cascade and pressure probes were installed on the blades 3 and 5. Figure 4.14a shows the locations of the pressure probes on the blade contour, where the coordinates $x$ and $y$ where rescaled by the axial chord length $C$. Figure 4.14b plots the predictions for the static pressure $p_{stat}$ along the blade for the SST turbulence model obtained by the in-house solver LINARS. On the pressure side, an excellent correlation between measurement and simulation was achieved, while on the suction side at $x/C \approx 0.2$ a minor deviation can be seen. This discrepancy could, for example, be caused by a small deviation of the blade alignment.



(a) Mach number $Ma$ $[-]$    (b) Streamwise acceleration $dU/ds$ $[1/s]$
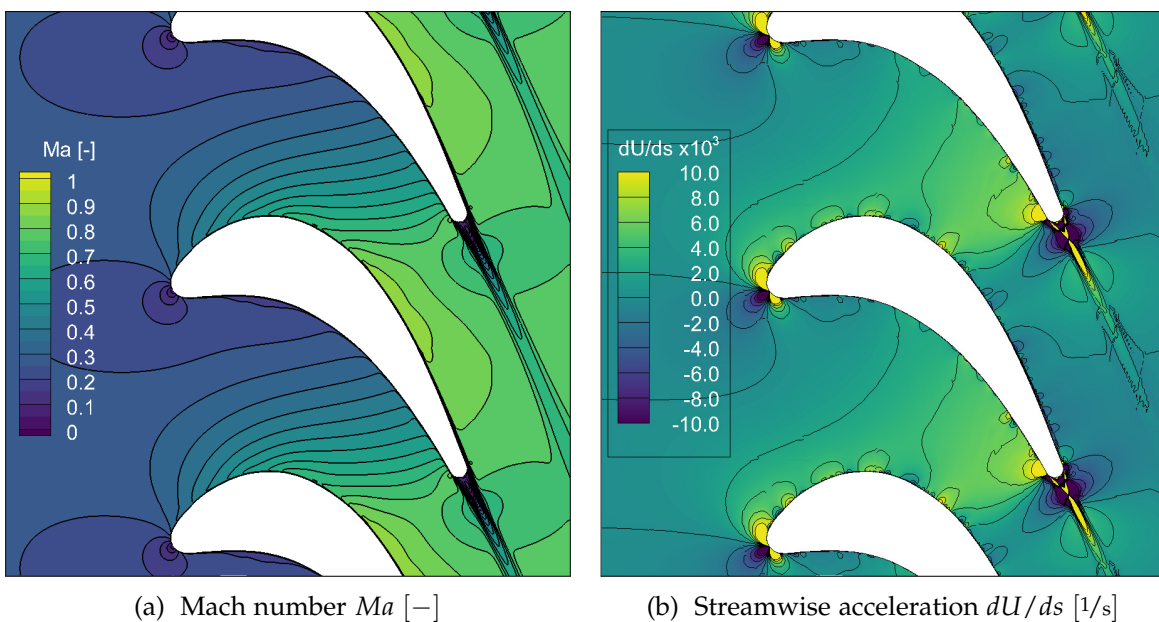
Figure 4.15.: Predictions for (a) the Mach number and (b) the streamwise acceleration for the flowfield, obtained by LINARS with the SST turbulence model.

The Mach number is defined as the ratio of the local velocity magnitude to the local speed of sound as $Ma = U/a$, where the speed of sound for an ideal gas can be calculated from $a = \sqrt{\gamma_c R T}$, where $\gamma_c$ is the ratio of the heat capacities and $R$ is the specific gas constant. Figure 4.15a shows the predictions for the Mach number together with Mach iso-lines in the flow field and Figure 4.15b plots the streamwise acceleration $dU/ds$ (see Eq. (2.107)) as obtained by the solver LINARS for the SST turbulence model. The maximum Mach number is $Ma \approx 0.76$ and there is no shock present. The flow around the profile stays attached on both pressure and suction side. Additionally, the unsteadiness of the curvature of the blade contour can be observed in Figure 4.15b, which causes small bubble like regions of acceleration and deceleration of the flow close to the solid wall.

### 4.2.3. Implementation validation

Figures 4.16, 4.17 and 4.18 display the wall shear-stress magnitude $\tau_W$ along the blade, where the SST model serves as the turbulent base-line. On the abscissa the axial coordinate, rescaled by the axial chord-length, is plotted ($x/C$). The pressure side is plotted as negative values for the relative coordinate $x/C$ and the suction side is plotted as positive values. All Figures show the predictions for the turbulence length scale set to (a) $l_{turb} = 0.6$mm and (b) $l_{turb} = 3$mm. Generally it can be seen that the higher value for $l_{turb}$ leads to earlier transition onset, shown by a sharp increase to the turbulent value of the wall shear stress magnitude $\tau_w$ on the suction side, due to lower values for turbulence dissipation rate $\omega$.

In regions, where the wall shear stress magnitude $\tau_w$ briefly is zero, a separation bubble could be present. Steep positive gradients of $\tau_w$ indicate transition from laminar to turbulent flow. Additionally, from comparison to the fully turbulent solutions given by the SST model, the transitional behavior of the models can be analyzed.

Figure 4.16 shows a comparison of the predictions with the $\gamma$-$Re_{\theta t}$ model obtained by the solvers LINARS, CFX and Fluent. On the pressure side transition onset can be seen at $x/C \approx -0.3$ for (a) $l_{turb} = 3$mm and at $x/C \approx -0.25$ for (b) $l_{turb} = 0.6$mm. For both variations, the flow relaminarizes at approximately mid-chord position. The flow then stays laminar until the wake separation at the trailing edge. The spike in the distribution of $\tau_w$ at $x/C \approx -0.825$ is probably caused by a discontinuity in the curvature of the blade in the computational mesh. All three solvers give similar predictions for the flow on the pressure side. On the suction side, laminar flow was predicted up to $x/C \approx 0.85$ for (a) $l_{turb} = 0.6$mm and $x/C = 0.75$ for (b) $l_{turb} = 3$mm. The prediction obtained from Fluent slightly deviates from the solutions obtained by LINARS and CFX for the variant (a) $l_{turb} = 0.6$mm by predicting a slightly retarded transition onset at $x/C \approx 0.9$. However, the overall agreement between the solvers is very good and this sets the expectations for the other transition models.

In Figure 4.17 a similar comparison for the $\gamma$ transition model is shown. The flow on the pressure side is predicted similarly to the $\gamma$-$Re_{\theta t}$ model. On the suction side it is noticeable that transition onset for (a) $l_{turb} = 0.6$mm is retarded to $x/C \approx 0.9$ and all three solvers correlate very well. For (b) $l_{turb} = 3$mm, the transition onset predicted varies between $x/C = 0.75$ and $x/C = 0.85$ for the three solvers. While LINARS and Fluent again agree very well, CFX predicts a more upstream transition onset which fits to the $\gamma$-$Re_{\theta t}$ result. A similar behavior of CFX, compared to LINARS and Fluent was already observed for the T3A test case.

Finally, for the $k$-$k_L$-$\omega$ model the predictions obtained by LINARS are compared to predictions obtained by Fluent. CFX currently does not offer the $k$-$k_L$-$\omega$ model. Sur-

(a) $l_\text{turb} = 0.6\text{mm}$



(b) $l_\text{turb} = 3\text{mm}$
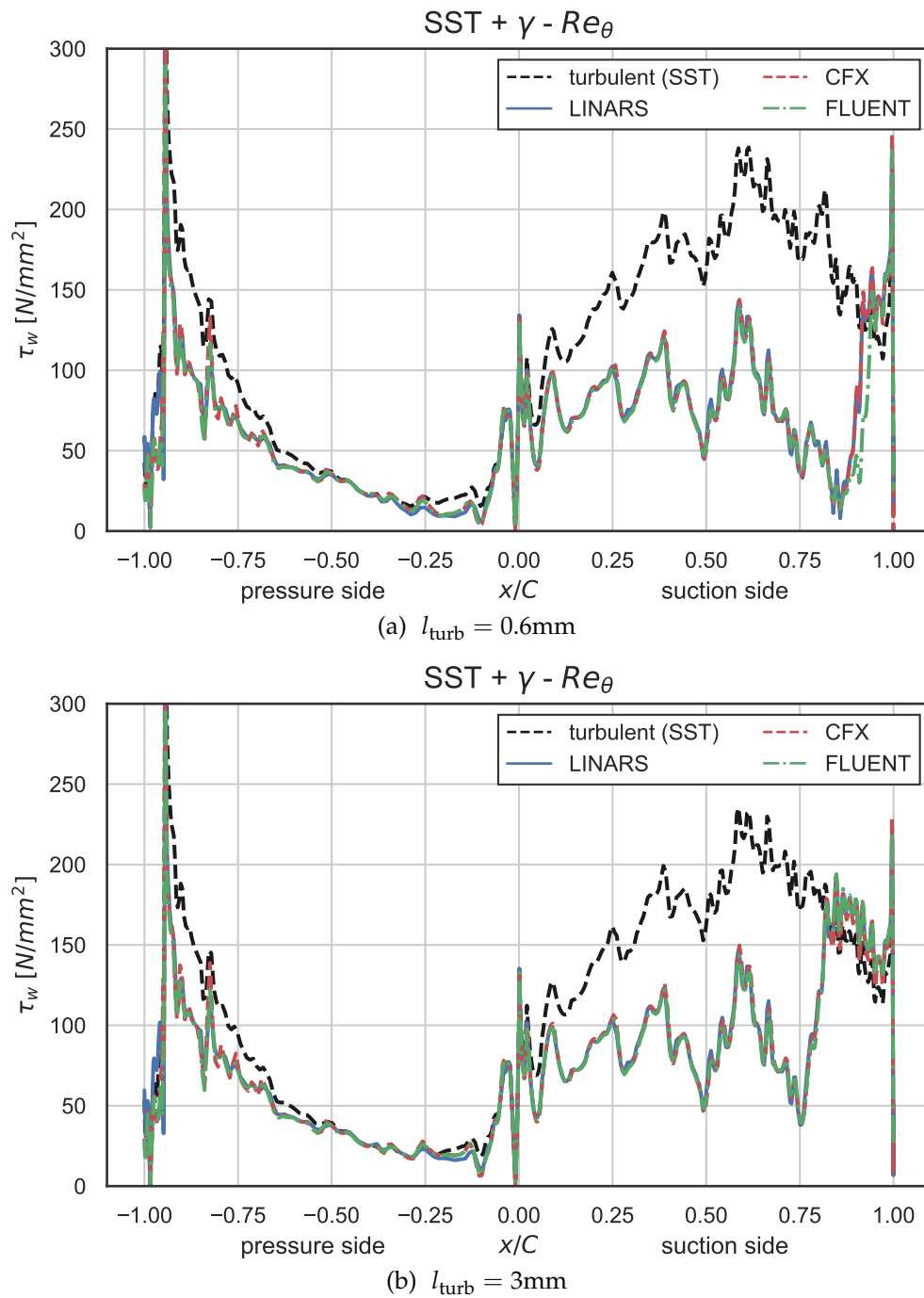
Figure 4.16.: Predictions for the wall shear stress magnitude $\tau_w$ over the relative axial coordinate x/C for the $\gamma$-$Re_{\theta t}$ transition model together with the fully turbulent solution of the SST turbulence model, obtained by the solvers LINARS, CFX and Fluent.

(a) $l_{\mathrm{turb}} = 0.6$mm



(b) $l_{\mathrm{turb}} = 3$mm

Figure 4.17.: Predictions for the wall shear stress over the relative axial coordinate x/C for the $\gamma$ transition model together with the fully turbulent solution of the SST turbulence model, obtained by the solvers LINARS, CFX and Fluent.

(a) $l_{\text{turb}} = 0.6\text{mm}$



(b) $l_{\text{turb}} = 3\text{mm}$

Figure 4.18.: Predictions for the wall shear stress over the relative axial coordinate x/C for the $k$-$k_L$-$\omega$ transition sensitive turbulence model, together with the fully turbulent solution of the SST turbulence model, obtained by the solvers LINARS and Fluent.

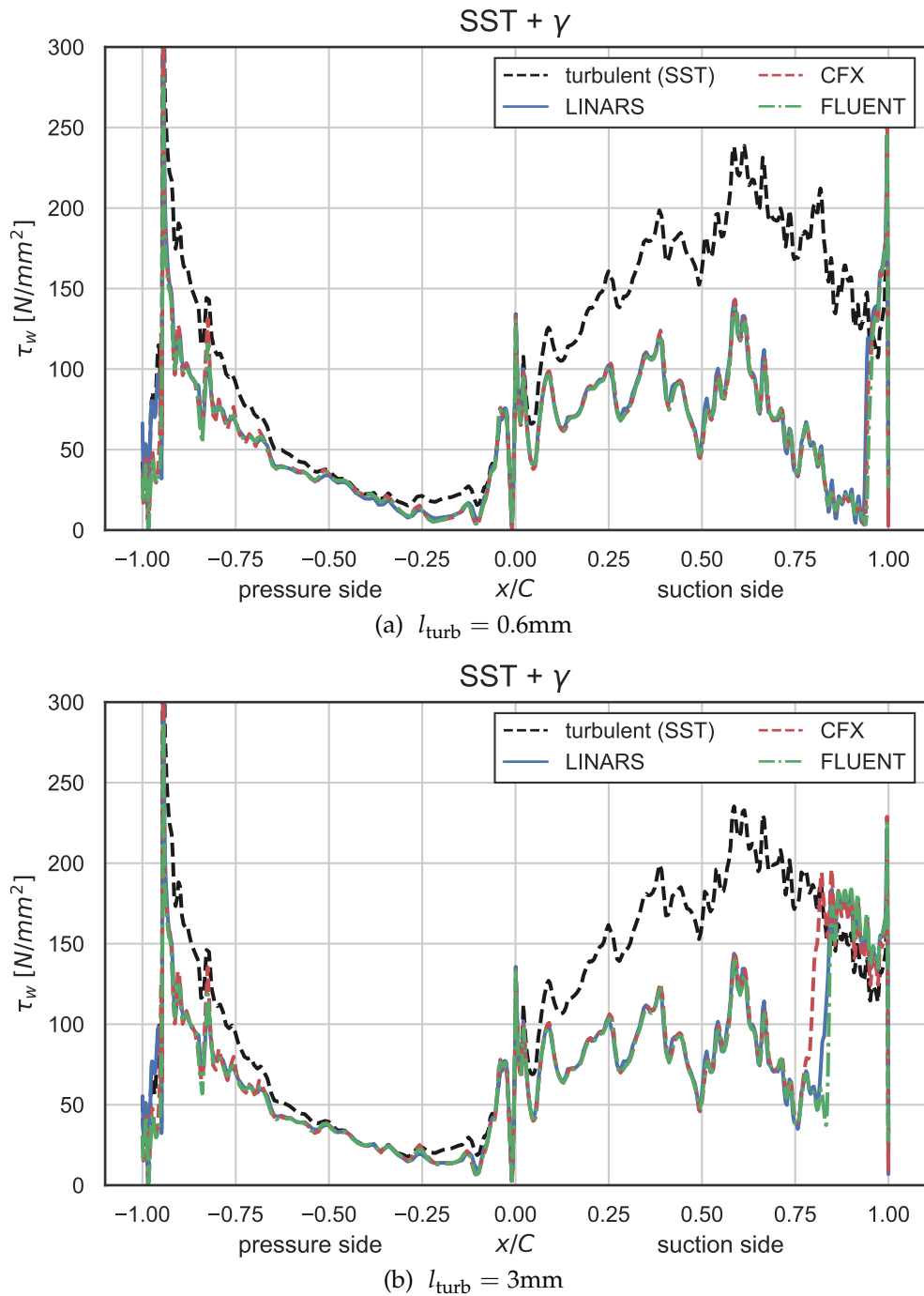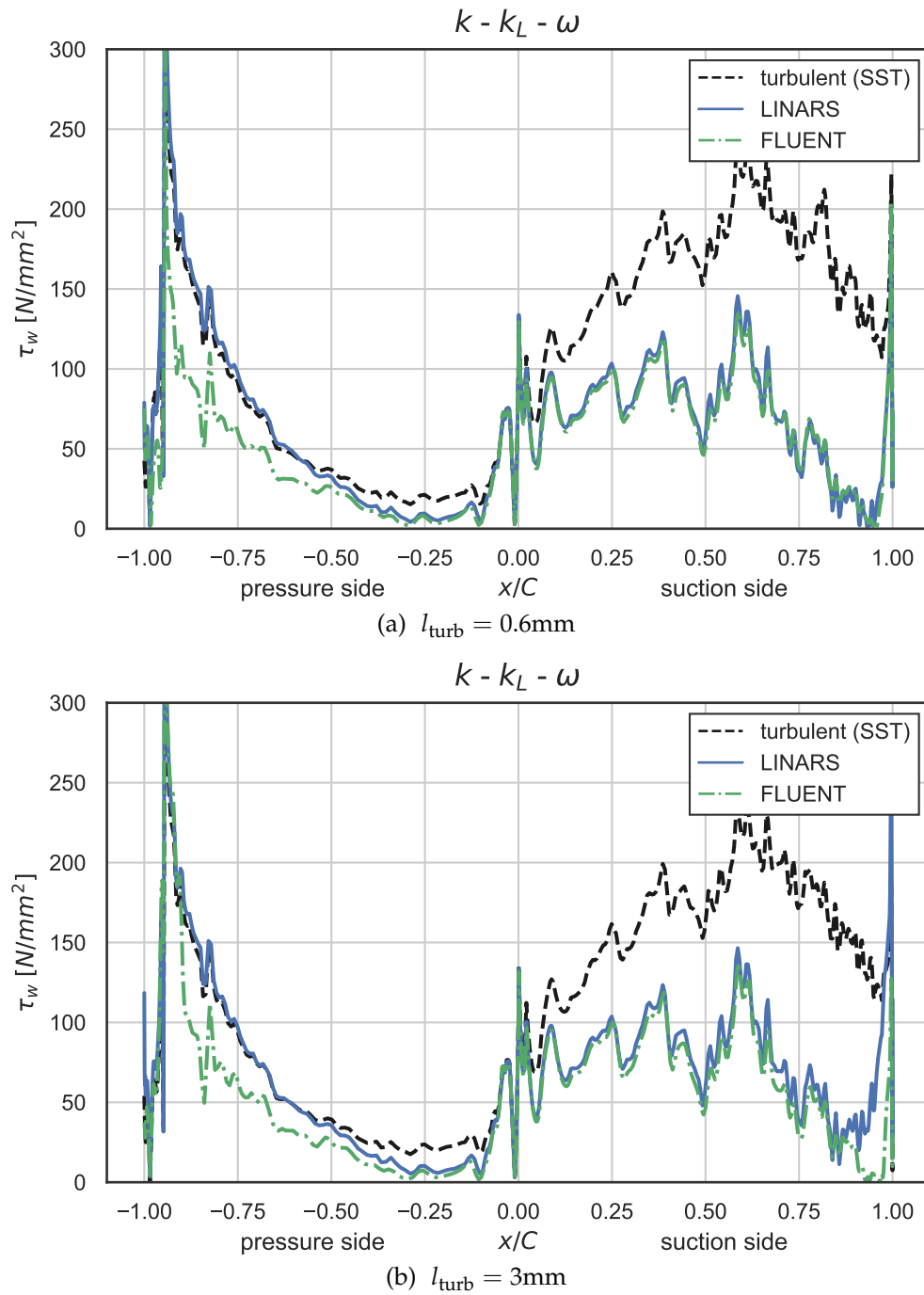prisingly, the predictions of Fluent show no transitional flow behavior on the pressure side nor on the suction side with peculiarly small values for $\tau_w$ at approximately $x/C = -0.3$. Also the turbulence length scale $l_{\text{turb}}$ shows no significant influence on the transitional behavior for the solutions obtained by Fluent. LINARS on the other hand predicts a gradual transition with a full agreement with the fully turbulent solution from $x/C \approx -0.55$. On the suction side the flow stays laminar up to the trailing edge. For case (a) $l_{\text{turb}} = 0.6$mm, another significant difference can be seen. While LINARS predicts an attached boundary layer up to the trailing edge, Fluent predicts separation from the blade further upstream, at $x/C \approx 0.9$. This can probably be explained as follows. LINARS predicts that the boundary layer transitions shortly before separating and Fluent predicts ongoing laminar flow which then separates, because a laminar boundary layer is more prone to separation (see section 1.2.1).

The $k$-$\overline{v^2}$-$\omega$ model is neither implemented in CFX nor Fluent and can therefore only be compared to the other models with LINARS, which can be seen in the next section.

## 4.2.4. Model comparison

Figures 4.19 and 4.20 show a comparison of all investigated models, where all predictions were obtained by the in-house solver LINARS. To be able to recognize small differences, the pressure side (Fig. 4.19) and suction side (Fig. 4.20) were plotted separately for both values of the turbulence length scale.

On the pressure side (Fig. 4.19) it can be seen that the $\gamma$ and $\gamma$-$Re_{\theta t}$ model agree very well and so do the $k$-$k_L$-$\omega$ and the $k$-$\overline{v^2}$-$\omega$ model, which was expected to some extent because the models belong to two different families of transition models. Again the very different behavior of those two families is remarkable, where the LCTMs only predict a short area of turbulent flow, but with earlier transition onset, compared to the physics-based models. On the other hand the $k$-$k_L$-$\omega$ and the $k$-$\overline{v^2}$-$\omega$ model predict a fully turbulent boundary layer starting from the location, where the $\gamma$ and $\gamma$-$Re_{\theta t}$ model predict relaminarization. The turbulence length scale only influences the transition onset on the pressure side predicted by the LCTMs, which is slightly retarded for the lower value of (a) $l_{\text{turb}} = 0.6$mm.

Figure 4.20 shows the predictions for the suction side, where the different models yield more comparable results as on the pressure side. All models predict laminar flow in the beginning and transition onset towards the trailing edge, where the $k$-$k_L$-$\omega$ predicts transition onset only shortly before separating from the blade, which is surprising because for the T3A test case the $k$-$k_L$-$\omega$ model predicted a very early transition onset compared to the other models. Also it is less influenced by the variation of the turbulence length scale. All other models show, as mentioned before, earlier transition onset for higher values of $l_{\text{turb}}$ which is caused by the reduced

turbulent dissipation rate. The $k\text{-}\overline{v^2}\text{-}\omega$ model shows very promising behavior by predicting transition onset similar to the $\gamma$ model. The $\gamma\text{-}Re_{\theta t}$ model always predicts a slightly more upstream transition onset than the other models.

### 4.2.5. Laser interferometric vibrometer measurements

Mayrhofer [70] and Mayrhofer and Woisetschläger [71] obtained the density fluctuations in proximity to the blade by laser interferometric vibrometer measurements. Figure 4.21 shows the density fluctuations $\rho'$ along the relative axial position $x/C$ in the frequency domain, where $F$ is the fluctuation frequency. It is assumed that at transition onset the fluctuation intensity rapidly increases across all frequencies, which is reflected in the plot by very dense iso-lines.

On the pressure side at $x/C \approx 0.84$ there is an increase in intensity. This surprisingly coincides with the discontinuity in the results of the RANS simulations, which was assumed to be non-physical and probably caused by a discontinuity in the curvature of the blade contour in the mesh. The correlation-based transition models predict the final transition onset close to the trailing edge of the blade, where the flow separates from the profile. The physics-based models, on the other hand, predict transition onset as early as $x/C \approx -0.5$. Therefore, no correlation between measurement and simulation can be observed for the pressure side.

Two regions can be discerned on the suction side, one at $x/C \approx 0.62$ and the second one at $x/C \approx 0.82$, respectively. The second region shows good agreement with the transition onset location predicted by the simulations for a turbulence length scale of $l_{\text{turb}} = 3\text{mm}$. Hampel et. al. [72] attributed the first change in the intensity to a possible separation bubble, followed by a transition onset at the second change in intensity. None of the RANS simulations indicate a separation bubble at this location, but it can not be ruled out that the simulation is missing a crucial component in order to predict this behavior.
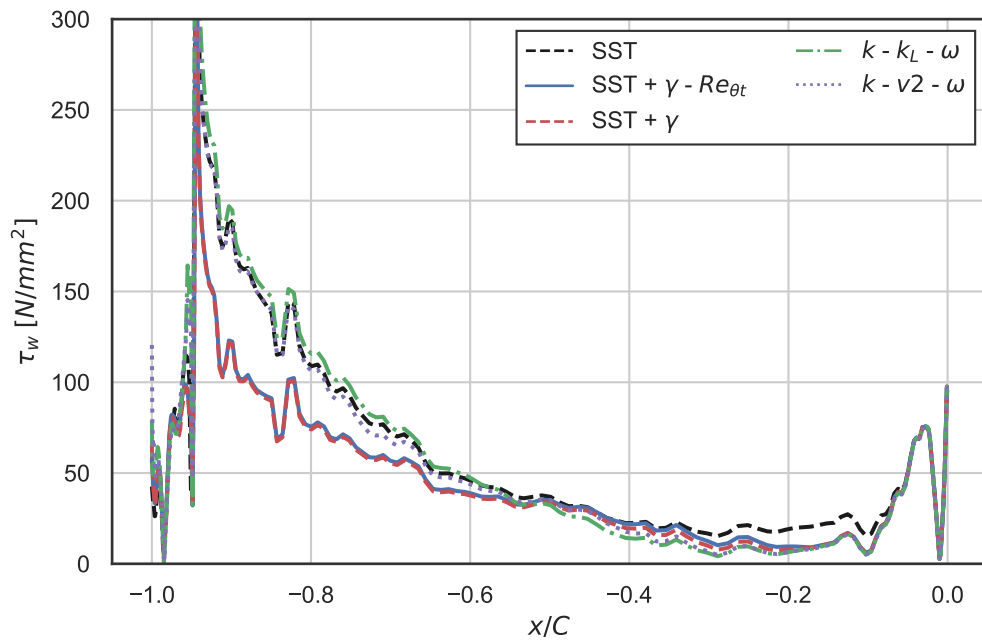
(a) $l_{\text{turb}} = 0.6\text{mm}$
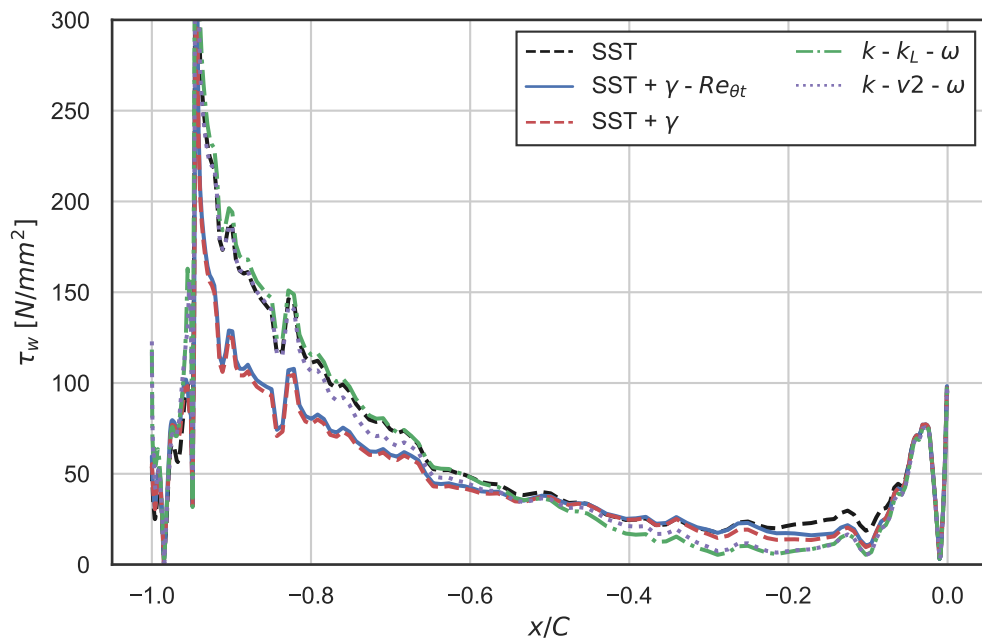


(b) $l_{\text{turb}} = 3\text{mm}$

Figure 4.19.: Predictions for the wall shear stress on the **pressure side** of the blade over the relative axial coordinate $x/C$ for all investigated transition models, together with the fully turbulent solution of the SST turbulence model, obtained by the solver LINARS.
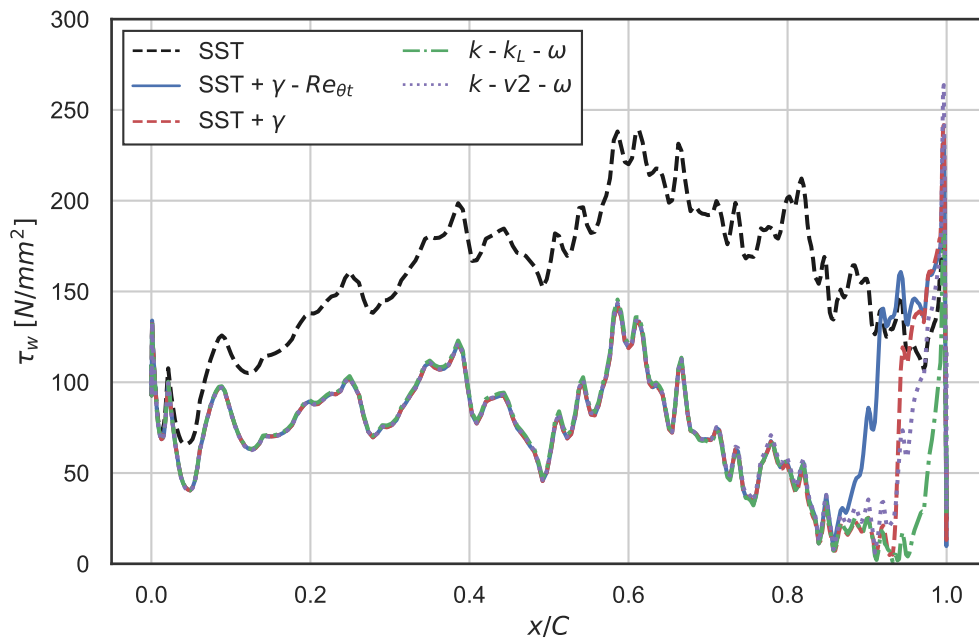
(a) $l_{\text{turb}} = 0.6\text{mm}$
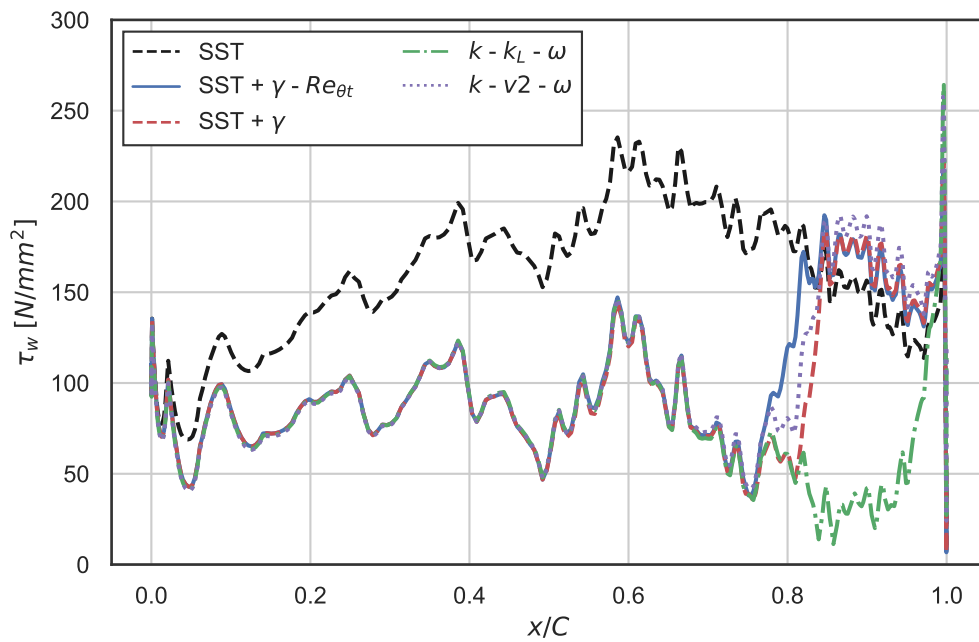


(b) $l_{\text{turb}} = 3\text{mm}$

Figure 4.20.: Predictions for the wall shear stress on the **suction side** of the blade over the relative axial coordinate $x/C$ for all investigated transition models, together with the fully turbulent solution of the SST turbulence model, obtained by the solver LINARS.

(a) pressure side

(b) suction side
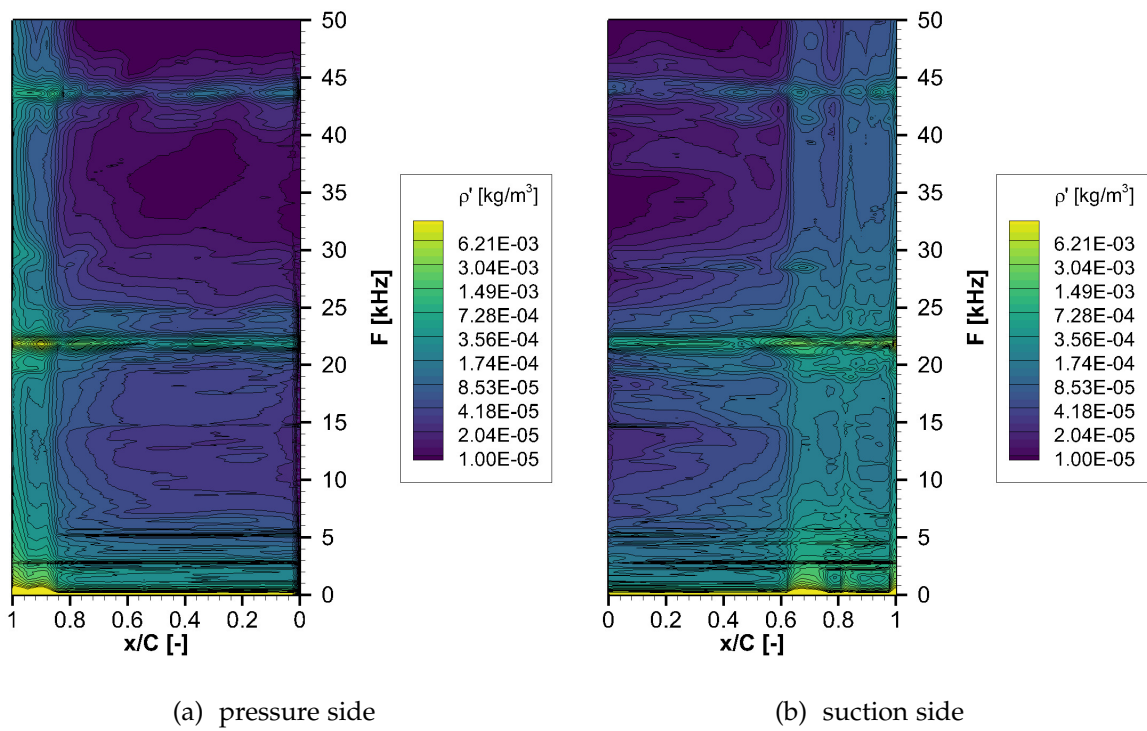
Figure 4.21.: Density fluctuations $\rho'$ in the frequency domain, where $F$ is the fluctuation frequency versus the relative axial position $x/C$ around to the blade (obtained from Mayrhofer and Woisetschläger [71]).

### 4.2.6. Large Eddy Simulation (LES)



(a) pressure gradient magnitude in $\mathrm{Pa/m}$

(b) Q-Criterion iso-surfaces, colored by the velocity gradient in $\mathrm{1/s}$
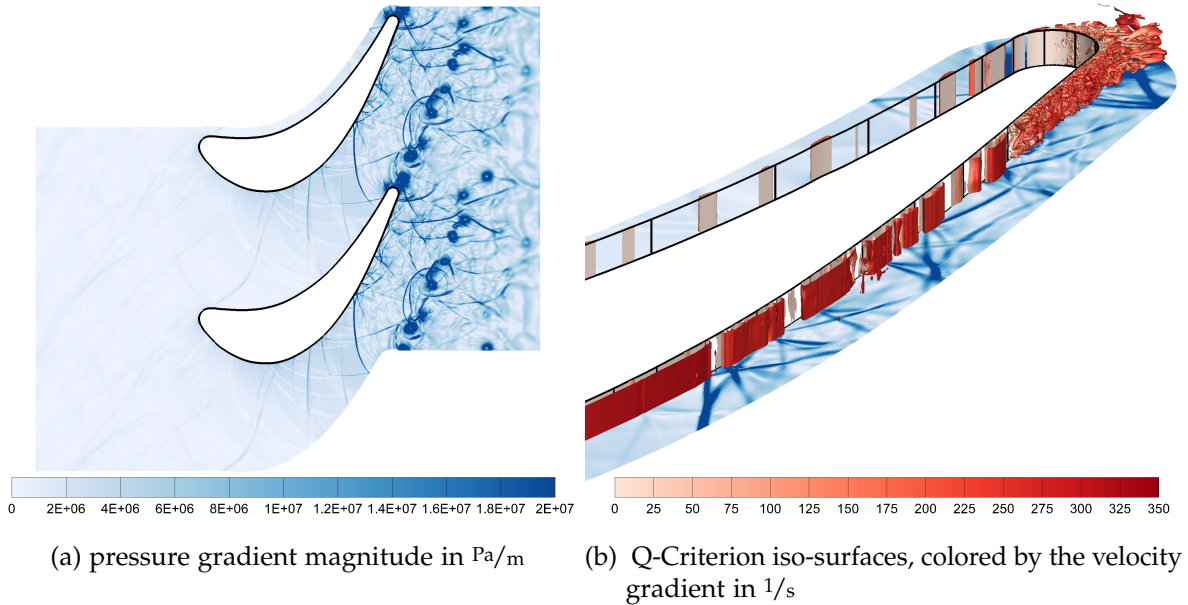
Figure 4.22.: Predictions for (a) the instantaneous pressure gradient magnitude and (b) the Q-Criterion, colored by the velocity gradient magnitude, together with the instantaneous pressure gradient magnitude (from Bertolini et. al. [57]).

Bertolini at. al. [57] carried out LES for the VKI test case and provided the following two figures. Figure 4.22a shows the instantaneous pressure gradient magnitude, where the Kármán vortex street in the wake of the blade is clearly visible. Additionally, pressure waves, traveling upstream the blade channel can be seen. On the suction side these pressure waves heavily interact with the boundary layer. Figure 4.22b shows the instantaneous pressure gradient magnitude together with iso-surfaces for the Q-criterion, which is used for vortex-identification and defined in vector notation by

$$Q = \frac{1}{2}\left(||\underline{\Omega}|| - ||\underline{S}||\right) > 0, \tag{4.5}$$

where the motivation behind the Q-criterion can readily be seen. It defines a vortex as a continuous fluid region, where the norm of the vorticity tensor dominates the norm of the strain-rate tensor [73], because by using the vorticity alone it can not be distinguished between swirling and shearing motions [74].

On the pressure side no transition until the trailing edge can be seen and confirms the results of the LCTMs. For the suction side it can be seen that reflected pressure waves interact with the laminar boundary layer, where gradually laminar instabilities form and finally transition to turbulent flow is observed close to the trailing edge [57],

which is in good agreement to the transitional RANS simulations (see section 4.2.4). Bertolini et. al. [57] attributed the increase in the fluctuation intensity at $x/C \approx 0.62$ to the interaction of reflected pressure waves with the boundary layer, where Hampel et. al. [72] suspected a separation bubble.

### 4.2.7. Conclusion

From the results of this test case, together with the results of the T3A test case, it is assumed that the $\gamma$ transition model was implemented correctly. The result obtained from the solver CFX showed a small deviation in the prediction of the transition onset on the suction side, compared to LINARS and Fluent. It is assumed that this difference is caused by the different numerical schemes used by the solvers.

The $k\text{-}k_L\text{-}\omega$ model, provided a substantially different solution for the pressure side, compared to Fluent. However, it is unclear if the solution obtained by Fluent is correct, because the model equations in the Fluent Theory Guide [58] are given in reference to the 2008 paper of Walters and Cokljat [48], which, as mentioned in section (2.4.3), contains several typographical errors. The in-house solver implementation is based on the publication of Fürst [83], where these errors were corrected. For the pressure side, the $k\text{-}\overline{v^2}\text{-}\omega$ model yields a comparable solution to the $k\text{-}k_L\text{-}\omega$ model. Additionally, a promising improvement in the transition onset prediction on the suction side was observed.

The comparison to the measurement and LES showed the great potential of LES for gaining further insight into the transition process, which subsequently can be used for validating transition models. It was observed that all transition models, except for the $k\text{-}k_L\text{-}\omega$ model, predict the transition onset on the suction side satisfactorily for the case (b), where the turbulence length scale was set to $l_{\text{turb}} = 3mm$. On the pressure side, laminar flow until close to the wake separation at the trailing edge was accurately predicted by the LCTMs.

## 4.3. MUR – Transonic guide vane

The MUR test case is a linear cascade of a highly loaded transonic turbine guide vane. It is such an interesting test case because Arts et. al. [75] published very accurate measurements of the heat-transfer along the blade profile for a large variation of boundary conditions. For this test case all simulations were carried out with the in-house solver LINARS.

### 4.3.1. Computational domain
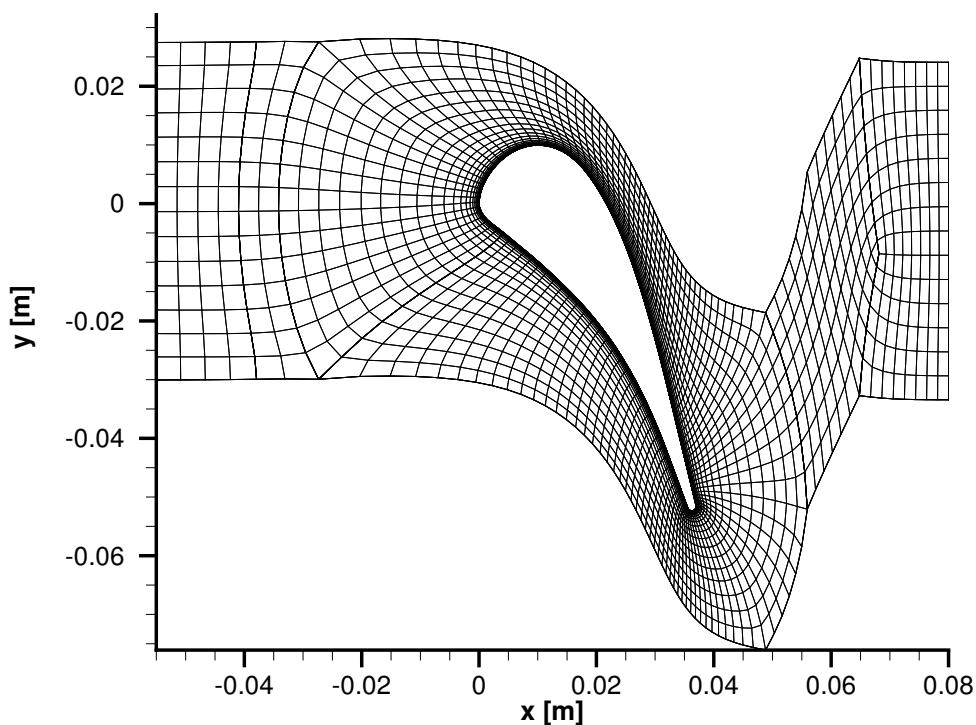


Figure 4.23.: Computational mesh for the MUR test case, showing every second grid point.

The inlet is positioned at $x = -0.055$ m and the outlet at $x = 0.08$m. The mesh consists of 15568 cells, with increased density in proximity to the blade in order to properly resolve the boundary layer. The block around the blade, including the channel between the blades, is meshed in O-form. Inlet and outlet blocks of the mesh are from the H-type. Figure 4.24 shows the dimensionless wall distance $y^+$ of the first cell around the blade for the investigated flow cases (see Table 4.6). For the high Reynolds number test cases it is well below unity and $y^+ < 0.5$ for the low Reynolds number test cases. The chord length of the blade is $L_c = 67.647$ mm, the axial chord length is $C \approx 36.98$ mm and the pitch is $g = 57.5$ mm.
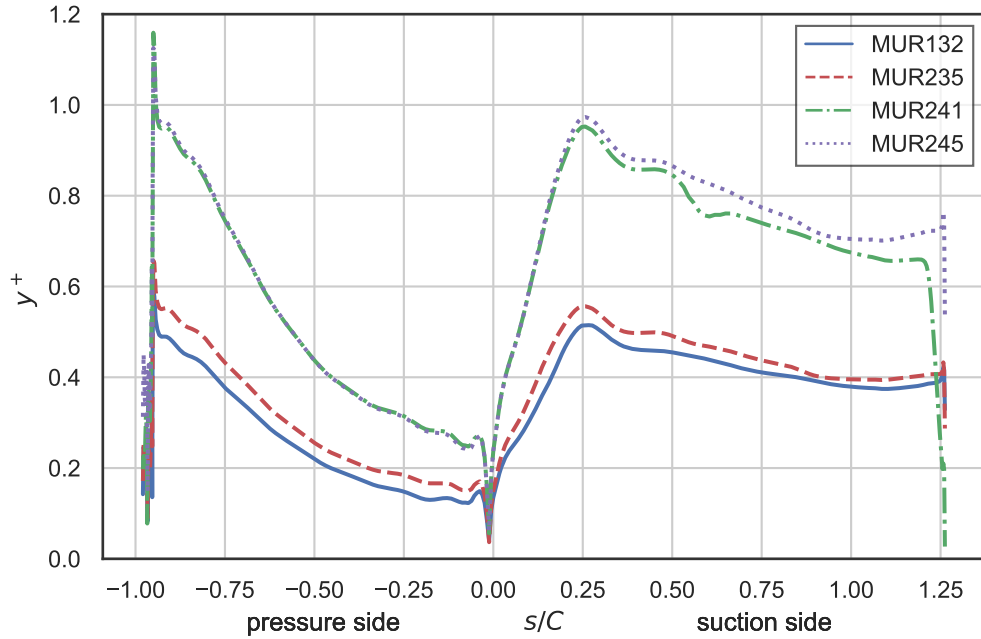
Figure 4.24.: Dimensionless wall distance $y^+$ for the first cell over the relative coordinate along the blade $s/C$ for the investigated MUR boundary conditions (see Table 4.6).

## 4.3.2. Boundary conditions and fluid properties

Table 4.6 lists the boundary conditions (BCs) for all performed MUR simulations, where the isentropic outlet Mach number $Ma_{is,out}$ and the isentropic outlet Reynolds number $Re_{is,out}$ are given as a reference only. Total pressure $p_{tot}$, total temperature $T_{tot}$ and the turbulence boundary conditions $l_{turb}$ and $Tu$ were set at the inlet. The flow at the inlet was normal to the inlet boundary ($\beta_{in} = 0$). Because no data for the turbulence dissipation was available, the turbulence length scale was estimated to be within the range of 0.5 to 5% of the chord length. In the present work, the results

| Case | $Tu_{in}$ | $l_{turb,in}$ | $p_{tot,in}$ | $T_{tot,in}$ | $p_{stat,out}$ | $T_w$ | $Ma_{is,out}$ | $Re_{is,out}$ |
|---|---|---|---|---|---|---|---|---|
| | % | mm | Pa | K | Pa | K | − | − |
| MUR132 | 0.8 | 2.05 | 1.757E5 | 408.5 | 1.289E5 | 299.75 | 0.680 | 0.9660E6 |
| MUR235 | 6 | 2.05 | 1.828E5 | 413.3 | 1.049E5 | 301.15 | 0.927 | 1.1521E6 |
| MUR245 | 4 | 2.05 | 3.384E5 | 412.6 | 1.949E5 | 300.75 | 0.924 | 2.1343E6 |
| MUR241 | 6 | 2.05 | 3.257E5 | 416.4 | 1.547E5 | 299.75 | 1.089 | 2.1139E6 |

Table 4.6.: MUR boundary conditions (see Arts et. al. [75])

| $R$ | $\gamma_c$ | $Pr$ |
|:---:|:---:|:---:|
| J/kg K | – | – |
| 287 | 1.4 | 0.72 |

Table 4.7.: MUR fluid properties
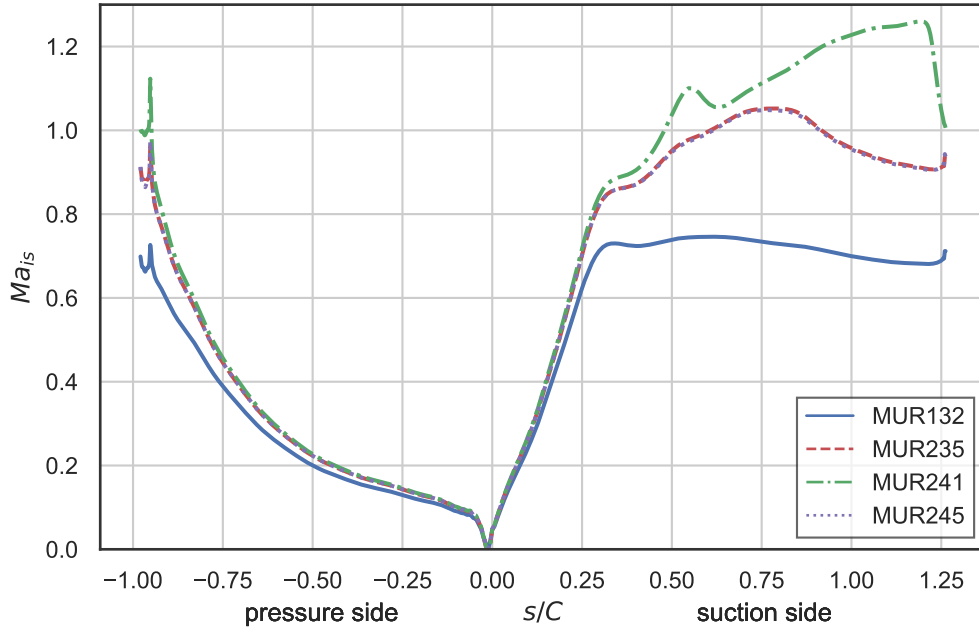


Figure 4.25.: Comparison of the isentropic Mach number $Ma_{is}$ around the blade, for all investigated MUR boundary conditions, obtained by LINARS for the SST turbulence model over the relative coordinate $s/C$ along the blade.

for a turbulence length scale $l_{\text{turb}} = 2.05\,\text{mm}$ are presented. The static pressure $p_{\text{stat}}$ was set at the outlet and the wall boundary conditions were chosen for a smooth wall with a constant temperature $T_w$. Periodic boundary conditions were set at the upper and lower domain boundaries, into the $y$-direction. As fluid air as an ideal gas was selected, where the viscosity $\mu$ was determined by Sutherland's law and the thermal conductivity $\lambda$ was calculated from the definition of the Prandtl number (Eq. (2.17)). Table 4.7 lists the used fluid properties.

Figure 4.25 shows the isentropic Mach number obtained from

$$Ma_{\text{is}} = \sqrt{\left(\left(\frac{p_{\text{tot, in}}}{p}\right)^{\frac{\gamma_c-1}{\gamma_c}} - 1\right)\frac{2}{\gamma_c - 1}}. \tag{4.6}$$

Due to the similar pressure ratio of the cases **MUR235** and **MUR245** a comparable distribution of the local isentropic Mach number can be observed. A distinction lies in the outlet Reynolds number, where the **MUR245** case shows almost double the value compared to **MUR235**. On the pressure side, the flow for all cases smoothly accelerates to the trailing edge, where for the high Mach number boundary condition (**MUR241**) an exit shock is present. On the suction side, all flows smoothly accelerate to $s/C \approx 0.3$. For the low-velocity boundary conditions (**MUR132**) then a plateau is reached. Further downstream, the isentropic Mach number is slightly reduced, resulting in a mildly adverse pressure gradient. For the two cases with the similar pressure ratio (**MUR235** and **MUR245**), after the short plateau the flow accelerates to a transonic state ($Ma_{\mathrm{is}} > 1$), reaching its maximum isentropic Mach number at $s/C \approx 0.75$, where it is constant for a short region. Afterward, the isentropic Mach number is reduced, where an adverse pressure gradient is encountered. The high-velocity case (**MUR241**) shows similar behavior with the short plateau at $s/C \approx 0.3$, but accelerates faster to a transonic state where at $s/C \approx 0.55$ the isentropic Mach number decreases due to the interaction with the inner branch of the exit shock of the neighboring blade. Further downstream the isentropic Mach number increases again until it reaches its maximum close to the trailing edge, where then an exit shock is encountered.

### 4.3.3. Evaluation procedure

Figures 4.27, 4.30, 4.33, and 4.36 plot the local heat transfer coefficient $\alpha$ (Eq. (4.7)) over the relative blade coordinate $s/C$ with its origin at the theoretical stagnation point. Negative values for $s/C$ correspond to the pressure side and positive values to the suction side, respectively. Similar to the wall shear stress magnitude $\tau_w$ a rapid increase in the heat flux $q_w$ and therefore in the heat transfer coefficient $\alpha$ indicates transition from laminar to turbulent flow. Results for all investigated models are plotted together with the prediction for the SST model as the fully turbulent base-line. The measurements are plotted as circular markers and the grayed area represents the measurement uncertainty according to Arts et. al [75]. The local heat transfer coefficient is defined in reference to the difference of the total inlet temperature and the wall temperature as

$$\alpha = \frac{q_w}{T_{\mathrm{tot,\ in}} - T_w},$$

(4.7)

where $q_w$ is the local heat flux at the wall.

For all investigated flow cases, first contour plots obtained with the SST turbulence model for the Mach number and the streamwise acceleration of the flow field are presented. Then predictions for the heat transfer coefficient $\alpha$ for all investigated models are compared to the measurements obtained by Arts et. al. [75]. Finally, plots,

where the region around the blades is greatly magnified by plotting the turbulence kinetic energy $k$ on a curvilinear grid, where the wall-normal coordinate is the dimensionless wall distance $y^+$ plotted on a logarithmic scale. The coordinate along the wall is rescaled by the axial chord length ($s/C$). These plots were inspired by Pecnik et. al. (see for example [76]).

### 4.3.4. MUR132 – Model comparison



(a) Mach number $Ma$ $[-]$        (b) Streamwise acceleration $dU/ds$ $[1/s]$
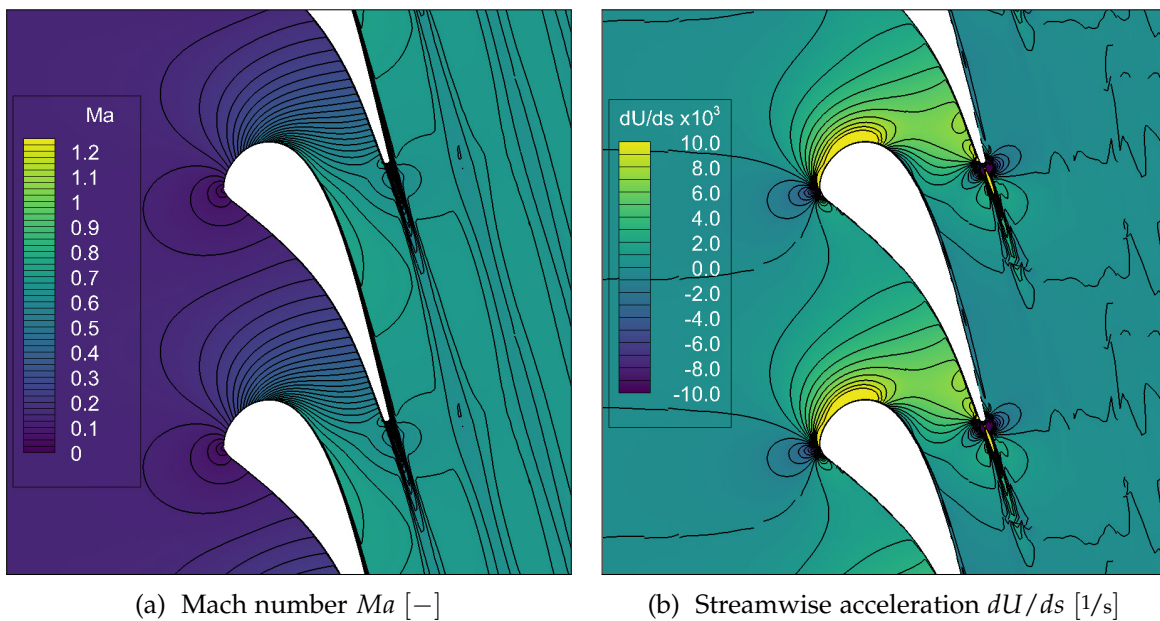
Figure 4.26.: Predictions of (a) the Mach number and (b) the streamwise acceleration in the flow field, obtained by LINARS with the SST turbulence model for the MUR132 case.

These boundary conditions were selected due to their very low free stream turbulence at the inlet of $Tu = 0.8\%$ and overall low Reynolds number. Predictions of the Mach number of the flow field can be seen in Figure 4.26, together with a prediction of the stream-wise acceleration. As described previously, the acceleration on the pressure side is smooth and steady until the trailing edge. On the suction side, after smooth acceleration to $Ma \approx 0.75$ the velocity stagnates and subsequently reduces towards the trailing edge, resulting in a mildly adverse pressure gradient seeing by the negative acceleration, there are no shocks present in the flow field.

Figure 4.27 shows the local heat coefficient $\alpha$ along the blade as predicted by the investigated transition models, together with the measurement and predictions from the SST turbulence model. All transition models predict laminar flow along the

Figure 4.27.: Heat transfer coefficient $\alpha$ over the relative coordinate $s/C$ for all investigated models as obtained by LINARS for the MUR132 case.

pressure side, which correlates very well with the measurement. On the suction side, the $\gamma$-$Re_{\theta t}$ and the $\gamma$ model predict laminar flow up to the trailing edge. The $k$-$\overline{v^2}$-$\omega$ model shows transition onset briefly before the flow separates from the blade and the $k$-$k_L$-$\omega$ model predicts transition onset further upstream at $s/C \approx$ 1.1 which is in remarkably good agreement with the measurements. Interestingly, pseudo-transitional behavior of the fully turbulent SST model can be seen. This is caused by the Kato and Launder formulation of the production term (Eq. (2.72)) for the turbulence kinetic energy. As described in the mathematical formulation of the SST model (see section 2.3.3), the Kato and Launder formulation avoids the unphysical production of turbulence kinetic energy near a stagnation point by using the magnitude of the vorticity tensor together with the mean value of the strain-rate tensor and exploiting the fact that the flow near a stagnation point is nearly irrotational, i. e. $\Omega \approx 0$.

Figure 4.28 shows a comparison for the turbulence kinetic energy $k$ in proximity to the wall for all investigated transition models together with a prediction obtained from the SST turbulence model. It can be seen that the $\gamma$ and the $\gamma$-$Re_{\theta t}$ model suppress the production of turbulence kinetic energy of the underlying SST model to the wake of the blade and the flow stays laminar on both sides. Both physics-based models start with production of $k$ close to the trailing edge on the suction side at

Figure 4.28.: Predictions of the turbulence kinetic energy $k$ in proximity to the wall, for all investigated transition models together with the prediction obtained with the turbulence model *SST* for the MUR132 boundary conditions.

$s/C \approx 1.1$, but for the $k\text{-}\overline{v^2}\text{-}\omega$ model the turbulence kinetic energy is concentrated in a thin layer, resulting in later transition onset, as seen in Figure 4.27. For the SST model it is also interesting, that the steady rise of $\alpha$ on the pressure side is not reflected by any noticeable production of turbulence kinetic energy, until $s/C \approx 0.7$. On the other hand, on the suction side the pseudo-transitional behavior is comprehensibly reflected by production of turbulence kinetic energy.

### 4.3.5. MUR235 – Model comparison



(a) Mach number $Ma$ $[-]$       (b) Streamwise acceleration $dU/ds$ $[1/\text{s}]$
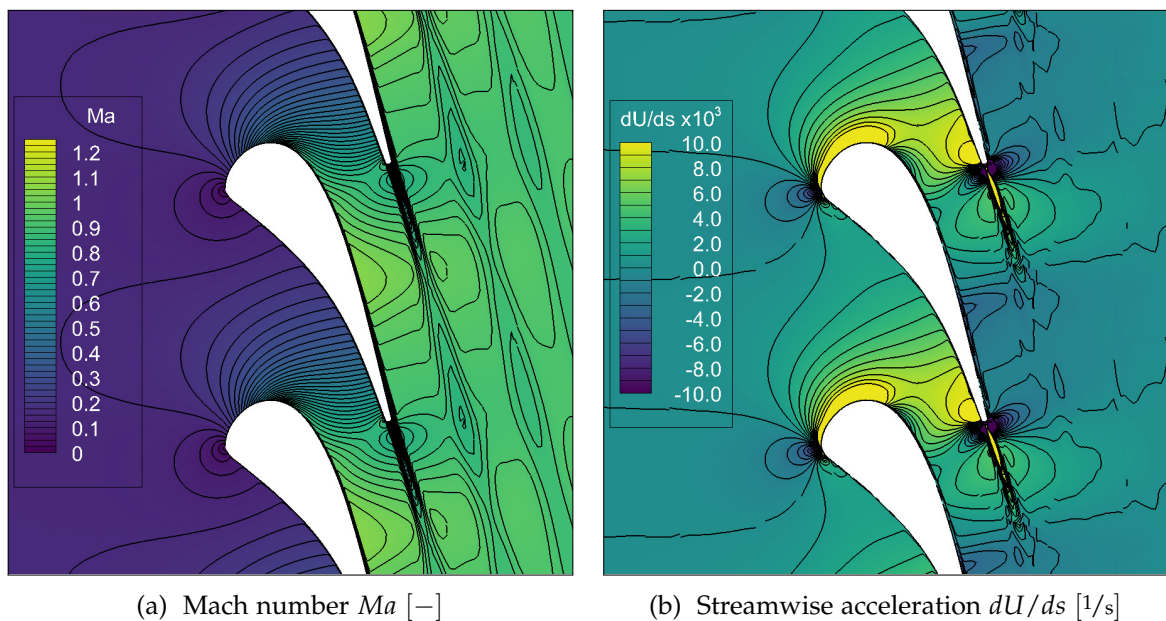
Figure 4.29.: Predictions of (a) the Mach number and (b) the streamwise acceleration in the flow field, obtained by LINARS with the SST turbulence model for the MUR235 test case.

Figure 4.29 again shows the Mach number and the streamwise acceleration together with isolines in the flow field as predicted by the SST turbulence model. The Mach number briefly reaches $Ma \approx 1$ at $s/C \approx 0.75$ on the suction side but decreases to sub-sonic conditions again. From the streamwise acceleration, it can be seen that acceleration on the pressure side steadily increases to the trailing edge, and on the suction side strong acceleration is encountered in proximity of the stagnation point, whereas in the downstream section of the blade an adverse pressure gradient is present. No shocks are present in the flow field.

Figure 4.30 again shows the local heat transfer coefficient $\alpha$ for all investigated models. Interestingly, it can be seen that the physics-based models yield a lower value for $\alpha$
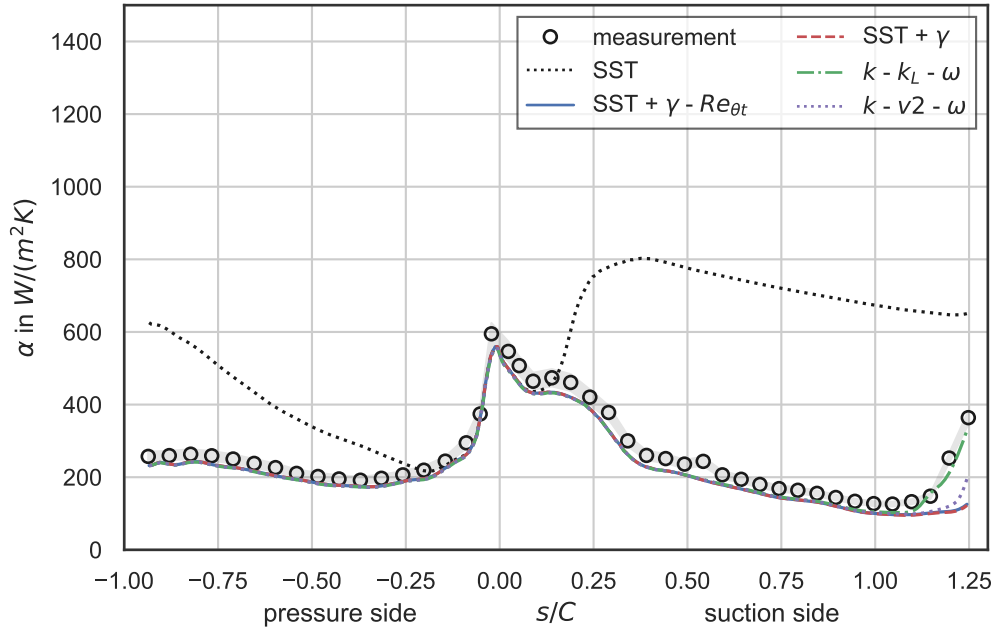
Figure 4.30.: Heat transfer coefficient $\alpha$ over the relative coordinate $s/C$ for all investigated models as obtained by LINARS for the MUR235 case.

near the stagnation point, which also influences the further distribution of the local value downstream on the pressure side. All transition models predict laminar flow on the pressure side and underestimate the value compared to the measurements significantly. On the other hand, the fully turbulent SST model overpredicts the value on the pressure side and the pseudo-transitional behavior can again be seen on the suction side. The difference of the prediction of $\alpha$ in the stagnation point between the SST based models and the physics-based models also influences the downstream prediction on the suction side, to $s/C \approx 0.25$, where all transitional predictions agree. The flow stays laminar to $s/C \approx 0.75$, where the $\gamma$-$Re_{\theta t}$ model predicts transition onset first. The other transition models predict the transition onset at $s/C \approx 1.0$, where the $k$-$k_L$-$\omega$ and the $k$-$\overline{v^2}$-$\omega$ model show similar and the $\gamma$ model a very short transition length. The value for $\alpha$ in the turbulent region is predicted in good agreement to the measurements, where the $\gamma$ model overshoots the measurement by a small amount. Overall it can be said that the $\gamma$-$Re_{\theta t}$ model offers the best prediction, compared to the measurement.

In Figure 4.28 $k$ in proximity to the wall is plotted largely magnified. For the LCTMs it can be seen that the production of turbulence kinetic energy of the underlying SST model is suppressed prior to transition onset, as expected. The plot for the $k$-$k_L$-$\omega$ model shows expected behavior as well, but for the $k$-$\overline{v^2}$-$\omega$ model spurious
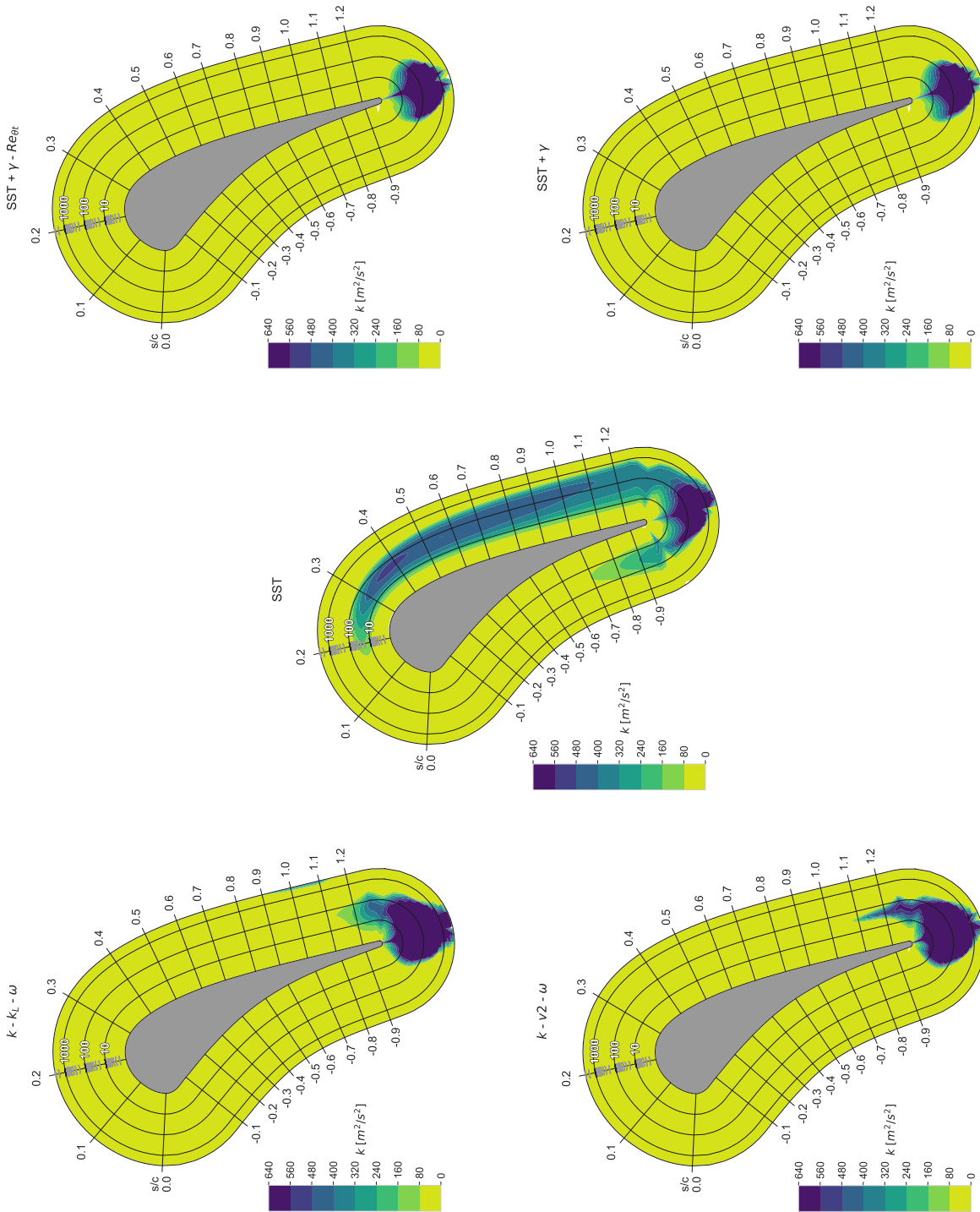
97

Figure 4.31.: Predictions of the turbulence kinetic energy *k* in proximity to the wall, for all investigated transition models together with the prediction obtained with the turbulence model *SST* for the MUR235 boundary conditions.

production of turbulence kinetic energy in the region $100 < y+ < 100$ can be seen, which most certainly is not intended, and it is interesting that this does not influence the transitional behavior of the model since the $k$-$k_L$-$\omega$ and the $k$-$\overline{v^2}$-$\omega$ model both yield a similar prediction of the local heat transfer coefficient as seen in Figure 4.30.

### 4.3.6. MUR245 – Model comparison



(a) Mach number $Ma$ $[-]$     (b) Streamwise acceleration $dU/ds$ $[1/\mathrm{s}]$

Figure 4.32.: Predictions of (a) the Mach number and (b) the streamwise acceleration in the flow field, obtained by LINARS with the SST turbulence model for the MUR245 case.

Figure 4.32 depicts the Mach number and the streamwise acceleration for the flow field, predicted by the SST turbulence model. Due to the similar pressure ratio between inlet to outlet to case MUR235 the Mach number is very similar. The main difference is the higher Reynolds number, which leads to an overall increased heat-transfer coefficient by about $200\,\mathrm{W/m^2\,K}$ (see Fig. 4.33). Even though a weak pressure side shock could be suspected there are no shocks present in the flow field.

Figure 4.33 shows the predictions of the local heat transfer coefficient $\alpha$ as predicted by the investigated transition models, together with the prediction obtained by the SST turbulence model. Close to the stagnation point, a noteworthy difference between the SST based LCTMs and the physics-based model can be seen. The pseudo-transitional behavior of the SST model is now limited to a very short region close to the stagnation point. On the suction side, predictions of all transition models merge at $s/C \approx 0.25$
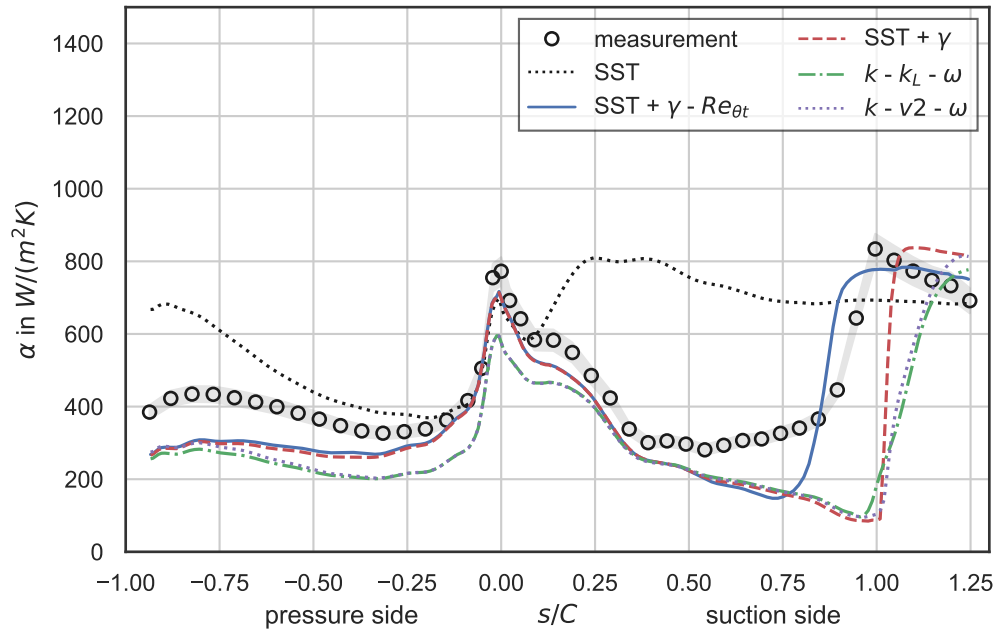
Figure 4.33.: Heat transfer coefficient $\alpha$ over the relative coordinate $s/C$ for all investigated models as obtained by LINARS for the MUR245 case.

and transition onset is predicted by all models at $s/C \approx 0.95$ with short transition lengths. All models underpredict the value of $\alpha$ starting from $s/C \approx 0.3$, to the transition onset, and overpredict it in the fully turbulent region. But the transition onset location correlates remarkably well with the measurement. On the pressure side, interestingly, the physics-based models predict transitional behavior, while the flow is predicted to be laminar up to the trailing edge by the LCTMs, a behavior on the pressure side that was already encountered in the VKI test case. The SST model yields a similar trend as the measurement but overestimates the value constantly by about $150\,\mathrm{W/m^2\,K}$. The physics-based models largely overestimate the value inside the fully turbulent region. The $k$-$k_L$-$\omega$ model predicts a slightly retarded transition onset at $s/C \approx -0.5$ compared to the $k$-$\overline{v^2}$-$\omega$ model at $s/C \approx -0.35$ on the pressure side.

Figure 4.34 shows the value for $k$, where we can again see that the $\gamma$-$Re_{\theta t}$ and $\gamma$ model suppress the production of turbulence kinetic energy from the underlying SST model prior to the transition onset. For the physics-based models, a behavior which correlates with the plot for $\alpha$ can be seen. Again the $k$-$\overline{v^2}$-$\omega$ model shows spurious production of turbulence kinetic energy in the region $100 < y+ < 100$, however the prediction of the transition onset is not affected.
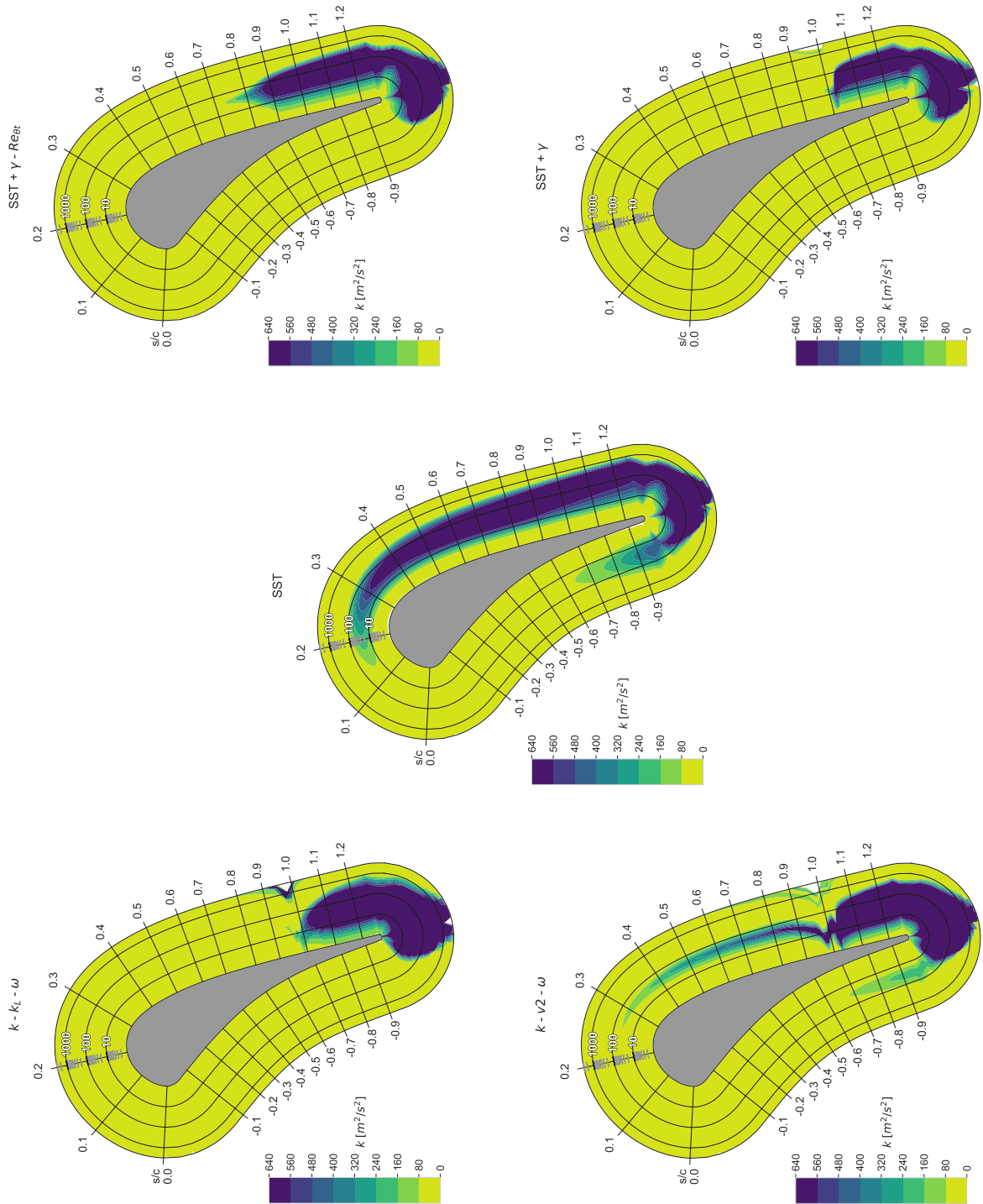
Figure 4.34.: Predictions of the turbulence kinetic energy *k* in proximity to the wall, for all investigated transition models together with the prediction obtained with the turbulence model *SST* for the MUR245 case.

### 4.3.7. MUR241 – Model comparison



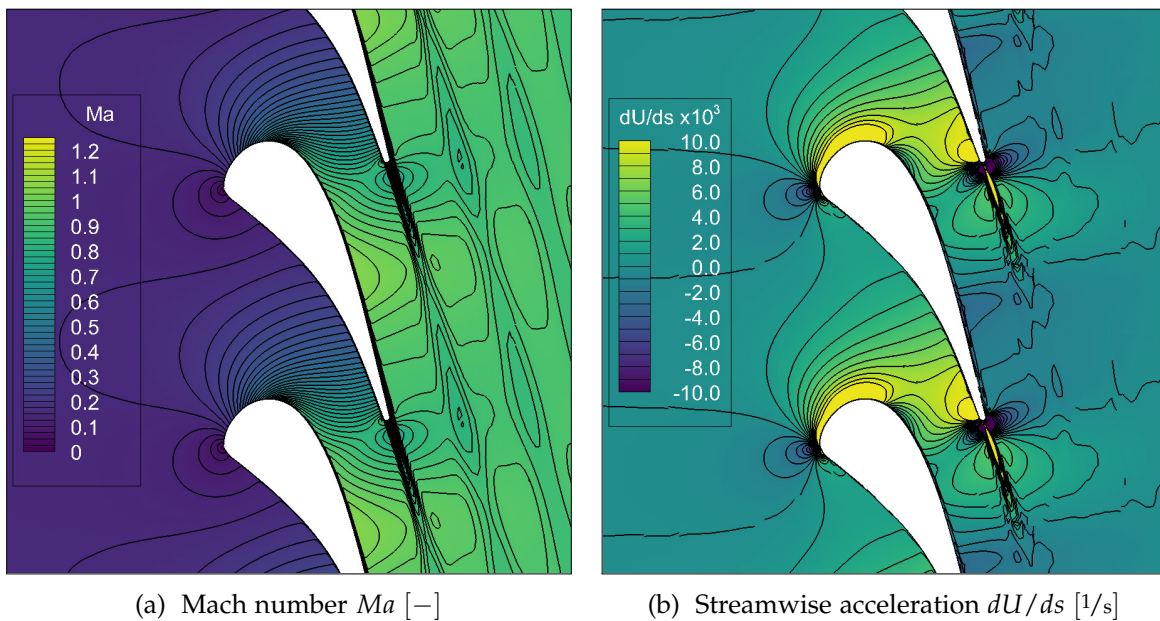(a) Mach number $Ma$ $[-]$      (b) Streamwise acceleration $dU/ds$ $[1/s]$
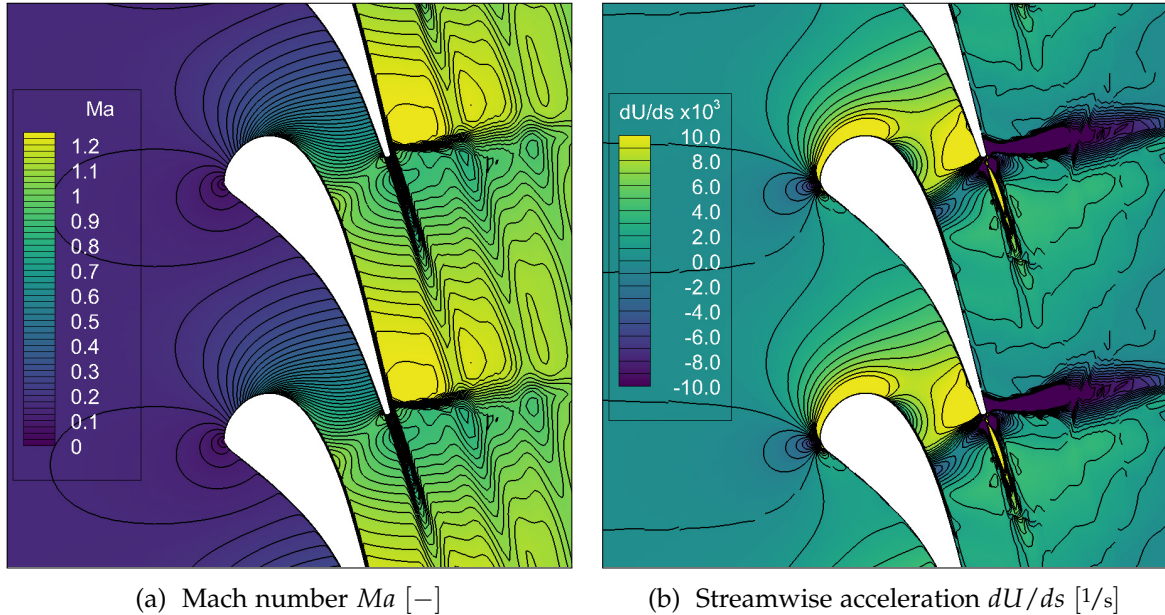
Figure 4.35.: Predictions of (a) of Mach number and (b) the streamwise acceleration in the flow field, obtained by LINARS with the SST turbulence model for the MUR241 case.

Figure 4.35 shows the Mach number and the streamwise acceleration as obtained by the SST turbulence model for the flow field. On the pressure side continuous acceleration can be seen, which shortly before the trailing edge reaches a transonic state. On the suction side, as discussed, a hump in the distribution of the Mach number can be seen and is caused by the inner branch of the exit shock (pressure side shock). Subsequently the flow accelerates until the maximal Mach number of $Ma \approx 1.25$ is reached near the trailing edge. A favorable pressure gradient is encountered in this section, which could result in relaminarization or at least stalling of the transition process. On the suction side an exit shock is visible which cuts the wake of the blade.

Figure 4.36 shows the local heat transfer coefficient $\alpha$ along the blade for all investigated models. Near the stagnation point a noteworthy difference in the predictions between the SST based models and the physics-based models can be seen, where the LCTMs predict the flow more accurately. On the suction side the predictions merge at $s/C \approx 0.3$ and further downstream all models predict transition onset. First the $\gamma\text{-}Re_{\theta t}$ model, at $s/C \approx 0.6$ shortly followed by the $k\text{-}\overline{v^2}\text{-}\omega$ model at $s/C \approx 0.75$. Further downstream, the $\gamma$ and the $k\text{-}k_L\text{-}\omega$ model predict transition at the same location $s/C \approx 0.9$. The measurement shows transition onset, similar to the $\gamma\text{-}Re_{\theta t}$ and $k\text{-}\overline{v^2}\text{-}\omega$
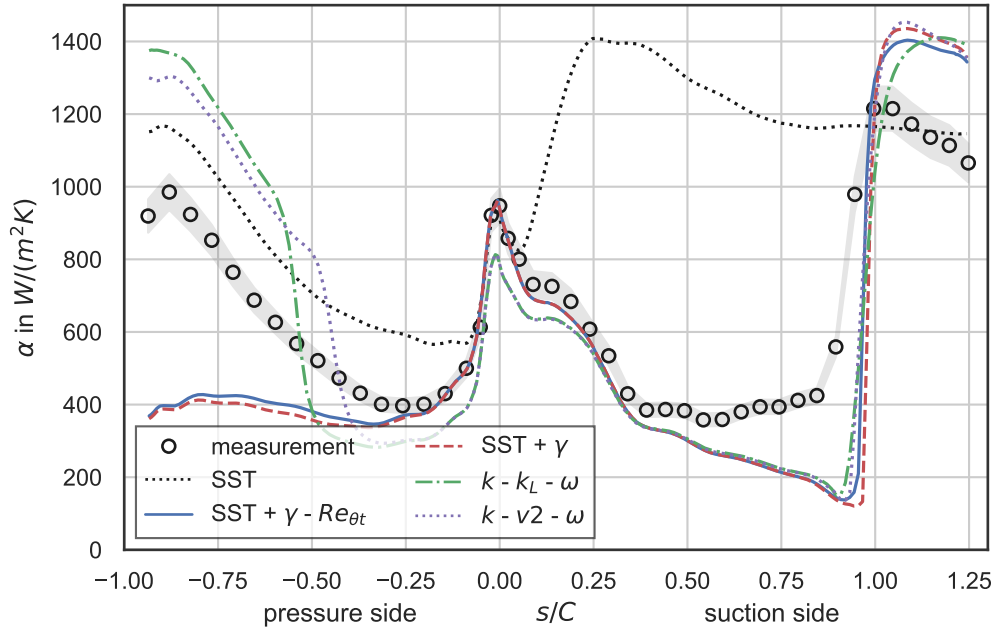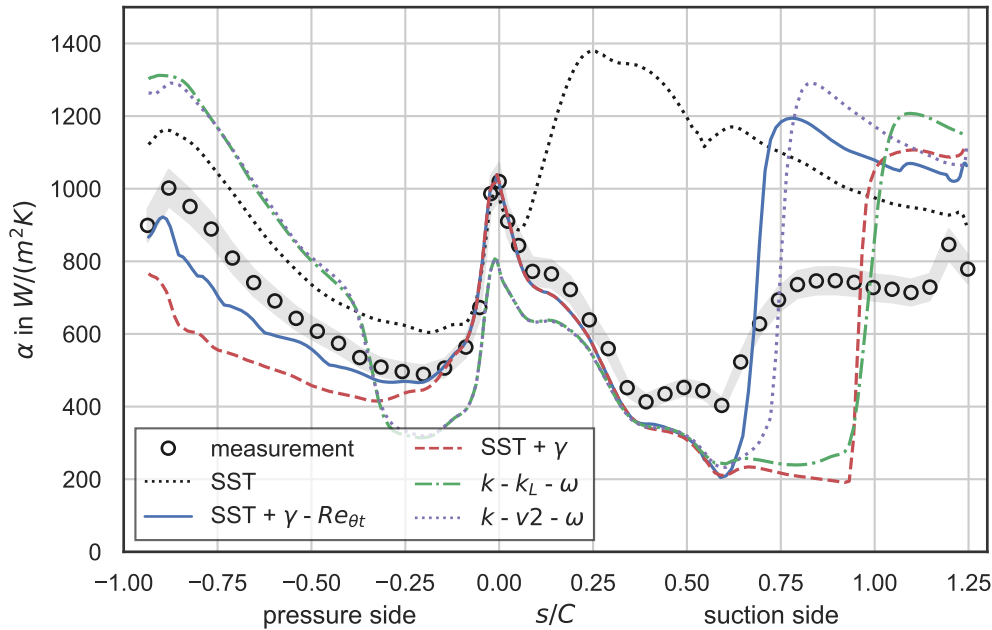
Figure 4.36.: Heat transfer coefficient $\alpha$ over the relative coordinate $s/C$ for all investigated models as obtained by LINARS for the MUR241 case.

model but the transition process seems to halt shortly afterward at $s/C \approx 0.8$, and finally transition occurs not before the trailing edge at $s/C \approx 1.2$. This behavior, caused by the favorable pressure gradient, is not captured by any of the models. Also, the value for $\alpha$ is again overpredicted in the fully turbulent region by all models. On the pressure side, it can be seen that the $\gamma$ model seems to predict laminar flow, while the $\gamma$-$Re_{\theta t}$ model yields a value between the laminar and turbulent solution. This prediction is in good agreement with the measurement. The $k$-$\overline{v^2}$-$\omega$ and the $k$-$k_L$-$\omega$ model both show early transition onset at $s/C \approx -0.3$ and stay fully turbulent thereafter, where the actual value for $\alpha$ is again significantly overpredicted.

Figure 4.37 shows the value for $k$ in proximity to the wall. On the pressure side, it can be seen, that both the $\gamma$ and the $\gamma$-$Re_{\theta t}$ model predict transition onset close to the trailing edge. It is not completely clear why the $\gamma$ and $\gamma$-$Re_{\theta t}$ model differ so much for $\alpha$. On the pressure side we see that the LCTMs suppress production of the turbulence kinetic energy of the underlying SST turbulence model. As previously observed the $k$-$\overline{v^2}$-$\omega$ model suffers from a spurious production of $k$, which, however, has no apparent influence on the actual value of $\alpha$ in the laminar region. This behavior was observed for several boundary conditions and could be caused by a blending or shielding function failing in the detecting of the boundary layer.
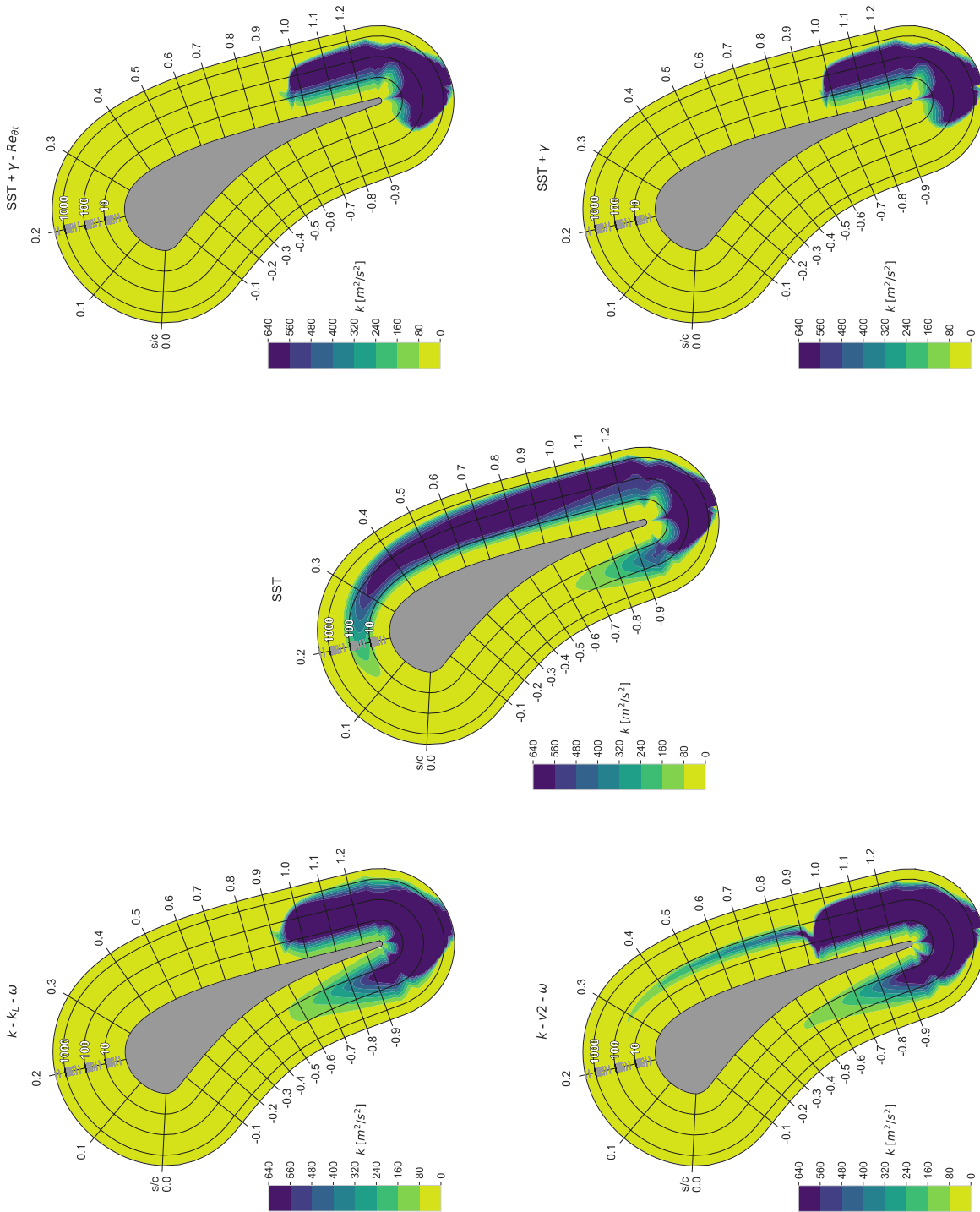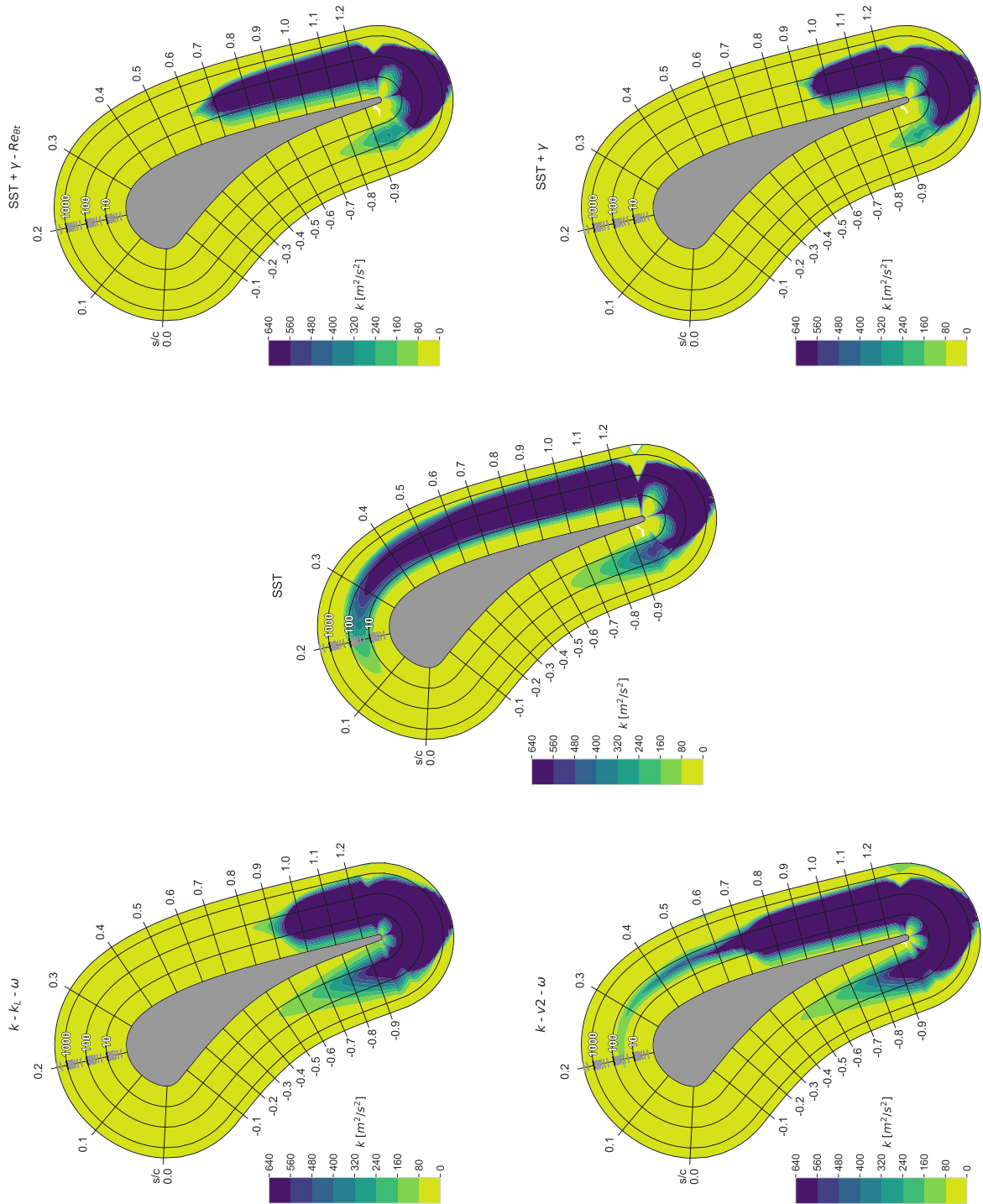
Figure 4.37.: Predictions of the turbulence kinetic energy $k$ in proximity to the wall, for all investigated transition models together with the prediction obtained with the turbulence model $SST$ for the MUR241 case.

### 4.3.8. Conclusion

From the accurate measurements of the heat-transfer along the vane obtained by Arts et. al. [75], four interesting cases were selected. Overall the $\gamma$-$Re_{\theta t}$ model showed the best agreement with the measurements and is not without reason the current industry standard. However, all other transition models predicted the transition onset on the suction side quite accurately, where it was observed that the $\gamma$-$Re_{\theta t}$ model predicts the transition onset further upstream and in better agreement to the measurements than all other models. On the pressure side, the heat-transfer coefficient is either over- or underpredicted vastly and overall no satisfying agreement with the measurement can be observed. Note that for the physics-based transition models alternative formulations for the closure of the turbulent heat-flux vector are available (see Appendix D) which maybe could improve the predictions.

With the help of wall near logarithmic plots of the turbulence kinetic energy, an unplausible spurious production of $k$ on the suction side was observed with the $k$-$\overline{v^2}$-$\omega$ model. Interestingly no influence on the prediction of the transition onset could be seen. The reason for this unphysical production could be a faulty calibrated shielding or blending function. A more detailed investigation of this irregularity could be worthwhile.

## 4.4. HPS – High pressure stator

For the final test case a two-stage two-spool counter-rotating turbine configuration was selected. It is based on a configuration, which was tested at the Transonic Test Turbine Facility (TTTF) of the ITTM, where the primary focus was on the design of the S-shaped intermediate turbine duct. In order to decrease the length and therefore the weight of an aero-engine an embedded duct design was developed, where the high pressure stator vanes were integrated into the duct design. This was done by arranging additional splitter blades between the aerodynamically optimized struts. The geometry of the splitters is highly optimized in order to homogenize the flow and provide a uniform inflow to the low pressure rotor (see for example the doctoral thesis of Spataro [77]). Figure 4.38 shows the blades in the duct. Similar to Bader and Sanz [78], who applied the $\gamma$-$Re_{\theta t}$ transition model, the capability of the in this thesis considered models on predicting boundary layer relaminarization was examined. Relaminarization is especially expected for the highly accelerated flow around the high pressure stator (HPS), hence the predictions for this subdomain are presented in this chapter. For a more general investigation of this and similar test cases see for example the work of Akin and Sanz [79], Bader and Sanz [80] or Spataro et. al. [81].



(a) Inlet to outlet view        (b) Outlet to inlet view
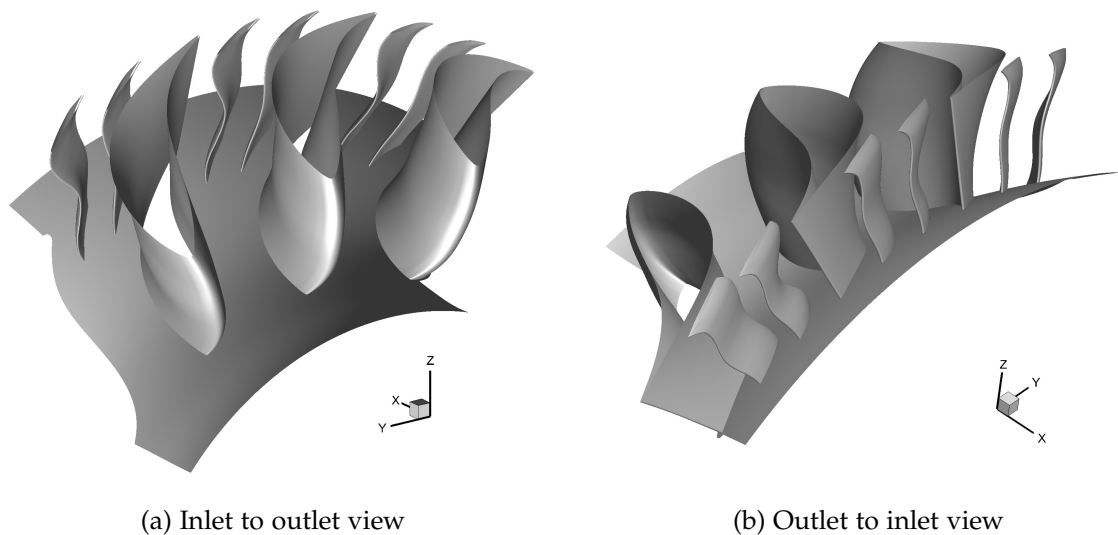
Figure 4.38.: Embedded duct design, where additional splitters are arranged between the struts. (a) shows the design from the inlet to the outlet and (b) offers a view from the opposite direction.

### 4.4.1. Computational domain

Figure 4.39 shows a close-up of the mesh for the HPS, where every second grid line of the wall-layer is shown. The shroud wall was hidden in order to provide an unobstructed view on the pressure and suction side of the HPS and the hub-wall grid lines.

Figure 4.40 shows the meridional contour together with the mesh for the computational domain, where plane $A$ is the inlet section and $F$ is the outlet. Planes $B$, $C$, $D$ and $E$ are interfaces between stationary and rotating domains. The high pressure rotor (HPR) and low pressure rotor (LPR) are counter-rotating with independent rotational speeds $n_r$ and connected by a S-shaped duct with an embedded design, termed turning mid turbine frame (TMTF). Table 4.8 lists the number of blades, vanes, and struts together with the height to axial chord length ratio $h/C$. The 16 struts of the TMTF are accompanied by 32 splitters. The mesh was generated by the meshing software AiGrid3D [53] and provided by ITTM. It consists of approximately 6.3 million cells and was split into 27 blocks for parallelization of the computation. The dimensionless wall distance for the first cell is between $0.1 \leq y^+ \leq 1$ for the most part and mesh independence studies were carried out by Bader and Sanz [78]. All computational results were obtained by the in-house solver LINARS.

| | HPS | HPR | TMTF | LPR |
|---|---|---|---|---|
| count | 24 | 36 | 16 | 72 |
| $h/C$ | 1.15 | 1.37 | 0.53 | 2.94 |

Table 4.8.: Blade, respectively, vane count and height to axial chord ratio $h/C$ for the subdomains of the HPS test case [81].

### 4.4.2. Boundary conditions and fluid properties

| | | | | | |
|---|---|---|---|---|---|
| $n_{r,HPR}$ | $-1151.917$ | $1/\mathrm{min}$ | $Tu_{in}$ | 10 | % |
| $n_{r,LPR}$ | $371.76$ | $1/\mathrm{min}$ | $l_{turb,in}$ | 1 | mm |
| $p_{tot,in}$ | $3.85\mathrm{E}5$ | Pa | $\beta_{in}$ | 0 | ° |
| $T_{tot,in}$ | $433.15$ | K | $p_{stat,out}$ | $3.85\mathrm{E}5$ | Pa |

Table 4.9.: HPS Boundary conditions

The inlet is positioned at plane $A$, where total pressure $p_{tot}$, total temperature $T_{tot}$, the inlet flow angle $\beta_{in}$ and the turbulence boundary conditions $Tu$ and $l_{turb}$ were prescribed. The flow at the inlet was set normal to the inlet boundary, i. e. $\beta_{in} = 0$.
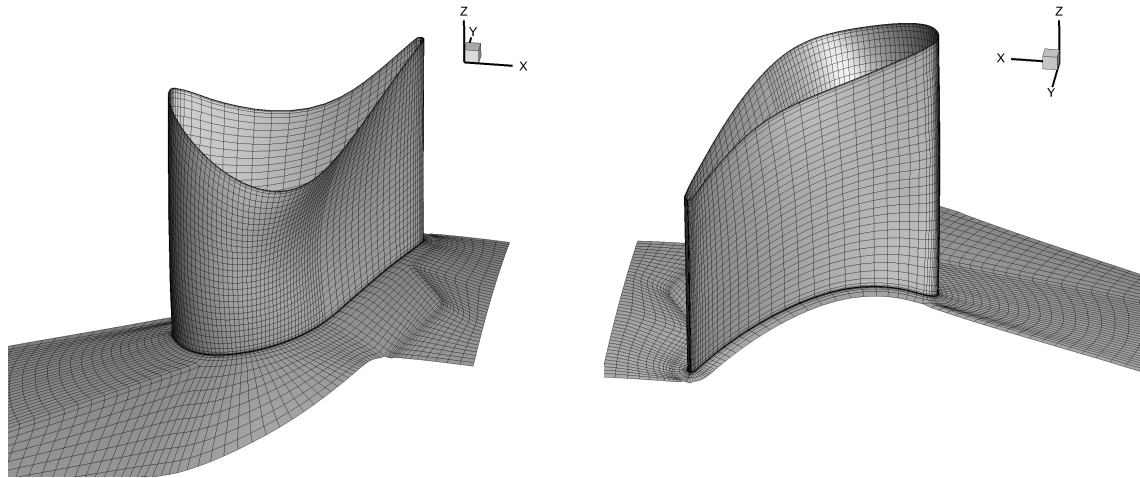
Figure 4.39.: Boundary layer mesh for the HPS and the hub, where every second grid-line is plotted.

The outlet is located at plane $F$, where static pressure $p_{stat}$ was set. For all blades, vanes, the hub and the shroud boundary conditions for adiabatic smooth walls were prescribed. The blades of the HPR and the LPR are counter-rotating, where the rotational speeds $n_r$ were specified. For the domain interfaces between rotating and stationary domains (planes $B$, $C$, $D$, $E$) a mixing plane approach is used. In that case, a circumferential averaging of flow quantities on radial bands is done. Additionally, tip leakage is considered for the HPR blades. Into the circumferential direction periodic boundary conditions were selected. As fluid, air as an ideal gas was chosen, where the viscosity $\mu$ was determined by Sutherland's law and the thermal conductivity $\lambda$ was calculated from the definition of the Prandtl number (Eq. (2.17)). Table 4.9 lists the boundary conditions and Table 4.10 summarizes the fluid properties.

| $R$ | $\gamma_c$ | $Pr$ |
|---|---|---|
| J/kg K | — | — |
| 287 | 1.4 | 0.72 |

Table 4.10.: HPS Fluid properties

Figure 4.41 shows the Mach number distribution in the flow field around the HPS on an evaluation plane at mid span obtained with the SST turbulence model. Subfigure 4.41a illustrates the position of the evaluation plane in a three-dimensional isometric view and Subfig, 4.41b provides a view from the top. At the trailing edge suction side a strong exit shock can be seen. On the pressure side a weaker shock originates, which is reflected on the suction side at mid chord. This results in a region on the suction side, where the velocity magnitude is approximately constant.
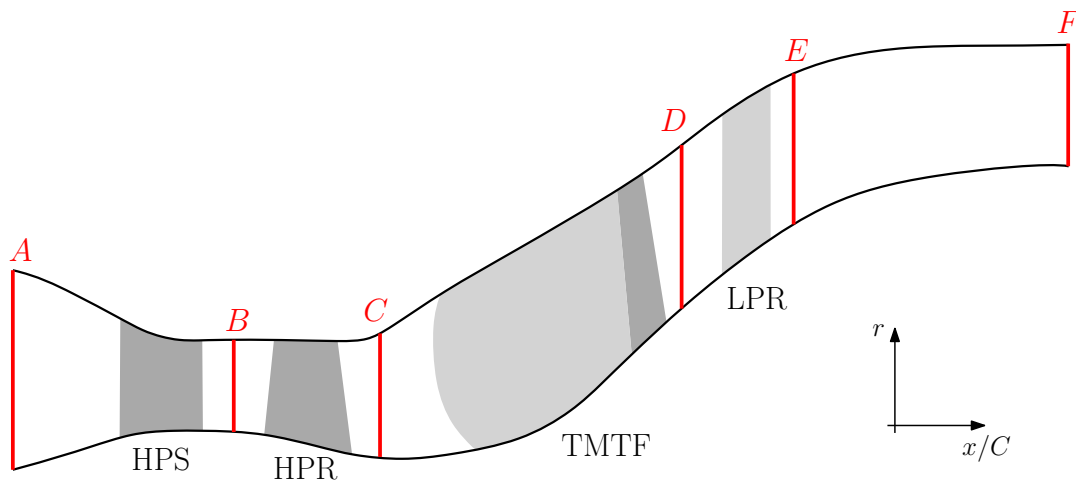
(a) Meridional contour (adopted from Bader and Sanz [78])
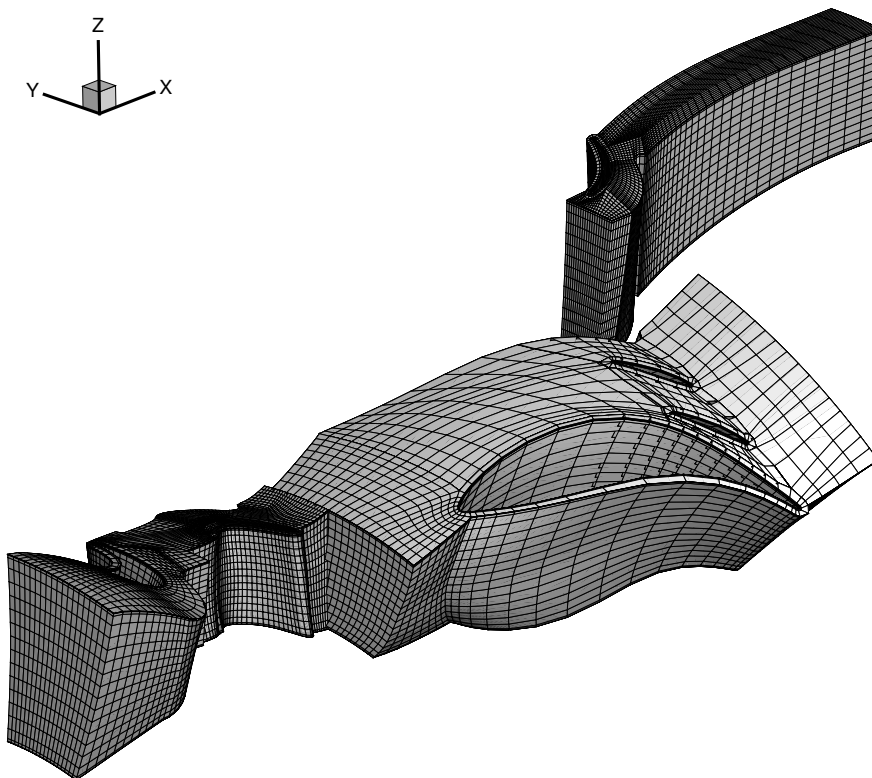


(b) Computational mesh

Figure 4.40.: Meridional contour (a) together with the grid (b) for the complete computational domain of the HPS test case, where every fourth grid line is plotted.
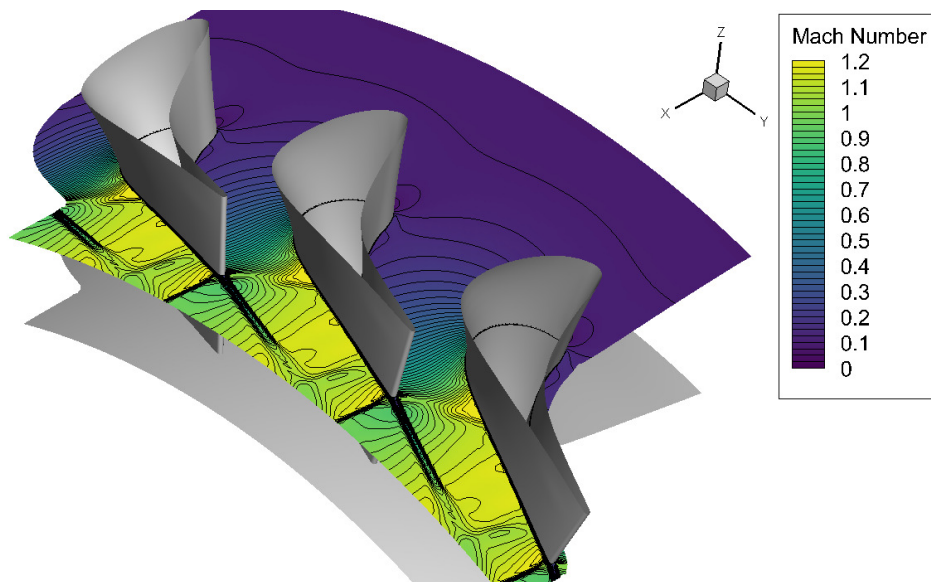
(a) Isometric view of the position of the mid span evaluation plane
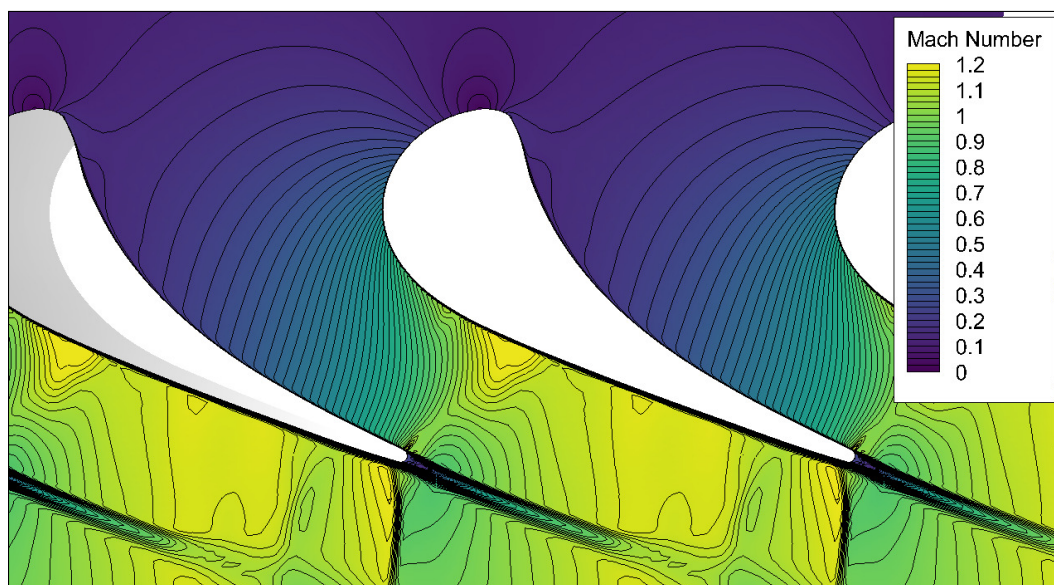


(b) Top view on the evaluation plane

Figure 4.41.: Contour plots of the Mach number together with iso-lines at mid span, where (a) illustrates the position of the evaluation plane at mid span and (b) shows it from top.

### 4.4.3. Model comparison

In order to visualize the predictions for the transition onset in a three-dimensional view, two intermittency like variables, termed $\gamma^*$, were defined for the physics-based models. According to Lopez and Walters [52], the $k$-$\overline{v^2}$-$\omega$ model yields $\overline{v^2} = k$ for fully turbulent regions and $\overline{v^2} < k$ for transitional regions. The intermittency like variable then is defined as the ratio

$$\gamma^* = \frac{\overline{v^2}}{k}.$$  (4.8)

For the $k$-$k_L$-$\omega$ model the ratio of the turbulence kinetic energy $k$ to the total kinetic energy $(k_L + k)$ is used as a transition indicator:

$$\gamma^* = \frac{k}{k_L + k}$$  (4.9)

Figure 4.42 displays the intermittency $\gamma$ and the transition indicator variable $\gamma^*$ for the ninth cell layer away from the vane wall and the seventh cell layer away from the hub. Pressure and suction side are plotted separately.

On the suction side transition onset of the LCTMs is observed throughout the whole span of the vane at a similar position, which is in proximity where the weak shock originating from the pressure side impacts. Although two significant differences can be seen. In the upper region of the vane, it appears that the transition process halts for a brief section with the $\gamma$-$Re_{\theta t}$ model, while for the $\gamma$ model a rapid transition occurs along the whole span. This could be caused by the model design choice, that the $\gamma$-$Re_{\theta t}$ model uses an empirical correlation for the transition length, while it is a constant value for the $\gamma$ model. The second difference is a short spanwise zone of further upstream transition onset in the lower part of the vane, predicted by the $\gamma$ model. The zone is located shortly before the weak shock impacts the suction side of the vane and is reflected subsequently, because the flow field is similar in this region for the $\gamma$-$Re_{\theta t}$ and the $\gamma$ model it is suspected that the $\gamma$ model simply is more sensitive to the change in the pressure gradient.

On the pressure side the predictions of the two LCTMs differ greatly. Downstream of the stagnation point the $\gamma$-$Re_{\theta t}$ model transitions to a fully turbulent state, where in the lower region of the vane partial relaminarization is indicated. The $\gamma$ model on the other hand predicts an intermittent state for the boundary layer and finally transitions to a fully turbulent state close to the trailing edge. At two spanwise positions, the flow stays in the intermittent state to the trailing edge.

The physics-based models predict a similar transition onset location on the suction side with the exception of a knife-like region in the upper third of the vane, where the transition onset is predicted considerably further downstream by the $k$-$\overline{v^2}$-$\omega$ model.

On the pressure side, the $k$-$k_L$-$\omega$ model predicts a comparable transition onset as the $k$-$\overline{v^2}$-$\omega$ model. Overall, the transitional region appears blurred without a sharp edge for the $k$-$k_L$-$\omega$ model which could indicate a longer transition length of the $k$-$k_L$-$\omega$ model or it could be caused by the choice for the transition indicator function $y^*$.

The above described anomalies are investigated in more detail at the end of this section.

Comparing the physics-based models to the LCTMs it is observed that transition onset on the suction side is retarded in the upper region of the vane. The predictions for transition onset on the pressure side look comparable but the physics-based models show no sign of relaminarization.

In order to visualize the effect of the turbulent boundary layer on the flow Figure 4.43 shows contour plots of the local skin friction coefficient $c_f$ for the LCTMs together with the ones obtained with the SST turbulence model as fully turbulent base-line. Figure 4.44 shows the same comparison but for the physics-based models, together with the SST turbulence model as a reference. The high $c_f$ values in the lower region on the suction side of the vane are caused by a separation bubble. On the suction side it can overall be clearly seen that the skin friction value is substantially lower for a laminar boundary layer and that the high $c_f$ value regions coincide with the previously showed turbulent regions.

The predicted values of $c_f$ on the pressure side by the physics-based models are substantially higher than the values obtained from the LCTMs. The $k$-$\overline{v^2}$-$\omega$ model predicts very high values for $c_f$ near the trailing edge on the suction side, even though the flow stays attached to the vane. The cause for this region is explained later in this chapter.

The following investigation of the boundary layer follows the same methodology as given by Bader and Sanz [78]. A quantification of the flow acceleration near the wall is given by the Launder acceleration parameter $K$, which is defined as

$$K = \frac{\nu}{U_\infty^2} \frac{dU_\infty}{ds}, \tag{4.10}$$

where $\nu$ is the kinematic viscosity, $U_\infty$ is the local free-stream velocity magnitude and $dU_\infty/ds$ is the streamwise acceleration at the boundary layer edge. Boundary layer relaminarization is expected for a critical value of 3E-6 $< K_c <$ 3.5E-6 [78]. $K$ has to be evaluated at the edge of the boundary layer, where the boundary layer thickness is determined by the method of Arnone and Pacciani [82] (see Bader and Sanz [78] for further information).

Figure 4.45 and 4.46 show the evolution of the boundary layer thickness $\delta$ together with the Launder acceleration parameter $K$ and the local skin friction coefficient

(a) $\gamma$-$Re_{\theta t}$ suction side

(b) $\gamma$-$Re_{\theta t}$ pressure side

(c) $\gamma$ suction side

(d) $\gamma$ pressure side

(e) $k$-$k_L$-$\omega$ suction side

(f) $k$-$k_L$-$\omega$ pressure side

(g) $k$-$\overline{v^2}$-$\omega$ suction side

(h) $k$-$\overline{v^2}$-$\omega$ pressure side
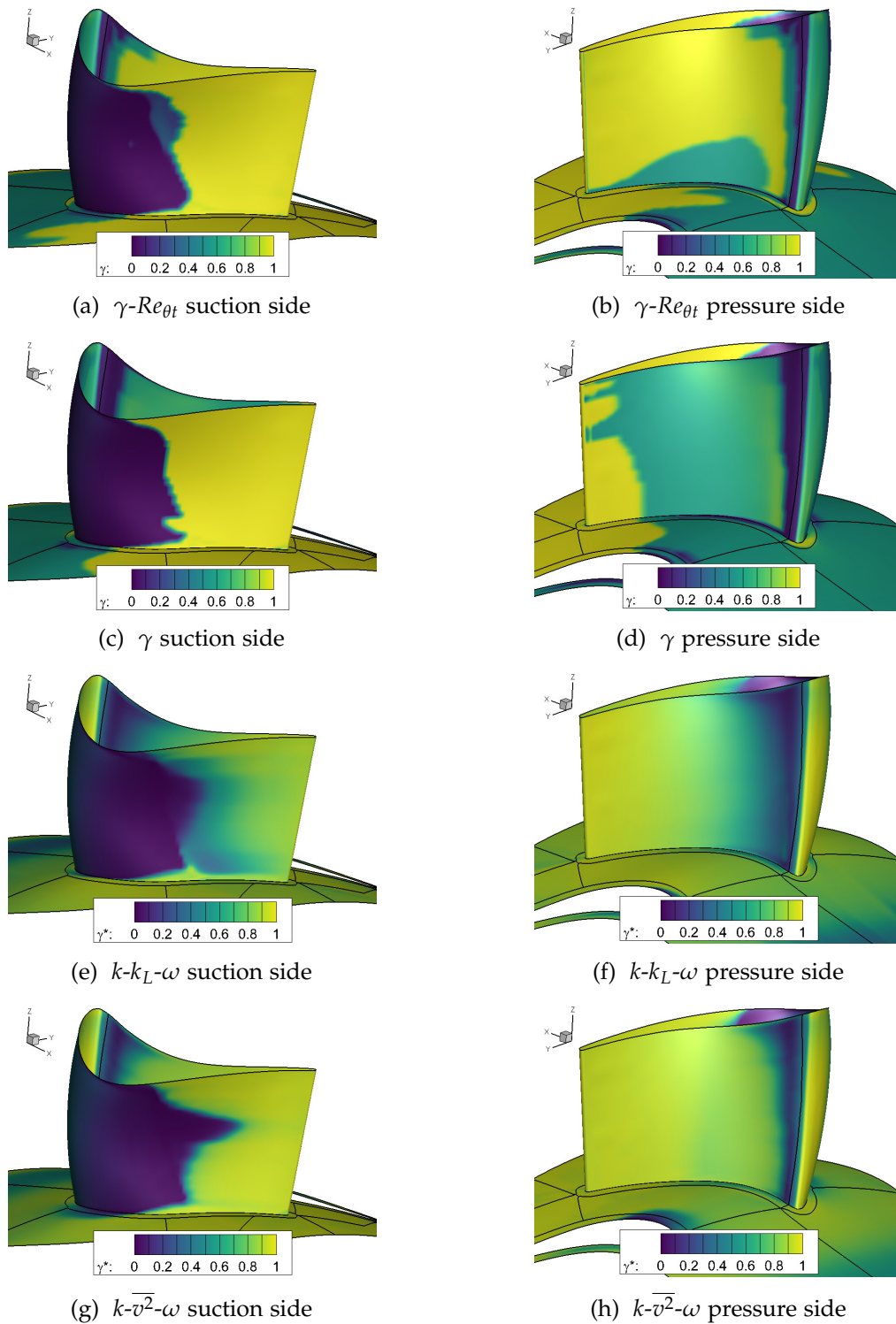
Figure 4.42.: Three-dimensional contour plots of the intermittency $\gamma$ for the LCTMs, together with the intermittency like variable $\gamma^*$ for the physics-based models.

(a) SST suction side

(b) SST pressure side

(c) SST + $\gamma$-$Re_{\theta t}$ suction side

(d) SST + $\gamma$-$Re_{\theta t}$ pressure side

(e) SST + $\gamma$ suction side

(f) SST + $\gamma$ pressure side
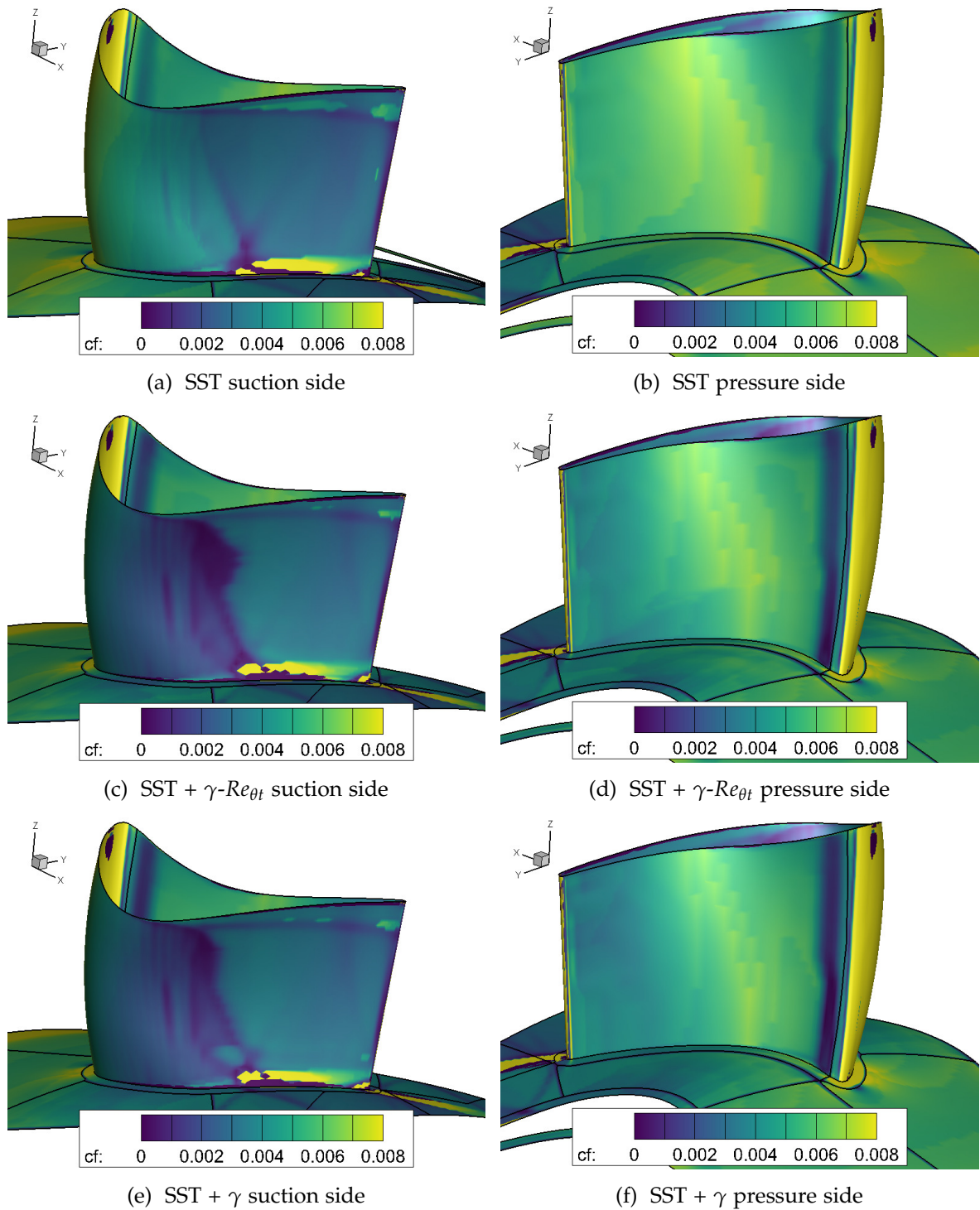
Figure 4.43.: Three-dimensional contour plots of the local skin friction coefficient $c_f$ on the vane and the hub for the LCTM transition models together with predictions for the SST turbulence model.

(a)  SST suction side

(b)  SST pressure side

(c)  $k$-$k_L$-$\omega$ suction side

(d)  $k$-$k_L$-$\omega$ pressure side

(e)  $k$-$\overline{v^2}$-$\omega$ suction side

(f)  $k$-$\overline{v^2}$-$\omega$ pressure side
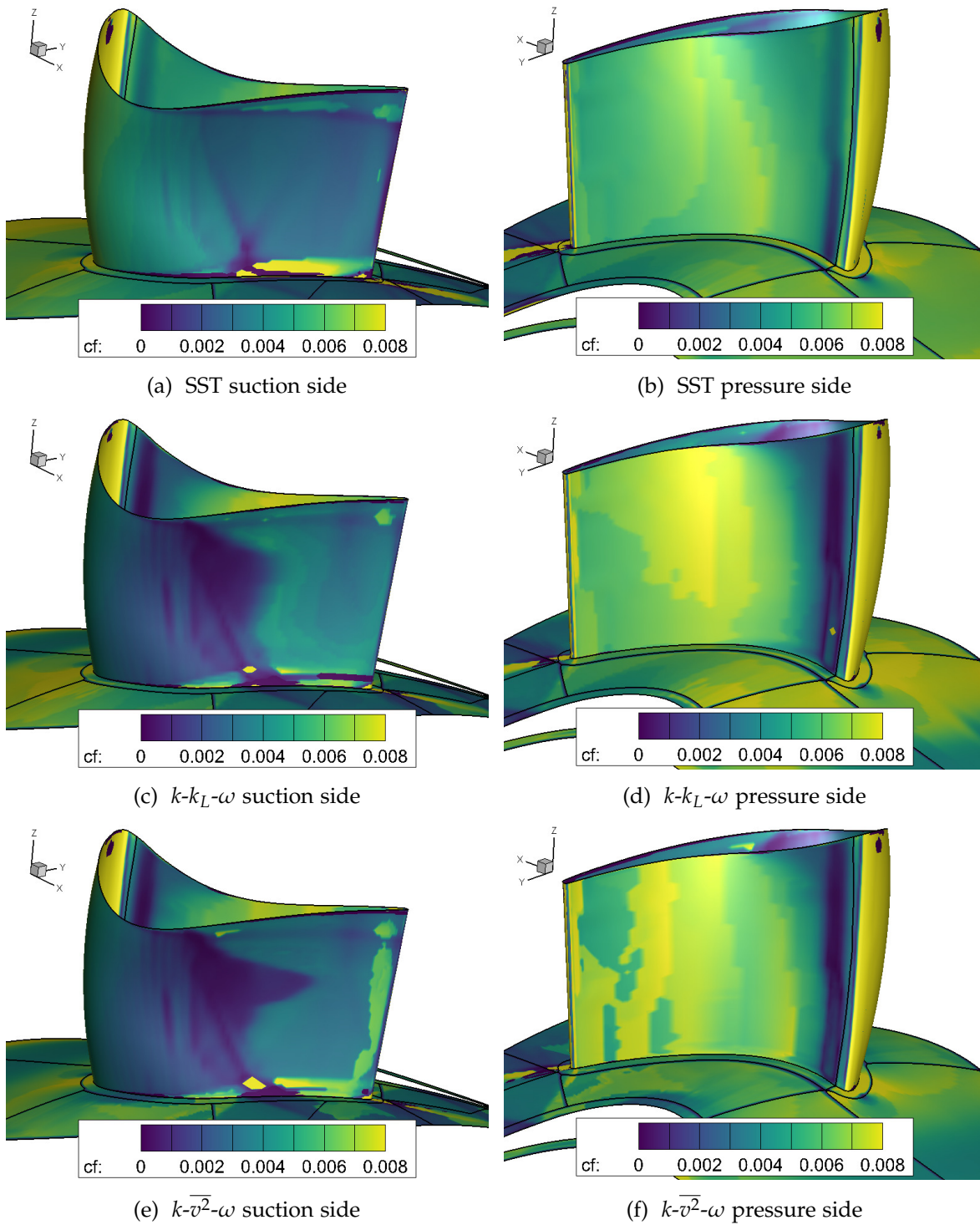
Figure 4.44.: Three-dimensional contour plots of the local skin friction coefficient $c_f$ on the vane and the hub for the physics-based transition models together with predictions for the SST turbulence model.
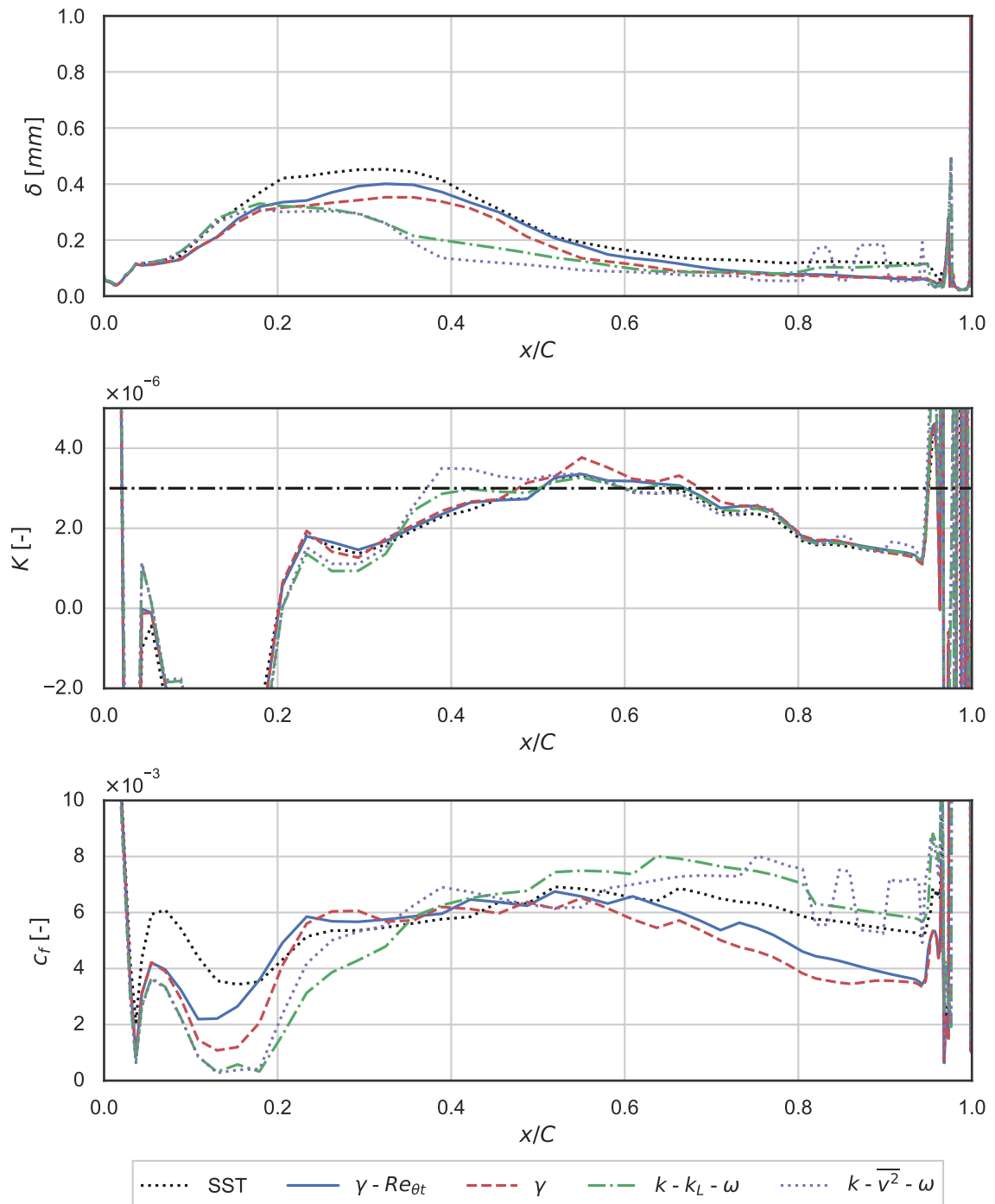
Figure 4.45.: Distribution of the boundary layer thickness $\delta$, Launder acceleration parameter $K$ and local skin friction coefficient $c_f$ along the **pressure-side** of the high pressure stator vane for all investigated transition models, together with the result of the SST turbulence model at mid span.
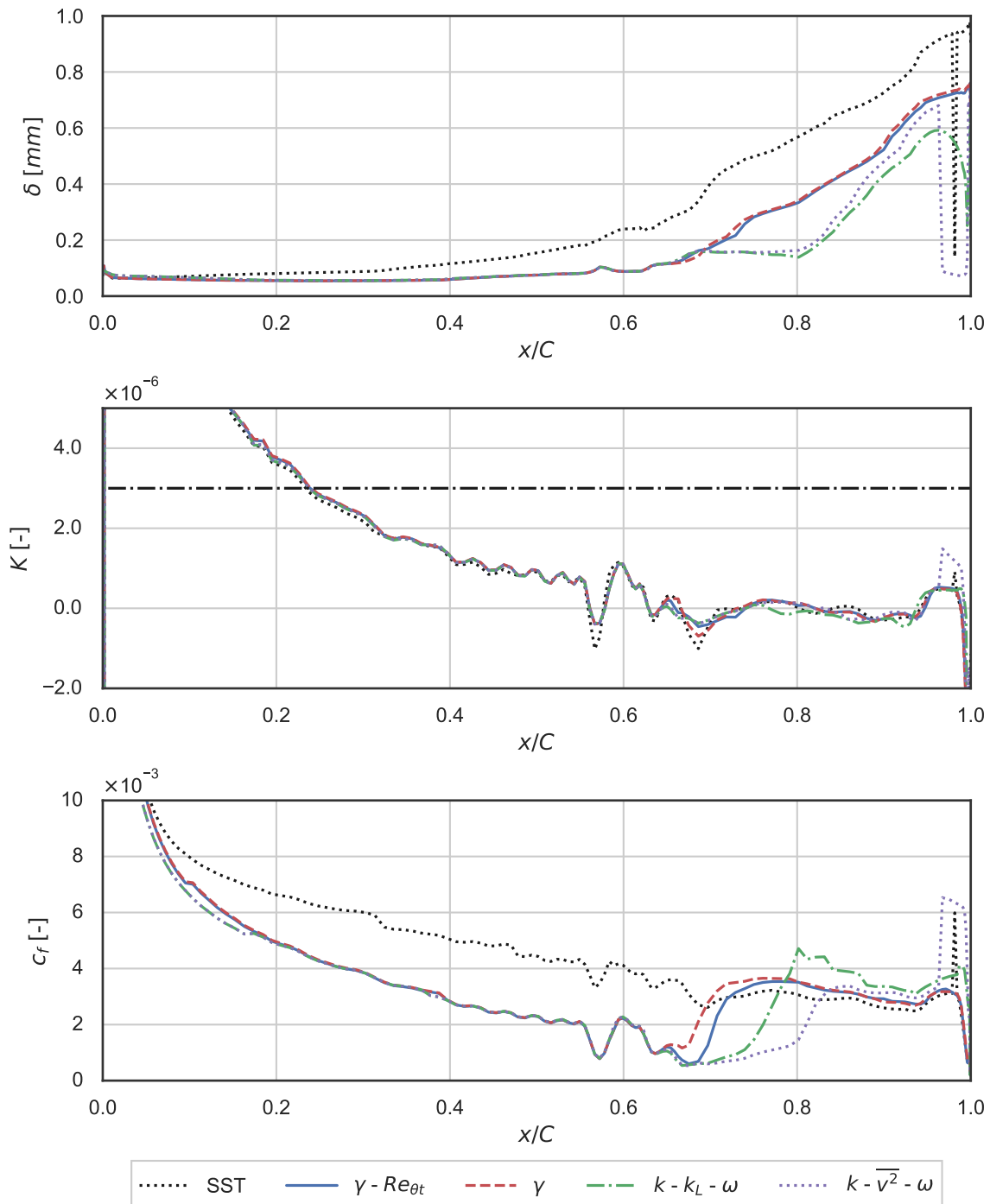
Figure 4.46.: Distribution of the boundary layer thickness $\delta$, Launder acceleration parameter $K$ and local skin friction coefficient $c_f$ along the **suction-side** of the high pressure stator vane for all investigated transition models, together with the result of the SST turbulence model at mid span.

$c_f$ along the HPS for the pressure side and for the suction side separately. All investigated models are plotted together with the SST turbulence model, which acts as the base-line for a fully turbulent boundary layer. The horizontal dash-dotted line in the plots for $K$ represents the critical value $K_c = 3\text{E-}6$, above which boundary layer relaminarization can be expected. On the abscissa of the plots the relative axial position of $x/C$ is plotted.

On the pressure side (Fig. 4.45), downstream of the stagnation point, at $x/C \approx 0.2$ the flow is highly accelerated. In this region, the $\gamma$-$Re_{\theta t}$ and the $\gamma$ model predict transition onset, indicated by the steep gradient in $c_f$. In the fully turbulent state, both models slightly overshoot the prediction of the SST model. The flow stays fully turbulent until $x/C \approx 0.45$. From this position forward it is assumed that the LCTMs predict relaminarization, indicated by the declining magnitude of $c_f$, and finally retransition in proximity to the trailing edge (see also Fig. 4.42). Because critical value $K_c$ is reached further upstream by the $\gamma$ model ($x/C \approx 0.455$) as compared to the $\gamma$-$Re_{\theta t}$ model ($x/C \approx 0.5$) the boundary layer relaminarization starts earlier. Therefore, the predicted value for $c_f$ is continuously on a lower level. The physics-based models, on the other hand, show no sign of relaminarization. It can be observed, that the transition length of the $k$-$k_L$-$\omega$ model is considerably longer than the transition length of the other models. Additionally, the $k$-$\overline{v^2}$-$\omega$ model shows unphysical instabilities in the boundary layer thickness $\delta$ and in the values for $c_f$ in the region of $0.8 \leq x/C \leq 0.95$. Between $0.25 \leq x/C \leq 0.6$ the predicted boundary layer thickness of the two families diverges substantially, where at the relative axial position $x/C \approx 0.4$ the by the LCTMs predicted boundary layers are almost twice as thick as the ones by the physics-based models .

For the suction side (Fig. 4.46) all predictions are almost identical to the position, where the $\gamma$ model predicts the earliest transition onset at $x/C \approx 0.655$, followed by the $\gamma$-$Re_{\theta t}$ model at $x/C \approx 0.7$. The predicted transition onset location coincides with a local minimum of the acceleration parameter, where the flow is deaccelerated. This is in vicinity of the impact and reflection of the weak shock coming from the neighboring vane pressure side. The physics-based models predict transition onset further downstream at $x/C \approx 0.75$ ($k$-$k_L$-$\omega$) and $x/C \approx 0.8$ ($k$-$\overline{v^2}$-$\omega$), respectively. Near the trailing edge the $k$-$\overline{v^2}$-$\omega$ model yields a sudden decrease in boundary layer thickness, which causes a very high value for $c_f$. This behavior appears to be non-physical, however the rapid increase in $c_f$ is easily explained by recalling the definition of $c_f$ (Eq. (4.4)), where the free-stream velocity at the boundary layer edge is part of the denominator. For the case that the boundary layer thickness is estimated too small, a wrong and also too small velocity will be taken from the boundary layer velocity profile as the free-stream velocity magnitude. What remains unclear is why the estimation of the boundary layer thickness repeatedly fails for the $k$-$\overline{v^2}$-$\omega$ model and seems to work satisfyingly for the other models. Finally, it is interesting that

the boundary layer thickness stays approximately constant between $0.7 \leq x/C \leq 0.8$ for the physics-based models and starts to grow again for both models at the same location, even though the transition onset is predicted differently.

By means of three additional plots, where $\delta$, $K$ and $c_f$ are plotted for a constant span of the vane, the previously mentioned anomalies in the predicted transition onset are discussed briefly. Figures 4.47, 4.49 and 4.48 present the pressure and suction side together in one plot, where the pressure side is plotted on negative values of the relative axial position $x/C$ and the suction side on the positive branch.

Figure 4.47 shows $\delta$, $K$, and $c_f$ at approximately 20% span along the vane, where the pocket-like early transition onset of the $\gamma$ model was observed. Predictions obtained from the LCTMs are plotted together with results from the SST turbulence model. The predictions are almost identical, except for the slightly earlier transition onset on the suction side of the $\gamma$ model. This coincides again with the impact of the weak shock, coming from the neighboring vane, where $K$ has a pronounced local minimum. It appears that the $\gamma$ model is more sensitive to the changing pressure gradient because the value for $K$ is equal to the predictions obtained by the $\gamma$-$Re_{\theta t}$ model. On the pressure side, boundary layer relaminarization is suspected due to the falling skin friction coefficient starting from $x/C \approx -0.4$, slightly more downstream from where the critical value $K_c$ is reached. No re-transitioning is indicated until the wake separation at the trailing edge.

Figure 4.48 shows $\delta$, $K$, and $c_f$ at approximately 75% span along the vane, where earlier halting of the transition process or an increased transition length of $\gamma$-$Re_{\theta t}$ model was suspected. Again only predictions obtained from the LCTMs are plotted, together with the fully turbulent base-line from the SST turbulence model. The assumption has to be dropped based on the plot, because clearly a comparable transition length can be seen on the suction side. Only the transition onset is predicted slightly retarded by the $\gamma$-$Re_{\theta t}$ model. Additionally, a discontinuity in the distribution of $K$ can be observed for the $\gamma$ model. On the pressure side the predictions are again quite similar, where the $\gamma$ model yields a slightly lower value for $c_f$ downstream of $x/C \approx -0.7$.

Figure 4.47.: Distribution of the boundary layer thickness $\delta$, Launder acceleration parameter $K$ and local skin friction coefficient $c_f$ along the high pressure stator vane for the LCTMs, together with the result of the SST turbulence model at approximately 20% span.

Figure 4.48.: Distribution of the boundary layer thickness $\delta$, Launder acceleration parameter $K$ and local skin friction coefficient $c_f$ along the high-pressure stator vane for the LCTMs, together with the prediction of the SST turbulence model at approximately 75% span.

Finally, Figure 4.49 considers the physics-based models and $\delta$, $K$, and $c_f$ are plotted at approximately 70% span, where in Figure 4.42 the knife-like region was observed and the $k\text{-}\overline{v^2}\text{-}\omega$ model predicted very far downstream transition onset. On the suction side, the later transition onset of the $k\text{-}\overline{v^2}\text{-}\omega$ model can be seen at $x/C \approx 0.85$, compared to $x/C \approx 0.8$ predicted by the $k\text{-}k_L\text{-}\omega$ model. On the pressure side, transition onset, indicated by a sharp increase of $c_f$ to the value of the fully turbulent solution, is predicted by both models at $x/C \approx -0.15$ and the flow is assumed to stay fully turbulent to the trailing edge. A rapid increase in $\delta$ can be observed on the pressure side at $x/C \approx 0.85$ followed by a rapid decrease at $x/C \approx 0.95$. On the suction side, a sudden reduction in $\delta$ is shown close to the trailing edge. Again it is assumed that in these regions the methodology for estimating the boundary layer thickness fails.

### 4.4.4. Conclusion

From this very complex fully three-dimensional test case only a small part, the flow around the HPS was investigated. Nevertheless, valuable insight into the characteristics of the investigated models was gained. First of all, it can be said that all models perform reasonably well and predict the transition onset on the suction side comparable to each other in proximity to the location, where the weak shock originating from the neighboring pressure side impacts the vane and is subsequently reflected. The anomalies in the otherwise sharp spanwise line of transition onset (see Fig. 4.42) were discussed in more detail.

On the pressure side, it assumed that the LCTMs are able to predict relaminarization, while the physics-based models are, under these flow conditions, not. Further investigations would be needed to assess if the physics-based models are able to predict relaminarization of the boundary layer at all for the flow inside thermal turbomachinery. The lack of relaminarization on the pressure side with the physics-based models is assumed to be the reason for the increased $c_f$ on the pressure side compared to the LCTMs.

During the simulations, severe stability issues were encountered with the $k\text{-}\overline{v^2}\text{-}\omega$ model. As the source for these stability issues, the newly introduced $k\text{-}\omega$ cross-diffusion term was identified. By employing a semi-automated procedure a converged solution could be obtained. See appendix C for more information on the used limiters and employed strategy. However, it appears that also the methodology for detecting the boundary layer thickness $\delta$ fails with the predictions obtained with the $k\text{-}\overline{v^2}\text{-}\omega$ model. Therefore, based on this test case, the $k\text{-}\overline{v^2}\text{-}\omega$ model cannot be recommended as the default transition model in its current implementation. Finally, the $\gamma$ transition model can be recommended unconditionally and would be a prime candidate for future work, where for example modified correlations could be developed.
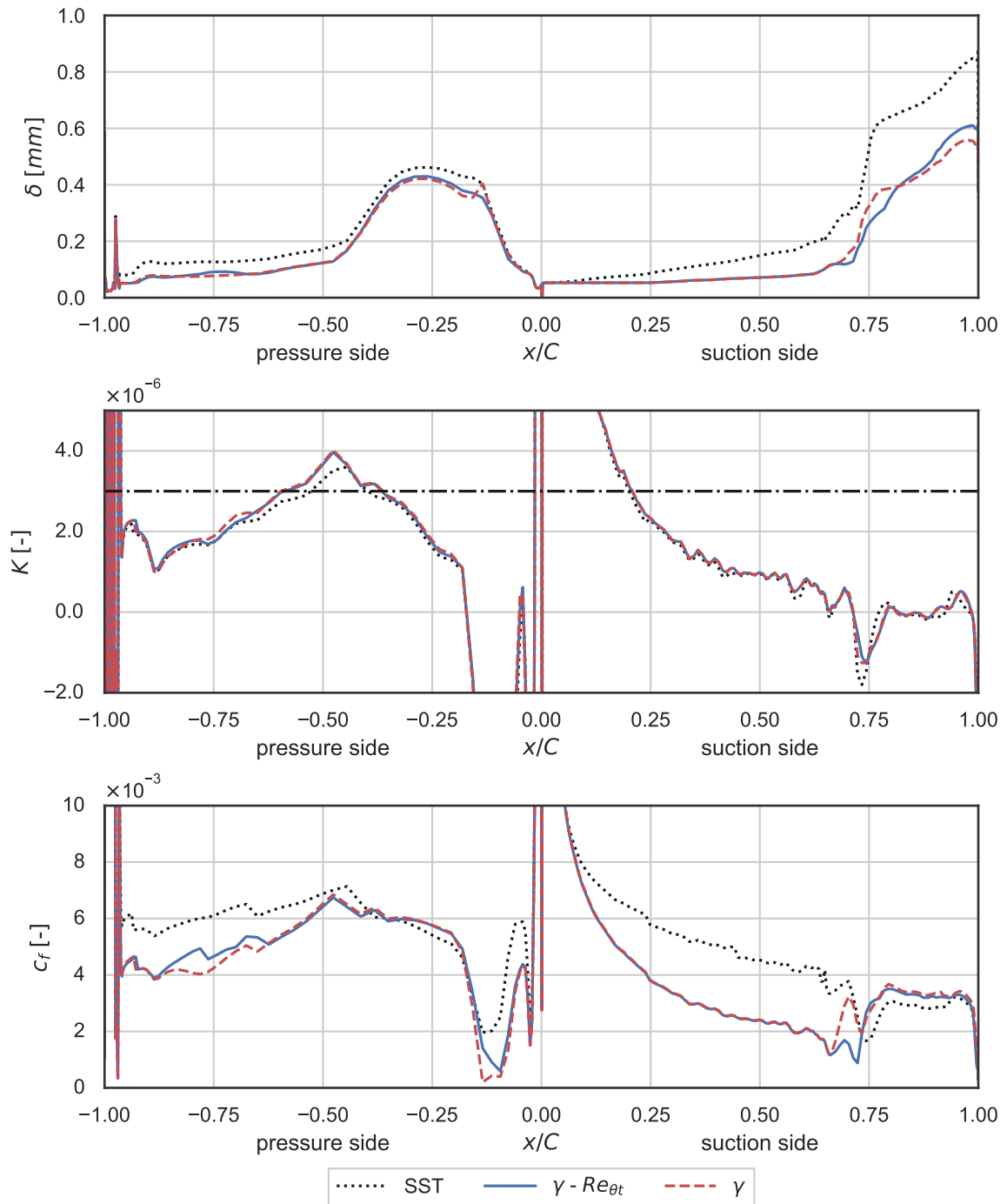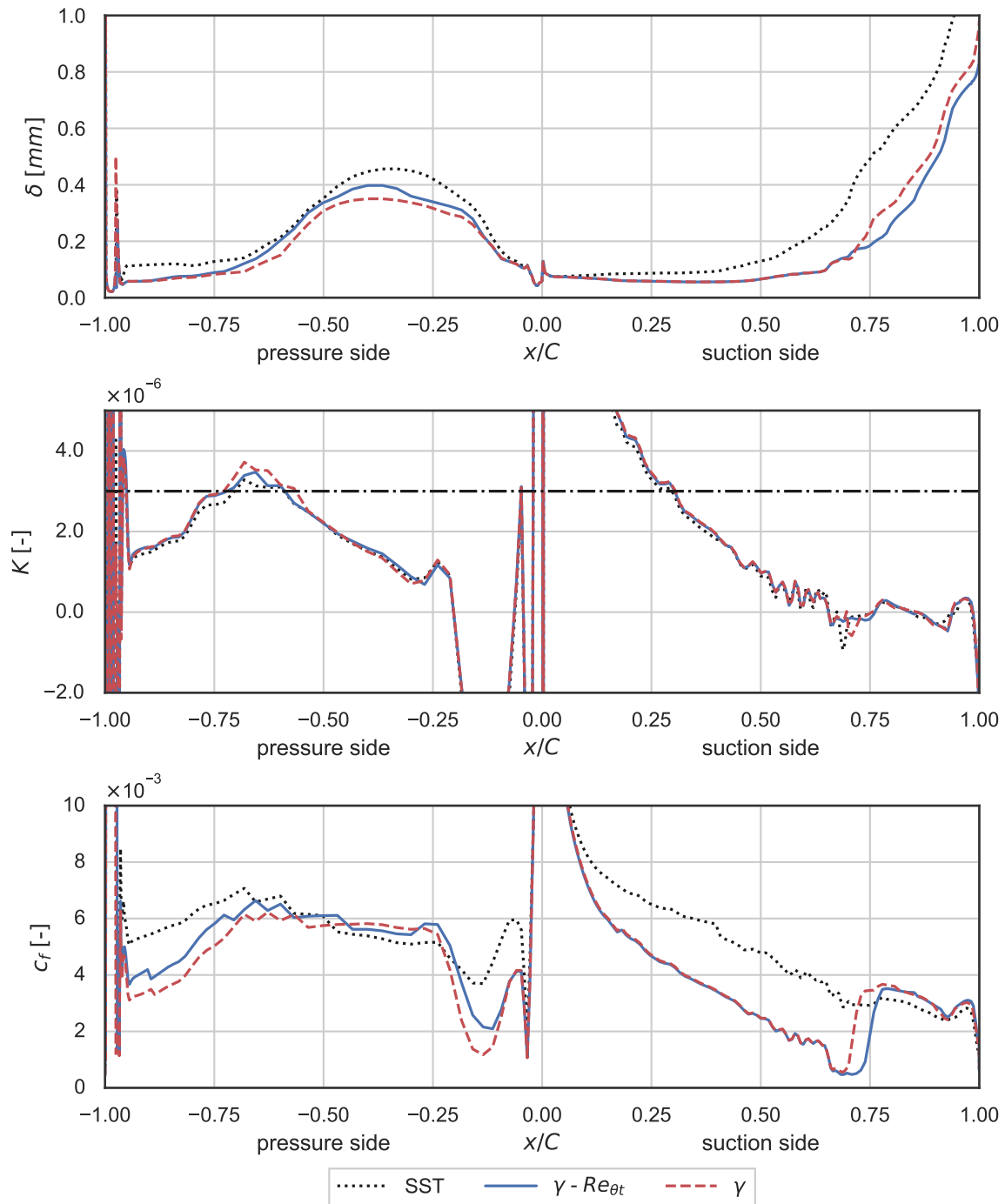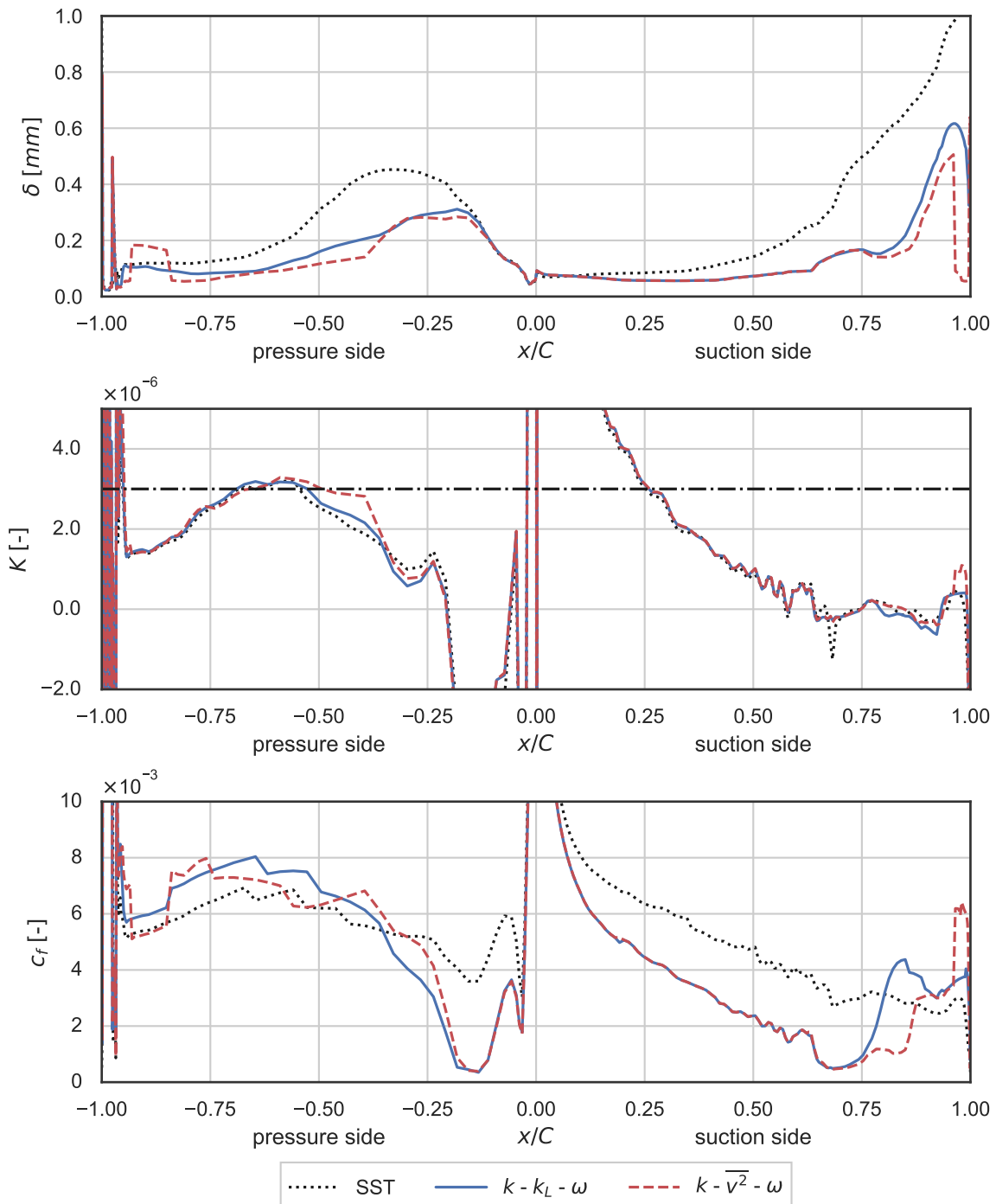
Figure 4.49.: Distribution of the boundary layer thickness $\delta$, Launder acceleration parameter $K$ and local skin friction coefficient $c_f$ along the high pressure stator vane for the physics-based transition sensitive turbulence models, together with the result of the SST turbulence model at approximately 70% span.

# 5. Summary and further work

The local correlation-based $\gamma$ transition model was successfully implemented into the in-house solver LINARS and showed a satisfying agreement of the results obtained by LINARS and ones of the commercial solvers ANSYS-CFX [60, 61] and ANSYS-Fluent [58, 59] for the considered cross-validation test cases T3A and VKI. Therefore it is assumed that the model was implemented correctly.

The flow on the pressure side of all blade and vane test cases was predicted comparably to the $\gamma$-$Re_{\theta t}$ model and transition onset was predicted slightly retarded for most test cases on the suction side. Nevertheless, the performance of the newly implemented model is quite impressive, considering that it uses only one additional transport equation and that the correlations were simplified substantially, compared to the $\gamma$-$Re_{\theta t}$ transition model.

For the physics-based models which were also implemented in the present work, the T3A cross-validation test case showed very good agreement between LINARS and Fluent for the $k$-$k_L$-$\omega$ model and between LINARS and results taken from the original publication [52] for the $k$-$\overline{v^2}$-$\omega$ model. The VKI cross-validation test case, on the other hand, showed substantially different results for the $k$-$k_L$-$\omega$ model on the pressure side compared to Fluent. However, it is unclear if the solution obtained by Fluent is correct, because the model equations in the Fluent Theory Guide [58] are given in reference to the 2008 paper of Walters and Cokljat [48], which, as mentioned in section (2.4.3), contains several typographical errors. The in-house solver implementation is based on the publication of Fürst [83], where these errors were corrected. Because Fluent is proprietary software, the source code cannot be reviewed. For the $k$-$\overline{v^2}$-$\omega$ model no alternative solver was readily available. Because the $k$-$\overline{v^2}$-$\omega$ model yields improved results for the prediction of the transition onset for all blade and vane test cases on the suction side and similar predictions as the $k$-$k_L$-$\omega$ model for the pressure side it is assumed that the implementations of both models are correct.

Even though the $k$-$\overline{v^2}$-$\omega$ model proved itself superior to the $k$-$k_L$-$\omega$ model in the present work, it can not be recommended as the standard transition model in its current implementation because during the fully three-dimensional (HPS) test case severe stability issues were encountered. As the source for these stability issues the $k$-$\omega$ cross-diffusion term was identified. This term was adopted by the original developers,

with minor modifications, from the SST turbulence model in order to improve the predictions for the wake-region of the boundary-layer and reduce the sensitivity on free-stream values of the specific turbulence dissipation rate $\omega$. By employing a semi-manual strategy, where first the cross-diffusion term was deactivated and later added in a limited form before it was added without limitation in its original formulation, a converged solution for the (HPS) test case was obtained. This result, however, still showed some unplausible discontinuities in the distribution of the boundary layer statistics (boundary layer thickness $\delta$, Kármán acceleration parameter $K$, and local skin-friction coefficient $c_f$). For more information on the used approach and implemented limiters, see Appendix C.

In future work, first of all it could be investigated, if the stability issues encountered in the fully three-dimensional HPS test case with the $k\text{-}\overline{v^2}\text{-}\omega$ model are isolated to LINARS or if other solvers behave similarly. For example, Fürst [84] provides a GNU General Public License v3 (GPLv3) licensed $k\text{-}\overline{v^2}\text{-}\omega$ implementation for the open-source solver OpenFOAM [85]. In case it turns out that this is a general problem with the model it could be worth to investigate if a limiter formulation exists which does not affect the solution but fixes the introduced stability issue. Otherwise, the in-house implementation should be reviewed again. In the course of the investigation of the stability issue, it would be worthwhile to further validate the results for the $k\text{-}k_L\text{-}\omega$ model, which is also readily available in OpenFOAM, and the $\gamma$ transition model, for which Fürst [84] also provides the GPLv3 licensed source-code for the OpenFOAM solver.

Next, the influence of the alternative turbulent heat-flux vector closure could be compared to the standard turbulent heat-flux vector closure via the turbulent Prandtl number, presented in section 2.2.5. First results can be seen in Appendix D. Another open question is the source of the spurious production of turbulence kinetic energy $k$ in the range of $100 < y^+ < 1000$ by the $k\text{-}\overline{v^2}\text{-}\omega$ model as shown in the MUR test cases (see for example Figure 4.34). Lopez and Walters [50] developed a fix for an unphysical production of turbulence kinetic energy $k$ under some special conditions by introducing an effective wall distance. This fix is already part of the original formulation of the $k\text{-}\overline{v^2}\text{-}\omega$ model and could be implemented into the in-house solver LINARS for the $k\text{-}k_L\text{-}\omega$ model. Usually, this particular problem is not encountered in internal flows, such as the flow inside thermal turbomachinery and therefore the implementation of this fix is not from high priority.

Furthermore, for the $\gamma$ model it would be very interesting if fine-tuning of the correlations allows to further improve the predictions for the considered test cases. Also, the parameter $C_{PG3}$, which corrects the critical value for the momentum thickness Reynolds number in regions with flow separation, is unused in the standard correlation, i.e. $C_{PG3} = 0$. An in-depth analysis of its influence on predictions could be a

rewarding task. Additionally, an investigation of the observed mesh-dependency of the $\gamma$ model - an in-depth investigation of the dependency on the expansion factor of the cells close to the wall was omitted in the present work - would be interesting.

On a more general thought, modifications capturing the influence of a rough wall, cross-flow or curvature on the transition onset comes to the mind. An approach for including cross-flow influence for the $\gamma$ model is documented in the CFX and Fluent Theory Guide [61, 58], including correlation parameters. Preliminary tests showed no influence of the cross-flow for the investigated test cases in the present work, however, a special test case could lead to more insight.

# Appendix

# Appendix A.

# Modified pressure gradient parameters for the $\gamma$ model

After observing differences in the predictions obtained by the solvers Fluent and CFX for the $\gamma$ model it was discovered that the pressure gradient parameters $C_{PG1} = 14.68$ and $C_{PG2} = -7.34$ were rescaled in Fluent to $C_{PG1} = 1$ and $C_{PG2} = -0.5$, respectively. In the Fluent Theory Guide 19.2 [58] it was documented that the coefficients in equations (2.125) and (2.128) were modified accordingly in order to yield identical values for the pressure gradient function $F_{PG}$ in comparison to the original set of parameters. Additionally, the min and max values of the limiter (Eq. 2.126) were increased by a factor of 10, which for consistency reasons should have been rescaled with the same factor of 14.68 as $C_{PG1}$ and $C_{PG2}$. However, this does not influence the value of $F_{PG}$, since $C_{PG1}^{\text{lim}}$ and $C_{PG2}^{\text{lim}}$ limit $F_{PG}$ before the limiter of $\lambda_{\theta L}$ affects the values of $F_{PG}$. It is important to also rescale the third pressure gradient parameter $C_{PG3}$, in case it is chosen to be non-zero.

The modified set of equations reads:

$$\lambda_{\theta L} = -0.1111 \frac{dV}{dy} \frac{d_w^2}{v} + 0.1875 \tag{A.1}$$

$$\lambda_{\theta L} = \min\left(\max\left(\lambda_{\theta L}, -10\right), 10\right) \tag{A.2}$$

$$F_{PG} = \begin{cases} \min\left(1 + C_{PG1}\lambda_{\theta L}, C_{PG1}^{\text{lim}}\right), & \lambda_{\theta L} \geq 0 \\ \min\left(1 + C_{PG2}\lambda_{\theta L} + C_{PG3}\min\left(\lambda_{\theta L} + 1.0, 0\right), C_{PG2}^{\text{lim}}\right), & \lambda_{\theta L} < 0 \end{cases} \tag{A.3}$$

Where the model constants are given by:

$$C_{PG1} = 1 \qquad C_{PG2} = -0.5 \qquad C_{PG3} = 0 \qquad C_{PG1}^{\text{lim}} = 1.5 \qquad C_{PG2}^{\text{lim}} = 3.0 \tag{A.4}$$

Figure A.1 shows a comparison between the original Menter correlations, used by CFX and LINARS, and the modified correlations, as implemented in Fluent. It can be seen that even though the local pressure gradient parameter $\lambda_{\theta,L}$ is different, the pressure gradient function $F_{PG}$ yields identical values when used together with the modified parameters (Eq. (A.4)).

Private communications via the ANSYS Support Firm CADFEM with the original developer Menter confirmed the assumption that these changes were only made for aesthetic or practical reasons, with the intent not to influence the predictions.



(a) Local pressure gradient parameter $\lambda_{\theta,L}$      (b) Pressure gradient function $F_{PG}$
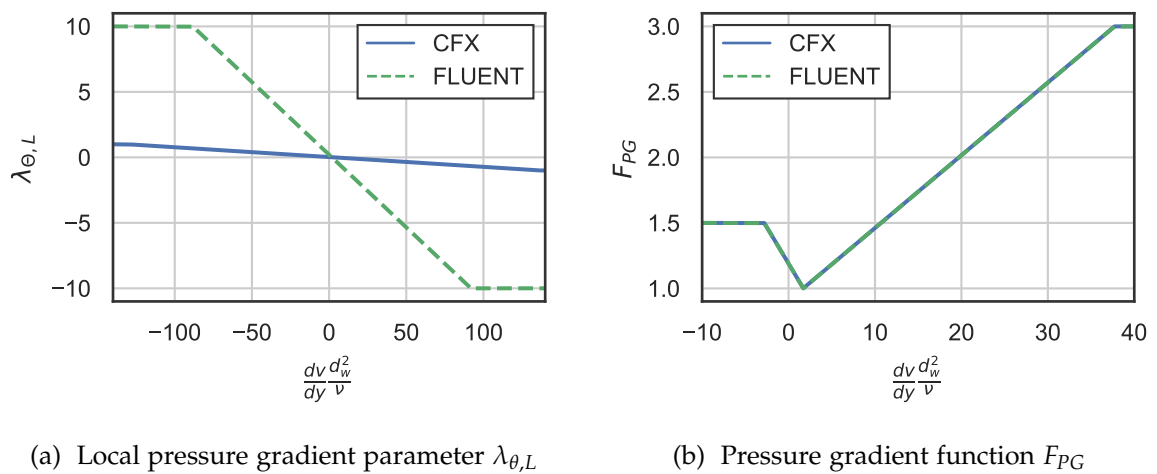
Figure A.1.: Comparison of the modified pressure gradient correlations used by Fluent with the original formulation used by CFX and LINARS. For the abscissa, the wall-normal velocity gradient times the ratio of the wall distance squared to the fluid viscosity is used.

# Appendix B.

# Turbulent length scale

For $k$-$\omega$ based turbulence models appropriate values for the turbulence kinetic energy $k$ and the specific dissipation rate $\omega$ have to be specified at the inlet. These values are often unknown and hard to estimate. Therefore, two more readily available quantities, the free-stream turbulence intensity $Tu$ and the turbulence length scale $l_{\text{turb}}$, are often used.

The turbulence intensity is defined as

$$Tu = 100 \frac{\sqrt{2/3k}}{U} \quad (\text{in } \%)\,, \tag{B.1}$$

where $U$ is the velocity magnitude. For the flow in thermal turbomachinery, values for the turbulence intensity at the inlet are typically assumed to be within 5% to 10%. The turbulence kinetic energy can be calculated by rearranging equation (B.1) as

$$k = \frac{3}{2} \left( U \frac{Tu}{100} \right)^2. \tag{B.2}$$

For the turbulence length scale $l_{\text{turb}}$ several estimations based on the flow-type and the geometry exist. For the flow in thermal turbomachinery $l_{\text{turb}}$ can be approximated with 0.5% to 5% of the blade chord length $C$. Based on dimensional considerations by Kolmogorov ($l_{\text{turb}} \sim \sqrt{k}/\omega$), the specific dissipation rate $\omega$ is given by

$$\omega = C_\mu^{\alpha_l} \frac{\sqrt{k}}{l_{\text{turb}}}, \tag{B.3}$$

where $C_\mu$ is a proportionality constant and usually equal to $C_\mu = 0.09$. The exponent $\alpha_l$ varies based on the turbulence model and solver implementation. Prior to version 16, Fluent and CFX used the same value $\alpha_l = -0.25$ as the in-house solver LINARS. According to the release notes of version 16.0 [86], the value was changed to $\alpha_l = -1$ for consistency reasons within the various models used in Fluent.

For the present work, two families of turbulence and transition models were considered. The $\gamma$-$Re_{\theta t}$ and $\gamma$ model are both coupled to the SST turbulence model and the $k$-$k_L$-$\omega$ and $k$-$\overline{v^2}$-$\omega$ model are from the same family of transition sensitive phenomenological turbulence models. From a comparison of various terms of the models, for example, the destruction terms in the $k$ transport equations (2.66) and (2.139), the conclusion that $\omega$ is smaller by the factor of $C_\mu = 0.09$ for the phenomenological models can be drawn. Figure B.1 shows predictions for the T3A test case (see section 4.1) and verifies this assumption. It can be seen that for a similar decay of the free-stream turbulence intensity, the values for $\omega$ are smaller by the factor $C_\mu = 0.09$. The in-house solver LINARS was designed to be self-consistent and applies this factor internally, by using $\alpha_t = 0.75$ for the phenomenological models. Fluent and CFX however use the same exponent $\alpha_t$ for all models, hence it is necessary to modify the turbulent length-scale itself.



(a) Turbulence intensity $Tu$

(b) Specific turbulence dissipation $\omega$
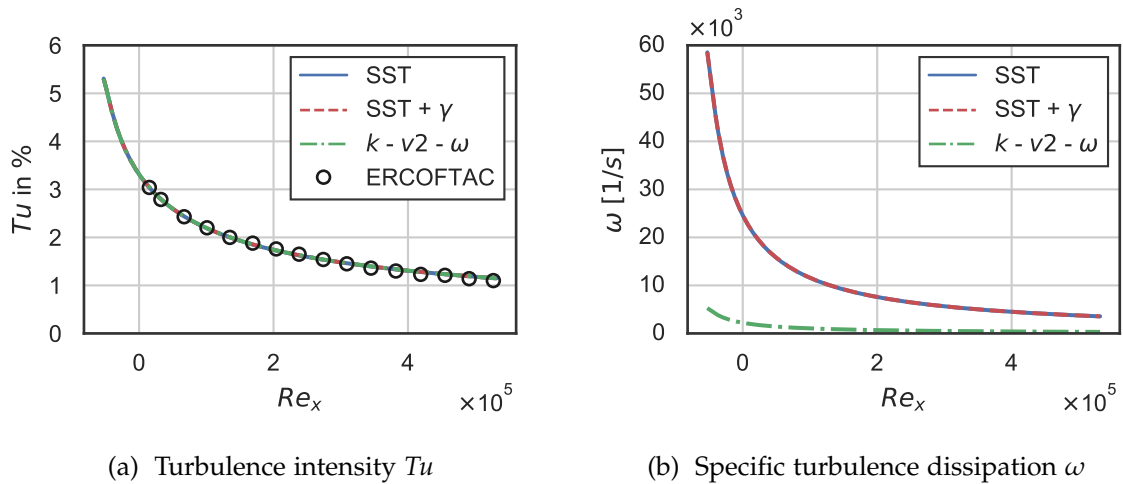
Figure B.1.: Predictions of the decay of the turbulence intensity and the turbulence dissipation along the upper domain boundary for the T3A test case (see section 4.1), as obtained by the solver LINARS for the SST, $\gamma$ and $k$-$\overline{v^2}$-$\omega$ model. The turbulence inlet conditions were set to $l_{\text{turb,inlet}} = 0.205$mm and $Tu_{\text{inlet}} = 5.4\%$.

Conversion factors can be calculated based on equation (B.3). In order to get comparable predictions the turbulence length scale used with LINARS has to be multiplied by the factor $0.09^{-0.75} \approx 6.086$ for all SST based simulations carried out with Fluent or CFX, and by the factor $0.09^{-1.75} \approx 67.62$, when using the $k$-$k_L$-$\omega$ model in Fluent. For the sake of readability, all references to the turbulence length scale $l_{\text{turb}}$ are made in reference to SST based models and the in-house solver LINARS.

# Appendix C.

# Stability issues of the $k$-$\overline{v^2}$-$\omega$ model in LINARS

Severe instabilities were encountered for all test cases with the $k$-$\overline{v^2}$-$\omega$ model, which caused the simulations to diverge. Convergent solutions could be obtained for the T3A test case and the linear cascade test cases VKI and MUR by reducing the Courant–Friedrichs–Lewy (CFL) number. However, the fully three-dimensional HPS test case could not be solved in this way. Further investigations identified the newly introduced cross-diffusion term $CD_{k\omega}$ (see section 2.4.4) as source for these instabilities. Therefore, a simple strategy was developed for obtaining a convergent solution for the HPS test case.

Excluding the $k$-$\omega$ cross-diffusion term restores the stability to the level of the $k$-$k_L$-$\omega$ model, but the predictions in the turbulent outer layer of the boundary layer in fully turbulent regions change and the model becomes more sensitive to $\omega$ values of the free-stream. Figure C.1 shows the small influence of the cross-diffusion term for the T3A test case, where the turbulent boundary conditions were $Tu_{\text{in}} = 5.4\%$ and $l_{\text{turb}} = 0.205$mm.

Hellsten [87] proposed for the limiter to use the maximum value of the cross-diffusion term throughout the computational domain multiplied by the constant factor 1E-8 to obtain a proper lower limit for the SST $k\omega$ cross-diffusion term. Equation (2.160) reads in modified form

$$CD_{k\omega} = \max\left(2\rho\sigma_{\omega 2}\frac{1}{\omega}\frac{\partial k}{\partial x_i}\frac{\partial \omega}{\partial x_i}, 10^{-8}CD_{k\omega,\text{max}}\right), \tag{C.1}$$

where $CD_{k\omega,\text{max}}$ is computed per grid-block for the sake of simplicity. Unfortunately, this approach did not fix the stability issues encountered in the HPS test case. Also it was observed that for some test cases the predicted transition onset would change (see for example Figure C.2).
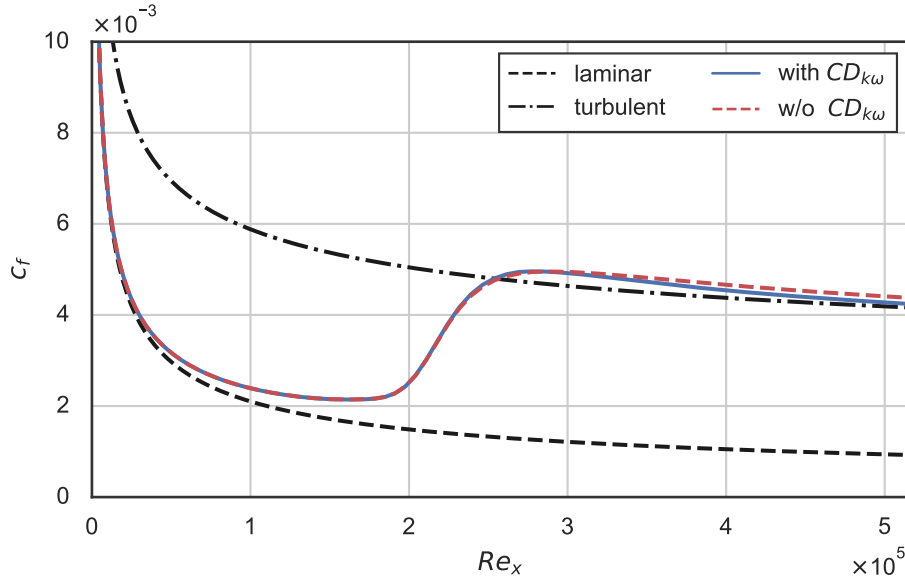
Figure C.1.: Predictions of the skin friction coefficient $c_f$ along the flat plate for the $k$-$\overline{v^2}$-$\omega$ model, with and without the $CD_{k\omega}$ term, versus the ERCOFTAC experiment and analytical solutions for fully turbulent and fully laminar flow.

Finally, a limiter for the Production terms $P_k$, $P_{\overline{v^2}}$, and $P_\omega$ was implemented in the spirit of the clip-limiter (see Eq. (2.71)) of the SST turbulence model. However, it was necessary to modify the limiting constant. Starting from 10, like in the SST model, the constant value of the limiter was increased until no more influence of the limiter on the predictions for several MUR boundary conditions could be observed. Finally, the limiter for the turbulence kinetic energy production term reads

$$\widetilde{P_k} = \min\left(P_k, 80\omega k\right), \tag{C.2}$$

effectively limiting the production to 80 times the destruction term. With this limiter, a converged solution of the HPS test case could be obtained. Restarting the computation from this solution with deactivated limiter it was possible to obtain a converged solution with the original model formulation.
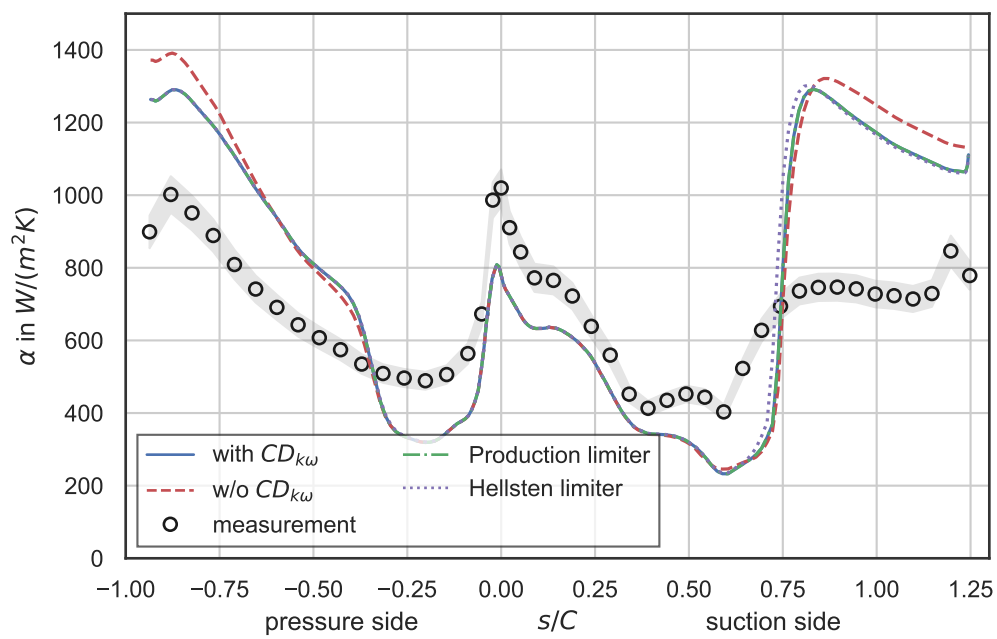
Figure C.2.: Predictions of the heat transfer coefficient $\alpha$ over the relative coordinate $s/C$ for all investigated limiters for the MUR241 case.

# Appendix D.

# Turbulent heat-flux vector closure for physics-based models

As mentioned in section 2.2.5, the physics-based transition models provide their own closure for the turbulent heat-flux vector $q_{ti}$. In the present work for all models a popular turbulent heat-flux vector closure based on the turbulent Prandtl number was used. Recalling the turbulent heat-flux closure based on the turbulent Prandtl number as

$$q_{ti} = c_p \overline{\rho u_j'' T''} = -\frac{\mu_t c_p}{Pr_t} \frac{\partial \widetilde{T}}{\partial x_i}. \tag{D.1}$$

The alternative formulation in the $k$-$k_L$-$\omega$ and the $k$-$\overline{v^2}$-$\omega$ model is according to Lopez and Walters [52] and Walters and Cokljat [48] given by

$$q_{ti} = c_p \overline{\rho u_j'' T''} = -\rho c_p \alpha_\theta \frac{\partial \widetilde{T}}{\partial x_i}, \tag{D.2}$$

where $\alpha_\theta$ is the turbulent thermal diffusivity, which for the $k$-$k_L$-$\omega$ model [48] is given by

$$\alpha_\theta = f_W \left( \frac{k}{k + k_L} \right) \frac{v_{t,s}}{Pr_\theta} + (1 - f_W) C_{\alpha,\theta} \sqrt{k} \lambda_{\text{eff}}, \tag{D.3}$$

and modified for the $k$-$\overline{v^2}$-$\omega$ model [52] as

$$\alpha_\theta = f_W \left( \frac{\overline{v^2}}{k} \right) \frac{v_{t,s}}{Pr_\theta} + (1 - f_W) C_{\alpha,\theta} \sqrt{\overline{v^2}} \lambda_{\text{eff}}. \tag{D.4}$$

For consistency reasons, it would be recommended to use the original formulations in case the heat-flux is from interest. Unfortunately, the current implementation yields unplausible results for which at the moment the reason is unknown and further investigations are recommended. Figure D.1 exemplary shows results for the heat transfer coefficient $\alpha$ over the relative coordinate $s/C$ for different turbulent heat-flux vector closures for the physics-based models for (a) the MUR235 and (b) the MUR241 case.
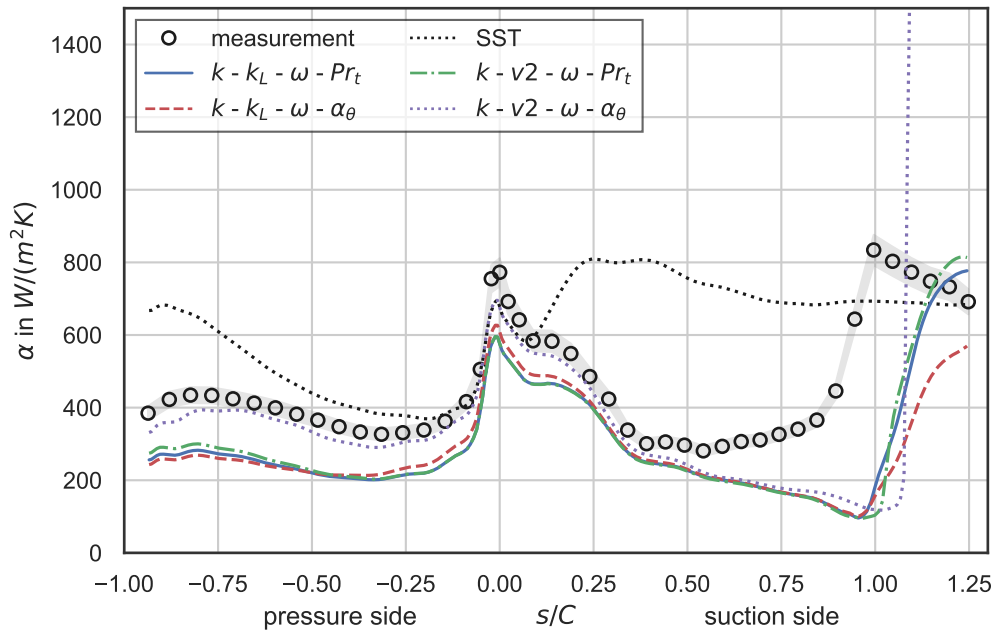
(a) MUR235
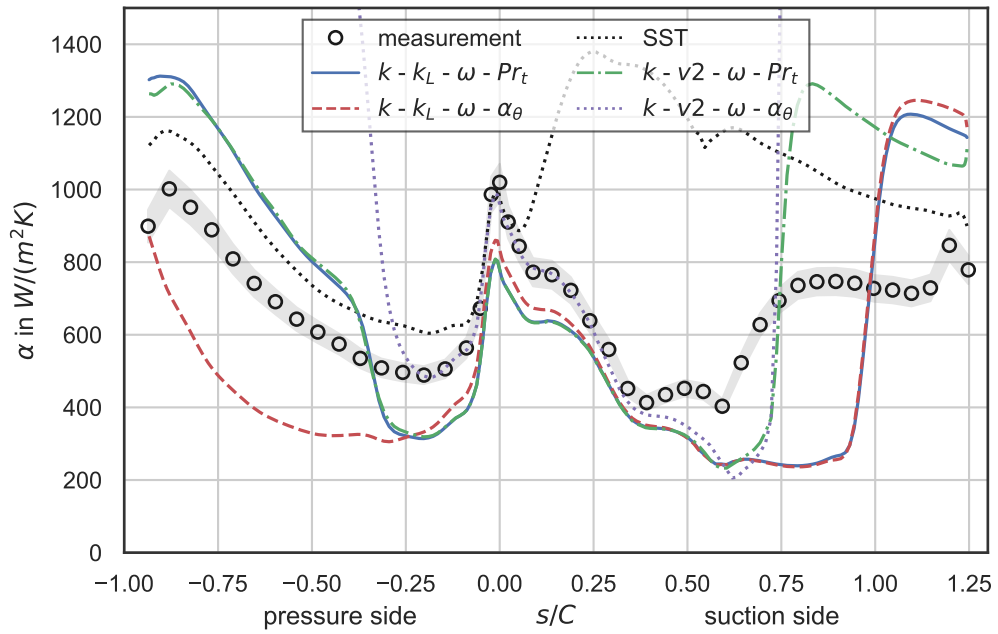


(b) MUR241

Figure D.1.: Heat transfer coefficient $\alpha$ over the relative coordinate $s/C$ for different turbulent heat-flux vector closures for the physics-based models for (a) the MUR235 and (b) the MUR241 case.

# Bibliography

[1]    P. A. Davidson. *Turbulence: An Introduction for Scientists and Engineers*. 2nd ed. Oxford Univ. Press, 2015. ISBN: 978-0198722588 (cit. on pp. 1, 2).

[2]    S. B. Pope. *Turbulent flows*. 1st ed. Cambridge Univ. Press, 2000. ISBN: 978-0521598866 (cit. on p. 1).

[3]    D. C. Wilcox. *Turbulence Modeling for CFD*. 3rd ed. DCW Industries, 2006. ISBN: 978-1928729082; (cit. on pp. 1, 10, 20, 25, 26, 28, 30, 31, 34).

[4]    P. Bradshaw. 'Understanding and prediction of turbulent flow'. In: *International Journal of Heat and Fluid Flow* (1997). DOI: 10.1016/S0142-727X(96)00134-8 (cit. on p. 1).

[5]    O. Reynolds. 'An experimental investigation of the circumstances which determine whether the motion of water shall be direct or sinuous, and of the law of resistance in parallel channels'. In: *Philosophical Transactions of the Royal Society of London. A* 174 (1883), pp. 935–982 (cit. on p. 1).

[6]    C. L. Fefferman. *Existance and Smoothness of the Navier-Stokes Equation*. Clay Mathematics Institute. 2000. URL: https://www.claymath.org/sites/default/files/navierstokes.pdf (visited on 15 Jan. 2019) (cit. on p. 4).

[7]    L. Prandtl. 'Über Flüssigkeitsbewegung bei sehr kleiner Reibung'. in German. In: *III. Internationaler Mathematiker-Kongress* (1904), pp. 484–491 (cit. on p. 5).

[8]    J. A. Żurański. *Windbelastung von Bauwerken und Konstruktionen*. in German. Müller, 1972. ISBN: 3481199511 (cit. on p. 6).

[9]    R. E. Mayle. 'The Role of Laminar-Turbulent Transition in Gas Turbine Engines'. In: Turbo Expo: Power for Land, Sea, and Air. (3 June 1991). DOI: 10.1115/91-GT-261 (cit. on p. 6).

[10]   H. Schlichting. *Boundary-Layer Theory*. 7th ed. McGraw–Hill Book Company, 1979. ISBN: 9780070553347 (cit. on pp. 7, 64).

[11]   F. M. White. *Viscous Fluid Flow*. 3rd ed. McGraw–Hill Book Company, 2006. ISBN: 9780071244930 (cit. on p. 7).

[12]   P. A. Durbin. 'Perspectives on the Phenomenology and Modeling of Boundary Layer Transition'. In: *Flow Turbulence Combustion* (2017). DOI: 10.1007/s10494-017-9819-9 (cit. on p. 8).

[13]  R. E. Mayle and A. Schulz. 'The Path to Predicting Bypass Transition'. In: Turbo Expo: Power for Land, Sea, and Air. (June 1996). Vol. Volume 1: Turbomachinery. DOI: 10.1115/96-GT-199 (cit. on p. 8).

[14]  H. Steiner. *Lecture Notes: Advanced Fluid Mechanics and Heat Transfer (321.106)*. in German. Graz University of Technology, 2016 (cit. on pp. 9, 10, 28).

[15]  B. Launder. *Lecture Notes: Fluid Mechanics*. University of Manchester, 2008. URL: http://cfd.mace.manchester.ac.uk/twiki/pub/Main/TimCraftNotes_All_Access/Fluid-Mechanics-BEL-L1.pdf (visited on 5 Apr. 2019) (cit. on p. 10).

[16]  J. R. Lücke. 'Turbulenzmodellierung zur Berechnung abgelöster Strömungen in Turbomaschinen'. in German. PhD thesis. RWTH Aachen, 1997 (cit. on p. 11).

[17]  F. R. Menter. 'Two-equation eddy-viscosity turbulence models for engineering applications'. In: *AIAA Journal* (1994). DOI: 10.2514/3.12149 (cit. on pp. 13, 32).

[18]  P. A. Durbin. 'Some Recent Developments in Turbulence Closure Modeling'. In: *Annual Review of Fluid Mechanics* (2018). DOI: 10.1146/annurev-fluid-122316-045020 (cit. on p. 13).

[19]  M. S. Gritskevich, A. V. Garbaruk, J. Schütze and F. R. Menter. 'Development of DDES and IDDES Formulations for the k-omega Shear Stress Transport Model'. In: *Flow, Turbulence and Combustion* (2011). DOI: 10.1007/s10494-011-9378-4 (cit. on p. 13).

[20]  H. K. Versteeg and W. Malalasekera. *An Introduction to Computational Fluid Dynamics: The Finite Volume Method*. 2nd ed. Pearson Education Limited, 2007. ISBN: 978-0131274983 (cit. on pp. 15, 25, 29, 30, 59).

[21]  D. C. Wilcox. *Turbulence Modeling for CFD*. 2nd ed. DCW Industries, 1998. ISBN: 978-1928729105; (cit. on pp. 15, 21, 31, 33).

[22]  O. Reynolds. 'On the Dynamical Theory of Incompressible Viscous Fluids and the Determination of the Criterion'. In: *Philosophical Transactions of the Royal Society of London. A* 186 (1895), pp. 123–164. DOI: 10.2307/90643. URL: https://www.jstor.org/stable/90643 (visited on 11 Feb. 2019) (cit. on pp. 20, 26).

[23]  F. G. Schmitt. 'Equations des Gaz Turbulents Compressibles'. In: *Journal de Mecanique* 4.3 (2007), pp. 361–390 (cit. on p. 20).

[24]  T. Cebeci and A. M. O. Smith. *Analysis of turbulent boundary layers*. Academic Press, 1974. ISBN: 0121646505 (cit. on p. 20).

[25]  F. G. Schmitt. 'About Boussinesq's turbulent viscosity hypothesis: historical remarks and a direct evaluation of its validity.' In: *Comptes Rendus Mécanique* 335 (2007), pp. 617–627. DOI: 10.1016/j.crme.2007.08.004 (cit. on p. 26).

[26]   J. Boussinesq. In: *Mémoires présentés par divers savants à l'Académie des Sciences XXIII* (1872). URL: https://gallica.bnf.fr/ark:/12148/bpt6k56673076 (visited on 11 Feb. 2019) (cit. on p. 26).

[27]   A. Smith and T. Cebeci. 'Numerical solution of the turbulent boundary layer equations'. In: *Douglas aircraft division report DAC 33735* (1967) (cit. on p. 26).

[28]   B. S. Baldwin and H. Lomax. 'Thin Layer Approximation and Algebraic Model for Separated Turbulent Flows'. In: *AIAA* (1978). DOI: 10.2514/6.1978-257 (cit. on p. 26).

[29]   P. R. Spalart and S. R. Allmaras. 'A One-Equation Turbulence Model for Aerodynamic Flows'. In: *La Recherche Aerospatiale* (1994) (cit. on p. 27).

[30]   A. N. Kolmogorov. 'Local Structure of Turbulence in Incompressible Viscous Fluid for Very Large Reynolds Number'. In: *Doklady Akademiya Nauk SSSR* (1941) (cit. on p. 27).

[31]   A. N. Kolmogorov. 'Equations of Turbulent Motion of an Incompressible Fluid'. In: *Izvestia Academy of Sciences USSR* (1942) (cit. on p. 27).

[32]   B. E. Launder and D. B. Spalding. 'The numerical computation of turbulent flows'. In: *Computer Methods in Applied Mechanics and Engineering* (1974). DOI: 10.1016/0045-7825(74)90029-2 (cit. on pp. 27, 29–31).

[33]   D. C. Wilcox. 'Formulation of the k-omega Turbulence Model Revisited'. In: *AIAA Journal* (2008). DOI: 10.2514/1.36541 (cit. on pp. 27, 31, 34).

[34]   F. R. Menter, M. Kuntz and L. Robert. 'Ten Years of Industrial Experience with the SST Turbulence Model'. In: Turbulence, Heat and Mass Transfer 4. (12–17 Oct. 2003). Ed. by K. Hanjalic, Y. Nagano and M. Tummers. Begell House, Inc. (cit. on pp. 27, 33, 35, 53).

[35]   D. C. Wilcox. 'Reassessment of the Scale-Determining Equation for Advanced Turbulence Models'. In: *AIAA Journal* (1988). DOI: 10.2514/3.10041 (cit. on pp. 27, 31, 32).

[36]   W. P. Jones and B. E. Launder. 'The prediction of laminarization with a two-equation model of turbulence'. In: *International Journal of Heat and Mass Transfer* (1972). DOI: 10.1016/0017-9310(72)90076-2 (cit. on p. 29).

[37]   F. R. Menter. 'Zonal Two Equation k-w Turbulence Models For Aerodynamic Flows'. In: 23rd Fluid Dynamics, Plasmadynamics, and Lasers Conference. (6 July 1993). American Institute of Aeronautics and Astronautics, 1993. DOI: 10.2514/6.1993-2906 (cit. on p. 32).

[38]   *Turbulence Modeling Resource.* Langley Research Center NASA. URL: https://turbmodels.larc.nasa.gov (visited on 12 Feb. 2019) (cit. on pp. 33, 34).

[39] M. Kato and B. E. Launder. 'The Modelling of Turbulent Flow Around Stationary and Vibrating Square Cylinders'. In: *Proc. 9th Symp. on Turbulent Shear Flows* (1993). URL: https://www.researchgate.net/publication/247931894_The_Modelling_of_Turbulent_Flow_Around_Stationary_and_Vibrating_Square_Cylinders (visited on 1 Oct. 2018) (cit. on pp. 34, 46).

[40] E. Dick and S. Kubacki. 'Transition models for turbomachinery boundary layer flows : a review'. In: *International Journal of Turbomachinery Propulsion and Power* (2017). DOI: 10.3390/ijtpp2020004 (cit. on pp. 36, 37).

[41] F. R. Menter, R. B. Langtry, S. R. Likki, Y. B. Suzen, P. G. Huang and S. Völker. 'A Correlation–Based Transition Model Using Local Variables–Part I: Model Formulation'. In: *Journal of Turbomachinery* (2006), pp. 413–422. DOI: 10.1115/1.2184352 (cit. on p. 37).

[42] R. B. Langtry, F. R. Menter, S. R. Likki, Y. B. Suzen, P. G. Huang and S. Völker. 'A Correlation–Based Transition Model Using Local Variables–Part II: Test Cases and Industrial Applications'. In: *Journal of Turbomachinery* (2006), pp. 423–434. DOI: 10.1115/1.2184353 (cit. on p. 37).

[43] F. R. Menter and R. B. Langtry. 'Transition Modelling for Turbomachinery Flows'. In: *Low Reynolds Number Aerodynamics and Transition*. Ed. by M. S. Genc. IntechOpen, 2012. Chap. 2. DOI: 10.5772/38675 (cit. on pp. 37, 38, 42, 53).

[44] M. E. Collins (Kelterer), R. Burgstaller and W. Sanz. 'Application of the gamma-Re theta transition model to transitional flow'. In: 10th International Symposium on Experimental and Computational Aerothermodynamics of Internal Flows. (4–7 July 2011) (cit. on p. 37).

[45] F. R. Menter, P. E. Smirnov, T. Liu and R. Avancha. 'A One-Equation Local Correlation-Based Transition Model'. In: *Flow, Turbulence and Combustion* (2015). DOI: 10.1007/s10494-015-9622-4 (cit. on pp. 43, 46, 53, 67).

[46] K. D. Walters and J. H. Leylek. 'A New Model for Boundary Layer Transition Using a Single-Point RANS Approach'. In: *Journal of Turbomachinery* (2004). DOI: 10.1007/s10494-015-9622-4 (cit. on p. 47).

[47] K. D. Walters and J. H. Leylek. 'Computational Fluid Dynamics Study of Wake-Induced Transition on a Compressor-Like Flat Plate'. In: *Journal of Turbomachinery* (2005). DOI: 10.1115/1.1791650 (cit. on p. 47).

[48] K. D. Walters and D. Cokljat. 'A Three-Equation Eddy-Viscosity Model for Reynolds-Averaged Navier–Stokes Simulations of Transitional Flow'. In: *Journal of Fluids Engineering* (2008). DOI: 10.1115/1.2979230 (cit. on pp. 47–49, 51–53, 88, 125, 139).

[49] J. Fürst, J. Příhoda and P. Straka. 'Numerical simulation of transitional flows'. In: *Computing* (2013). DOI: 10.1007/s00607-012-0266-0 (cit. on p. 47).

[50] M. Lopez and K. D. Walters. 'A Recommended Correction to the kT–kL–w Transition–Sensitive Eddy–Viscosity Model'. In: *Journal of Fluids Engineering* (2016). DOI: 10.1115/1.4034875 (cit. on pp. 47, 126).

[51] C. Bechter. 'Berechnung transitionaler Strömungen in Turbomaschinen mit Hilfe des Laminar-Kinetic-Energy-Modells'. in German. MA thesis. Graz University of Technology, 2014 (cit. on pp. 47, 61).

[52] M. Lopez and K. D. Walters. 'Prediction of transitional and fully turbulent flow using an alternative to the laminar kinetic energy approach'. In: *Journal of Turbulence* (2016). DOI: 10.1080/14685248.2015.1062509 (cit. on pp. 49, 50, 53, 68, 70, 71, 74, 111, 125, 139).

[53] P. Pieringer. *AiGrid 3D*. Version VS 1.3. Springer und Pieringer EDV. Dienstleistungen OEG. 11 July 2017. URL: http://www.acoustic-interfaces.at/sites/aigrid.htm (visited on 20 Mar. 2019) (cit. on pp. 56–58, 61, 75, 107).

[54] B. Yagdi. 'Numerische Untersuchung von Transition in Turbinenkaskaden'. in German. MA thesis. Graz University of Technology, 2012 (cit. on pp. 56, 58).

[55] ITTM, Graz University of Technology. *LINARS*. 2019. URL: https://www.tugraz.at/institutes/ittm/capabilities/simulations/computational-fluid-dynamics/ (visited on 17 Apr. 2019) (cit. on p. 58).

[56] R. Pecnik, P. Pieringer and W. Sanz. 'Numerical Investigation of the Secondary Flow of a Transonic Turbine Stage Using Various Turbulence Closures'. In: Volume 6: Turbo Expo 2005, Parts A and B. 2005, pp. 1185–1193. DOI: 10.1115/GT2005-68754 (cit. on p. 58).

[57] E. Bertolini, P. Pieringer, J. Woisetschläger and W. Sanz. 'Prediction of transition in a turbine cascade using LES'. In: 12th International ERCOFTAC Symposium on Engineering Turbulence Modelling and Measurements. (26–28 Sept. 2018) (cit. on pp. 59, 75, 87, 88).

[58] ANSYS Inc. *ANSYS FLUENT 19.1 Theory Guide*. 2018 (cit. on pp. 59, 61, 88, 125, 127, 131).

[59] ANSYS Inc. *ANSYS FLUENT 19.1 User's Guide*. 2018 (cit. on pp. 59, 61, 125).

[60] ANSYS Inc. *ANSYS CFX 19.1 Theory Guide*. 2018 (cit. on pp. 59, 61, 125).

[61] ANSYS Inc. *ANSYS CFX 19.1 User's Guide*. 2018 (cit. on pp. 59, 61, 125, 127).

[62] W. Sanz. *Lecture Notes: Computational Fluid Dynamics (319.082)*. Graz University of Technology, 2016 (cit. on p. 59).

[63] Python Software Foundation. *Python Language Reference*. Version 3.7.1. 12 Oct. 2018. URL: http://www.python.org (visited on 17 Apr. 2019) (cit. on p. 59).

[64] E. Jones, T. Oliphant, P. Peterson et al. *SciPy: Open source scientific tools for Python*. 2019. URL: http://www.scipy.org/ (visited on 17 Apr. 2019) (cit. on p. 59).

[65]  M. Waskom, O. Botvinnik, D. O'Kane, P. Hobson, J. Ostblom, S. Lukauskas et al. *mwaskom/seaborn: v0.9.0 (July 2018)*. July 2018 (cit. on p. 59).

[66]  Anaconda, Inc. *Anaconda Software Distribution*. Version 2018.12. Dec. 2018. URL: https://www.anaconda.com/distribution/ (visited on 17 Apr. 2019) (cit. on p. 59).

[67]  Tecplot, Inc. *Tecplot 360 EX*. Version 2017 R1. 2017. URL: https://www.tecplot.com/documentation/ (visited on 17 Apr. 2019) (cit. on p. 59).

[68]  J. Coupland. *Flat plate transitional boundary layers*. ERCOFTAC Fluid Dynamics Database. 1990. URL: http://cfd.mace.manchester.ac.uk/ercoftac/ (visited on 15 Mar. 2019) (cit. on pp. 62, 63, 72).

[69]  J. Coupland. *Flat plate transitional boundary layers*. ERCOFTAC Fluid Dynamics Database. 1990. URL: http://cfd.mace.manchester.ac.uk/ercoftac/database/cases/case20/Case_data (visited on 15 Mar. 2019) (cit. on pp. 62, 72).

[70]  N. Mayrhofer. 'Optische Strömungsmessung in Turbomaschinen mit Laser-Interferometern'. in German. PhD thesis. Graz University of Technology, 2001 (cit. on pp. 75, 77, 83).

[71]  N. Mayrhofer and J. Woisetschläger. 'Frequency analysis of turbulent compressible flows by laser vibrometry'. In: *Experiments in Fluids* 31.2 (1 Aug. 2001), pp. 153–161. ISSN: 1432-1114. DOI: 10.1007/s003480000268 (cit. on pp. 75, 77, 83, 86).

[72]  B. Hampel, N. Mayrhofer and J. Woisetschläger. 'Frequenzanalyse einer Turbinenschaufelgitterströmung mittels Laser-Vibrometer und holographischer Interferometrie'. in German. In: GALA-Fachtagung Lasermethoden in der Strömungsmeßtechnik. (10–12 Sept. 2002). ISBN: 3860092332 (cit. on pp. 83, 88).

[73]  G. Haller. 'An objective definition of a vortex'. In: *Journal of Fluid Mechanics* 525 (2005), pp. 1–26. DOI: 10.1017/S0022112004002526 (cit. on p. 87).

[74]  S. Kida and H. Miura. 'Identification and analysis of vortical structures'. In: *European Journal of Mechanics - B/Fluids* 17.4 (1998). Special Issue Dynamics and Statistics of Concentrated Vortices in Turbulent Flow (Euromech Colloquium 364), pp. 471–488. DOI: https://doi.org/10.1016/S0997-7546(98)80005-8 (cit. on p. 87).

[75]  T. Arts, M. Lambert de Rouvroit and A. W. Rutherford. *Aero-thermal investigation of a highly loaded transonic linear turbine guide vane cascade. A test case for inviscid and viscous flow computations*. Von Karman Institute for Fluid Dynamics, 1 Sept. 1990. URL: https://repository.tudelft.nl/view/aereports/uuid:1bdc512b-a625-4607-a339-3cc9b371215e (visited on 25 Sept. 2018) (cit. on pp. 89, 90, 92, 105).

[76] R. Pecnik, W. Sanz, A. Gehrer and J. Woisetschläger. 'Transition Modeling Using Two Different Intermittency Transport Equations'. In: *Flow, Turbulence and Combustion* (2003). DOI: 10.1023/B:APPL.0000004983.49982.69 (cit. on p. 93).

[77] R. Spataro. 'Aerodynamic Design and Investigation of an Embedded Concept for Turning Mid Turbine Frames'. PhD thesis. Graz University of Technology, 2013 (cit. on p. 106).

[78] P. Bader and W. Sanz. 'On Boundary Layer Relaminarization in an Highly Accelerated High Pressure Turbine Stator Flow'. In: Turbo Expo: Power for Land, Sea, and Air. 2017. DOI: 10.1115/GT2017-63296 (cit. on pp. 106, 107, 109, 112).

[79] B. M. Akin and W. Sanz. 'The Influence of Transition on CFD Calculations of a Two-Stage Counter-Rotating Turbine'. In: Turbo Expo: Power for Land, Sea, and Air. 2014. DOI: 10.1115/GT2014-26044 (cit. on p. 106).

[80] P. Bader and W. Sanz. 'Steady and Unsteady CFD Calculation of the Laminar-to-Turbulent Transition in a Turning Mid Turbine Frame With Embedded Design'. In: Turbo Expo: Power for Land, Sea, and Air. 2015. DOI: 10.1115/GT2015-42617 (cit. on p. 106).

[81] R. Spataro, E. Göttlich, C. Santner and F. Heitmeir. 'A Numerical Comparison on the Aerodynamic Performances of a Two-stage Two-spool Turbine Facility Predicted by Steady and Unsteady Simulations'. In: 2013, pp. 827–839. URL: https://www.euroturbo.eu/publications/proceedings-papers/etc2013-039/ (visited on 26 May 2019) (cit. on pp. 106, 107).

[82] A. Arnone and R. Pacciani. 'IGV-rotor interaction analysis in a transonic compressor using the navier-stokes equations'. In: *Journal of Turbomachinery* (1996) (cit. on p. 112).

[83] J. Fürst. 'Numerical simulation of transitional flows with laminar kinetic energy'. In: *Engineering MECHANICS* (2013). DOI: 10.1007/s00607-012-0266-0 (cit. on pp. 88, 125).

[84] J. Fürst. *Turbulence model repository*. URL: https://github.com/furstj/myTurbulenceModels/tree/master/turbulenceModels/RAS (visited on 28 Apr. 2019) (cit. on p. 126).

[85] The OpenFOAM Foundation. *OpenFOAM*. 2019. URL: https://openfoam.org/ (visited on 28 Apr. 2019) (cit. on p. 126).

[86] ANSYS Inc. *Release Notes 16*. ANSYS Inc. 2015. URL: http://storage.ansys.com/doc_assets/release_notes/Release_Notes_160.pdf (visited on 20 Mar. 2019) (cit. on p. 133).

[87]    A. Hellsten. 'Some improvements in Menter's k-omega SST turbulence model'. In: 29th AIAA, Fluid Dynamics Conference. (15 June 1998). American Institute of Aeronautics and Astronautics. DOI: 10.2514/6.1998-2554 (cit. on p. 135).